AERODYNAMIC LOAD CONTROL OF WIND TURBINES

Mustafa Ibrahim Salim Al-Guburi

Submitted in accordance with the requirements for the degree of
Doctor of Philosophy

The University of Leeds
Institute of Thermo-fluids (iTF)
School Of Mechanical Engineering

January, 2021

The candidate confirms that the work submitted is his own, except where work which has formed part of jointly-authored publications has been included. The candidate confirms that appropriate credit has been given within the thesis where reference has been made to the work of others.

Acknowledgements

I would like to sincerely thank my supervisors, Dr Andrew shires and Dr Carl Gilkeson for their inestimable assistance and patience throughout my PhD journey. Their insights and valuable advice paved the road toward accomplishing the goals of this work.

I would like to acknowledge the Higher Committee for Education Development in Iraq (HCED) for funding my PhD.

I am indebted to my beloved wife Randa, my wonderful daughter Basma and the lovely twins Sama and Mazin for their everlasting support and love during my PhD

I wish to express my love and gratitude to all my family, especially my father, Ibrahim, my mother, Suaad, my brothers Mazin and Salim and my kind sisters Alaa, Israa and Taymaa, for their support, patience and understanding through all stages of my life and especially during my PhD.

Also, for all my friends with special thanks to the Elite – especially Caesar Saad, Hasanain Ayed and all my colleagues at the University of Leeds for their friendship, input and valuable discussions.

Finally, I would like to extend the acknowledgement to Mr. Yaser Taha, Mr. Hayder Yaareb, Mr. Zaydoon Tareq, Dr Farqad Talib and Dr Ali Hussain for their continuous encouragement during my study.

Abstract

The energy captured by a wind turbine is limited due to the variability of wind speed and direction during typical operating conditions, and also by the efficiency of the turbine (or power coefficient), which represents the amount of power that can be extracted from the available wind power. Utilizing passive and active flow control devices has the potential to improve the energy capture, especially in the pre-stall region. This can be achieved by changing the local aerodynamic characteristics on the aerofoil/blade to increase lift at low wind speeds, potentially allowing the turbine to capture more energy between the cut-in and rated wind speeds. This study explores the feasibility of using circulation control to improve the performance of horizontal axis wind turbines (HAWTs). Firstly, the baseline offshore NREL 5 MW HAWT model was analysed to validate the modelling approach and to determine the most effective region on the blade and its operating conditions, for flow control. Subsequently, a 2D parametric study was performed to generate a high-performance aerofoil with integrated circulation control. Parameters including the jet opening height, its chord-wise location and trailing edge curvature (based on an ellipse) were considered. Results from twenty-eight different combinations of these parameters highlight a robust design solution. This solution is then evaluated over a 5% span-wise region along the NREL 5 MW baseline wind turbine blade, for a range of steady wind speeds and nozzle pressure ratios (NPR). Results show that passive control using centrifugal pumping does not generate a sufficient mass flow rate to be aerodynamically effective. As an alternative, forced pumping using a compressor has the capacity to increase the shaft power at all wind speeds, of up to 11% and 18.4% for NPR ratios of 1.5 and 1.8, respectively. However, the estimated cost to provide this pressurised air exceeds the power gained, and further investigation is required to develop the overall concept.

Table of Contents

List of figures

List of tables

List of abbreviations

2D	Two-dimensional
3D	Three-dimensional
AFC	Active flow control
AOA	Angle of Attack
BEM	Blade Element Momentum Theory
BL	Boundary Layer
CC	Circulation Control
CFD	Computational Fluid Dynamics
COE	Cost of energy
DNS	Direct numerical simulation
FAST	Fatigue, Aerodynamics, Structures, and Turbulence
FDM	Finite difference method
FEM	Finite element method
GWEC	Global wind energy council
HAWT	Horizontal axis wind turbine
INS	Indirect numerical simulation
LE	Leading edge
LES	Large eddy simulation
NACA	National Advisory Committee for Aeronautics
NPR	Nozzle Pressure Ratio
NREL	National Renewable Energy Laboratory
RANS	Reynolds-Averaged Navier-Stokes
RSM	Reynolds Stress Model
SA	Spalart-Allmaras
SIMPLE	Semi implicit method for pressure linked equations
SST	Shear Stress Transport
TE	Trailing edge
TSR	Tip speed ratio
VAWT	Vertical axis wind turbine
V & V	Verification and validation
ZNMF	Zero net-mass flux

Nomenclature

A	Swept area
AOA	Angle of Attack
a	Axial induction factor
a'	Tangential induction factor
a_1, a_2, a_3	Semi-major axis of the ellipse
b	Semi-minor axis of the ellipse
B	Number of blades
c	Chord length
C_d	Drag Coefficient
C_l	Lift Coefficient
C_m	Moment Coefficient
C_P	Power Coefficient
C_p	Pressure Coefficient
c_p	Specific heat at constant pressure
$C\mu$	Blowing Coefficient
f	Friction factor
F_t	Tangential force
F_n	Normal force
h	Nozzle height
M	Mach Number
$\dot{m}$	Mass flow rate
P	power
p	Pressure
Q	Torque
R	Blade length
r	Radial spanwise position
R_g	Gas constant
Re	Reynold number
T	Temperature
U_∞	Free stream wind velocity
U_r	relative wind velocity
u	X-Velocity Component

v	Y-Velocity Component
z	Z-Velocity Component
$y+$	Nondimensional cell wall distance

Greek letters

β	Pitch angle
γ	Specific heat ratio
δ	Boundary layer thickness
μ	Dynamic Viscosity
υ	Kinematic Viscosity
ρ	Density
τ_w	Wall shear stress
Ω	Rotor angular velocity
ω	Wind rotational speed

Subscripts

∞	Free-stream condition
j	Jet
o	Stagnation condition
p	Plenum

Chapter 1 INTRODUCTION

1.1 General overview

Wind power is a renewable source of energy, the amount of air used to generate electrical power today will not deplete in the future [1]. Wind energy is also a clean source of non-polluting electricity [2]. Unlike conventional power plants, wind farms emit no air pollutants or greenhouse gases, which lead to global warming phenomena [3]. Wind power or wind energy is the process by which the wind is used to generate mechanical or electrical power and is one of the fastest-growing forms of electrical power generation in the world. In 2018, the global cumulative installed wind capacity increased to 591 GW [4]. Figure 1-1 shows the global wind power capacity and its growth during the past two decades; the use of wind energy has increased by a factor of about 25. In the UK alone, the total onshore wind turbine installation is up to 13 GW and about 10 GW offshore [4].

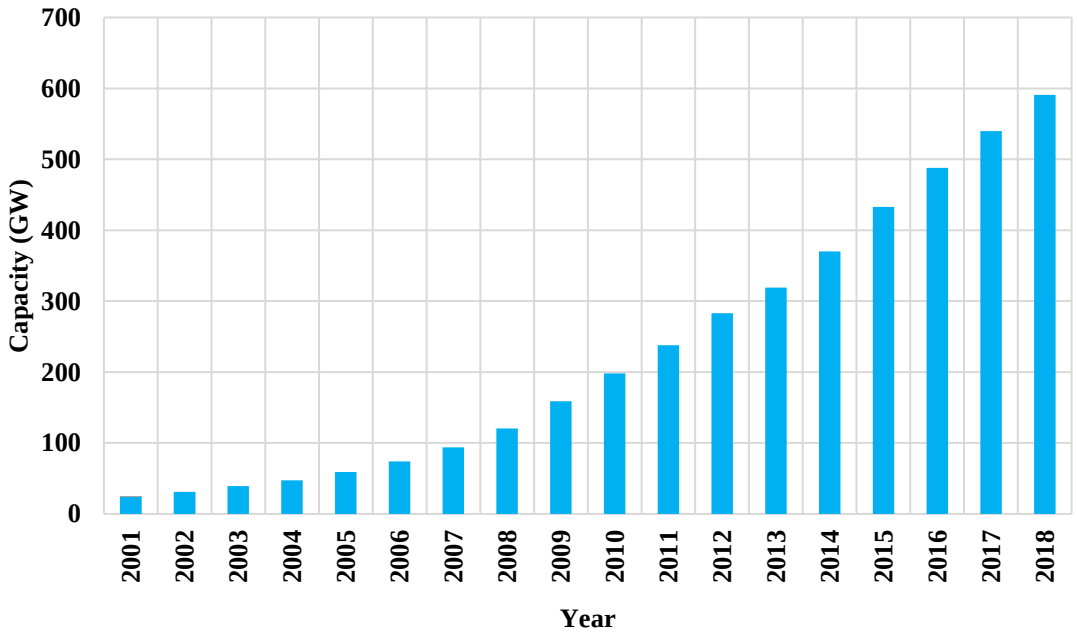

Figure 1-1: The global wind power capacity 2001–2018 [4]

Western European countries spend great efforts to replace the traditional fossil fuel-based energy production methods by renewable energy. For example, Denmark has a suitable wind speed average of about 5 m/s at 10 m height, so they take advantage of this situation to produce about 47 % of total energy generated from wind [4] . Moreover, they

have a future vision to achieve exclusively renewable energy by 2050. Their plan includes the exporting of any surplus power to adjacent countries [5].

Historically, the first evidence of using windmills was found in the middle-east about 900 AD [5, 6]. The main purpose of these mills was to grind grain or pump water. Posteriorly, these windmills have been utilized to produce electrical power by connecting it with electrical generators by, for example, James Blyth (in 1887), which is the concept of a wind turbine [7]. Later on, the development of wind power to generate electricity can be broken down into three main stages:

- **Early 1900s**: Primarily attempts to produce electrical power by wind turbines. The first designs could only produce energy at low rates and it was stored in batteries. The interest in this type of electrical production had gradually decreased later on due to the high productivity and relatively low capital costs of diesel generators , water turbines and steam turbines [7, 8].
- **1973:** The international oil crisis that occurred that year brought renewed attention to wind energy [3, 8]. Many industrial countries planned to be less dependent on the imported oils. Therefore, they sponsored a number of research programmes in order to develop renewable energy sources, especially wind power.
- **Late 1990s-now:** The direct impact of conventional electrical power sources and impact on global warming and greenhouse phenomena has been raised [4]. The environmental concerns led wind power to be one of the most promising types of power production over the past two decades as many global agreements were made. For example, the Kyoto protocol (1997) and the Paris agreement (2015) indicate the commitment of key nations to develop clean sources of energy to combat climate change. This stage has coincided with the maturation of the industry and associated reductions in costs and withdrawal of subsidies have been realised, ensuring that wind is becoming increasingly competitive with fossil fuels.

1.2 Advantages of wind energy

Generating electrical power by means of wind turbines provides two main advantages, which are:

- **Environmental:** Wind turbines produce clean and safe energy without CO_2 emission, not including those associated with the manufacture, installation and (eventually) disposal. Therefore, it does not contribute to both global warming and

acid rain, which are the major problems with fossil fuels. Moreover, there are no risks of disasters which can occur in, for example, the nuclear industry [3, 8].

- **Economical:** Countries who depend on imported oil or coal could be less dependant and more self-sufficient if they use alternative renewable sources such as wind, solar or tidal power. Additionally, investments in renewable energy will provide new jobs as it needs qualified labour during the manufacturing, installation and maintenance processes [9].

1.3 Issues and concerns

Despite its valuable long-term advantages, there are some drawbacks of wind power as discussed below:

- **Cost:** Compared with fossil-fuelled power plants, wind power requires higher capital cost [8]. Figure 1-2 shows the capital cost percentages for an onshore wind turbine [10] which indicates that the main cost (about 80%) is for wind turbine components. However, wind power is a very promising technology if the levelised cost of electricity (LCOE) is considered, which includes operations, maintenance and decommissioning costs over the lifetime of the project and is therefore more comparable with energy produced from other means such as nuclear [3, 11]:

$$\text{LCOE} = \frac{\text{Capital Cost} + \text{Operations Cost} + \text{Maintenance}}{\text{Lifetime Energy Production}}$$

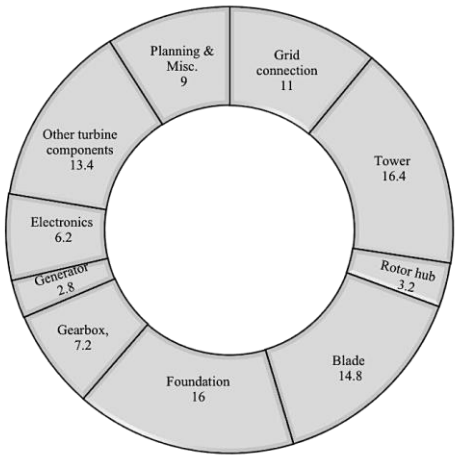

Figure 1-2: Capital cost breakdown of a typical onshore wind turbine [10]

- **Secondary environmental issues:** These issues include acoustic noise, visual impact and bird deaths. High levels of mechanical and aerodynamic noise can be

produced as the blades rotate. The rotation can also cause the death of the birds and bats flying near the turbines. Generally, these issues have been solved or reduced by selecting the proper locations, particularly those in offshore regions [8, 9].

- **Energy storage and transmission:** The sun is the main driver of wind energy on earth [12]. Wind is caused by unequal heat distribution on the earth's surface [2]. The ratio of absorption of heat is different between an area of water and an area of land. During the day, the seas absorb the sun's heat gradually then release it in the same way during the night. On land these phenomena occur more quickly, this makes a temperature difference. At the surface, warm air rises leaving a low-pressure zone leading to a pressure gradient; this initiates wind movement from high pressure zones to lower ones. Furthermore, the Coriolis force caused by the earth's rotation and the frictional forces at the earth's surface are also associated with creating the world's major wind systems [12]. In addition, wind may not always be available at the most demanding electricity times, which represents the main challenge in the wind power field. Wind power cannot easily be stored, although small-scale power generation can be stored in batteries [2, 3]. Moreover, suitable wind sites are often located far from cities or electrical power consumers so transmitting power is a major challenge. Using hybrid electrical power systems, which combine alternating types of power, could alleviate this issue.

1.4 Motivation

Due to a significant evolution of the size of wind turbines during the last two decades, more power capture is typically sought through increases in the swept area [5] as shown in Figure 1-3. For instance, the largest wind turbine is the upgraded Vestas V164, providing 9.5 MW of rated power which was scheduled to be installed in the North Sea (near Belgium) in 2019. This offshore wind turbine design has an overall height of 220 m and is 164 m in diameter [13]. However, larger blade length leads to an increase in blade weight, which leads to greater fatigue load of the rotor (more details in section 2.6) and supporting tower. Consequently there is a research interest on increasing the aerodynamic efficiency of wind turbines, by applying different types of flow control devices for example, to increase capacity without increasing size and weight. These devices are mainly adopted from advances and applications in aircraft aerodynamics [14].

For this research it is important to have a suitable baseline but there is a scarcity of geometry and performance data in the public domain for commercial MW scale horizontal axis wind turbines,. The US National Renewable Energy Laboratory (NREL) developed a theoretical 5 MW baseline wind turbine for this purpose, with a blade length of 63 m [15], which is closely based on the REpower 5M turbine, and has been extensively used by researchers for the development of computational methods and the evaluation of flow control [16]. These studies have implemented different types of passive and active flow control devices such as: multiple dielectric barrier discharge (multi-DBD) plasma actuators [17], vortex generators (VGs) and Gurney flaps (GFs) [16] and microtab, micro jet and divergent trailing edge (DTE) designs [18]. Active flow devices can be utilized to increase the torque of the blade at low wind speeds, allowing the turbine to cut-in and capture more energy at an earlier stage. Also, it can be used as an emergency shut down device in case of extreme gust conditions [19].

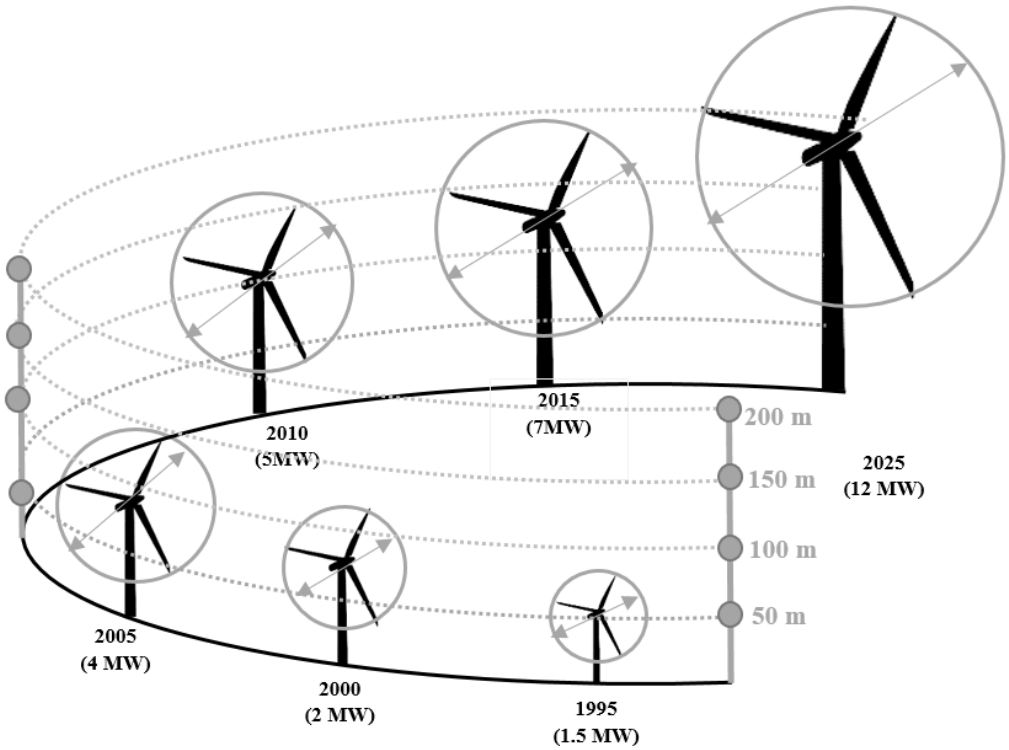

Figure 1-3: Wind turbines' size trend, adopted from [16]

One of the most promising techniques is the application of circulation control (CC). It has been demonstrated for various aerospace applications [20] but is relatively untried for wind energy. Here, a CC device is typically located at the trailing edge of an aerofoil and consists of jet nozzles that blow high momentum flow tangentially over a rounded trailing edge. The presence of the air jet produces a pressure force, which deflects the jet

streams toward the aerofoil surface. If there is a rounded trailing edge surface, the pressure force can overcome the centrifugal force of the jet, leading to flow curvature which is known as the Coanda effect [21, 22] and is explained in more detail in section 2.6.4. As a consequence the rear flow separation point will be delayed and move toward the lower side of the aerofoil, thereby increasing circulation and lift. The trailing edge shape and curvature is a critical factor in the successful application of this technique; deploying a large radius rounded trailing edge increases the Coanda effectiveness and therefore lift. However, this also leads to a high drag penalty. To minimise this, the lower surface of the trailing edge can be designed with a flat surface while keeping the upper surface highly cambered. The cambered upper surface creates a large jet-turning angle, producing high lift. Circulation control technology offers great potential to increase the lift and therefore the power generation assisting in-turbine rotation start-up and low speed performance. However this is dependent on whether the additional aerodynamic drag, weight and manufacturing cost of the installation of CC within turbine blades can be overcome [23].

1.5 Research objectives

The main aim of this research is to investigate the potential benefits of applying a circulation control technique to a horizontal axis wind turbine (HAWT) blade. This investigation is taking into account the aerodynamic benefits and balancing these with relevant energy losses. The literature review in chapter 2 describes the gaps in knowledge (section 2.8) which will be addressed by satisfying the following objectives:

1. Develop a validated approach to modelling the aerodynamic performance of rotating HAWT blades, and of CC aerofoils, using CFD. This requires a thorough understanding of prediction approaches and analysis of flow around a typical blade.
2. Review the applicability of the common flow control techniques and with an emphasis on the benefits of circulation control technology applied to a HAWT and to generate a new 2D aerofoil which harnesses circulation control.
3. Investigate the feasibility of integrating the new aerofoil design to a large, commercial, three-dimensional HAWT for the purpose of power augmentation via circulation control.
4. Determine the required amount of energy needed for a useful gain in net power generation, accounting for overall gains and losses.

1.6 Thesis structure

This thesis consists of eight chapters. The general background on worldwide wind power generation capacity and main advantages and issues have already been introduced in this chapter.

Chapter 2 will illustrate the aerodynamic performance of modern wind turbines focusing on HAWT designs, which will be considered in this research. The main components and terminology of HAWTs are defined. Also, the concepts of the main active flow control devices and their operation are reviewed.

In chapter 3, a review of the methods of prediction and analysis of flow around a given wind turbine is conducted, especially relating to the Blade Element Momentum (BEM) theory and computational fluid dynamics (CFD).

Three-dimensional numerical simulations are developed in chapter 4 for two baseline HAWT geometries, to verify the modelling approach by comparing the CFD results with experimental data.

In chapter 5, a 2D parametric study is described to generate a high-performance aerofoil integrating circulation control. Parameters including the jet opening height, its chord-wise location and trailing edge curvature (based on an ellipse) are considered.

In chapter 6, the 2D-CC aerofoil design is adapted and applied to a high-fidelity three-dimensional model of the NREL 5 MW wind turbine, and the required cost of pumping is calculated and discussed.

Chapter 7 discusses key elements of this study and finally, in chapter 8, the conclusions and outlook for the future work are presented.

Chapter 2 LITERATURE REVIEW

2.1 Introduction

In the first part of this chapter (section 2.2), the configuration of typical HAWTs and their components and operational conditions will be discussed. The second part (sections 2.3 to 2.5) discusses the aerofoil theory including forces and boundary layer description. The third part (section 2.6) briefly summarises different flow control techniques with a more detailed study on circulation control, including a comparison among commonly used devices with consideration for their structural design, maintenance and cost. In section 2.7, a review of related work is carried out on the integration of circulation control for aerodynamic applications and possible numerical methods to predict the flow around HAWTs. Finally, the gaps in knowledge and research questions are addressed.

2.2 Overview of Horizontal Axis Wind Turbine (HAWT) technology

There are two types of wind turbines depending on the blade rotation axis. The first type is the vertical axis wind turbine (VAWT). The second type is the horizontal axis wind turbine (HAWT) [11, 12]. The general configurations of these types are shown in Figure 2-1.

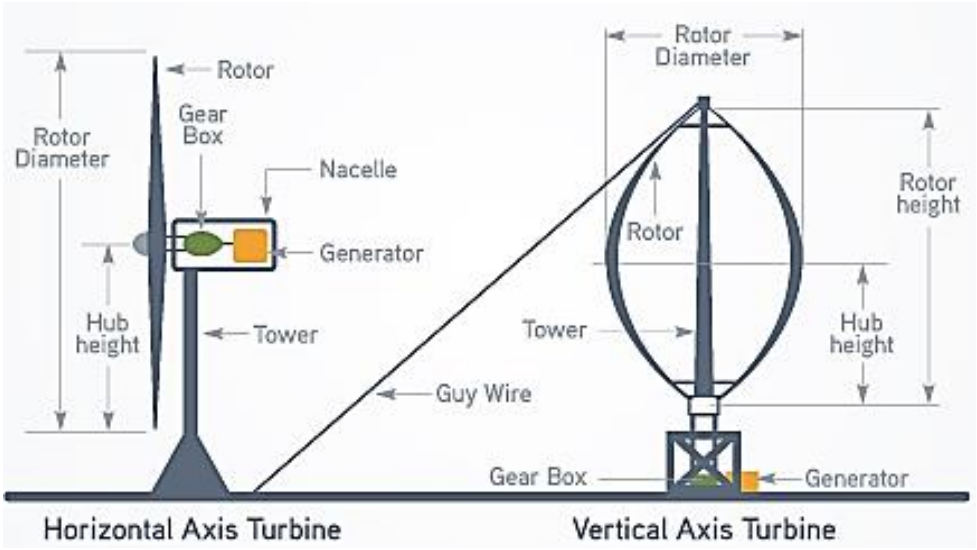

Figure 2-1: Types of wind turbines [24]

A HAWT rotates around a horizontal axis and has the main rotor shaft and electrical generator mounted at the top of a tower. There are two types of HAWT, upwind and downwind designs [24]. For the more common upwind design**,** the generator shaft is positioned horizontally, and the wind encounters the blade before the tower. Turbine blades are made stiff to prevent them from being deflected into the tower by high winds,

and they are placed at a sufficient distance in front of the tower and are sometimes tilted up by a small amount. For the downwind type, the generator shaft is positioned horizontally, and the wind encounters the tower first and then the blade. Horizontal downwind does not need an additional mechanism for keeping it in line with the wind, and in high winds the blades can be allowed to bend, which reduces their swept area and thus their wind resistance. However, tower's wake effect should be considered (more details in section 3.3).

2.2.1 Basic components of the HAWT

Typical wind turbines involve a set of rotor blades (usually two or three) rotating around a hub. The hub is connected to a gearbox and a generator, located inside the nacelle, which houses the electrical components. The basic components of a wind turbine system are shown in Figure 2-2 and outlined as follows [25]:

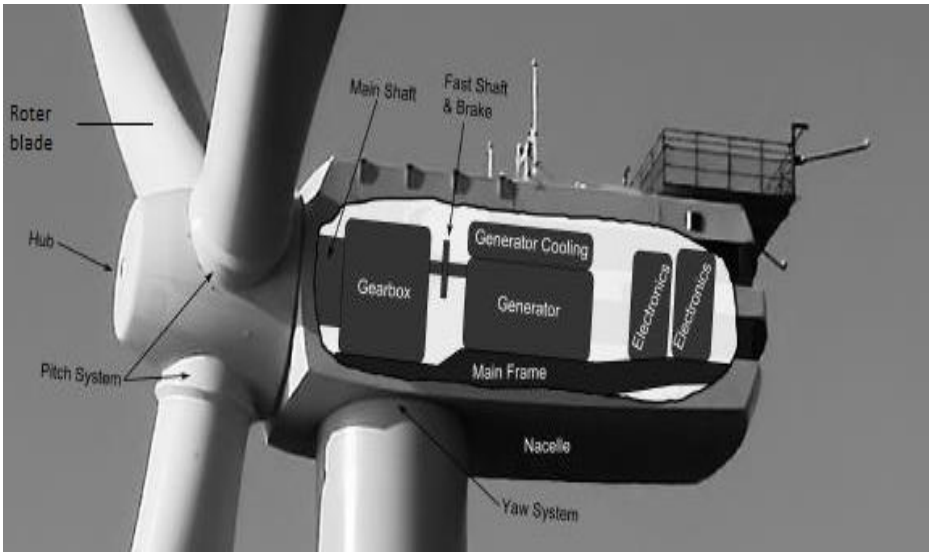

Figure 2-2: Basic components of HAWT [24]

- **The nacelle:** Located on the top of the wind turbine tower and involves the main shaft, the gearbox, the fast shaft, the brake, the generator and electrical components and the yaw system.
- **Rotor blades:** The blades' diameter is a pivotal factor in turbine power generation. Generally, the output power increases with the diameter. The number of rotor blades greatly impacts a given wind turbine performance. The term solidity defines the total blade area over the swept area. Small turbines may have more than 3 blades (high solidity), but these are usually suitable for low rotational speed wind turbines. On the other hand, high rotational speed wind turbines typically have only 2 or 3 blades and can hence achieve similar wind energy utilization with low solidity and driving torque [26, 27]. Increasing the number

of blades to more than 3 can improve slightly the power coefficient but this will lead to greater costs. Additionally, the blade design and materials also affect the output power. Blades are usually made of fiberglass reinforced with polyester, carbon fibre or wood epoxy [5].

- **Gearboxes and direct drives:** Wind turbines often utilise a gearbox to increase the shaft's rotational speed (typically 18 - 50 RPM) to a speed suitable for the generator (typically 1500 RPM). Recently, new research is investigating the use of direct drive generators with no gearbox to avoid the power losses and gears' cost [5] .
- **Brake:** In case of very high winds and storms, it is essential to stop the turbine's rotation to protect the turbine components from damage.
- **Controller:** A combination of electrical and electronic components, which regulate the turbine speed. Normally, the controller starts up the turbine at wind speeds around 3.5 to 6 m/s and stops the turbine at around 25 m/s, to avert the damage caused by high winds.
- **Generator:** Converts the mechanical power (shaft rotation) to 60-cycle alternating current (AC) electricity.
- **The yaw mechanism:** This mechanism is responsible for turning the nacelle as the wind direction changes to enable the blades to face towards the wind. Additionally, the yaw system prevents the rotor blades from damage under severe wind conditions. Usually, the yaw mechanism is equipped with sensors such as a traditional anemometer and wind vanes to detect the wind velocity and direction, respectively. More advanced technologies are used in modern wind turbines such as Light Detection and Ranging (LIDAR) system, which is a laser-based optical remote sensing method used to measure the speed of aerosols (e.g. dust, water, pollution) traveling in the wind. To do this, light produced by a moving laser beam is reflected by individual aerosols with changes in frequency of the emitted light allowing the doppler shift to be determined. This in turn enables measurement of the wind speed and direction from a distance [1].
- **Tower:** Supports the nacelle and rotor blades. It is typically made as a hollow steel tube, enabling access and electric cables to pass through it to be connected to the electricity network.

- **Base:** Onshore turbines are constructed on a concrete base foundation. These foundations ensure easy tower erection or dismantling as well. For offshore turbines, the base of the turbine can be gravity-type, monopile, tripod or jacket foundations [28]. The selection criteria for these types depends on the depth of water and the type of the soil under the water. Figure 2-3 shows various types of offshore foundations.

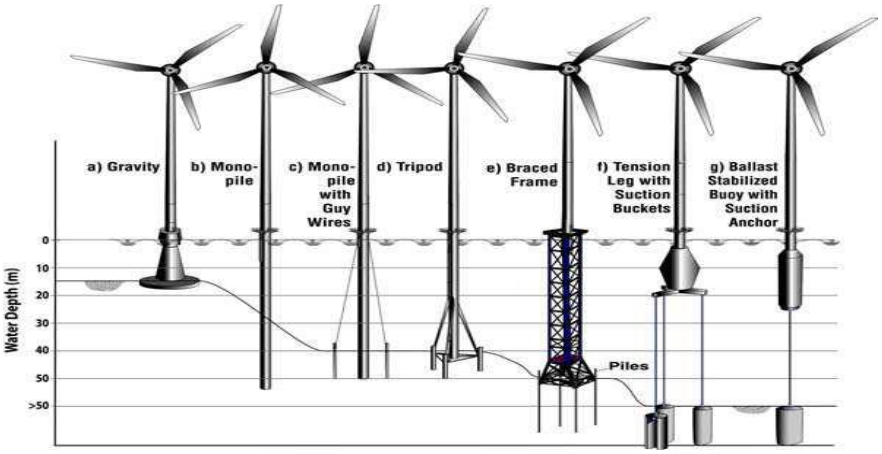

Figure 2-3: Types of offshore foundations [28]

2.2.2 Wind turbine design speed

There are three design speeds that should be considered to extract the optimum output power from a wind turbine, which are illustrated and defined as below [29] and shown in Figure 2-4:

- **Cut-in speed**: The minimum wind speed that allows the wind turbine to produce applicable power. This wind speed is commonly between 3.5 to 6 m/s for most turbines [1].
- **Rated speed**: Rated wind speed, which is between 11 to 15 m/s, enables wind turbines to produce rated designed power. At the region between cut-in and rated speeds, the power output is directly related to the wind speed, i.e. the output power increases as the wind speed increases. To maximise the energy yield of a wind turbine, flow control techniques can potentially be utilised to improve aerodynamic efficiency over this range. Above the rated speed it is necessary to curtail power to the rated value typically by using blade pitching for large rotors, otherwise using stall regulation.
- **Cut-out speed**: for the safety of wind turbine components, it is necessary to cease the power generation at very high wind speeds or gusts. The wind speed at which shutdown occurs is usually between 20 to 35 m/s [1].

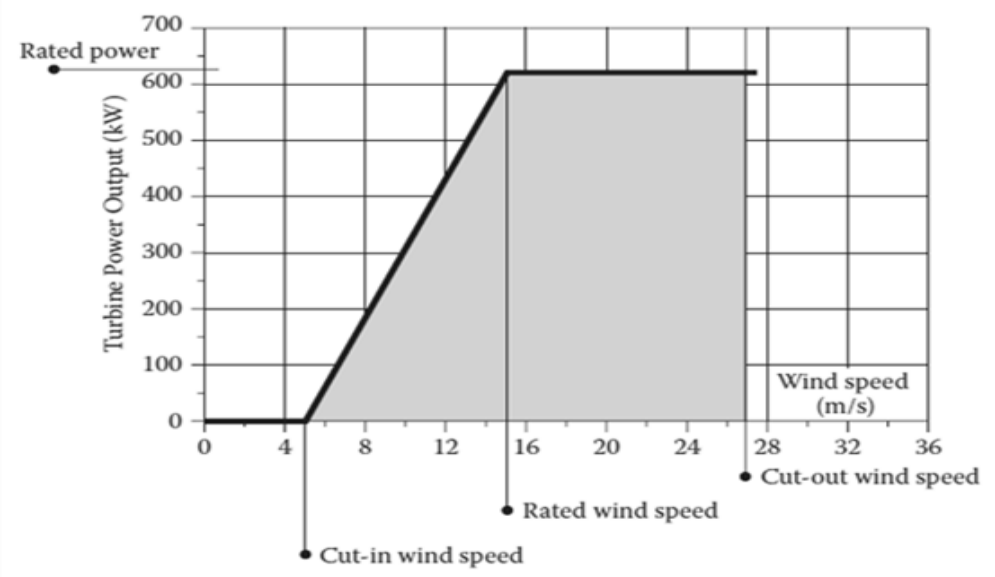

Figure 2-4: Typical wind turbine design speeds [1]

2.2.3 Power output from an ideal turbine

Wind turbines convert the available kinetic energy from wind into mechanical and subsequently electrical power by generators. In this regard, extracting the maximum energy from the wind is the principal purpose of wind turbine design. The kinetic energy available in wind, *E*, is given by:

$$E = \frac{1}{2} m U_{\infty}^2 \tag{2-1}$$

where *m* is the mass (kg) contained in a cylindrical volume of air of a unit length that will pass through the rotor and U_{∞} is the free-stream wind speed (m/s) in front of the rotor. Therefore, the available power, P_a, which is the energy derivative with respect to the time is:

$$P_a = \frac{dE}{dt} = \frac{1}{2} \frac{dm}{dt} U_{\infty}^2 \tag{2-2}$$

Here, $\frac{dm}{dt}$ is the mass flow rate, $\dot{m}$, and it is defined as:

$$\dot{m} = \rho A U_{\infty} \tag{2.3}$$

where ρ is the air density (kg/m^3) and *A* is the area swept by the turbine blades (m^2). Hence, Equation 2-2 can be re-written as follows:

$$P_a = \frac{1}{2} \rho A U_{\infty}^3 \tag{2-4}$$

Equation (2-4) indicates the significance of the free-stream wind speed because of its cubic relationship to wind speed. Accordingly, installing wind turbines in a high wind speed region should be a primary consideration.

If all the available power in the wind is extracted, then, in theory, air velocity would be reduced down to zero behind the rotor (i.e. no flow) which is impractical behaviour [27]. In practice, there is a maximum theoretical limit of the extracted power, P_e, which is achievable from a wind turbine. The ratio between the extracted power and the available power is defined as the power coefficient, C_P, for the wind turbine, namely:

$$C_P = \frac{P_e}{P_a} \tag{2-5}$$

Many aerodynamic models have been developed in order to describe the energy conversion process. The simplest model is the actuator disc model which is based on theoretical assumptions and is independent of rotor design.

The concept is based on more than a century-old Rankine-Froude momentum theory for an actuator disk, which was first applied for propellers. The axi-symmetric stream tube shown in Figure 2-5, is commonly assumed to simplify the analysis and predict the theoretical performance limits for a wind turbine. Here, a permeable (porous) disc represents the turbine rotor which allows the air to flow through it. The theory assumes incompressible steady uniform flow upstream of the disc, unchanged velocity at the disc, no flow rotation formed by the rotor and that the flow passing through the disc is unaffected by the outside free-stream. the actuator disc reduces the momentum of the flow in the plane of the rotor, with the result that the flow decelerates as it approaches the rotor and further decelerates downstream of the rotor until a steady flow is recovered in the wake. Therefore, the corresponding static pressure will increase as well as the cross-sectional area as the flow expands to maintain an equal mass flow rate along the stream-tube according to the mass conservation principle.

The thrust force, F_x, in the stream tube provided by the rotor is equal and opposite to the rate of change of momentum, according to Newton's 2nd law. Therefore, using the numbered locations on the stream tube shown in Figure 2-5, F_x is given by:

$$F_x = U_1 (\rho A_1 U_1) - U_4 (\rho A_4 U_4) \tag{2-6}$$

Also, the mass flow rate is the same along the stream tube, hence:

$$\dot{m} = \rho A_1 U_1 = \rho A_4 U_4 \tag{2-7}$$

Equation (2-6) can be also be written as follows:

$$F_x = \dot{m} (U_1 - U_4) \tag{2-8}$$

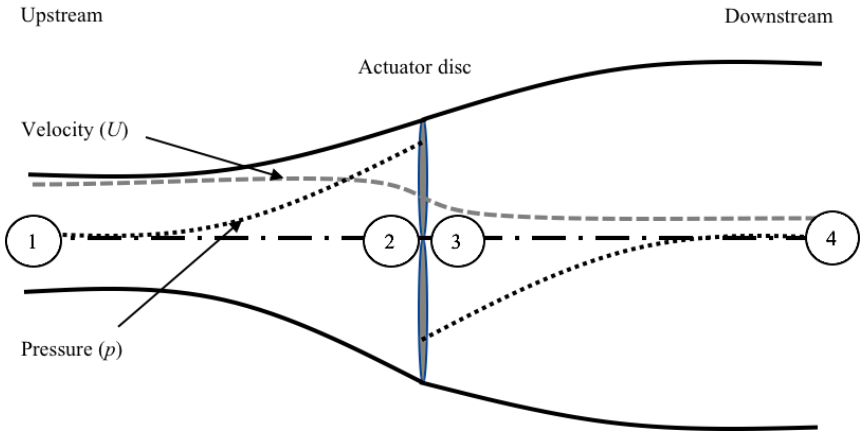

Figure 2-5: Actuator disc model [27]

Now Bernoulli's principle can be applied on either side of the disc separately, without work done. Upstream, the air enters the stream tube at point 1 with free-stream conditions for both velocity and static pressure. Then as the air approaches the disc at point 2, the velocity will gradually slow down while the static pressure increases. Therefore, applying Bernoulli's theorem:

$$p_1 + \frac{1}{2}\,\rho\, U_1^2 = p_2 + \frac{1}{2}\,\rho\, U_2^2 \qquad (2\text{-}9)$$

Downstream, the velocity across the disc is unchanged and it is less than the free-stream, while the static pressure rises gradually until it reaches the ambient static pressure toward the outlet of the stream tube, which is expressed mathematically as follows:

$$p_3 + \frac{1}{2}\,\rho\, U_3^2 = p_4 + \frac{1}{2}\,\rho\, U_4^2 \qquad (2\text{-}10)$$

The thrust force can be also defined as the net of the forces acting on the disc sides. Since the disc cross-sectional area is the same ($A_2 = A_3$), therefore:

$$F_x = (p_2 - p_3)\, A_2 \qquad (2\text{-}11)$$

Air leaves the disc with the same velocity, $U_2 = U_3$. Also, both the inlet and the outlet static pressure are equal to the free-stream static pressure, i.e. $p_1 = p_4$. The combination of Equations (2-9) and (2-10) and substituted into (2-11) yields:

$$F_x = \frac{1}{2}\,\rho\, A_2\, (U_1^2 - U_4^2) \qquad (2\text{-}12)$$

Next, substituting Equation (2-12) into (2-8) and recalling that the mass flow rate at the disc is $\dot{m} = \rho\, A_2\, U_2$, gives:

$$U_2 = \frac{1}{2}\,(U_1 + U_4) \tag{2-13}$$

Clearly, this indicates that the air velocity at the disc is the average of the inlet and outlet velocities. Considering that U_2 is a fraction of the free-stream velocity U_1, it is possible to introduce an axial induction factor, a, as follows:

$$a = \frac{U_1 - U_2}{U_1} \tag{2-14}$$

Then,

$$U_2 = U_1\,(1 - a) \tag{2-15}$$

Accordingly, substituting in Equation (2-13), gives:

$$U_4 = U_1\,(1 - 2a) \tag{2.16}$$

The extracted power, P_e, is equal to the thrust multiplied by the velocity at the disc. Recalling that U_1 is the freestream velocity, U_∞ and substituting Equations (2-15) and (2-16) into (2-12), yields:

$$P_e = \frac{1}{2}\,\rho\, A_2\, U_\infty^3\, 4\, a\, (1-a)^2 \tag{2-17}$$

where A_2 is the swept area. To determine the power coefficient, C_P, for the wind turbine, substituting Equation (2-17) into (2-5) gives:

$$C_P = 4\, a\, (1-a)^2 \tag{2.18}$$

For the maximum power coefficient, Equation (2-18) can be derived in respect to a and equated to zero, as follows:

$$\frac{dC_P}{da} = 4\,(1-a)(1-3a) = 0 \tag{2-19}$$

Equation (2-19) reveals that for the maximum power coefficient, a = 1/3. Therefore $C_{p\,max}$ = 16/27 = 0.593 which the maximum power coefficient that can be obtained by an ideal turbine, and this is known as the Betz limit after Albert Betz who first derived it in 1920 [30].

Following the same procedure, it is possible to write the axial thrust on the disc in terms of the induction factor by substituting Equations (2-15) and (2-16) into the thrust force equation (2-12), which gives:

$$F_x = \frac{1}{2}\,\rho\, A_2\, U_\infty^2\, 4\, a\, (1-a) \tag{2-20}$$

Similarly, for the thrust coefficient, C_T, which is the ratio of the thrust force to the dynamic force, it can be expressed as follows:

$$C_T = \frac{\frac{1}{2}\,\rho\; U_\infty^2\; 4\,a\,(1-a) A_2}{1/2\;\rho\; U_\infty^2\, A_2} = 4\,a\,(1-a) \qquad (2\text{-}21)$$

It is clear from equation (2.21) that the maximum C_T (i.e. C_T = 1) occurs when a = 1/2. Also, at the maximum power, when a = 1/3, C_T has the value of 8/9 as shown in Figure 2-6.

A limitation of the actuator disc model appears when the axial induction factor is equal or exceeds the value of 1/2 because the air velocity behind the rotor, which is given by Equation (2-16) above, becomes zero or a negative value.

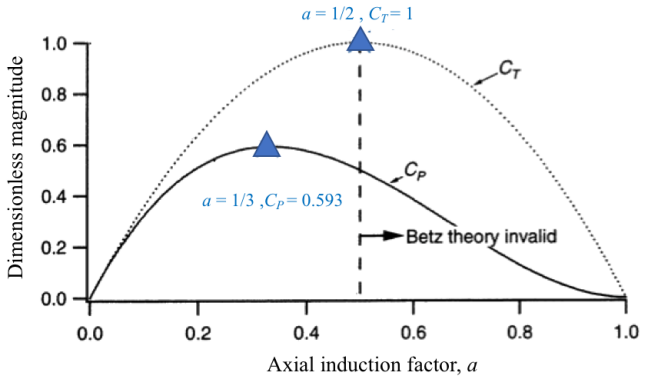

Figure 2-6: Graphical illustration of the induction factor limit [27]

2.2.4 Aerofoil design parameters

Aerofoil-shaped profile sections are very common in aerodynamics applications such as propellers, fans, compressors as well as wind turbine blades [2, 3]. Their interaction with the surrounding flow generates forces with different directions and magnitudes (lift, drag and pitching moment which are discussed in section 2.3). Aerofoils are based on two dimensional thin shapes, their leading and trailing edge geometry varies as the flow regime varies (i.e. subsonic, transonic or supersonic) [25, 26]. The subsonic aerofoil type has a rounded leading edge and a comparatively sharp trailing edge. The main terminology of the aerofoil (Figure 2-7) is summarised in Table 2.1, below [25, 27].

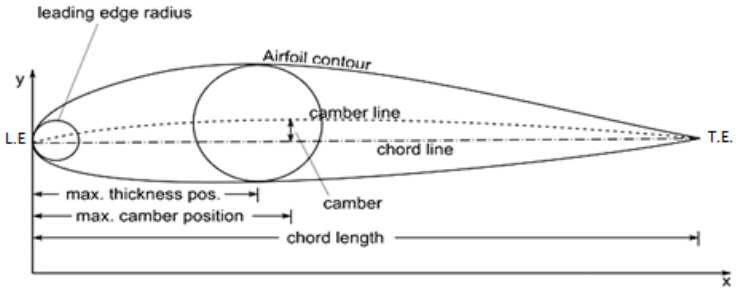

Figure 2-7: Main characteristics of the aerofoil shapes [26]

Early wind turbines utilised the same aerofoils that were designed for aviation, especially helicopters, such as the National Advisory Committee for Aeronautics (NACA) cambered 4-digit series due to their high maximum lift coefficient and availability of wind tunnel experimental data. However, practical operation had shown that the stall behaviour (see section 2.5) of these aerofoil types led to significant losses of the captured energy. Since the early 1990s, special aerofoils tailored for HAWT structural and aerodynamic requirements have been developed, such as the NREL, Risø and Delft series. Modern HAWTs use a high lift-to-drag ratio for the primary and tip regions of the blade and a thicker version of the same aerofoil for the blade root, mainly for structural support [26].

Table 2.1: Aerofoil terminology [27]

Terminology	**Definition**
Leading edge (L.E)	The front point of the aerofoil.
Trailing edge (T.E)	The rear point of the aerofoil
Suction side	Represented by the upper line starting from the leading edge to the trailing edge, which is the low-pressure region.
Pressure side	A relatively high-pressure region
Chord length (*c*)	The direct line linking the leading edge and the trailing edge of the aerofoil.
Camber line	The mean line of the aerofoil which has the same distance between suction and pressure sides, at any given chord position.
Leading edge radius	The radius of the aerofoil leading edge.
Maximum thickness	The maximum perpendicular distance between suction and pressure sides.
Point of max. thickness	The chord-wise position coinciding with maximum thickness location.
Maximum camber	The maximum distance between the chord line and the camber line.
Point of max. Camber	The position of maximum camber on the chord line
Angle of Attack (AoA or α)	The angle between relative wind and the chord line

2.3 Forces acting on an aerofoil

As the air passes over an aerofoil it generates lift and drag aerodynamic forces, relative to the resultant velocity vector, as shown in Figure 2-8. The definitions of each force are discussed in the following sections [26, 31].

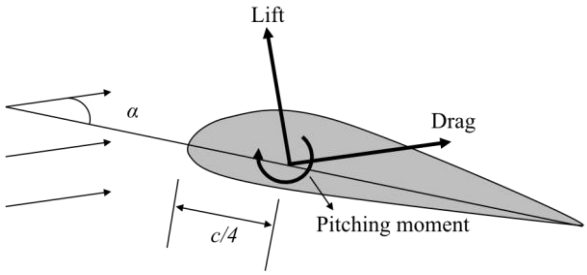

Figure 2-8: Forces and moment that act upon an aerofoil [27]

2.3.1 Lift force and circulation

Lift is a mechanical force generated by the interaction and contact of an aerofoil with incoming flow. According to Newton's second law of motion, a force is produced as a result of a mass acceleration, where acceleration is defined as a change in velocity with time. The velocity is a vector quantity which has a magnitude (i.e. speed) and direction [1, 35]. As for cambered aerofoil applications, the aerodynamic shape of an aerofoil generally produces a net downward deflection or turning of the incoming flow in terms of speed, direction or both as shown in figure 2-9a. Due to this downward deflection a net upward aerodynamic force is generated (according to Newton's third law), but it also creates a variation in velocity magnitude around the aerofoil surface as well as a corresponding static pressure variation. Integrating this surface pressure distribution, is generally a more convenient method of determining the magnitude of this aerodynamic force, which is the method used in CFD [27]. For a thin aerofoil, shown in figure 2-9b, at point A, air is undisturbed by the presence of the aerofoil, the pressure is atmospheric (= p_{atm}) and the streamlines are straight and horizontal. Moving along a dashed line from

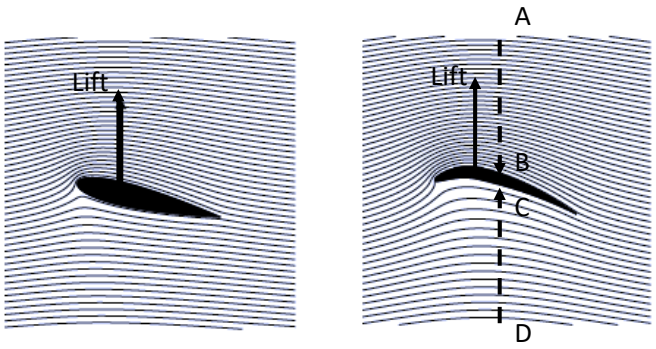

Figure 2-9: Lift generation around (a) cambered and (b) thin aerofoils [35]

point A towards the surface, point B, the streamlines become increasingly curved and there must now be a pressure gradient across the streamlines. From the direction of curvature, it is observed that the pressure drops from point A to B (i.e, $p_B < p_{atm}$).

Similarly, moving from point D to C, the streamlines exhibit more curvature but here the pressure increases towards the surface. At point C the pressure is therefore greater than that at D (i.e, $p_C > p_{atm}$). Hence $p_B < p_C$ and this generates a resultant pressure force on the aerofoil, acting upwards, i.e. lift.

Since pressure force acts normal to the surface it can be resolved into a normal (Lift) and tangential (Drag) component relative to the Inflow direction [32]. Thus, the pressure distribution around an aerofoil is considered as a dominant factor in determining the lift magnitude, while the shear stress effect is negligible.

For a Potential (i.e. irrotational) flow it is necessary to impose the Kutta condition to ensure that turning of the incoming flow occurs such that it represents the physical flow around a lifting aerofoil. As illustrated in Figure 2-10(a), for the theoretical potential flow around an aerofoil there are two stagnation points where the flow velocity is zero. The streamlines are divided either side of the first stagnation point near the leading edge and meet at the second stagnation point further downstream. In this case the flow at the lower surface turns around the sharp trailing edge resulting in a reverse flow region, which is not what we observe in a real flow (unless stalled). For the real steady flow over an aerofoil it is expected that the flow leaves the sharp trailing edge smoothly as represented in Figure 2-10(c). For this to happen, there must be some rotation of the flow i.e. the potential flow pattern (shown in Figure 2-10(a)) requires the superposition of a circulatory tendency (shown in Figure 2-10(b)) to form the flow patterns seen in real life (shown in Figure 2-10(c)). Circulation causes the flow to leave tangentially to a sharp T.E. instead of being parallel to the free-stream [24, 32]. This is known as the Kutta condition since it was first observed by the German mathematician M. Wilhelm Kutta in 1902 [35]. Based on the above, a real flow field can be thought of as the summation of the potential and a circulatory flow.

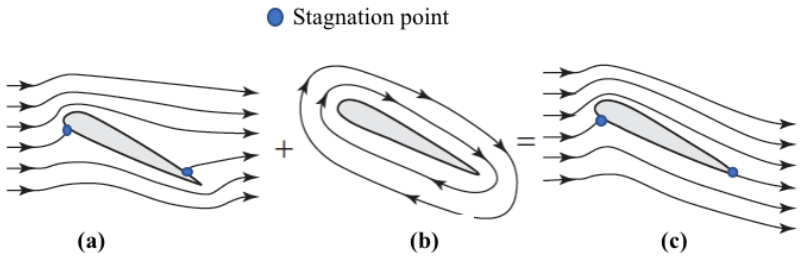

Figure 2-10: Flow past an aerofoil (a) potential (b) circulatory flow and (c) real flow [32]

Mathematically, the generated lift is expressed by the Kutta-Joukowski theorem as follows [1]:

$$L = \rho U \Gamma \tag{2-22}$$

where L is the lift, ρ is the air density, U is the free-stream velocity and Γ is the circulation around the body. The circulation is equal to the sum of the tangential velocity, V along a closed route, s, and it is calculated as follows:

$$\Gamma = \oint V \, ds \tag{2-23}$$

For a symmetric aerofoil at $\alpha = 0^{o}$, the rear stagnation point is coincident with the trailing edge and the flow leaves the surface smoothly. Here, the Kutta condition is satisfied without any circulation and therefore, there is no lift force generated.

For non-symmetric or cambered aerofoils, their curved camber line provides further downwash, in addition to the effects of angle of attack, so that lift is generated at zero angle of attack. Therefore, the maximum lift-to-drag ratio of cambered aerofoils is higher than their symmetric counterparts. For this reason, cambered aerofoils are commonly used in wind turbine applications.

The lift coefficient, C_l, is ratio of lift force to dynamic force as follows [26]:

$$C_l = \frac{L}{1/2 \ \rho U^2 c} \tag{2-24}$$

where, L is the lift force per unit span (N/m), ρ is fluid density (kg/m^3), U is the wind speed (m/s), c is chord length (m).

2.3.2 Drag force

The parallel component of the aerodynamic force, drag, is in the same direction as the resultant incoming airflow. The drag force is comprised of viscous friction forces at the surface of the aerofoil and the unequal pressure acting on the aerofoil surfaces facing toward and away from the incoming flow. The drag coefficient is given by [26]:

$$C_d = \frac{D}{1/2 \ \rho U^2 c} \tag{2-25}$$

where D is the drag force per unit span (N/m). Also,

$$C_d = C_{df} + C_{dp} \tag{2-26}$$

Where C_{df} and C_{dp} are coefficients of the viscous friction and pressure drag, respectively. Typically, for wind turbine applications, C_{dp} is larger than C_{df} [32]. In addition, for 3D wind turbine blades, another drag coefficient, namely the induced drag

coefficient, C_{Di}, should be considered. The induced drag is created by the vortices at the tip of the blade due the pressure difference between its suction and pressure sides. This will cause the flow at the tips to curl around from the lower to the upper surface in a circular motion which results in a trailing vortex.

2.3.3 Pitching moment

The moment generated due to the aerodynamic forces around an aerofoil aerodynamic centre is known as the pitching moment, *M*. It has been found both experimentally and theoretically by NASA [27, 33] that, if the aerodynamic force is applied at a location 1/4 chord downstream from the leading edge on low-speed aerofoils [31], the magnitude of the aerodynamic pitching moment remains nearly constant with angle of attack up to 10 degrees [35, 36].The pitching moment coefficient, C_m, is positive when it tends to turn the aerofoil in Figure 2.8 clockwise (nose up) and is defined as follows [26]:

$$C_m = \frac{M}{1/2 \ \rho U^2 c^2} \tag{2-27}$$

2.4 Boundary layers and pressure gradients

In most aerodynamic applications, flow development around a solid body is affected by the growth of the adjacent viscous region, which is called the boundary layer (BL). The existence of this layer was first proposed by Prandtl in 1904 [34] who suggested that the flow around the body may be considered in two regions: the BL region, where the flow is dominated by shear stresses; and the inviscid region, where the flow is dominated by inertial forces as described in Figure 2.11. The flow adjacent to a solid surface (e.g. turbine blade) is affected by shear stresses resulting in a surface flow velocity $u = 0$, which is known as the no-slip condition. The thickness of the BL grows with the distance travelled, *x*, as more fluid from the inviscid region is entrained within the BL. For Newtonian fluids such as air, the wall shear stress is given by [1, 35]:

$$\tau_w = \mu \frac{\partial u}{\partial y} \tag{2-28}$$

where τ_w is the wall shear stress, μ is the fluid viscosity and $\partial u / \partial y$ is the velocity gradient at the wall.

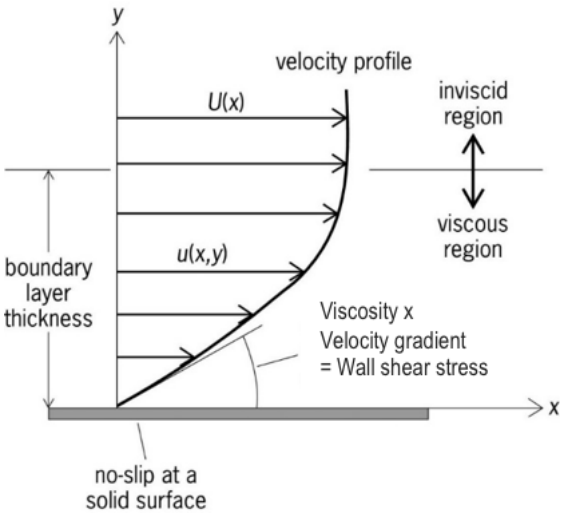

Figure 2-11: Typical boundary layer velocity profile [1]

BL development depends on both local pressure gradients and the fluid velocity. Another factor to consider is the Reynolds number, *Re*, which is the ratio of inertial to viscous forces. It is defined as follows:

$$Re = \frac{\rho U L}{\mu} \tag{2-29}$$

where L is a characteristic length scale, which depends on the application. In the case of a wind turbine, L generally refers to the chord length, c.

The BL thickness, δ, is defined as the height above the surface when the local velocity, u, reaches a prescribed proportion of the freestream velocity, U. Typically, the edge of the boundary layer is considered to be $0.99U$ although it continuously blends into the free-stream in reality [1]. Considering flow over a flat plate, typically, boundary layers begin as laminar and at some point downstream, transition to a turbulent boundary layer, as shown in Figure 2-12.

The same process occurs as a boundary layer develops over an aerofoil. Starting from the front stagnation point near the leading edge, aerofoil curvature leads to a rapid increase in the flow velocity from zero to the maximum at the aerofoil shoulder, which is typically around the point of maximum thickness on the suction side. Here, the pressure decreases from the maximum at the stagnation point reaching the lowest value (suction peak) at the shoulder. The pressure gradient in this region is known as a favourable pressure gradient since the flow is accelerating and the static pressure is reducing.

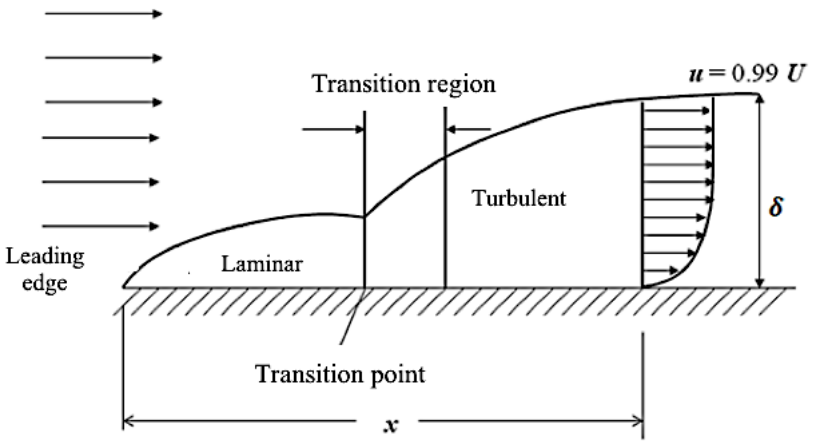

Figure 2-12: Typical boundary layer development along a flat surface [1]

Downstream of the suction peak, the flow velocity decelerates and the static pressure recovers back toward the freestream static pressure near the trailing-edge; this is known as an adverse pressure gradient [1, 35].

At some point along the aerofoil surface, the boundary layer will transition from a laminar to a turbulent state. BL transition occurs when small disturbances to the flow are no longer absorbed by the free-stream. These disturbances grow by taking energy from the original laminar BL and they continue growing until the flow becomes fully turbulent. Higher adverse pressure gradients lead to an expansion of disturbances leading to a turbulent boundary layer. Therefore a BL is more likely to remain laminar within a favourable pressure gradient, though Reynolds number is also a significant factor in the transition mechanism [32]. A turbulent BL will grow at a faster rate due to increased entrainment, which is the process of air being drawn in from the outer free-stream. In strong adverse pressure gradients, the boundary layer deceleration can result in the normal velocity gradient (and consequently the wall shear stress) becoming zero. Adverse pressure gradients exceeding this critical value, can cause the near wall boundary layer to reverse against the free-stream direction which leads to separation from the surface i.e. at the separation point, as presented in Figure 2-13 [1, 35].

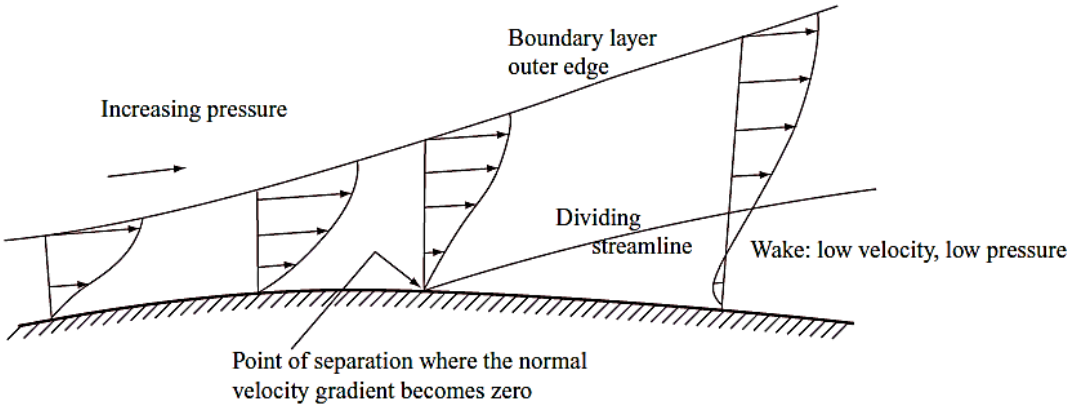

Figure 2-13: Boundary layer separation over a curved surface [1]

A local non-dimensional coefficient, the pressure coefficient, C_p, is a useful parameter in fluid mechanics and it is given by [35, 36]:

$$C_p = \frac{p - p_\infty}{1/2\ \rho U^2} \tag{2-30}$$

where p is the local static pressure (Pa), p_∞ is the free-stream static pressure (Pa). This parameter can be used to visualise the pressure distribution around an aerofoil as well as the pressure gradients, both favourable and adverse. In figure 2.14, a typical pressure distribution is shown around an aerofoil using surface pressure represented by vectors. The arrow length represents the C_p magnitude and the direction represents the sign. For outward facing arrows, pressure is lower than the ambient value, giving a negative C_p. In contrast, the inward-facing arrows represent higher pressure with respect to the ambient value, which implies a positive C_p. Maximum C_p occurs at the stagnation point which is 1 for incompressible flows. Figure 2.15 illustrates the typical C_p distribution over an aerofoil. It is customary to plot C_p values with a reversed y-axis so that negative pressures are at the top of the plot to coincide with the suction side of the aerofoil. Therefore, the suction surface of a conventional lifting aerofoil corresponds to the upper curve, with the pressure side represented by the lower curve.

For a symmetric aerofoil with zero angle of attack, the pressure is equally distributed over both suction and pressure sides. Therefore, no lift is generated. As the angle of attack increases, the front stagnation point will move downward. Consequently, an unequal pressure gradient will be generated between the suction and pressure sides leading to lift production, see Figure 2.14. This process can continue until the stall angle is reached. For cambered aerofoils, the pressure difference exists even at zero angle of attack as described earlier, in 2.3.1.

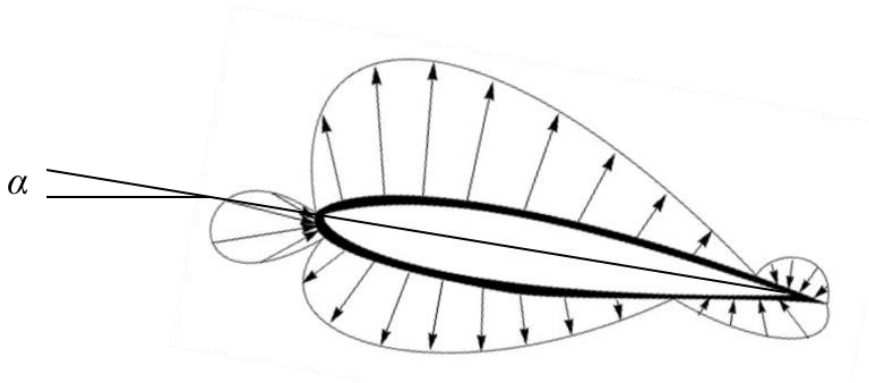

Figure 2-14: A schematic representation of the pressure distribution around a symmetric aerofoil at an angle of attack [35]

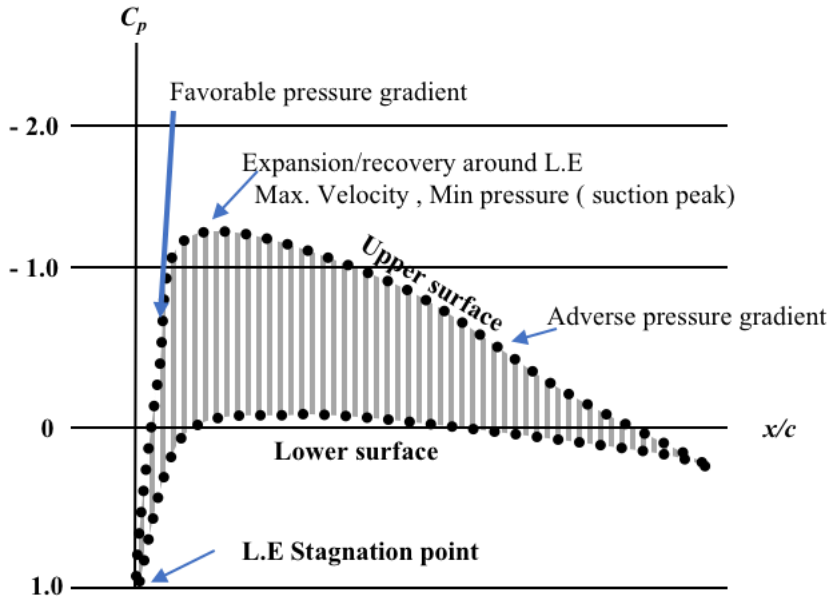

Figure 2-15: Typical pressure coefficient C_p for a cambered aerofoil [35]

2.5 Effect of angle of attack and Reynolds number on lift and drag coefficients

In general, HAWTs are designed to operate at low angles of attack and a Reynolds number (based on chord) in the range 0.5-10 million [26, 27] depending on rotor size. The Reynolds number determines the boundary layer transition point, amongst other parameters such as pressure-gradient, freestream turbulence and surface roughness. As the Reynolds number increases, the location of the transition point moves toward the leading edge. At the typical HAWT Reynolds range above, it is therefore expected that transition occurs close to the leading edge and most of the BL will be turbulent. Turbulent

mixing causes energy to be exchanged between the boundary layer and the free-stream and serves to distribute this energy throughout the boundary layer which enables it to overcome inertia effects, which delays flow separation such that it occurs nearer to the trailing edge [26, 27].

At low angles of attack the flow separates at the trailing-edge. As angle of attack, and therefore adverse pressure gradients, increase the flow separation will start to move forward as shown for AoA=5º in Figure 2-16, which is called buffet onset or the pre-stall condition [35]. Here, the lift coefficient continues to increase linearly with AoA, while the drag coefficient is almost constant and significantly lower than the lift coefficient. However, if the angle of attack increases beyond a certain critical value (i.e. the stall angle typically 10º-16º, depending on the Reynolds number [1]), the separated flow region extends over a large region and lift starts to reduce. This also results in an increase in drag and the maximum lift is achieved in this region. Exceeding the stall angle leads to further BL separation and considerable lift reduction as well as high pressure drag [37]. This region is known as the deep-stall region. Figure 2-16 illustrates this separation behaviour and stalled flow characteristics around an aerofoil.

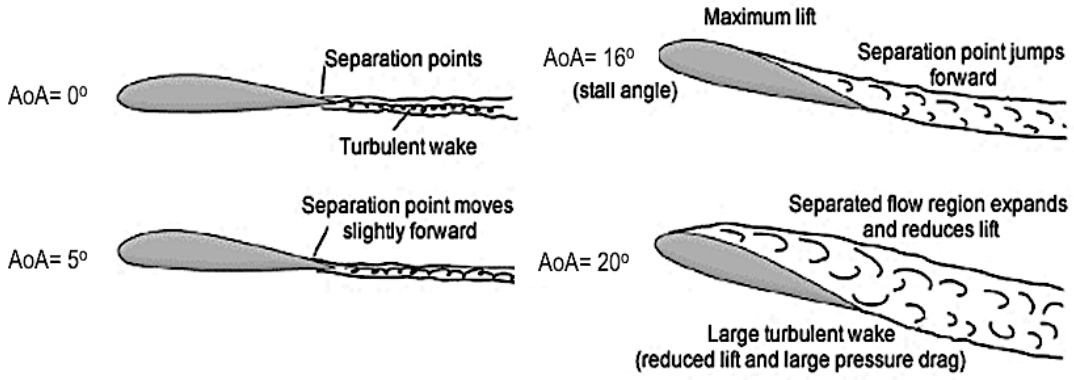

Figure 2-16: Separation and stalled flow around an aerofoil, adapted from [37]

2.6 Overview of aerodynamic load control

The total loads that wind turbine blades are subjected to can be divided into three distinct classes [14, 25]:

1. **Gravitational loads**: These occur due to a periodic span-wise weight induced moment. The maximum is attained when the blade is horizontally positioned as shown in Figure 2-17. Due to gravity, the root of the blade is subjected to a sinusoidal

effect of tensile and compressive stresses within a single blade rotation as represented in Figure 2-17. As gravity momentarily pulls down on the blades in the horizontal position, this induces peak tension at the top of the blade root and peak compression at the bottom. As the blade rotates half a turn, these forces will be applied on the opposite side of the blade. The process leads to periodic cycling of tension and compression in the root. Typically, a wind turbine is designed to operate for about 25 years [26]. If such a turbine rotates at 72 rpm, this means it is subjected to about 9.46 x10^8 stress cycles from gravity, which reflects the significance of gravitational loads on fatigue life and, therefore, the need to reduce the weight of large turbine blades.

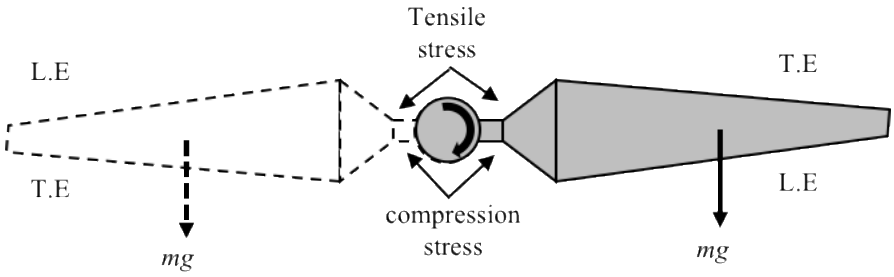

Figure 2-17: Effect of tensile and compressive stresses within a single blade rotation

2. **Inertial Loads**: including the inertial forces acting on the blade due to the rotor acceleration or deceleration. Also, it includes the blades coned backwards due to centrifugal loads. Moreover, the yaw movement of the rotor induces a gyroscopic load which is perpendicular to the plane of rotation.

3. **Aerodynamic Loads**: steady and uniform wind speed with constant rotor speed generates a time-independent load, which can be determined by blade element theory that allows the prediction of lift, drag and power coefficients. Additionally, wind turbulence generates a non-periodic component of aerodynamic force, which can only be estimated with advanced numerical models, such as simulations produced by Computational Fluid Dynamics (CFD).

Obtaining the maximum energy yield from a wind turbine is the desired design criterion, and it is established that the output power increases as the wind velocity increases (as discussed in section 2.2.3). Consequently, a turbine needs to be controlled in order to maximise yield at different speeds and to maintain a constant power above

the rated speed. If the wind turbine is subjected to very high wind speeds (i.e. exceeding the designed cut-out velocity), the turbine should be stopped to avoid possible damage to any of its mechanical or electrical components [38].

Turbine controls are commonly divided into two categories, passive control and active control [14]. Under these main categories, many control techniques are possible, as illustrated in Figure 2-18, which will be discussed in detail in this chapter.

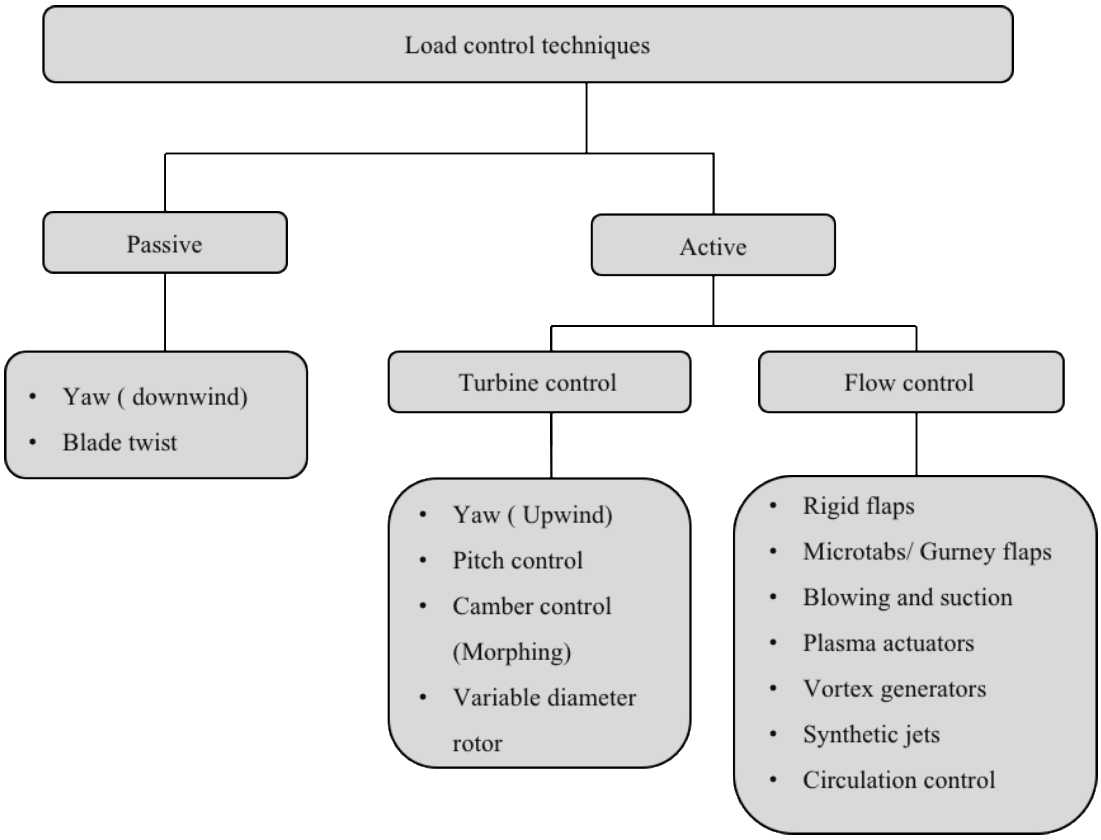

Figure 2-18: Load control techniques [14]

2.6.1 Passive control

Passive techniques are used to raise a given turbine's performance without applying external energy. Examples of this include yaw (downwind) of free-to-yaw downwind turbine and the blade twist [39]. The passive free-to-yaw mechanism, usually used in small scale turbines, utilize the wind force in order to adjust the direction of the turbine rotor as the wind direction changes. The blade twist (aero-elastic twist) technique uses the blade itself as a controller and is a so-called smart blade. The blade is made of a special type of composite material (anisotropic) which is able to respond to the wind velocity variation by changing shape in response to changing pressure field during the operation [40].

2.6.2 Active turbine control

As the result of the significant evolution of wind turbines' size, blade load control has become the main challenge for large wind turbines [14, 25, 39]. Many advanced techniques have been investigated aimed at developing control methods to mitigate blade loading.

Yaw (Upwind): The yaw drive is generally used in almost all modern wind turbines, which is utilised to rotate the nacelle to reduce the yaw misalignment and get as much swept area of air through the rotor disc as possible. Moreover, it is also used to limit the output power by controlling the yaw of the turbine. In this case, the rotor should be turned out of the wind direction in high wind speeds to limit the airflow through the rotor and therefore, limit power extraction [41].

Pitch control: The pitching control technique can mitigate the load by changing the angle of attack, α, to the oncoming wind [42]. The conventional techniques of pitch control use a collective mode, in which all blades are modified jointly. Developed methods of pitch control are: (i) cyclic pitch and (ii) individual pitch. These ideas originated from the rotorcraft field and have been adapted to the wind industry [41].

Camber control (Morphing): The morphing concept includes a wide spectrum of shape change such as variation in camber, twist and span. Camber control is an effective technique of aerodynamic force control by changing the shape of the aerofoil section. This method has direct effects on the force distribution on the blade, so it can be used for active load mitigation purposes [11, 43].

Variable diameter rotor: The concept is based on the power equation (discussed previously in section 2.2.3) which states that the output power increases as the blade diameter (swept area) increases. At low wind velocity, extending blade length enables the wind turbine to provide greater harvesting area. However, the increased diameter yields larger blade roots and tower base loads. The blades retract to their original length as the wind velocity reaches the sufficient values to avoid excessive loads [40].

2.6.3 Active flow control

Active flow control (AFC) systems on wind turbines can potentially be utilised to increase lift of the blade at low wind speeds, allowing the turbine to cut-in and capture more energy at low wind speeds, which is the aim of the current work. The operation of AFC devices also has some other uses such as alleviating the excessive loads (extreme,

fatigue, cyclic, etc.) caused by continuous variations in the wind [14]. Also, they are used to reduce the load on the drive train and the nacelle structure and tower of the wind turbine. In addition, they can be used as an emergency shut down device in case of extreme gusts.

The work carried in this thesis focuses on active load control, specifically, circulation control, which can be achieved by changing the local aerodynamic characteristics on the aerofoil/blade to maximise power production. The following sections review commonly used AFC techniques [12, 19-24, 29-37, 42] as shown in Figure 2-19. In general, these devices are applied near the blade's tip to gain more torque by increasing the moment arm. However, the comparisons between each technique is challenging due to the fact that they are applied in different operating conditions with fundamentally different aerodynamic characteristics.

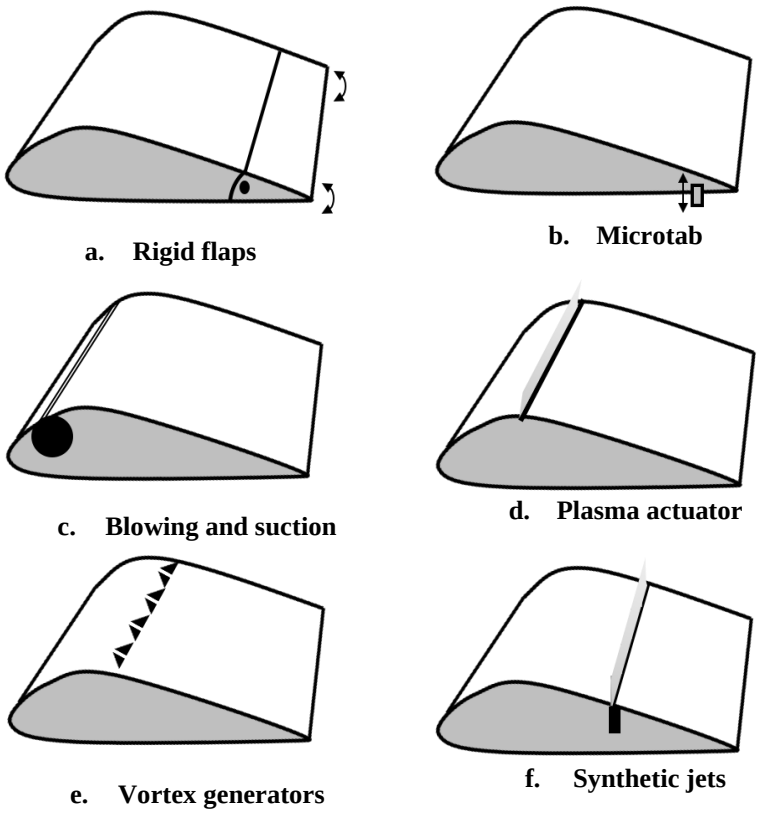

Figure 2-19: Active flow devices configuration [12]

a. Rigid flaps

Flaps (Figure 2.19 a) have been used in aviation particularly to improve the take-off and landing performance of aircraft and it functions as a powerful type of flow control technique, effectively changing the camber of the section [14, 38, 39]. Based on the torsional stiffness of aerofoil materials, the effect of flaps on the aerodynamic loads

varies as the material's stiffness does [23, 24]. For stiff aerofoil materials, while the flap turns toward the pressure surface (lower), the load increases. Conversely, when the flaps turn towards the opposite surface (upper), the load decreases. This mechanism is pronounced for torsionally soft materials. The rotation of flaps toward the lower surface will generate a pitching moment [14, 42] that can twist the blade itself toward the pressure surface which results in a lower angle of attack, therefore, the load decreases. In the opposite manner, as the flaps tend to the suction side, the angle of attack increases, thereby the load increases. The advantage of using flaps is due to their simplicity and low power requirement to make the movement; a slight movement up or down enables the aerofoil to control the C_L and C_D curves. Moreover, the flaps could be mounted along the blade span or on discrete segments on the blade. However, the main concerns about this type of control are large size, additional weight, complex linkage systems, slow response, additional power requirements and aero acoustic noise [40].

b. Microtabs/ Gurney Flap

Microtabs (Figure 2.19 b) are small flat plates (1-2 % *c*) placed perpendicularly to the aerofoil surface near the trailing edge, and they have been developed from the basic principles of Gurney flaps [19]. Microtabs are on-off devices, therefore, they can be applied in both directions (i.e. pressure side or suction side). To increase the lift, the tabs are deployed on the lower surface. Alternately, lift decreases by deploying the tabs on the upper surface (suction) [14]. The presence of these tabs will affect the flow around the aerofoil by shifting the point of flow separation. The minute size of these tabs enables rapid actuation response because of their design simplicity. Therefore, they need very low activation power. These features make microtabs very common as active flow control devices. However, the actuator location and aeroacoustic noise due to the air leakage between the tabs and the aerofoil surface are the main areas of study as well as investigations into the mechanical/ electrical point-of-view [44].

c. Blowing and suction

This type of active flow control device consists of vertical slots located near the trailing edge and/or the leading edge of the aerofoil (Figure 2.19 c). Injection of very high momentum air into the boundary layer from blowing devices will favourably change the flow characteristics around the aerofoil. Supplying high-momentum air to the aerofoil surface will replace the low-momentum air that has been affected by skin friction [33]. This will help to overcome the adverse pressure gradient and postpone boundary

layer separation towards the trailing edge which increases the lift augmentation as discussed in section 2.5. The replacement of low-momentum air can also be achieved using suction slots, which enable the formation of a new (fresh) boundary layer. These devices can be operated with pulsed or steady jets, although the pulsing system is more effective [45]. Although these devices are very effective in terms of flow control, their reliability is poor. The difficulties of slot manufacturing and operation due to their small size, is complicated by icing, and contamination issues. Moreover, the complexity of air storage, a ducting system and weight are counted as major disadvantages [46].

d. Plasma actuators

Plasma actuators (Figure 2.19 d) are another variation of boundary layer control which consists of thin electrodes isolated by a dielectric insulator [40]. A high voltage AC potential is provided to the electrodes. When the current amplitude is sufficiently high, the air ionises in the region of the largest electric potential. The ionised air, or plasma, in the presence of the electric field created by the electrodes produce a body force on the surrounding air [25]. It has been shown that plasma actuators placed near to the trailing edge can delay separation at high angles of attack and impact lift at low angles of attack.

e. Vortex generators

Vortex generators (Figure 2.19 e) are aerodynamic objects designed as small vanes that each generate a vortex, which mixes the free stream with the slow-moving air to get it moving again. This procedure is achieved by re-energizing of the boundary layer. Vortex generators can be deployed permanently or as on-off devices [47, 48].

f. Synthetic jets

Synthetic jet control (Figure 2.19 f) consists of an embedded oscillating diaphragm which is located inside the aerofoil with small span-wise cavities. It has been found that the best locations of these jets is 10-20 % c (i.e. near the leading edge) [49]. During operation, the diaphragm oscillates and jets are formed as the flow is locally sucked into the cavity and then ejected again. This generates a discrete vortical shape as the flow exits the cavity. Here, the jets are formed by the advection and interaction of these vortices with the local flow in the boundary layer, which serves to replace the low-momentum flow. Accordingly, the adverse pressure gradient will be alleviated and boundary layer separation is postponed towards the trailing edge, which consequently increases the lift. As there is no need to add fresh air from storage, this process is also known as a zero net-mass flux (ZNMF) method which leads to the delay of the boundary

layer. The ZNMF process also means there is no need for an air delivery or storage system, therefore, there is less weight in addition to the location facilities from the mechanical installation point-of-view. However, the small cavities of the diaphragms require more stringent maintenance due to icing or soiling conditions [42].

2.6.4 Circulation control technology

It has been established in section 2.3.1, that the lift generated by an aerofoil is directly related to the amount of circulation around it according to the Kutta-Joukowski theorem. The circulation control concept is defined as an enhancement of circulation by applying the Coanda effect at the trailing edge; it does not involve significantly changing the aerofoil geometry or the angle of attack. Typically, the traditional sharp trailing edge, which determines the location of the rear stagnation point, is modified to be a rounded shape. Accordingly, the rear stagnation point will be allowed to move around the rounded trailing edge and its location will be controlled by the amount of energy imparted on the flow through a blown nozzle. By blowing high-momentum air tangentially over the rounded trailing edge through a jet nozzle (Figure 2-20) [34], aerodynamic benefits are obtained.

To implement the Coanda effect, named after Romanian aeronautical engineer Henri Coanda in 1934, it is necessary to pressurise air in an internal plenum and to release the air tangentially through a nozzle at the surface to create an air jet. The behaviour of the air jet sheet downstream of the nozzle is largely determined by the equilibrium of radial forces. It is useful therefore to consider a fluid element within the jet sheet as depicted in figure 2-20. If we initially assume inviscid, incompressible and steady flow so that it obeys Bernoulli's equation, the higher velocity of the jet sheet relative to the external flow gives an inside static pressure that is less than the outside static pressure. This radial pressure gradient is therefore forcing the jet sheet to adhere to the trailing-edge surface. The fluid element also experiences an outward centrifugal force. The jet stream will consequently wrap around the curved trailing edge as a result of the balance between the centrifugal force and the radial pressure gradient, delaying the point of separation relative to an unblown case [21].The relation between radial pressure gradient and the centrifugal force is given by substituting the equation for centripetal force into Newton's 2nd law of motion as follows [35, 36]:

$$\frac{\partial p}{\partial n} = \frac{\rho U_j^2}{R_t} \tag{2-31}$$

Where $\frac{\partial p}{\partial n}$ is the radial pressure gradient, U_j is the jet velocity (m/s) and R_t is the T.E curvature radius (m).

The average jet velocity tends to reduce with distance around the T.E as a result of losses due to viscosity. This causes the wall pressure to rise, creating an adverse pressure gradient and eventual separation. Whilst the inner jet stream is attached, the outer free-stream flow will be entrained due to viscous effects causing both an enhancement of overall circulation around the aerofoil and a deceleration of jet momentum which eventually leads to flow separation [35, 36, 50]. At supersonic jet speeds shock-wave/boundary-layer interaction will also promote separation, placing an upper limit on the nozzle pressure ratio.

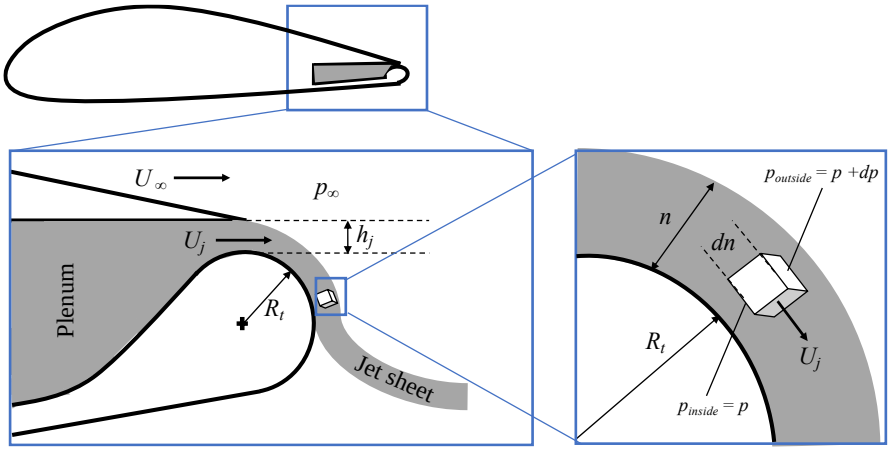

Figure 2-20: Circulation control concept [36]

Early CC designs deployed a large-radius rounded trailing edge to increase the lift [51]. However, these designs produced a higher drag penalty when the jet was turned off. To avoid this penalty the lower surface of the trailing edge can be made as a flat surface while keeping the upper surface highly curved; this creates a large jet-turning angle, producing high lift. Circulation control technology is not only capable of increasing the lift, but also power generation in the context of wind turbines, with a further benefit of assisting with rotation start-up [52]. However, the additional weight and manufacturing cost and installation of the air ducts are the main design concerns. Additionally, the aeroacoustic noise produced by the air ducts represents one of the drawbacks of this technology [52], however, it has received attention in the literature as outlined below.

Pioneering experimental and numerical circulation control research was conducted by Englar *et al* [21, 53, 54] to study lift force augmentation by applying the Coanda effect on a modified circular T.E. According to these studies, a dimensionless relationship between slot height, *h*, aerofoil chord, *c*, and trailing edge radius was proposed as shown

in Figure 2-21. It was found that selection of these parameters to generate effective CC aerofoil requires a balance between the lift augmentation, additional base drag when the jet is off and the power required to pump the air jet.

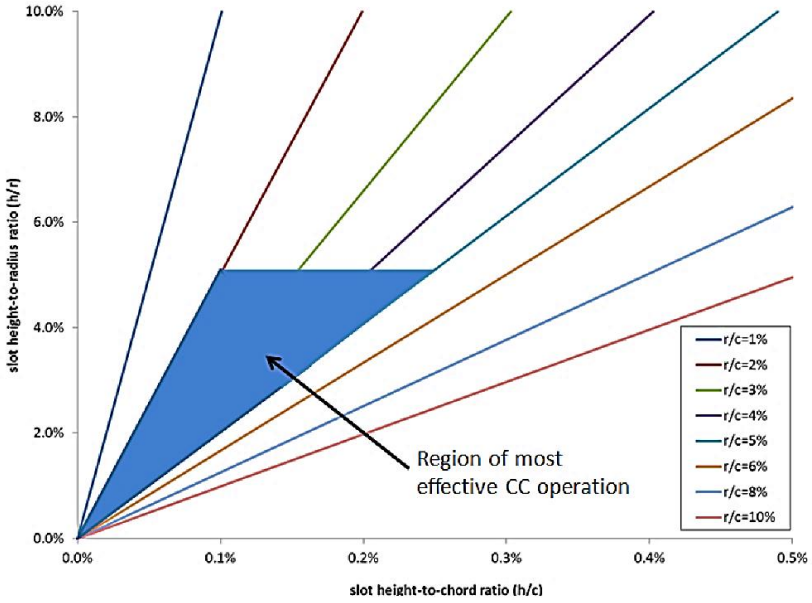

Figure 2-21 : Englar's [49] region of most effective CC operation as mentioned in [51]

Experimental studies by Englar found that elliptical Coanda surfaces produce more lift compared to a circular curvature T.E. especially at higher jet velocities. This was also in agreement with Alexander *et al* [55] and Schlecht et al [56]. Englar also developed a widely used benchmark CC aerofoil (CC-E0020EJ, see chapter 5), which was tested in the Basic Aerodynamic Research Tunnel at NASA Langley as well as the Model Test Facility at the Georgia Tech Research Facility.

Various research programmes have been accomplished to simulate the accurate behaviour of circulation control geometries using CFD. The 2004 NASA/ONR workshop reports most of those efforts [57, 58]. These validation data provide better understanding of the complex flow physics around and downstream of the T.E. These studies conclude that a very fine mesh is required around the T.E. in order capture the Coanda effect, otherwise the numerical results will be unreliable.

Economon *et al* [59] carried out a detailed parametric study of mesh refinement, turbulence model and blowing coefficient on the CC-E0020EJ geometry that was developed by Englar. Turbulence models studied included Spalart-Allmaras (SA), Standard $k-\epsilon$, and SST $k-\omega$ variants. They found that the pressure coefficient distribution along the aerofoil chord is highly sensitive to the choice of turbulence model used. Each

model determined different jet stream separation points on the T.E. as shown in figure 2-22, where S is the separation point.

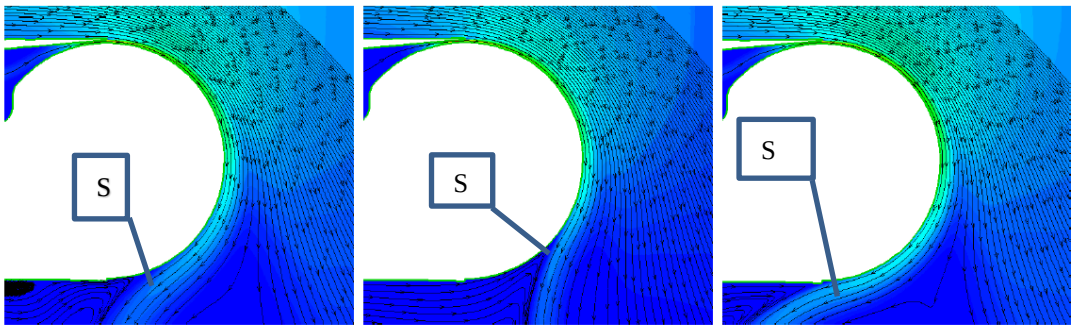

(a) **(b)** **(c)**

Figure 2-22: Separation location for (a) Standard $k-\epsilon$, (b) SA and (c) SST k-ω turbulence models [59]

Mc Grain *et al* [60] performed a 2D computational study of circulation control applied to vertical axis wind turbines (VAWTs) with different tip speed ratios (TSR). The aim of the research was to analyse the effect that circulation control technology has on the pressure gradients around the wind turbine's aerofoil section. Computational Fluid Dynamics (CFD) simulations using the commercial software package ANSYS-FLUENT showed that circulation control results in a much lower pressure reduction (0.5- 5 KPa) within the immediate vicinity of the wind turbine compared with non-controlled VAWT designs.

Shires *et al* [61] studied the effect of trailing edge aerofoil shape versus the jet momentum coefficient ($C\mu$) for a CC-VAWT design. A 2D CFD simulation based on the NACA0018 section quantified the aerodynamic characteristics of the aerofoil with and without blowing using the commercial CFD solver STAR CCM+. The air jet was provided by a uniform inflow velocity boundary condition at the jet nozzle boundary. The study concluded that the trailing edge shape could be optimized to improve the CC output (i.e. lift-to-drag ratio) from 14.1 to 27.8 at 0° angle of attack.

Forster *et al* [62] implemented a gradient-based optimisation scheme seeking an optimum modified T.E configuration for CC applications. This study indicated that the lift augmentation could be enhanced by 8% -16% compared to the baseline elliptical T.E as a result of aerodynamic shape optimisation under the same blowing conditions. Figure 2-23 (a) shows the initial T.E and (b) shows the optimised surface.

In summary, what the work illustrated above shows, is that the position of a typical CC jet is crucial and T.E design requires careful consideration; these two aspects are central themes of the present study.

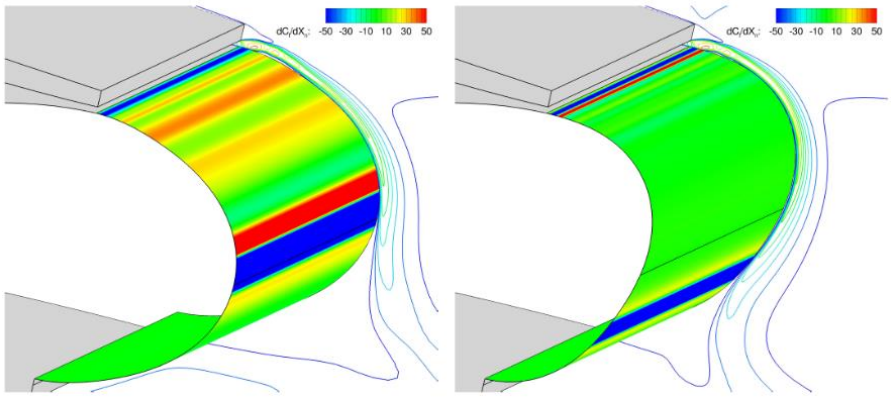

(a) **(b)**

Figure 2-23: Contours of surface sensitivity (a) initial T.E. and (b) optimised T.E [62]

2.7 Circulation control applied to 3D HAWTs

As described in previous sections, many researchers have carried out studies on circulation control for various applications. However, the major studies which are more closely aligned to the present study, a 3D HAWT, are described here. It should be noted that only a few such studied are available in the literature.

Trevelyan [63] applied CC to a Tjaerborg 2MW, 30 m blade length HAWT by modifying the T.E. of the NACA 4415 aerofoil using a jet flap that enables the jet to flow around the flap surfaces from upper and lower slots. The study focused on the power enhancement at the above rated speed of the turbine operation where the wind velocity is typically in the range between 15- 25 m/s. In their work, they used CFD for a 2D modification study, before continuing in 3D using only BEM. The study calculated the power required to supply the air to the slot location by means of both self-pumping due to turbine rotation and an additional compressor provided to the internal pipe within the blade. The study concluded that power variations of -160kW to +270 kW based on the flap angle can be achieved by applying CC to a 62-88% proportion of the blade length at a wind speed of 15m/s, with a maximum momentum coefficient of 0.01. The main drawback in this study is, intuitively, that the trailing edge CC becomes ineffective for lift augmentation at such high wind speeds. This is because flow separation occurs at a point on the aerofoil upper surface (suction side) far from the T.E., as discussed previously in section 2.5. In these cases, CC is unable to reattach the flow. Also, regarding the 2D study, only a jet flap was used; no consideration for Coanda surface geometry parameters, especially the curvature radius, was afforded. In addition, for the

3D aspect of this study, it was only performed analytically based on BEM; the flow behaviour around a full 3D rotor was not investigated.

Tongchitpakdee [42] developed a computational study based on the NREL Phase VI, 5 m blade length, equipped with circulation control and a Gurney flap. He looked into two approaches of introducing the Coanda jet, that is, at appropriately chosen points in the vicinity of the trailing and leading edges of S809 aerofoil. At high speed, a leading-edge jet was found to be helpful in increasing power generation for leading-edge separation cases, while T.E. blowing may produce the opposite effect. This underlines the importance of where to introduce circulation control and it highlights a potential pitfall if it is incorrectly applied. Djojodihardjo *et al* [50] also investigated jet placement on the S809 aerofoil as part of a 2D study. Parameters including jet location, modified T.E. radius and jet height were considered. The results highlight that effective CC performance could be achieved when the jet is introduced close to the baseline T.E., which agrees with Tongchitpakdee. However, neither of these studies accounted for the required power supply.

In another relevant study, Kara *et al* [64] performed a 3D CFD investigation to measure the effect of implementing CC to the Controls Advanced Research Turbine (CART 3) HAWT. This is rated at 600 kW and it has a 20 m blade length which consists of S816, S817 and S818 aerofoils. Their trailing edge modification extended along the entire blade length. The results showed that power increases by about 60% when CC was applied using a constant momentum coefficient of 0.025. Obviously, this high-power enhancement is only achieved because CC is applied along the full length of the blade; it doesn't account for the power cost to inject this amount of energy in the first place. Therefore, the significant power improvement is misleading because the cost is not considered in these figures. Table 2-2 illustrates the main limitations and drawbacks for the above-mentioned studies, which represent some of the gaps in knowledge in this area.

Table 2.2: Limitations and drawbacks of the related works

#	Author / year	Rotor / blade length	Limitation/ drawbacks
1	Trevelyan [63]/ 2002	Tjaerborg 2MW / 30 m	• CC applied for post stall region. • T.E parametric study not included.
2	Tongchitpakdee [42]/ 2005	NREL Phase VI / 5 m	• Power requirement not considered.
3	Kara *et al* [64]/ 2013	CART3 / 20 m	• Power requirement not considered. • T.E parametric study not included.

2.8 Gaps in knowledge and research questions

According to the literature, most numerical studies on circulation control techniques are based on 2D aerofoils or small-scale wind turbine blades. Implementing CC on a commercial scale, three-dimensional HAWT blade, such as the NREL 5 MW, 63 m blade's length has, to the author's knowledge, not been studied before; it is a challenge to describe the flow around and downstream of the rotor and to measure the impact on the generated torque and, therefore, power. Additionally, pressure delivery systems and the required pumping power for HAWT designs have received little attention in the literature. As a result, this research is intended to address the following research questions:

1. Can circulation control produce aerodynamic benefits for a typical commercial scale HAWT?
2. Where should circulation control be introduced along the blade length?
3. What modifications are required to the baseline T.E to implement CC successfully?
4. Is it possible to provide sufficient pressure using passive means to deliver a suitable nozzle pressure ratio (NPR) to the plenum location where CC is introduced?
5. What are the trade-offs between NPR, T.E. parameters and CC power requirements, and is there a net performance gain?

Chapter 3 THEORY

3.1 Introduction

Wind turbines convert the kinetic energy of wind into mechanical and subsequently electrical energy. The focus of this research is the application of circulation control to commercial scale (i.e. multi Megawatt) horizontal axis wind turbines to improve this energy capture. Due to a scarcity of geometry and performance data for these turbines in the open literature the fictitious NREL offshore 5 MW baseline wind turbine [15] with a diameter of 126 m, which is closely based on the REpower 5M turbine, has been adopted as the baseline turbine. This has been used extensively by researchers for the development of computational methods and the evaluation of flow control [16-18]. However, since there is no real-world or experimental data available for this turbine, the research has also considered the smaller NREL Phase VI (10 m diameter) turbine which has published wind tunnel data, and was consequently used for developing modelling strategies. In order to predict and analyse the flow around and downstream of a wind turbine, three different approaches are feasible.

Firstly, full-scale field or wind tunnel testing enables flow calibration under varying conditions and to develop accurate measurement protocols. Wind tunnels typically produce accurate data, however, it is a very complex and costly process. However, accurate wind tunnel data is required to understand the flow fundamentals that are so crucial for evaluating numerical methods.

Analytical methods are also very useful because they are based on mathematical models to describe the flow around the rotor. These methods are dependent on simplifying assumptions to predict the performance, which can have an impact on accuracy and reliability. However, they have the distinct advantage of being fast and efficient. The most common and reliable method is the Blade Element Momentum (BEM) method which is uncomplicated and relatively simple to implement. This theory is explained in the next section.

Computational Fluid Dynamics (CFD) is considered as the best alternative to previous approaches as will be briefly described in section 3.8. With the advancement in computers and their memory capacities, simulations of the flow past a wind turbine are widely accessible now by using CFD codes and supercomputers.

In addition to low-fidelity BEM and high-fidelity CFD, there are other hybrid vortex wake models which combine BEM and CFD. However, they will not be used in the

current study. The remainder of this chapter describes BEM and CFD in greater detail because these two methods form the basis of the work contained in this thesis.

3.2 Blade Element Momentum (BEM) theory

The generation of power by wind turbines is caused by the interaction between the wind and the turbine rotors [26]. Many studies have been conducted to obtain the steady state performance of wind turbine rotors [29]. The conventional analysis of wind turbine aerodynamics was firstly presented by Betz and Glauert in the 1930s [65] which is called the Blade Element Momentum (BEM) theory. BEM merges two theories: Momentum theory and Blade Element (strip) theory. The definition and mathematical models underpinning BEM are explained in the following sub-sections [26, 27].

3.2.1 Momentum theory

The actuator disc theory was used in section (2.2.2) to determine the maximum theoretical power output, Betz limit. Its main deficiency is that it neglects the viscous effect and the rotational effect in the wake, which is physically unrealistic. This theory can be extended to the case where the rotating rotor generates angular momentum in (Figure 3-1a), which can be related to rotor torque and it is known as rotor disk theory. The rotor disc theory deals with the torque, thereby moving from Betz's completely abstract turbine rotor to a more realistic turbine rotor that delivers energy to a generator using torque. The work done by that torque on the generator is converted into electrical energy.

Due to the interaction between the rotor and the air passing through it, the air flow gains a rotation speed, ω, in the opposite direction of the rotor (Figure 3-1b). Consequently, the fluid elements have velocity components in an axial and tangential direction. Consider an annular stream tube, which has a radius, r, and radial width, dr, and a cross-sectional area equal to $2\pi rdr$. This tube is used to determine the variations of both axial and rotational induced velocity components, as illustrated in Figure 3-1. The blades rotate with an angular velocity, Ω, and the blade wake rotates with an angular velocity, ω. The flow around the blades starts at stage 2 in Figures 3-1 and ends at stage 3 (Figure 3-1c). At inlet to the blade the flow is assumed to not rotate, and at the exit from the blade the flow rotates at a rotational speed ω. Bernoulli's theorem can be applied to the flow across the disc to calculate the pressure difference as follows [1] :

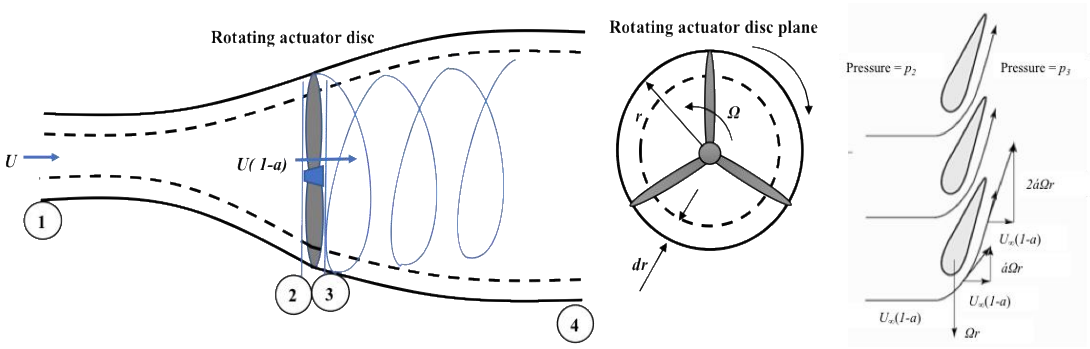

(a) **(b)** **(c)**

Figure 3-1: Rotational momentum model, adapted from[26,1]

$$p_2 + \frac{1}{2}\,\rho\,[(U_\infty(1-a))^2 + (\Omega r)^2 + \omega^2] = p_3 + \frac{1}{2}\,\rho\,[(U_\infty(1-a))^2 + (\Omega(1+2\acute{a})r)^2 + \omega^2] \quad (3\text{-}1)$$

Consequently,

$$p_2 - p_3 = 4\,\acute{a}(1+\acute{a})\,\frac{1}{2}\,\rho\Omega^2 r^2 \quad (3\text{-}2)$$

Where a', is the tangential induction factor = $\frac{\omega}{2\Omega}$,which is used to express the change in the tangential velocity behind the rotor.

Accordingly, the resulting thrust on an annular element between stages 2 and 3, is given as follows*:*

$$dF_x = (p_2 - p_3)\,dA = \left[4\,\acute{a}(1+\acute{a})\,\frac{1}{2}\,\rho\Omega^2 r^2\right] 2\pi r dr \quad (3\text{-}3)$$

Following the previous linear momentum concept described in section 2.2.3, the thrust on an annular cross-section is defined in equation 2.20, which used an axial induction factor, *a*. Equating the two expressions for thrust gives:

$$\frac{a\,(1-a)}{\acute{a}(1+a)} = \frac{\Omega^2 r^2}{U_\infty^2} = \lambda_r^2 \quad (3\text{-}4)$$

where, λ_r is the local speed ratio.

The conservation of angular momentum is applied to determine the torque, *Q*, applied on the rotor, which is equal to the rate of change of angular momentum of the wake. Hence,

$$dQ = d\dot{m}\,\omega r\,r = (\rho\,U_2\,2\pi r\,dr)\omega r\,r \quad (3\text{-}5)$$

Recalling that $U_2 = U_\infty(1-a)$ and $\acute{a} = \omega/2\Omega$, equation (3-4) can be written as follows:

$$dQ = 4\,\acute{a}(1-a)\frac{1}{2}\,\rho U_\infty \Omega\, r^2\, 2\pi r dr \qquad (3\text{-}6)$$

Momentum theory has therefore yielded equations for the axial (Equation 3-3) and tangential force (Equation 3-6) on an annular element of fluid.

3.2.2 Blade Element theory (BET)

The blade element theory (BET) assumes that the blade of a wind turbine is divided into a sufficient number (usually between ten and twenty [66]) separated segments, *N*, along the rotor radius (i.e. blade's length) that act as 2D aerofoil sections, see Figure 3.2. Each of the blade elements will experience a slightly different flow condition because they have a different rotational speed Ωr, and possibly a different chord length *c* and twist angle γ [25]. The net performance characteristics are determined by numerical integration along the blade span.

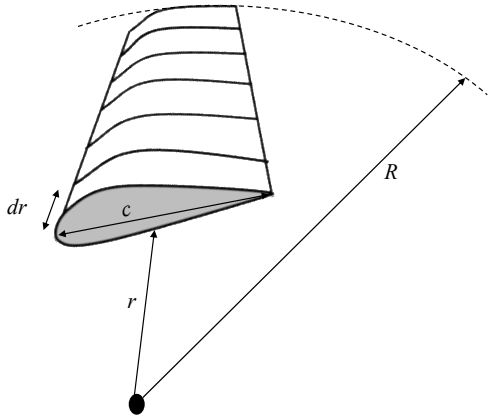

Figure 3-2: Blade element model [26]

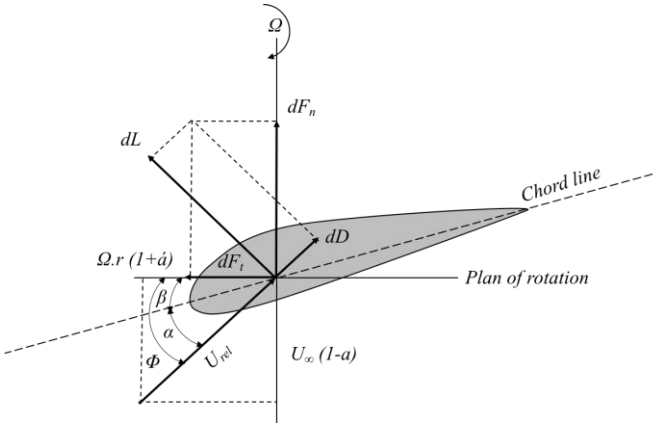

Figure 3-3: Blade section geometry for analysis of a HAWT [26]

Moreover, BET assumes that there is no aerodynamic interaction between the adjacent segments. Also, the generated forces on the 2D segment (i.e. aerofoil) are determined solely by using the local flow conditions and aerodynamic coefficients. Wind tunnel measurements for lift and drag coefficients are used to calculate the aerodynamic forces of each segment [1].

Figure 3-3 shows that the velocity components of each segment are determined in terms of free-stream velocity, flow induction factors and rotor rotational speed. The flow induction factors a and $\acute{a}$ were described earlier in section 3.2.1. Accordingly, the following relationships can be obtained:

$$\Phi = \beta + \alpha \tag{3-7}$$

where Φ is the inflow angle, β is the section pitch angle and α is the angle of attack.

Therefore,

$$tan\,\Phi = \frac{U_\infty(1 - a)}{\Omega r\,(1 + \acute{a})} \tag{3-8}$$

Relative velocity:

$$U_{rel} = \frac{U_\infty(1 - a)}{sin\,\Phi} \tag{3-9}$$

Lift force:

$$dL = \frac{1}{2}\rho\, C_L\, U_{rel}^2\, c\, dr \tag{3-10}$$

Drag force:

$$dD = \frac{1}{2}\rho\, C_D\, U_{rel}^2\, c\, dr \tag{3-11}$$

Normal force, which is equivalent to the thrust force, F_x, (introduced in the momentum theory):

$$dF_n = dL\,cos\,\Phi + dD\,sin\,\Phi \tag{3-12}$$

Tangential force (which acts parallel to the aerofoil /blade motion):

$$dF_t = dL\,sin\,\Phi - dD\,cos\,\Phi \tag{3-13}$$

For a rotor which has B blades, the differential thrust can be expressed follows:

$$dF_n = B\,\frac{1}{2}\,\rho\, U_{rel}^2\,(C_L\,cos\,\Phi + C_D\,sin\,\Phi)\,c\,dr \tag{3-14}$$

Hence, the differential torque, which results from the tangential force, F_t, operating at a distance r from the centre, can be determined as follows:

$$dQ = B\, r\, dF_t \tag{3-15}$$

So,

$$dQ = B\, \frac{1}{2}\, \rho\, U_{rel}^2\, (\, C_L\, sin\, \Phi - \, C_D\, cos\, \Phi)\, c\, r\, dr \tag{3-16}$$

3.2.3 BEM model

The coupling of the momentum theory with the blade element theory is necessary since the performance of the individual aerofoil sections affects the induction factors of the momentum theory. An iterative numerical scheme (see figure 3.4) is therefore required in order to solve the thrust and torque equations that are obtained using both mentioned theories and to achieve a fully converged solution [26]. The BEM model calculations start by guessing the values of the induction factors a and a' and determine the forces on each segment independently.

For wind turbines' design and analysis, BEM uses the following approach [27]:

A local solidity expression $\sigma = \frac{Bc}{2\pi r}$ is applied in the thrust and torque equations (3-14) and (3-16), respectively, along with equation (3-9), yielding:

$$dF_n = \sigma\, \pi\, \rho\, \frac{U_\infty^2 (\, 1 - a)^2}{sin^2\, \Phi}\, (\, C_l\, cos\, \Phi + \, C_d\, sin\, \Phi)\, r\, dr \tag{3-17}$$

$$dQ = \sigma\, \pi\, \rho\, \frac{U_\infty^2 (\, 1 - a)^2}{sin^2\, \Phi}\, (\, C_l\, sin\, \Phi - \, C_d\, cos\, \Phi)\, r^2\, dr \tag{3-18}$$

By equating the torque equations (3.6) and (3.18), and setting C_d equal to zero, this simplification gives negligible errors for low drag coefficient aerofoils [27] and the following expression can be obtained:

$$\frac{\acute{a}}{(\, 1 - a)} = \frac{\sigma\, C_l}{(\, 4\lambda_r\, sin\, \Phi)} \tag{3-19}$$

Similarly, for the normal force equations (3-3) and (3-17):

$$\frac{a}{(\, 1 - a)} = \frac{\sigma\, C_l\, \, cos\, \Phi}{(\, 4\, sin^2\, \Phi)} \tag{3-20}$$

Once the induction factors have been determined, the power contribution for each segment can be obtained from the following expression:

$$dP = \, \Omega\, dQ \tag{3-21}$$

Accordingly, the total power will be:

$$P = \int_{r_h}^{R} dP \; dr = \int_{r_h}^{R} \Omega \, dQ \; dr \tag{3-22}$$

Where r_h is the hub radius.

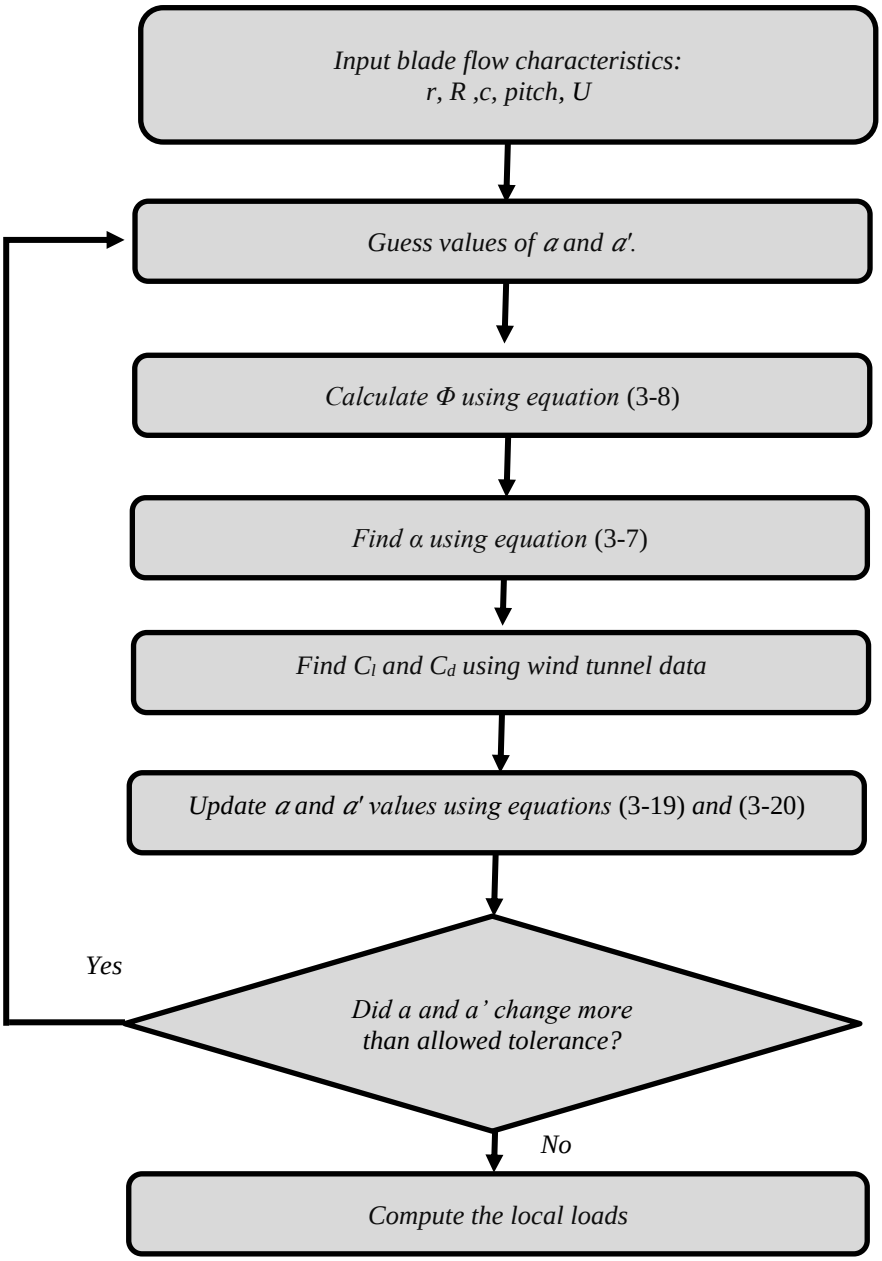

Figure 3-4: : BEM algorithm [27]

3.2.4 BEM limitation

BEM is widely used to predict the output power generated from a wind turbine due to reasonably accurate results in comparatively short computational time. However, because of its simplicity, it does have considerable limitations [67, 68].

The main drawback of BEM is the inaccurate far wake prediction that occurs at high tip speed ratios, resulting in an axial induction factor of greater than 0.4 [27]. In this region, BEM predicts negative wake flow velocities. Thus, basic BEM theory requires a number of empirical models, such as Glauert and Wilson models [27], in order to correct the relationship between the thrust coefficient and the axial induction factor *a*.

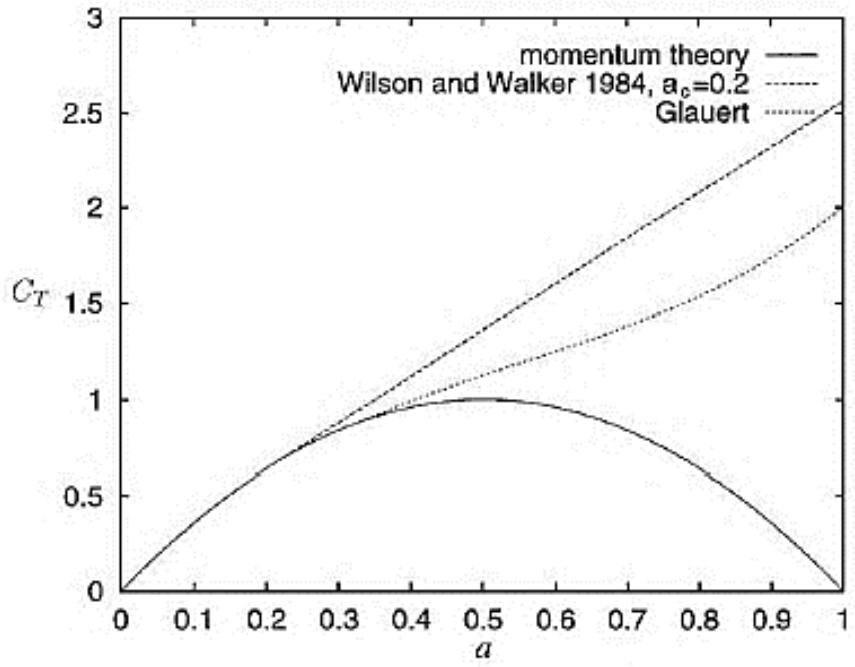

Figure 3-5: Axial induction factor correction models [27]

In addition, a correction model is required to account for tip losses; without this, there may be great uncertainty in results. The tip losses are produced as a result of the pressure difference that is created between the pressure and the suction sides on a typical blade. Here, the flow tends wrap around the blade tip, from the pressure side to the suction side, reducing the lift force and power production [69] Therefore, a number of correction factors are used to improve the basic BEM theory, such as Prandtl's factor. Furthermore, the hub-loss model is required to correct the induced velocity resulting from a vortex being shed close to the hub.

Another drawback of BEM is that the sectional force prediction is based on the lift and drag coefficients that were experimentally obtained from the 2D static aerofoil in a

wind tunnel. That means, BEM assumes the segments along the span work independently which neglects any spanwise or rotational flow effects. For HAWT applications, it is proven that, if the same aerofoil is used this can lead to delayed stall [69]. In other words, the angle of attack at which stall occurs is lower for a static blade than for an equivalent rotating blade. This in turn has a significant effect on the aerodynamic coefficients which results in more power production than expected. According to [1], just before stall occurs, the rotation of the blade produces a centrifugal force which acts on the fluid in the boundary layer. This in turn causes a radial flow which may reduce the displacement thickness thereby reducing the likelihood of flow separation, and increasing the lift relative to a non-rotating flow.

In summary, the major drawback of the BEM approach is that it requires empirical corrections to enhance its performance. Despite this, BEM is a fast and low computational cost method, which is widely used for wind turbine blade design. However, Computational Fluid Dynamics (CFD), which is a numerical method based on the Navier-Stokes equations, has become more popular for wind turbine designers and researchers. This is because CFD enables visualisation of more detailed information regarding the flow around wind turbines. Furthermore, the full blade geometry can be considered and flow separation simulated. Moreover, running CFD simulations does not require previous wind tunnel data in order to calculate the power output. Hence, CFD can be utilised to analyse the performance of modified aerofoils/blades. However, compared to BEM, the computational cost is significantly higher.

3.2.5 FAST

The Fatigue, Aerodynamics, Structures, and Turbulence (FAST) code is a comprehensive aero elastic simulator tool capable of predicting both the extreme and fatigue loads of two and three-bladed horizontal-axis wind turbines, developed by NREL [70]. FAST is a rapid and comprehensive multi-physics simulator incorporating a quasi-steady Blade-Element/Momentum method for aerodynamics analysis. It has been certified by Germanischer Lloyd for predicting HAWT loads and consequently widely used to validate CFD results. Many recent studies have implemented the FAST code to verify CFD simulations, especially for the NREL 5 MW baseline rotor [16-18], and the current study will also use FAST to verify CFD results for this rotor.

3.3 Turbulent flow

Wind turbulence is caused by many factors [71]. As discussed in section 1.3, thermal effects force air masses to move vertically due to the temperature variations within atmospheric layers [72]. The friction caused due to Earth's surface and obstacles such as trees, buildings and rough terrain can deflect airflow, causing turbulent wakes around the obstacle [73]. In the context of wind turbines, another source of turbulence is the wind turbine itself [74], turbine rotors themselves generate turbulence in their wakes even if the first row of turbines on a wind farm encounters smooth or non-turbulent flow [73]. Therefore, due to the continuous change of the wind direction, flow fluctuations occur as a three-dimensional spatial distribution producing rotational flow structures, called eddies [71]. According to Kolmogorov [75], turbulent flow spans a wide range of scales categorised from a large-scale (L_o) at which the energy is supplied, to a small-scale (l_o) at which energy is dissipated by viscosity [76]. The energy transfers between these various eddy sizes consecutively from the larger eddies progressively to the smaller ones. This process is called the turbulent energy cascade as shown in Figure 3.6.

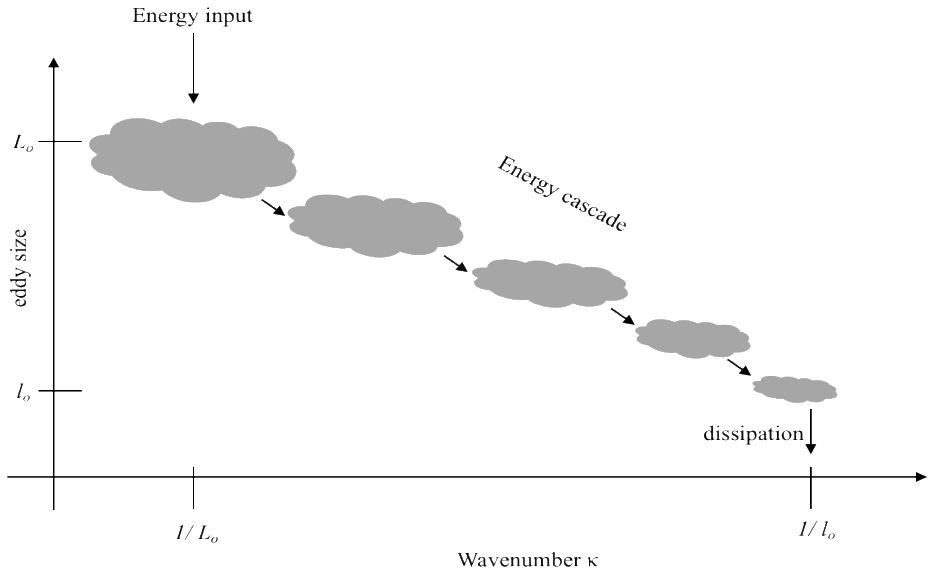

Figure 3-6: Turbulent energy cascade [75]

Turbulence is a complex and chaotic phenomenon. To solve the Navier-Stokes equations, which account for turbulence, some physical quantities should be taken into account such as pressure and air density in addition to the motion of the air itself, in three dimensions. The derivation of Navier-Stokes equation is described in the next section.

3.4 Governing equations

The governing equations of fluid flow represent mathematical expressions of the fundamental conservation laws of physics. These equations are known as the Navier-Stokes (NS) equations, which are a set of partial-differential equations (PDEs) based on the conservation of mass, momentum and energy. These equations describe the relationship between the velocity, pressure, density and temperature (in the energy equation) of a moving fluid, as defined below:

- Continuity equation: The fluid mass is conserved as it can be neither created nor destroyed
- Momentum equation: According to the Newton's 2nd law of motion, the rate of change in momentum is equal to the sum of forces that act on the fluid. These forces are mainly due to gravity, pressure difference and viscosity of the fluid.
- Energy equation: According to the 1st law of thermodynamics, the rate of change of the energy is equal to the sum of the rate of heat addition to the rate of work done on a fluid particle, however, the energy equation is not relevant to wind turbine applications due to the isothermal nature of typical flow fields [18].

Mathematical expressions for continuity and momentum equations are shown and explained in the following sub-sections by applying an Eulerian approach. This represents the control volume as a fixed and infinitesimally small element of a cubic shape with dimension of *dx*, *dy* and *dz* and the fluid flows through it.

3.4.1 Continuity equation

The continuity equation for a three-dimensional flow, is defined as the temporal change of mass inside the control volume. It is equal to the net of flows into and out of the control volume. It is expresses as follows [35]:

$$\underbrace{\frac{\partial \rho}{\partial t}}_{\text{(i)}} + \underbrace{\frac{\partial(\rho u)}{\partial x} + \frac{\partial(\rho v)}{\partial y} + \frac{\partial(\rho w)}{\partial z}}_{\text{(ii)}} = 0 \qquad (3\text{-}23)$$

where ρ is the fluid density (kg/m^3) and u, v and w are the velocity components of flow in the x, y and z-directions respectively. The terms of equation (3-23) are defined as:

(i) The rate of change in time of the density (mass per unit volume).

(ii) The net flow of mass out of the fluid element, also known as the convective term. Convection is a physical process that occurs in a fluid flow in which some property is transported by the ordered motion of the flow.

The continuity equation above applies to the general case of unsteady, compressible and three-dimensional flow. For incompressible flows, ρ is constant, therefore $\partial\rho/\partial t = 0$, regardless of whether the flow is steady or unsteady. Therefore, equation (3-23) can be reduced to*:*

$$\frac{\partial u}{\partial x}+\frac{\partial v}{\partial y}+\frac{\partial w}{\partial z}=0 \qquad (3\text{-}24)$$

3.4.2 Momentum equations

Fluid momentum is defined as the mass of a fluid particle multiplied by its velocity. The momentum equation relates the time rate of change of the fluid momentum to the forces which act on it [77]. These forces include the surface forces (pressure and viscous) and body forces (e.g. gravity, centrifugal, Coriolis and electromagnetic forces). For three-dimensional flow, the general form for each direction is given as follows:

$$\rho\frac{\partial u}{\partial t}+\rho\left[u\frac{\partial u}{\partial x}+v\frac{\partial u}{\partial y}+w\frac{\partial u}{\partial z}\right]=-\frac{\partial(-p+\tau_{xx})}{\partial x}+\frac{\partial\tau_{yx}}{\partial y}+\frac{\partial\tau_{zx}}{\partial z}+B_x \qquad (3\text{-}25a)$$

where p is the pressure and τ is the normal or tangential (shear) viscous stress. The first script of these stresses identifies the plane on which it acts, while the second identifies the direction of the force. B_x is the body force in the x-direction.

Similarly, the momentum equations for y and z directions are given as follows:

$$\rho\frac{\partial v}{\partial t}+\rho\left[u\frac{\partial v}{\partial x}+v\frac{\partial v}{\partial y}+w\frac{\partial v}{\partial z}\right]=\frac{\partial\tau_{xy}}{\partial x}+\frac{\partial\left(-p+\tau_{yy}\right)}{\partial y}+\frac{\partial\tau_{zy}}{\partial z}+B_y \qquad (3\text{-}25b)$$

$$\rho\frac{\partial w}{\partial t}+\rho\left[u\frac{\partial w}{\partial x}+v\frac{\partial w}{\partial y}+w\frac{\partial w}{\partial z}\right]=\frac{\partial\tau_{xz}}{\partial x}+\frac{\partial\tau_{yz}}{\partial y}+\frac{\partial(-p+\tau_{zz})}{\partial z}+B_z \qquad (3\text{-}25c)$$

For a Newtonian fluid, the viscous stresses are proportional to the rates of deformation. This relation is known as Stokes hypothesis. Accordingly, the nine viscous stresses can be written as follows*:*

$$\tau_{xx}=2\,\mu\frac{\partial u}{\partial x}+\lambda\left(\frac{\partial u}{\partial x}+\frac{\partial v}{\partial y}+\frac{\partial w}{\partial z}\right) \qquad (3\text{-}26a)$$

$$\tau_{yy}=2\,\mu\frac{\partial v}{\partial y}+\lambda\left(\frac{\partial u}{\partial x}+\frac{\partial v}{\partial y}+\frac{\partial w}{\partial z}\right) \qquad (3\text{-}26b)$$

$$\tau_{zz} = 2\,\mu\frac{\partial w}{\partial z} + \lambda\left(\frac{\partial u}{\partial x} + \frac{\partial v}{\partial y} + \frac{\partial w}{\partial z}\right) \quad (3\text{-}26c)$$

$$\tau_{xy} = \tau_{yx} = \mu\left(\frac{\partial u}{\partial y} + \frac{\partial v}{\partial x}\right) \quad (3\text{-}26d)$$

$$\tau_{xz} = \tau_{zx} = \mu\left(\frac{\partial u}{\partial z} + \frac{\partial w}{\partial x}\right) \quad (3\text{-}26e)$$

$$\tau_{yz} = \tau_{zy} = \mu\left(\frac{\partial v}{\partial z} + \frac{\partial w}{\partial y}\right) \quad (3\text{-}26f)$$

Here, μ is the proportional constant to relate stresses to the linear deformations and λ is a proportional constant to relate stresses to the volumetric deformation.

Substituting Equation (3-26) into equation (3-25) yields the Navier-Stokes (NS) equations which were derived independently by M. Navier, in France and G.G. Stokes, in England, in the early 1800's [77] . The general form of NS equations are as follows:

x- direction, also known as *u*-momentum:

$$\underbrace{\rho\frac{\partial u}{\partial t}}_{(i)} + \underbrace{\rho\left[u\frac{\partial u}{\partial x} + v\frac{\partial u}{\partial y} + w\frac{\partial u}{\partial z}\right]}_{(ii)} = \underbrace{-\frac{\partial p}{\partial x}}_{(iii)} + \underbrace{\mu\left[\frac{\partial^2 u}{\partial x^2} + \frac{\partial^2 u}{\partial y^2} + \frac{\partial^2 u}{\partial z^2}\right]}_{(iv)} + \underbrace{B_x}_{(v)} \quad (3\text{-}27a)$$

The terms of equation 3.27a are defined as:

(i) Local acceleration at any point in the flow.

(ii) Convection term.

(iii) Pressure gradient.

(iv) Diffusion or viscosity term. Diffusion is a physical process that occurs in a fluid flow in which some property is transported by the random motion of the fluid molecules. Diffusion is related to the stress tensor and to the viscosity of the fluid.

(v) Body forces.

Similarly, the momentum equations for *y* and *z* directions are written as:

$$\rho\frac{\partial v}{\partial t} + \rho\left[u\frac{\partial v}{\partial x} + v\frac{\partial v}{\partial y} + w\frac{\partial v}{\partial z}\right] = -\frac{\partial p}{\partial y} + \mu\left[\frac{\partial^2 v}{\partial x^2} + \frac{\partial^2 v}{\partial y^2} + \frac{\partial^2 v}{\partial z^2}\right] + B_y \quad (3\text{-}27b)$$

$$\rho\frac{\partial w}{\partial t} + \rho\left[u\frac{\partial w}{\partial x} + v\frac{\partial w}{\partial y} + w\frac{\partial w}{\partial z}\right] = -\frac{\partial p}{\partial z} + \mu\left[\frac{\partial^2 w}{\partial x^2} + \frac{\partial^2 w}{\partial y^2} + \frac{\partial^2 w}{\partial z^2}\right] + B_z \quad (3\text{-}27c)$$

Tensor notation, in particular, the Einstein notation is often used to re-write the NS equations in a more compact and shorthand form. For incompressible 3D flow, and neglecting the body force terms in equations (3-24) and (3-27), the NS equations are given by [77]*:*

$$\frac{\partial u_i}{\partial x_i} = 0 \tag{3-28}$$

$$\frac{\partial u_i}{\partial t} + u_i \frac{\partial u_i}{\partial x_j} = -\frac{1}{\rho} \frac{\partial p}{\partial x_i} + \nu \frac{\partial^2 u_i}{\partial x_j \partial x_j} \tag{3-29}$$

where i and j = 1,2,3. These subscripts represent the vector notation of the velocity and direction (e.g. $u_1=u$, $u_2=v$ and $u_3=w$. Also, $x_1=x$, $x_2=y$ and $x_3=z$). Kinematic viscosity $\nu = \mu/\rho$.

The continuity and momentum equations build a system of coupled partial, non-linear differential equations of 2nd order with four unknowns (u, v, w and p). Theoretically, it can be solved simultaneously. However, dealing with the entire flow field where the properties at any point are influenced by every other point in the flow field causes great difficulties. Therefore, in practice, these equations are too difficult to solve analytically.

During the last 3 decades, the use of high-performance computing (HPC) have made it possible to solve approximations to the NS equations using discretisation techniques, such as finite difference and finite volume methods. This field is known as Computational Fluid Dynamics (CFD) and all CFD solvers must abide by the fundamental principles of the NS equations. A well-known approximation applied for turbulent flows in CFD was introduced by Reynolds (1895). This approximation considers the sum of the mean and superimposed fluctuating components of flow variables, such as pressure or velocity, within a given flow field; this is explored in greater detail in 3.7). This leads to the Reynolds Averaged Navier Stokes (RANS) equations as will be described in the next section.

3.5 Turbulent prediction approaches

There are three approaches for turbulent flow prediction, namely Direct numerical simulation (DNS), Large eddy simulation (LES) and the previously mentioned RANS. These approaches are defined below and illustrated in figure 3.7 [77, 78]. They vary in complexity and accuracy depending on the range of length and time scales required to be studied.

In the direct numerical simulation (DNS), all the length and time scales are completely resolved. That means the structure of the turbulence from the largest eddies to the smallest eddies (according to Kolmogorov scales) are computed. Accordingly, DNS provides a high level of flow description and accuracy. However, DNS requires massive computational effort to cope with using a large enough domain which includes the largest eddies and very fine grids. Therefore, it is only practical for small-scale flow problems. The computational cost increases with Re^3 [78, 79].

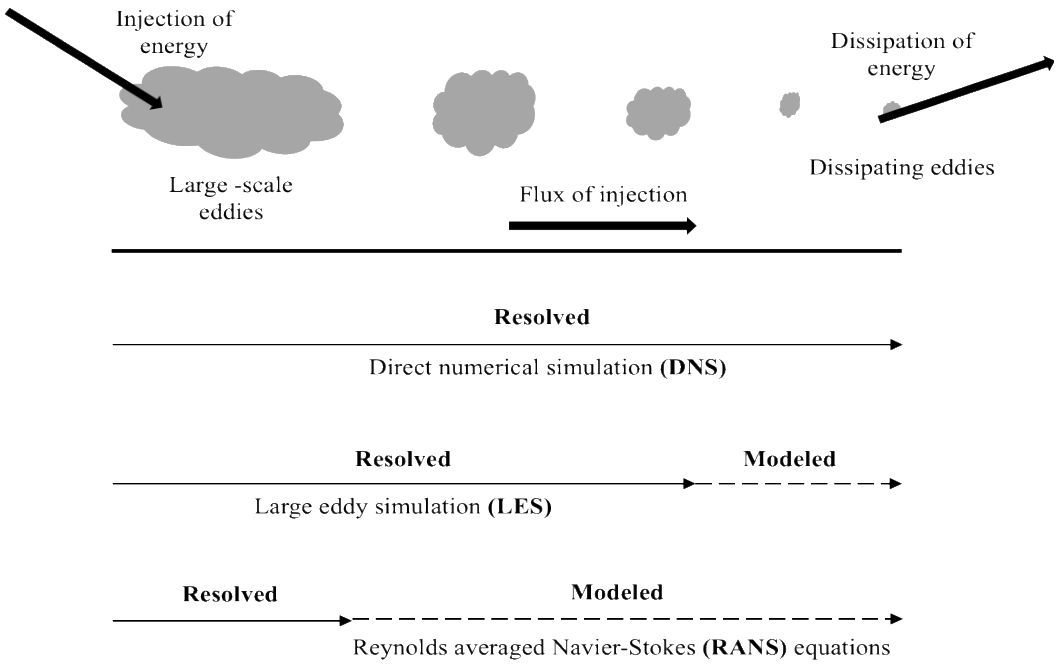

Figure 3-7: Turbulent flow prediction approaches [77]

As for large eddy simulation (LES), large-scale motion is completely resolved but small-scale motion is modelled. This enables much coarser meshes and larger time-steps, compared with DNS [80].

Regarding Reynolds Averaged Navier-Stokes (RANS), only the averaged motion is resolved, and the effect of turbulent fluctuations is modelled. It is the least computationally expensive method used for turbulence modelling, but it is not applicable for certain phenomenon, such as instabilities.

Generally, DNS and LES provide more accurate results than RANS but due to the high computational requirements, they are unattractive for use in industrial applications [81]. Table 3.1 compares the computational requirements for each approach in terms of grid size, number of iterations needed for convergence and the running time required [82, 83]. Moreover, each one of the prediction approaches is applicable to specific flow types.

DNS is restricted to flows with low-to-moderate Reynolds number, while LES can be used to describe the unsteady, large-scale turbulent structures. Therefore, it can be used to study unsteady aerodynamic loads on structures and the generation of sound. It is also applicable for more complex turbulent-flow phenomena, such as high-speed compressible and reacting flows. Although LES can be used to study flow fields around wind turbines, in the context of this thesis, it is not feasible to conduct a large number of simulations using the technique; the use of a RANS-based approach is required.

Table 3.1: computational requirement comparison [71, 74, 75]

No.	Approach	Grid size	Cycles to convergence	Normalized Running time
1	Direct numerical simulation (DNS)	10^{14}- 10^{16}	10^{8}	10^{10}
2	Large eddy simulation (LES)	10^{9} – 0^{11}	10^{6}	10^{8}
3	Reynolds Averaged Navier-Stokes (RANS)	10^{6} - 10^{7}	10^{3}	10^{2}

3.6 Near Wall treatment

Generally, walls are the main source of vorticity in turbulent flow applications. Due to the surface friction that causes a no-slip condition, the fluid velocity reduces from the free-stream velocity to zero in a thin region near a stationary solid wall. Near the wall, the presence of surface shear stresses will initiate an angular deformation for fluid particles (i.e. rotation) and thus the vorticity is generated. In this regard, vorticity can be defined as the tendency of fluid particles to spin. Vorticity may thus be considered as a measure of the local angular velocity of the fluid. For wind turbine applications, for example, flow separation is strongly dependent on a correct prediction of the development of turbulence near walls. Therefore, it is important to ensure an accurate prediction of flow and turbulence characteristics, which includes rotational flow, within the boundary layer. The inner region of a typical boundary layer can be divided into three sublayers, which are viscous, log-law and buffer layers. Each layer is modelled differently and the non-dimensional wall distance, $y+$, is used to define the first cell height within the viscous sub-layer. Figure 3.8 illustrates the non-dimensional velocity, $u+$, as a function of $y+$ across the three sub-layers. These are defined as:

- **Viscous sublayer**: the fluid layer in contact with the wall which is subjected to the viscous effects and is characterised with almost laminar flow whereby $y+ < 5$.

- **Log-law layer**: The turbulent log-law layer is subjected to both viscous and turbulent effects.
- **Buffer layer**: located between the viscous sublayer and the log-law layer.

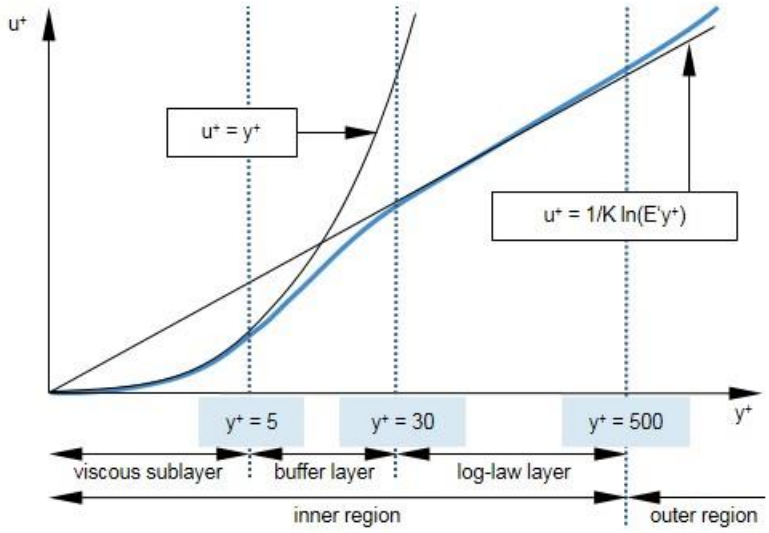

Figure 3-8: Wall boundary sublayers [84]

3.7 RANS approach

As mentioned earlier, due to the irregular (non-periodic) behaviour of turbulent flow, the flow properties fluctuate in the time and space in three-dimensions. RANS assumes that a flow variable at a given spatial point and instant in time can be represented as the sum of the mean value $\bar{u}$ and random fluctuations $\acute{u}$ about the mean value. Accordingly, the spatial-temporal variation for velocity, u, is expressed as [79, 85].

$$u = \bar{u} + \acute{u} \tag{3-30}$$

and the pressure is given by:

$$p = \bar{p} + \acute{p} \tag{3-31}$$

Such assumptions are known as Reynolds decomposition and the process is called Reynolds-Averaging. Applying equations (3-30) and (3-31) for an incompressible fluid with constant viscosity, μ, for the Navier–Stokes equations (3-28) and (3-29) along with applying the following rules of averaging (equation (3-32)), yields the Reynolds-Averaged Navier-Stokes (RANS) equations (3-33) [79, 85]:

$$
\begin{aligned}
\overline{\bar{u}_i} &= \bar{u}_i \\
\overline{\acute{u}_i} &= 0 \\
\overline{\bar{u}_i + \acute{u}_i} &= \bar{u}_i + \overline{\acute{u}_i} = \bar{u}_i \\
\overline{\bar{u}_i \acute{u}_i} &= 0 \\
\overline{\acute{u}_i \acute{u}_j} &< 0 \\
\overline{\bar{u}_i^2} &= \bar{u}_i^2 \\
\overline{\frac{\partial u_i}{\partial x_j}} &= \frac{\partial \bar{u}_i}{\partial x_j}
\end{aligned}
\tag{3-32}
$$

$$
\frac{\partial \bar{u}_i}{\partial x_i} = 0 \tag{3-33a}
$$

$$
\frac{\partial \bar{u}_i}{\partial t} + \bar{u}_j \frac{\partial \bar{u}_i}{\partial x_j} = -\frac{1}{\rho}\frac{\partial \bar{p}}{\partial x_i} + \frac{1}{\rho}\frac{\partial}{\partial x_j}\left[\mu \frac{\partial \bar{u}_i}{\partial x_j} - \rho \overline{u_i' u_j'}\right] \tag{3-33b}
$$

Comparing the momentum equation (3-33b) with the NS equations (3-29) shows that there is an extra stress term on the right-hand side. The term $-\rho \overline{u_i' u_j'}$ is known as the Reynolds stress tensor, $R_{ij,}$ which is a function of the fluctuating velocity components and fully written as follows:

$$
R_{ij} = \overline{u_i' u_j'} = \begin{pmatrix} \overline{u_1'^2} & \overline{u_1' u_2'} & \overline{u_1' u_3'} \\ \overline{u_2' u_1'} & \overline{u_2'^2} & \overline{u_2' u_3'} \\ \overline{u_3' u_1'} & \overline{u_3' u_2'} & \overline{u_3'^2} \end{pmatrix} \tag{3-34}
$$

Because of symmetry (e.g. $\overline{u_1' u_2'} = \overline{u_2' u_1'}$), there are six unknown terms in equation (3-33b) which implies that the RANS system of equation is not closed as there are more unknowns than equations. In order to solve the closure problem, the unknown variables are replaced in terms of known variables. This procedure is known as turbulence modelling. The required nonlinear Reynolds stress term requires additional modelling to close the RANS equation, to enable it to be solved, and has led to the creation of many different turbulence models. The Boussinesq approximation [79] assumes that the turbulent shear stresses are proportional to the mean strain rate with a turbulent eddy viscosity μ_t, therefore*:*

$$
R_{ij} = -\rho \overline{u_i' u_j'} = \left[\mu_t \left(\frac{\partial u_i}{\partial x_j} + \frac{\partial u_i}{\partial x_i}\right) - \frac{2}{3}\rho\, k\, \delta_{ij}\right] \tag{3-35}
$$

where μ_t is the eddy (turbulent) viscosity, which is calculated by using a turbulence model (discussed in section 3.9), k is the turbulent kinetic energy and δ_{ij} =1 for $i=j$ and =0 for $i \neq j$ which is known as Kronecker delta.

3.8 Computational Fluid Dynamics (CFD)

As already described, the aerodynamics of the flow over a wind turbine has been predicted using several methods. The most common and reliable method is the Blade Element Momentum (BEM) method which is uncomplicated and relatively simple to implement. The more advanced and progressive method is CFD, which is typically based on numerically solving the RANS equations with a suitable turbulence model [86]. CFD analysis of wind turbines can be implemented at a low cost compared to a wind tunnel or full-scale experiments. The dependence on CFD codes has been increasing during the last decade for wind turbine performance analysis [87]. With the advances in computer capability and their increasing memory capacities, the simulation of the flow past a wind turbine is widely available now by using commercial CFD codes and supercomputers. However, the simulation of all complicated flow phenomena related to wind turbine aerodynamics, such as vortex shedding, is still a challenge whilst employing CFD codes [86]. Generally, CFD models consist of three main steps, namely: pre-processing, solving and post-processing.

3.8.1 Pre-processing

Pre-processing is the first step in the CFD simulation process, whereby the geometry is characterised in the best possible layout and the fluid domain of interest is defined. Next, the domain is discretised into a "mesh" of cells or elements [84]. There are different methods for carrying out mesh generation within STAR CCM+, the commercial CFD package which will be utilised throughout the method/results sections in this thesis. STAR CCM+ provides two steps for surface meshing, namely the surface remesher and the surface wrapper. The surface remesher improves the quality of the surface and optimises it for the volume mesh. The surface wrapper is used to overcome CAD geometry issues such as multiple or intersecting parts, for example.

For the volume mesh, STAR CCM+, supports three volume mesh element types namely tetrahedral, polyhedral and hexahedral, in the form of the trimmed mesh (which introduces hanging nodes) as shown in Figure 3-9. Mesh size can be refined at desired regions using brick, cone, cylindrical and spherical control volumes; these can be

positioned in regions where high flow gradients are expected such as near blade tips, for example. Moreover, wall-adjacent prism layers can be added allowing the solver to determine the near wall flow and potential BL flow separation accurately.

Tetrahedral meshes (Figure 3-9 (a)) present a simple solution and employ the minimum amount of computational time. However, this model is not recommended for complicated geometries with too much detail. Polyhedral meshes offer a much better computationally-efficient and more accurate solution compared to the tetrahedral model. However, the output quality of this model is dependent on the overall model quality.

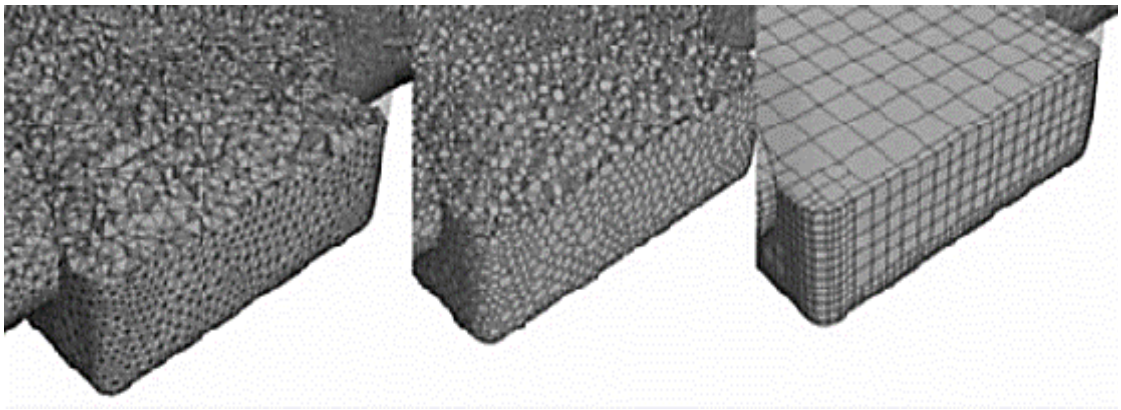

(a) Tetrahedral **(b) Polyhedral** **(c) Trimmed**

Figure 3-9: Volume mesh models [84]

Trimmed hexahedral meshes are equivalent to polyhedral meshes in terms of computational expense and accuracy. Also, they are independent of model quality. Moreover, they are beneficial in modelling external aerodynamic flows due to their alignment with the local flow direction and ability to be refined in regions where viscous effects dominate, such as wakes and the BL. Accordingly, the trimmed hexahedral model is suitable for volume meshing and was used in the present study.

3.8.2 Solver

After identifying the flow physics, the fluid material properties, turbulence model, and the boundary conditions, a solver should be used to generate flow simulations. Typical boundary conditions used in the present study include the velocity inlet boundary condition which defines the freestream (wind) velocity on the upstream boundary of the computational domain. The pressure outlet boundary condition is used to specify the pressure at the outlet boundary. For the wall boundary conditions there are two types of definitions which are no-slip and slip wall (or symmetry). In viscous flows, the no-slip wall boundary condition is utilised for the wind turbine blade surface and any other solid walls such as the nacelle. The slip wall condition is used at symmetry boundaries as the

shear stress is zero. The periodic boundary condition is commonly used for periodically repeating applications. For a wind turbine blade, the periodic condition can be applied to represent the rotational components of the flow, simplifying the analysis since only a single blade needs to be modelled. Rotational inflow and outflow boundaries are dynamically matched.

The SIMPLE algorithm [88] gives a method of linking the calculation of pressures and velocities. It is an iterative method and requires a sequential calculation when other scalars are connected to the momentum equations. The sequence of procedures in a CFD calculation is given in Figure 3-10. The SIMPLE algorithm is commonly used in incompressible problems such as the ones in this thesis. Other algorithms do exist such as SIMPLEC and PISO but they are not applicable to the work in later chapters.

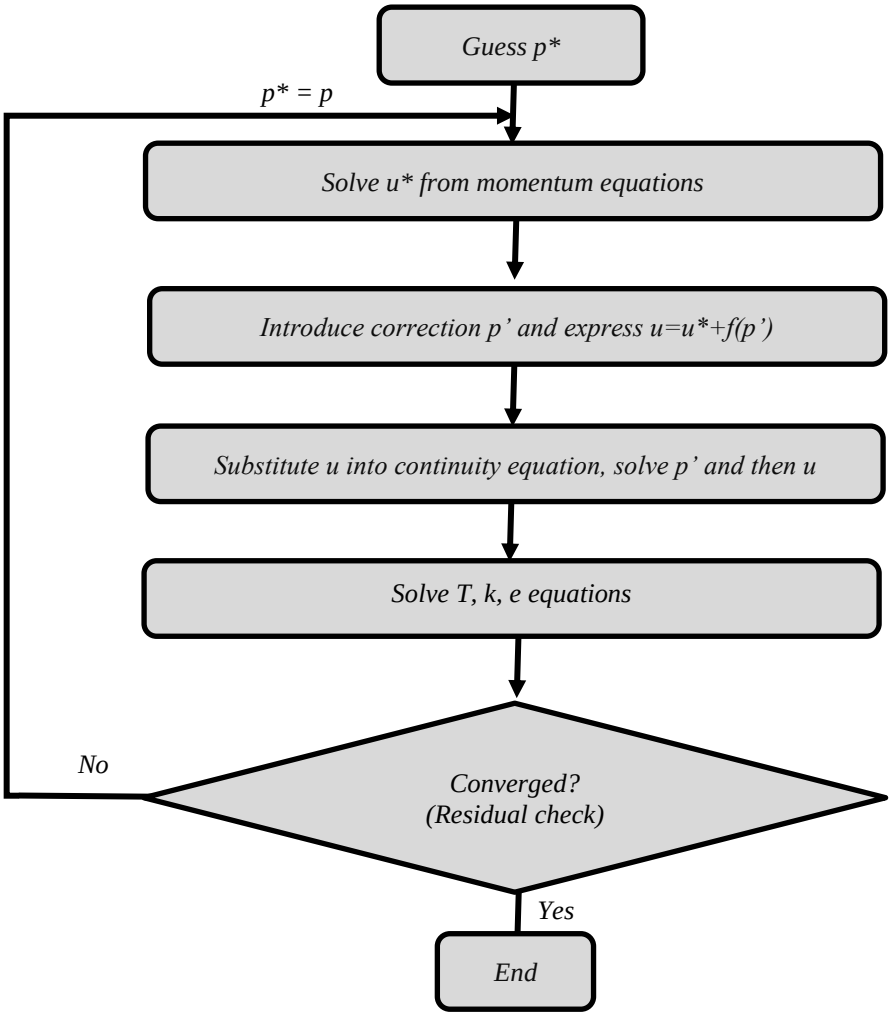

Figure 3-10: SIMPLE algorithm [88]

3.8.3 Post-Processing

The final step after obtaining a converged solution is to analyse the results with different methods to characterise the resulting flow fields both qualitatively and quantitatively. In order to obtain a history of reported values, reports can be monitored during the run of the simulation. For wind turbine applications, analysing and visualising the boundary layer, flow separation and the pressure coefficient are commonly used to study the flow around and downstream of the blades. These flow features were described in the previous chapter. Lift and drag forces are obtained from a surface integral of the pressure and skin friction distributions around the blade.

3.9 Turbulence models used in HAWT

Most RANS turbulence models utilise the Boussinesq eddy viscosity assumption when modelling Reynolds stresses. In order to produce a solvable closed equation, for example, one of the models listed in table 3-2 can be used to solve the RANS equations [89, 90]. The mathematical representation of each model is described in the following sections.

Although there are many other turbulence models, the models listed below are commonly used to predict the flow field around wind turbines according to a considerable amount of literature [31, 86, 91-96]. For the validation of the present work, the three models shown in Table 3-2 will be used. Moreover, the performance of these models will be assessed regarding modelling of jet flow behaviour in chapter 5.

Table 3.2: Summary of turbulence models used in HAWT [31, 86, 91-96]

No.	Model	Findings summary
1	**Spalart–Allmaras (SA)**	• Good performance at pre-stall region. • Less sensitive in the near wall and therefore requires a region presenting the effects of viscosity in the boundary layer.
2	**Realizable $k-\varepsilon$**	• Over prediction of power values.
3	**Shear-stress transport (SST) $k-\omega$**	• Relatively good solutions for the flow with a mild separation. • An excellent prediction ability for wall characteristics. • A limitation to the accurate prediction of aerodynamic characteristics at extremely high angles of attack.

3.9.1 Spalart-Allmaras (SA)

This is a one-equation turbulence model and it is commonly used to solve a transport equation for turbulent viscosity while the turbulent kinetic energy equation is ignored [97]. Originally, it was developed for aerospace and turbomachinery applications including wall-bounded flows. It offers excellent results for boundary layers subjected to adverse pressure gradients. The standard form of the SA model is a low-Re model and to ensure that viscous effects are captured, the wall $y+$ value must be around 1 near the boundary. This requires a very fine mesh to ensure that the first layer of the grid lies in the viscous sublayer.

The transport equation for the SA model is driven by considering:

$$\mu_t = \rho\tilde{v} f_{v1} \tag{3-36}$$

or,

$$v_t = \mu_t / \rho = \tilde{v} f_{v1} \tag{3-37}$$

where μ_t is the eddy viscosity, $\tilde{v}$ is the kinematic eddy viscosity variable and f_{vl} is the damping function, given by:

$$f_{v1} = \frac{\psi^2}{\psi^3 + C_{v1}^3} \tag{3-38}$$

where:

$$\psi \equiv \frac{\tilde{v}}{v} \tag{3-39}$$

The transport equation for the SA model is given by:

$$\frac{\partial\tilde{v}}{\partial t} + u_j\frac{\partial\tilde{v}}{\partial x_j} = c_{b1}\tilde{S}\tilde{v} - c_{w1} f_w\left(\frac{\tilde{v}}{\tilde{d}}\right)^2 + \frac{c_{b2}}{\sigma}\frac{\partial\tilde{v}}{\partial x_k}\frac{\partial\tilde{v}}{\partial x_k} + \frac{1}{\sigma}\frac{\partial}{\partial x_k}\left[(v+\tilde{v})\frac{\partial\tilde{v}}{\partial x_k}\right] \tag{3-40}$$

where,

$$\tilde{S} \equiv S + \frac{\tilde{v}}{\kappa^2 d^2} f_{v1} \tag{3-41}$$

$$f_{v2} = 1 - \frac{\psi}{\psi f_{v1} + 1} \tag{3-42}$$

$$S \equiv \sqrt{2\,\Omega_{ij}\Omega_{ij}} \tag{3-43}$$

where Ω_{ij} is the rotation tensor and defined as:

$$\Omega_{ij} = \frac{1}{2}\left(\frac{\partial u_i}{\partial x_j} + \frac{\partial u_j}{\partial x_i}\right) \tag{3-44}$$

$$f_w = g - \left[\frac{1 + C_{w3}^6}{g^6 + C_{w3}^6}\right]^{\frac{1}{6}} \quad (3\text{-}45)$$

$$g = r + C_{w2}(r^6 - r) \quad (3\text{-}46)$$

$$r \equiv \frac{\tilde{v}}{\tilde{S}\kappa^2 d^2} \quad (3\text{-}48)$$

where *d* is the distance from the closest surface. The other parameters are model constants given as follows:

C_{b1} = 0.1355, C_{b2} =0.622, C_{v1} =7.1 , $\sigma\tilde{v}$ =2/3

$Cw2 = \frac{C_{b1}}{\kappa} + \frac{(1+C_{b2})}{\sigma}$, C_{w2} =0.3, C_{w3} =2 and κ = 0.41

3.9.2 Realizable $k-\varepsilon$ model

The $k-\varepsilon$ turbulence model is a two-equation variant which solves transport equations for the turbulent kinetic energy, *k*, and the turbulent dissipation rate, *ε*, in order to resolve the turbulent eddy viscosity [98] . There are three types of $k-\varepsilon$ model, namely standard (STD), renormalization group theory (RNG) and Realizable $k-\varepsilon$ models. Although they are introduced with the same transport equation, the methods of calculating turbulent viscosity are different. The Realizable $k-\varepsilon$ model is adapted from the STD $k-\varepsilon$ model and it determines the eddy viscosity as a function of turbulent kinetic energy, *k*,and the turbulent dissipation rate, *ε*, as follows [99]:

$$\mu_t = \rho C_\mu \frac{k^2}{\varepsilon} \quad (3\text{-}49)$$

The turbulent kinetic energy equation is:

$$\frac{\partial k}{\partial t} + U_j \frac{\partial k}{\partial x_j} = \tau ij \frac{\partial U_i}{\partial x_j} - \varepsilon + \frac{\partial}{\partial x_j}\left[(v + v_T/\sigma_k)\frac{\partial k}{\partial x_j}\right] \quad (3\text{-}50)$$

The turbulent dissipation rate equation is:

$$\frac{\partial \varepsilon}{\partial t} + U_j \frac{\partial \varepsilon}{\partial x_j} = C_{\varepsilon 1}\frac{\varepsilon}{k}\tau ij \frac{\partial U_i}{\partial x_j} - C_{\varepsilon 2}\frac{\varepsilon^2}{k} + \frac{\partial}{\partial x_j}\left[(v + v_T/\sigma_\varepsilon)\frac{\partial \varepsilon}{\partial x_j}\right] \quad (3\text{-}51)$$

Relevant closure coefficients and relations are given by:

$$C_\mu = \frac{1}{A_o + A_s U^* \frac{k}{\varepsilon}} \quad (3\text{-}52)$$

while the value of C_μ is constant in STD k–ε model.

$A_o = 4.04$, $A_s = \sqrt{6}\cos\vartheta$, $\vartheta = \left(\frac{1}{3}\right)\cos^{-1}(\sqrt{6}\,W)$,

$$W = \frac{S_{ij}S_{ji}S_{ik}}{\tilde{S}}, \quad \tilde{S} = \sqrt{S_{ij}S_{ij}}$$

$C_{\varepsilon 1} = \max(0.43, \frac{\eta}{\eta+5})$, $C_{\varepsilon 2} = 1.9$, $\sigma_k = 1.0$, $\sigma_\varepsilon = 1.2$ and $\eta = \frac{Sk}{\varepsilon}$

$$U^* \equiv \sqrt{S_{ij}S_{ij+}\widetilde{\Omega}_{ij}\widetilde{\Omega}_{ij}} \tag{3-53}$$

$$\tilde{\Omega}_{ij} = \bar{\Omega}_{ij} - \varepsilon_{ijk}\,\omega_k \tag{3-54}$$

where $\bar{\Omega}_{ij}$ is the mean rate-of-rotation tensor in a moving reference frame with an angular velocity ω_k.

3.9.3 Shear-stress transport (SST) k - ω model

The k−ω turbulence model is another two-equation model proposed by [100]. This model incorporates features of the $k-\varepsilon$ model in non-wall regions with the accurate boundary layer treatment of the standard $k-\omega$ model [101]. The turbulent eddy viscosity in the standard form is defined as [100]:

$$\mu_t = \rho\frac{k}{\omega} \tag{3-55}$$

whereas for the (SST) k - ω model:

$$\mu_t = \frac{\rho\alpha_1 k}{max(\alpha_1\omega, SF_2)} \tag{3-56}$$

The turbulent kinetic energy equation is given by:

$$\frac{\partial k}{\partial t} + U_j\frac{\partial k}{\partial x_j} = P_k - \beta^* k\omega + \frac{\partial}{\partial x_j}\left[(v + v_t/\sigma_k)\frac{\partial k}{\partial x_j}\right] \tag{3-57}$$

The turbulent dissipation rate equation is given by:

$$\frac{\partial \omega}{\partial t} + U_j\frac{\partial \varepsilon}{\partial x_j} = \alpha S^2 - \beta\omega^2 + \frac{\partial}{\partial x_j}\left[(v + v_t/\sigma_\omega)\frac{\partial \varepsilon}{\partial x_j}\right] + 1(1 - F_1)\sigma_{\omega 2} \tag{3-58}$$

Relevant closure coefficients and relations are given by:

$$F_2 = tanh\left[max\left(\frac{2\sqrt{k}}{\beta^*\omega y}, \frac{500v}{y^2\omega}\right)^2\right] \tag{3-59}$$

$$P_k = min\left(\tau_{ij}\frac{\partial U_i}{\partial x_j}, 10\,\beta^* k\,\omega\right) \tag{3-60}$$

$$F_1 = tanh\left\{min\left[max\left(\frac{\sqrt{k}}{\beta^* \omega y}, \frac{500v}{y^2 \omega}\right), \frac{4\,\sigma_{\omega 2}\,k}{CD_{kw} y^2}\right]^4\right\} \quad (3\text{-}61)$$

$$CD_{kw} = max\left(2\,\rho\sigma_{\omega 2}\,\frac{1}{\omega}\,\frac{\partial k}{\partial x_j}\,\frac{\partial \omega}{\partial x_i}, 10^{-20}\right) \quad (3\text{-}62)$$

3.10 Numerical errors and uncertainty

In the context of trust and confidence in CFD modelling, the following definitions of error and uncertainty are commonly used [77]:

- **Error:** a recognisable deficiency in a CFD model that is not related to the lack of knowledge. Typical errors are:
  - Numerical errors: roundoff errors, iterative convergence errors, discretisation errors.
  - Coding errors: faults or 'bugs' in the software.
  - User errors: human errors through wrong use of the software.
- **Uncertainty:** a potential deficiency in a CFD model that is caused by lack of knowledge. These are:
  - Input uncertainty: inexactness due to limited information or approximate representation of geometry, boundary conditions or material properties.
  - Physical model uncertainty: inconsistencies between real flows and CFD due to unsuitable definition of physical or chemical processes (e.g. turbulence) or due to simplifying assumptions in the modelling approach (e.g. incompressible flow, steady flow).

As these errors and uncertainty are inevitable aspects of CFD modelling, it is necessary to develop careful methods to increase the level of confidence in the results. In this context, the following procedures are performed:

- **Verification:** the process of determining that a model implementation accurately defines the user's conceptual description of the model and the solution to the model.

- **Validation:** the process of assessment of the accuracy of the model representation of the real world from the perspective of the intended uses of the model.

These concepts will be the basis for the work undertaken in subsequent chapters. In particular, validation will be carried out using experimental data and numerical errors will be eliminated or minimised using appropriate choices.

Chapter 4 THREE DIMENSIONAL HAWT VALIDATION STUDY

4.1 Introduction

The overall aim of this research is to implement and test the feasibility of applying circulation control to the NREL 5 MW baseline wind turbine. As was discussed in chapter 3, no real world or wind tunnel data is available for this large turbine. Therefore, the FAST BEM method will be used to validate CFD simulation results for this turbine, allowing code-to-code validation. However, experimental validation is still desirable to guide the CFD simulation approach. Accordingly, the smaller NREL phase VI HAWT, which has substantial and widely available experimental data, will be used to validate the computational approach and is described in this chapter.

4.2 NREL phase VI HAWT

During the past 25 years, the US National Renewable Energy Laboratory (NREL) in Colorado has performed a series of full-scale field and wind tunnel tests of Horizontal Axis Wind Turbines (HAWTs) under their Combined Experimental Rotor programme. The phase VI turbine tests (Figure 4-1), completed in 1999, provided data measured in a large wind tunnel facility, including power as a function of wind speed and surface pressure measurements at 5 span-wise stations (*r/R* 30 %, 46.7%, 63.3%, 80% and 95%) for a 2-bladed rotor [102]. These are widely used to validate aerodynamic computational and theoretical performance models [91, 92, 94, 103-106]. The stall-regulated control technique limits the peak generated power despite the wind velocity increasing. To ensure that the generator is not overloaded, the power curve dramatically falls once blade stall occurs then increases gradually. This rotor's attributes are listed in Table 4.1.

Table 4.1: NREL Phase VI blade attributes [102]

No. of blades	2 x 5.029 m
Blade rotation	72 RPM
Cone angle	0^o
Rotor location	Upwind
Power regulation	Stall regulated
Blade tip pitch angle	3^o (leading edge down)
Blade profile	S809 , *t/c* = 21% throughout the span
Blade chord length	0.358 m – 0.728 m (linearly tapered)
Twist angle	Non-linear twist along the span

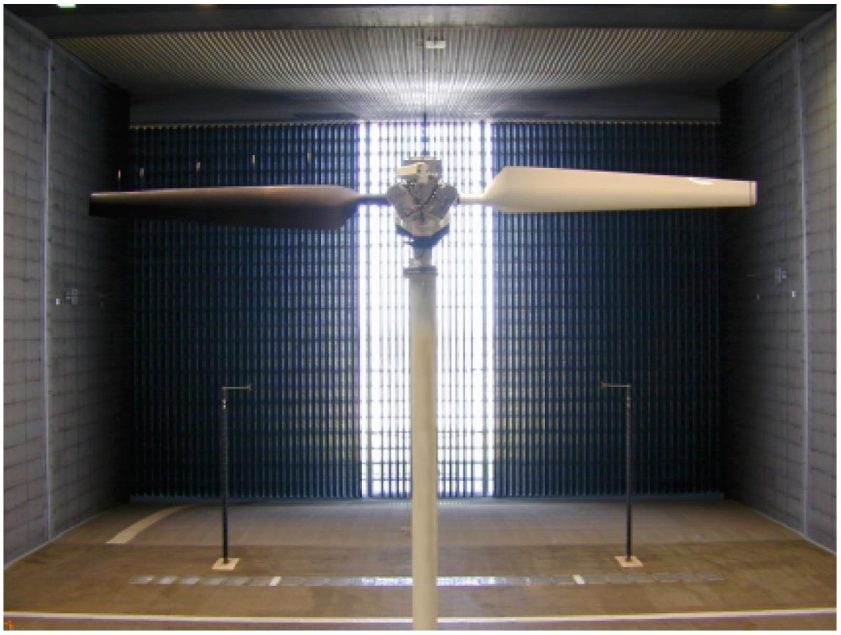

Figure 4-1: NREL phase VI wind tunnel test configuration [102]

4.2.1 Blade geometry

The NREL phase VI rotor geometry uses the S809 aerofoil, which is 21 % thick and is considered to be from one of the thickest aerofoil families. This group of aerofoils was mainly designed by NREL to generate a higher lift force and lower drag compared to other more traditional aerofoil families [107] developed for aerospace applications. A profile of the S809 aerofoil is shown in figure 4.2 [108]

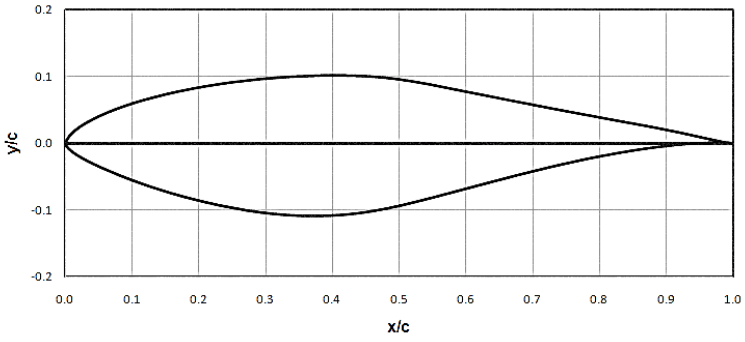

Figure 4-2: S809 aerofoil profile [107]

Further details about the blade geometry, including the chord distribution are shown in figure 4.3a [102, 109]. Figure 4.3b shows the CAD model of the generated blade using SolidWorks 2014 x64 edition, which accounts for the local chord and angle of twist distribution along its span. These are specified in table 4.2. A square tip is assumed due to insufficient details provided by NREL in this region [102, 109].

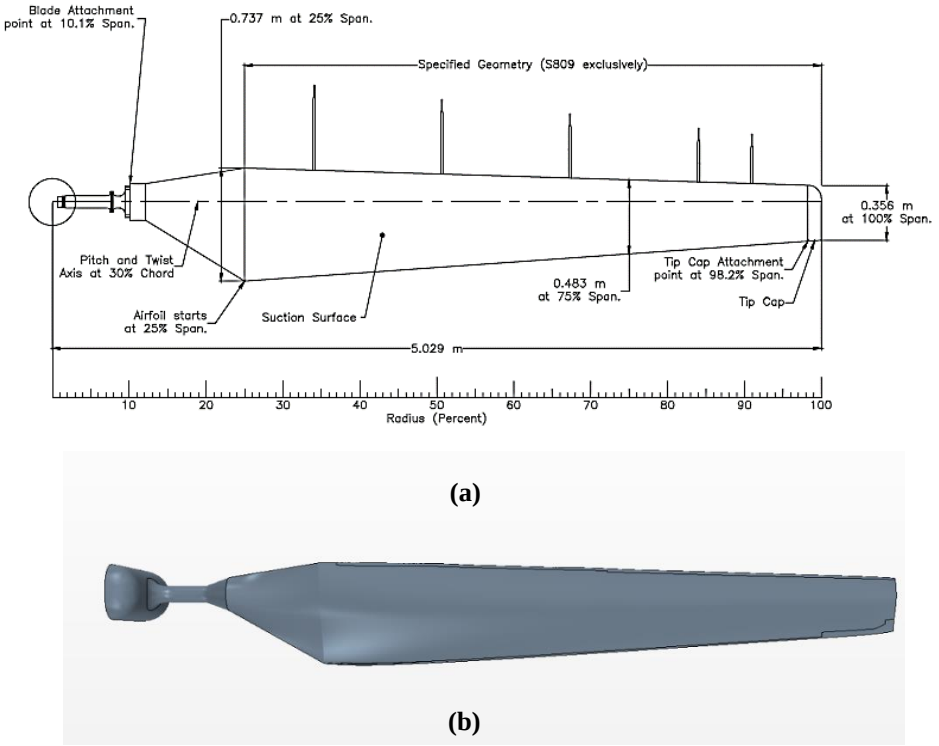

Figure 4-3: (a) NREL VI geometry layout [102]and (b) SolidWorks CAD model

Table 4.2 Local chord and twist angle distribution along the NREL phase VI blade [102]

Section	Radial distance, *r* (m)	Chord length, *c* (m)	Twist angle (º)
1	0	Hub	Hub
2	0.508	0.218	0
3	0.660	0.218	0
4	0.883	0.183	0
5	1.008	0.349	6.7
6	1.067	0.441	9.9
7	1.133	0.544	13.4
8	1.257	0.737	20.040
9	1.343	0.728	18.074
10	1.510	0.711	14.292
11	1.648	0.697	11.909
12	1.952	0.666	7.979
13	2.257	0.636	5.308
14	2.343	0.627	4.715
15	2.562	0.605	3.425
16	2.867	0.574	2.083
17	3.172	0.543	1.150
18	3.185	0.542	1.115
19	3.476	0.512	0.494
20	3.781	0.482	-0.015
21	4.023	0.457	-0.381
22	4.086	0.451	-0.475
23	4.391	0.420	-0.920
24	4.696	0.389	-1.352
25	4.780	0.381	-1.469
26	5.029	0.358	-1.775

4.2.2 Computational domain

The wind tunnel dimensions used for the experiments were 24.4 m x 36.6 m. In order to cover these dimensions, the computational domain for the CFD validation study is displayed in figure 4.4. This is called the free configuration domain, where the rotor blade is modelled while the wind tunnel walls and the corresponding blockage effect are ignored. This configuration was performed originally by Sørensen *et al* [110] and demonstrated a good agreement compared to experimental data for the NREL Phase VI rotor. Many other CFD studies have applied this type of domain [18, 42, 91, 93] and so it is replicated for this study.

Since Sørensen *et al*. (2002) recommend a larger computational domain than the wind tunnel dimension, it is a half cylinder with a radius of 3R, where R is the blade length (5.03 m). The half cylindrical sector is used to simulate a single blade which, with periodic boundaries, allows a more efficient computation of the two-bladed rotor. The left side of the domain (inlet) is set to be 3R in front of the blade and right side (outlet) is set to be 5R after the blade. The coordinate system convention is for *x* to be aligned with the free stream direction and *z* along the blade span. The domain rotates about the *x*-axis. The rotation rate of the periodic walls is set to be 72 rpm to simulate the turbine rotation condition.

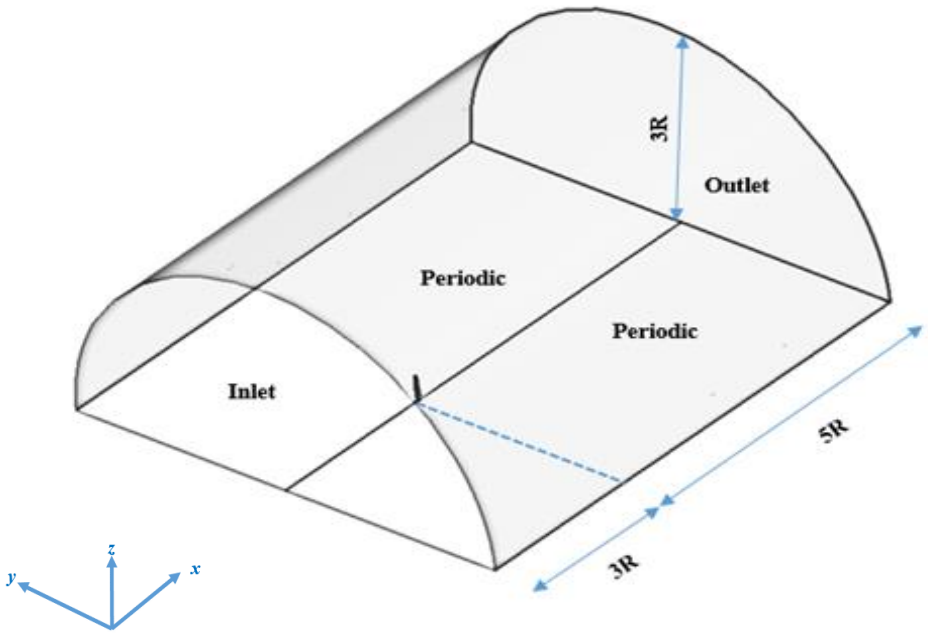

Figure 4-4: Domain sizing of NREL phase VI rotor blade

4.2.3 Mesh refinement

The generation of the mesh has a significant impact on the convergence and accuracy of subsequent CFD simulations. This includes the domain size, volumetric control, cell sizing control as well as the prism layer attributes. The domain is built to be large enough to capture the flow phenomena as it passes over the rotating blade of the turbine. In order to obtain a suitable mesh for the current work, two types of mesh refinement were implemented. Firstly, the size of the cells was reduced in particular regions on the blade where large flow gradients occur, namely at the leading and trailing edges. Secondly, extra control volumes were added to increase the resolution of the mesh before, around and after the blade as shown in Figure 4-5 and Figure 4-6.

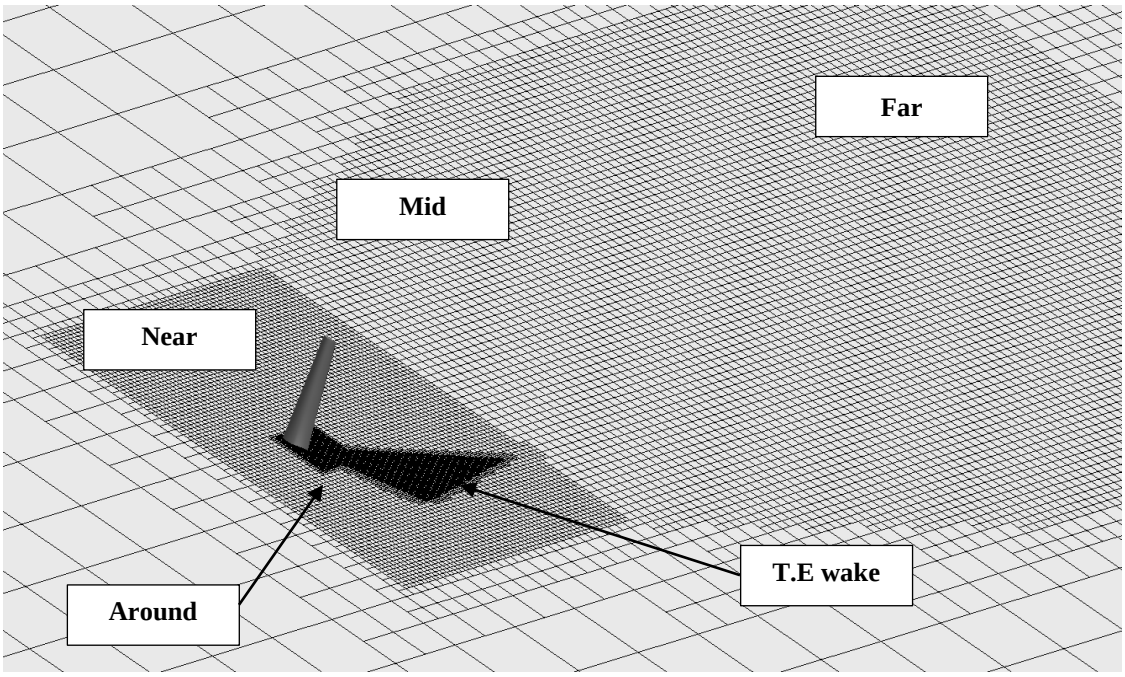

Figure 4-5: mesh resolution at *r/R* = 63% plane section

The trimmer mesh model associated with the surface remesher, and prism layer mesher methods were the most suitable method using STAR CCM+ V11.04.012. The Trimmer mesh model is beneficial for modelling external aerodynamic flows (such as a wind turbines) due to its capability of refining cells in wake regions. This model is based on using a hexahedral template mesh which trims the core mesh using the initial surface of the blade. The template can be aligned in a Cartesian coordinate system to any direction specified by the user [84]. These were deliberately designed to capture off-surface flow features such as the wake, for example, see T.E. wake box in figure 4.5 (this can resolve wakes for a range of angles of attack). The template mesh includes refinement

that is based on the mesh size. Also, a growth rate ratio is defined as (1.2) to ensure smooth transition of the cell sizes from small to large.

Regarding the surface remesher, it is used to discretise the initial geometry surface to enhance its quality by retriangulating the surface while excluding specific edges or boundaries in order to maintain the original triangulation from the imported mesh.

In addition, prism layers were generated on the walls and they provide two main advantages: firstly, they allow high aspect-ratio cells without incurring an excessive stream-wise resolution; secondly, they reduce the numerical diffusion near the wall by aligning the subsurface layers with the flow [84]. For the purpose of a mesh-independence study, four different grids were generated and defined as coarse, medium, fine, and very fine. The performance of each grid is assessed in section (4.2.5).

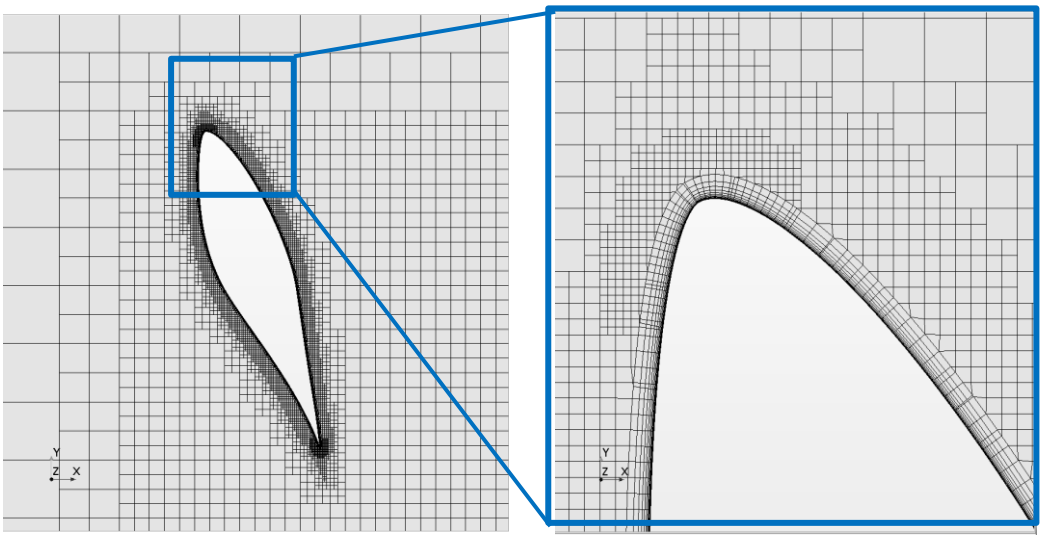

***r/R* = 30%**

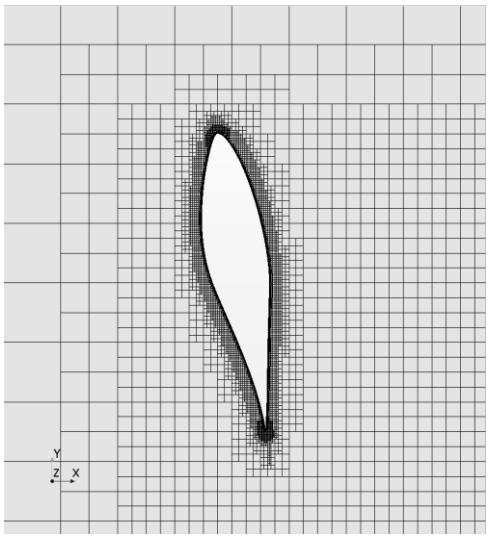

***r/R* = 47%**

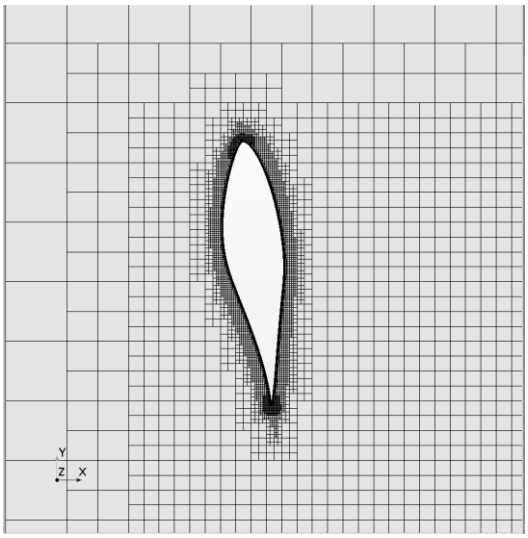

***r/R* = 63%**

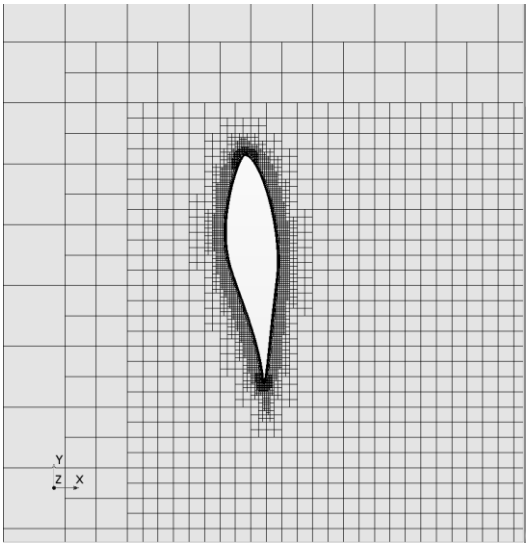

***r/R* = 80%**

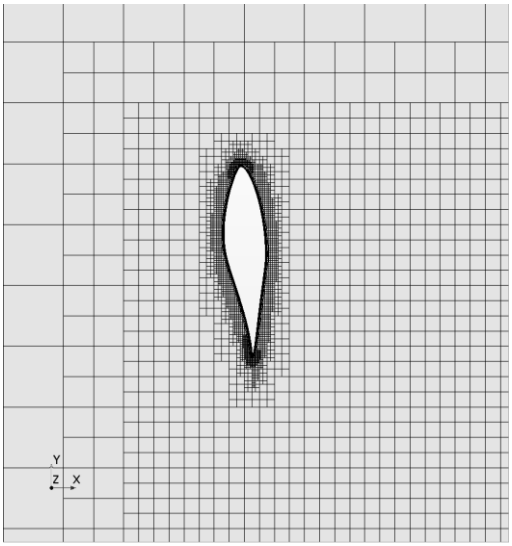

***r/R* = 95%**

Figure 4-6: mesh resolution around the blade at different span-wise locations

4.2.4 Solver setup and boundary conditions

In the present work, three-dimensional, steady state, incompressible (ρ = 1.18415 kg/m^3) flow around one blade of the NREL phase VI HAWT is simulated. The minimum Reynolds number at wind velocity 5 m/s is calculated at the root according to Table 4.2 (section 8) which was around 0.516M. While at the tip (section 26), it was around 0.922M. Therefore, the dominant flow around the whole blade is turbulent. Three RANS-based turbulence models are examined using the segregated solver. During the experimental test, the turbine was controlled to operate at constant rotational speed at 72 rpm with 0° yaw angle of the oncoming flow [111]. This is achieved by using a fixed-pitch design. As the wind speed increases, so does the angle of attack and the flow about the blade eventually stalls, providing self-regulation of power at higher wind speeds.

As described in section 3.8.2, various boundary conditions were applied in the CFD simulation, with solid wall boundary conditions on the rotor blade and the hub. Other external boundary conditions for the domain are defined in table 4.3. The inlet boundary condition depends on the free-stream velocity, which is varied from 5 m/s up to 25 m/s as applied in the NREL phase VI experiments. At the pressure outlet condition, the gauge pressure is set to 0 Pa (gauge) (atmospheric pressure). All simulations were run on the University of Leeds HPC systems ARC2/ARC3. The solution convergence was recognised by monitoring the residual history and the torque over 2000 iterations. However, an acceptable convergence was noticed after 1500 iterations, when the convergence criteria settled below 10^{-6} for all variables for wind velocity up to 10 m/s. Convergence stability was affected above 10 m/s wind velocity cases, as will be discussed later.

Table 4.3: Computational conditions

Parameter	Value
Simulation type	3D, steady, incompressible
Solver type	Segregated flow solver, SIMPLE algorithm
Turbulence models	SA, SST $k-\omega$ and Realizable $k-\varepsilon$
Blade rotation	72 rpm (stall regulated) [111]
Blade	No-slip wall ($u=v=w$ =0 m/s)
Inlet	Velocity Inlet (5-25 m/s)
Outer domain shell	Slip wall
Outlet	Pressure outlet = 0 Pa (Gauge)
Base	Symmetry, periodic interface, slip wall

4.2.5 Mesh independence study

A mesh independence study, shown in table 4.4, shows the total number of cells required to achieve an acceptable level of numerical accuracy as well as agreement with the experimental data. As already mentioned, four different grids were generated and defined as coarse, medium, fine, and very fine. For each grid, the same conditions were evaluated for two wind velocities (5 and 10 m/s) using the same turbulence model (SST k–ω**)**.

Clearly, the results obtained on both fine and very fine grids produce almost the same result and they agree very closely with the experimental data for both wind velocities simulated, see table 4.4. For the fine grid, it was found that the difference between the experimental and the CFD values of blade torque are 0.3% and 0.32% at a wind velocities of 5 and 10 m/s respectively, as shown in figure 4.7. Accordingly, the fine grid is used in all subsequent computations.

It should be noted that first cell height on the blade was systematically controlled to achieve $y^+ \leq 3$, as shown in figure 4.8. The wall y^+ varies from 0.1 at the root, where local Reynolds number value is relatively low, up to 3 at the blade tip and the average is 1.4. This y^+ range ensures that flow gradients adjacent to walls are captured with sufficient accuracy.

Table 4.4: Mesh refinement investigation at 5 m/s wind velocity

Grid	Blade cell size (m)	Number of prism layers	Total prism layers thickness (m)	Total cells number (M)	Torque per one blade (N.m)
Coarse	0.015	20	0.012	5.8	139.72
Medium	0.010	15	0.010	8.2	147.83
Fine	0.007	13	0.006	11.1	156.25
Very Fine	0.005	13	0.006	14.2	156.13
Experimental	-	-	-	-	**155.78**

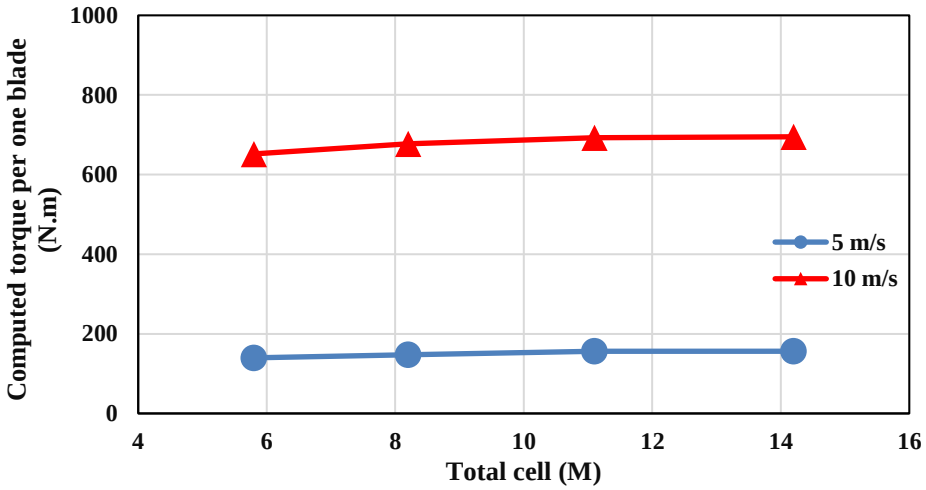

Figure 4-7: Mesh-independence study comparison

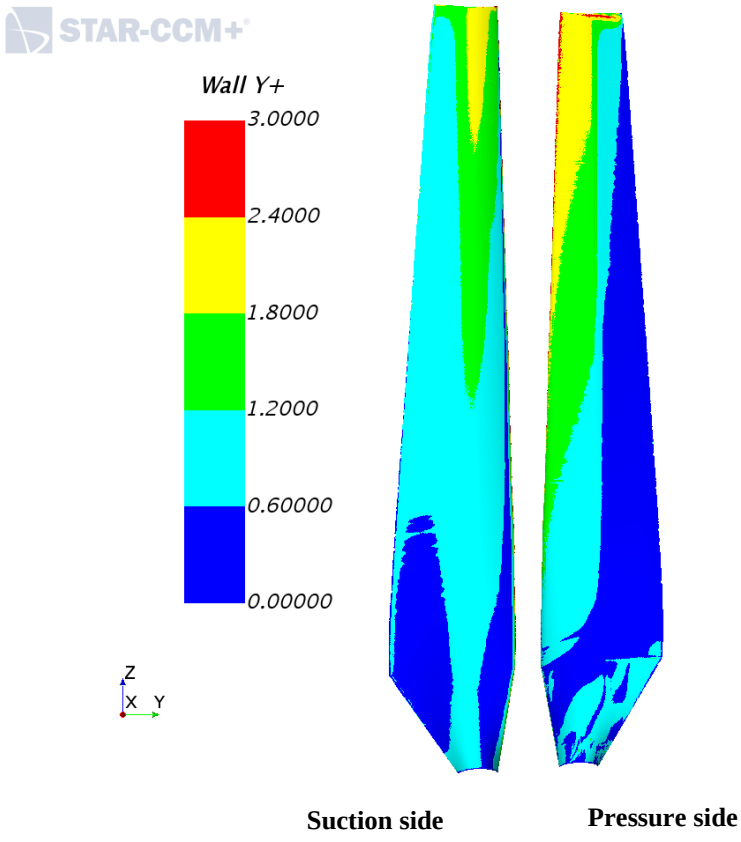

Figure 4-8: Wall *y+* on the NREL phase VI blade surfaces for a wind velocity of 10 m/s

4.2.6 Turbulence model sensitivity study

In order to compare the turbulence models' applicability to predict the complex flow associated with rotating wind turbines, three models (SA, SST k–ω and Realizable k−ε) were investigated. The equations and features of each model were described in chapter 3. The comparison between the CFD results of each model and the experimental data is presented in figure 4.9, using the settings in table 4.3 and fine mesh grid for all models.

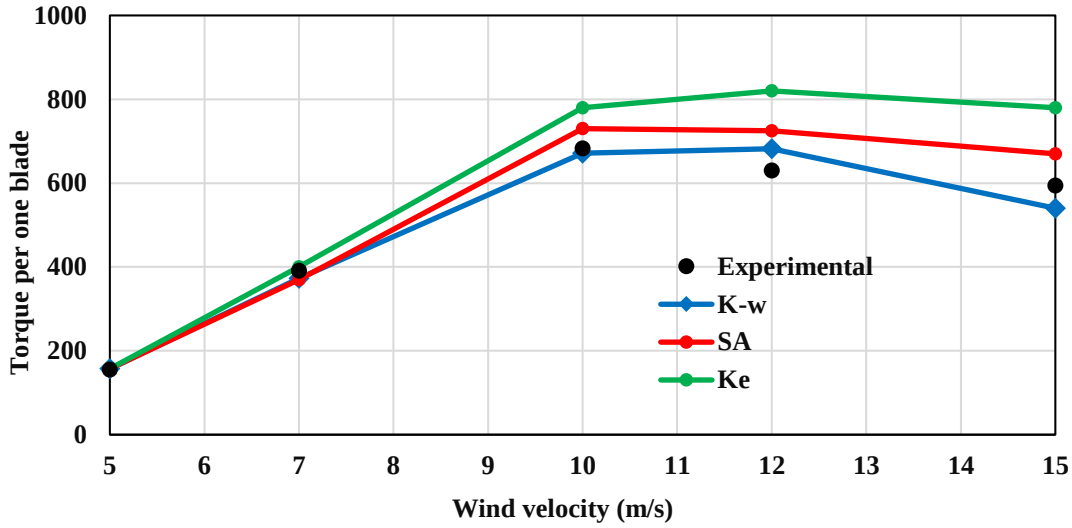

Figure 4-9: Turbulence model sensitivity study comparison

It can be noticed that the torque computed by the Realizable k−ε turbulence model is over predicted compared to the experimental data for wind velocity higher than 7 m/s. While SA and SST k–ω models show more accurate results for 5m/s and 7m/s wind speed cases, as the flow is predominantly attached. Extending to near stall, at about10 m/s, the SS*T* k–ω model shows superior results compared to the other models in view of the experimental wind tunnel results. However, for the post-stall, above 10 m/s wind velocity, both SA and SST k–ω models fail to capture the unsteady flow conditions around the blade. Each model behaves differently as the turbulence implementation for each is different. The SA model is an economical model, which solves one transport equation to measure the kinematic eddy viscosity. However, the slightly less efficient SST k-ω model exhibits more accurate prediction of the adverse pressure gradients and separating flow. Therefore, as this turbulence model shows greater accuracy for the two velocity cases explored, it is selected for all further CFD studies for the 3D-HAWT.

4.2.7 Mechanical power and flow features

The results achieved thus far using CFD have been compared with experimental wind tunnel data of torque in order to validate the CFD method. Another important parameter is the output mechanical power, P (W), which is calculated using:

$$P = BQ\Omega \tag{4-1}$$

where Q is the torque per blade about the flow axis (N.m), Ω is the rotor angular velocity (rad/s) and B is the number of blades.

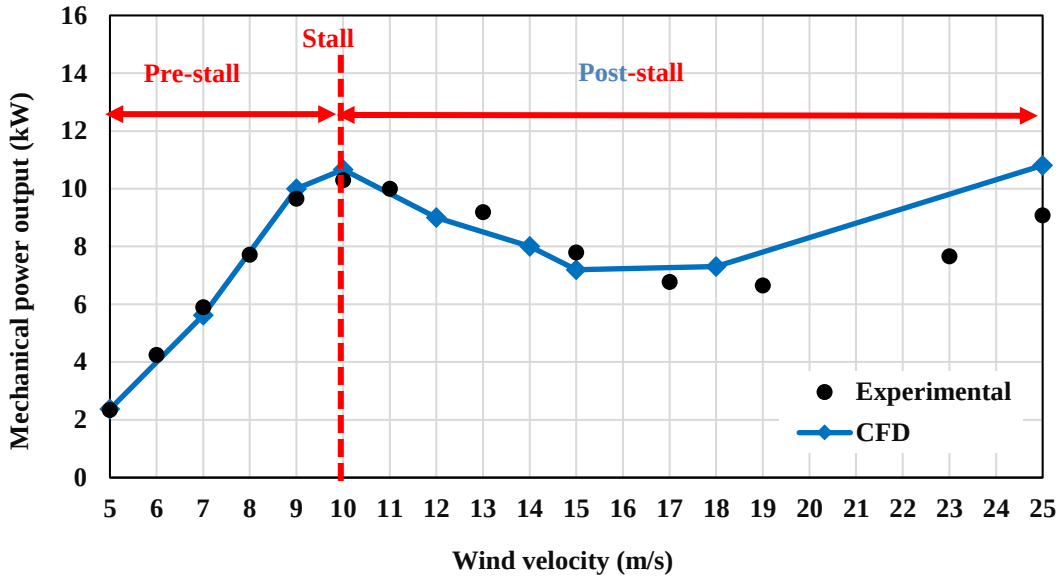

Figure 4-10: Mechanical power output comparison

The numerical results of the power curve are divided into three stages as indicated in figure 4.10. These regions are pre-stall, stall and post-stall. The flow separation and wake behaviour vary at each stage, which is captured with varying levels of accuracy by the CFD approach adopted here. The flow over the NREL phase VI HAWT is presented and visualised at each stage as described below.

4.2.7.1 Pre-stall stage

In terms of mechanical power, there is a good agreement between wind tunnel data and the CFD results for the wind velocity up to 8 m/s. Within the pre-stall region shown in Figure 4.10, the wind speed is relatively low. The streamlines around the blade remain fully attached along the blade. This flow pattern is visualised in figures 4.11 for a wind velocity of 7 m/s, for example, at different blade sections which were used in the wind tunnel. Moreover, the comparison of the pressure coefficient distribution at different

span-wise locations was very close to the wind tunnel results; where no flow separation has been indicated for all sections as shown in Figure 4.12. This underlines the ability of the CFD code to successfully model the flow behaviour in this regime.

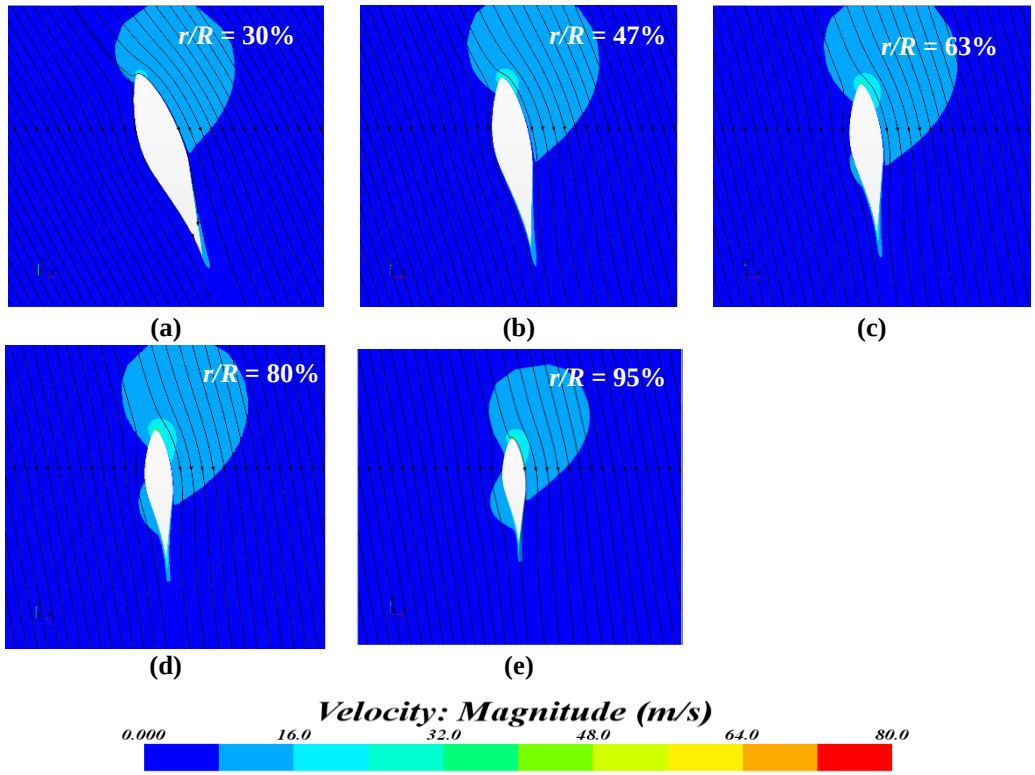

Figure 4-11: Velocity magnitude contours at different blade sections at a 7 m/s wind velocity

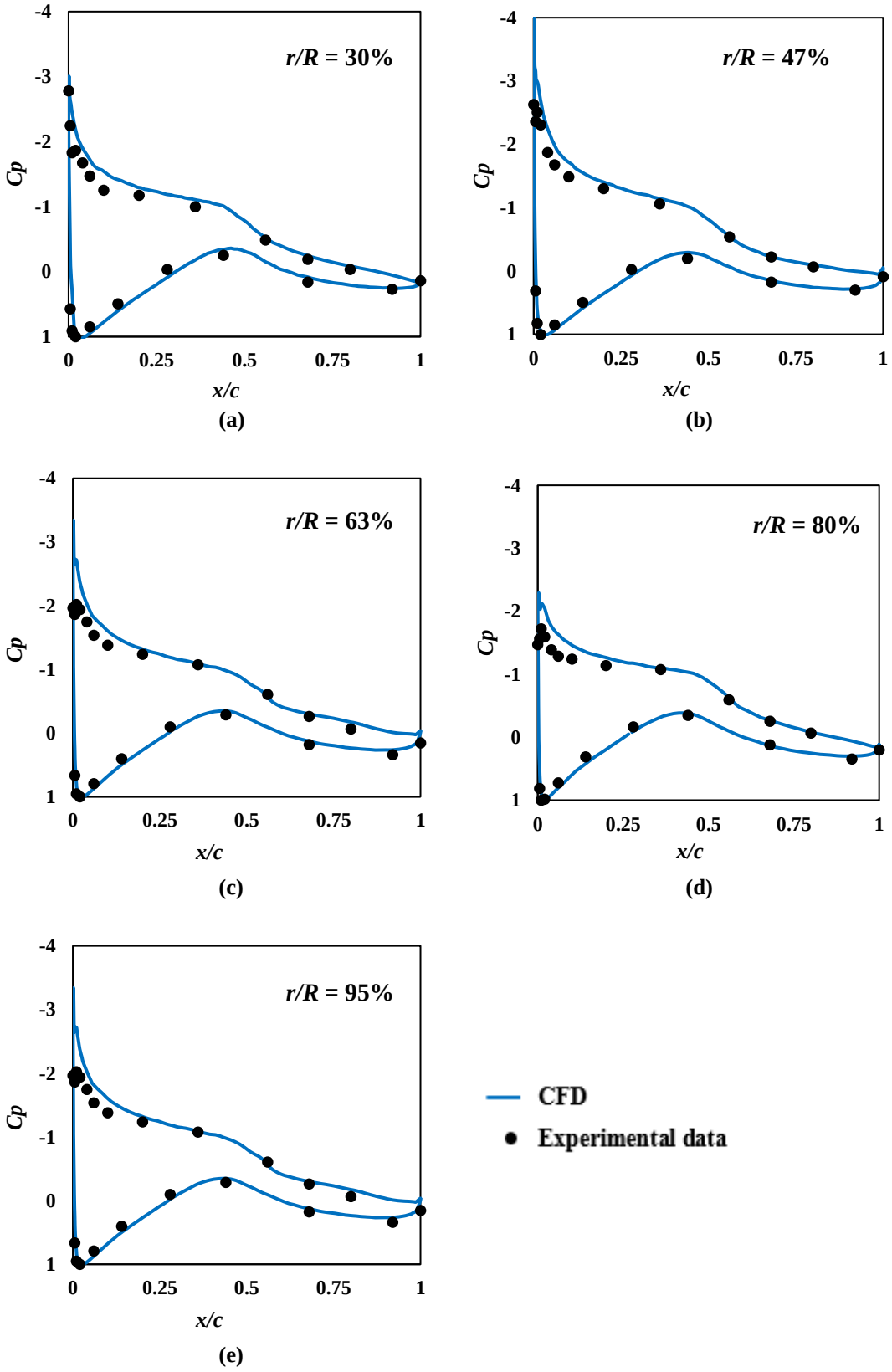

Figure 4-12: Pressure coefficient comparison at different blade sections at 7 m/s wind velocity

4.2.7.2 Stall Stage

This stage occurs at around 10 m/s wind velocity. The flow begins to separate on the blade's suction side, which leads to aerodynamic stall which affects the prediction accuracy. Figures 4.13 (a) and (b) clearly show a leading-edge flow separation at *r/R* =30% and 47% of the span. In practice, due to the blade rotation, there is also a span-wise flow that initiates a flow separation region starting from the root at *r/R*= 0% to reach its maximum before the 63% section. Afterward, the separation decreases at 80% section, and eventually disappears at the 95% section as a result of a low local angle of attack on the blade tip, as shown in Figure 4-14.

The corresponding pressure coefficient distribution at this wind velocity of 10 m/s is provided in figure 4-15. The flow separation is indicated by a flatter pressure distribution on the measured suction side at 30% and 47% sections (Figures 4-15(a) and (b), respectively). It can be noticed that the CFD poorly predicted the adverse pressure gradients at these particular span locations due to the difficulties in capturing separation phenomena. In addition, the CFD results demonstrate a significant suction peak at *x/c* = 0, while the experimental data prove that the separation starts at the leading edge. This issue is also reported in previous CFD studies [18, 42, 87, 89, 109].

However, the CFD results exhibit very close results compared to the wind tunnel data for the remaining blade regions considered (Figure 4.13). This indicates that the turbulence model used is capable of predicting the attached flow over the blade suction surface but it fails to capture the separation phenomenon.

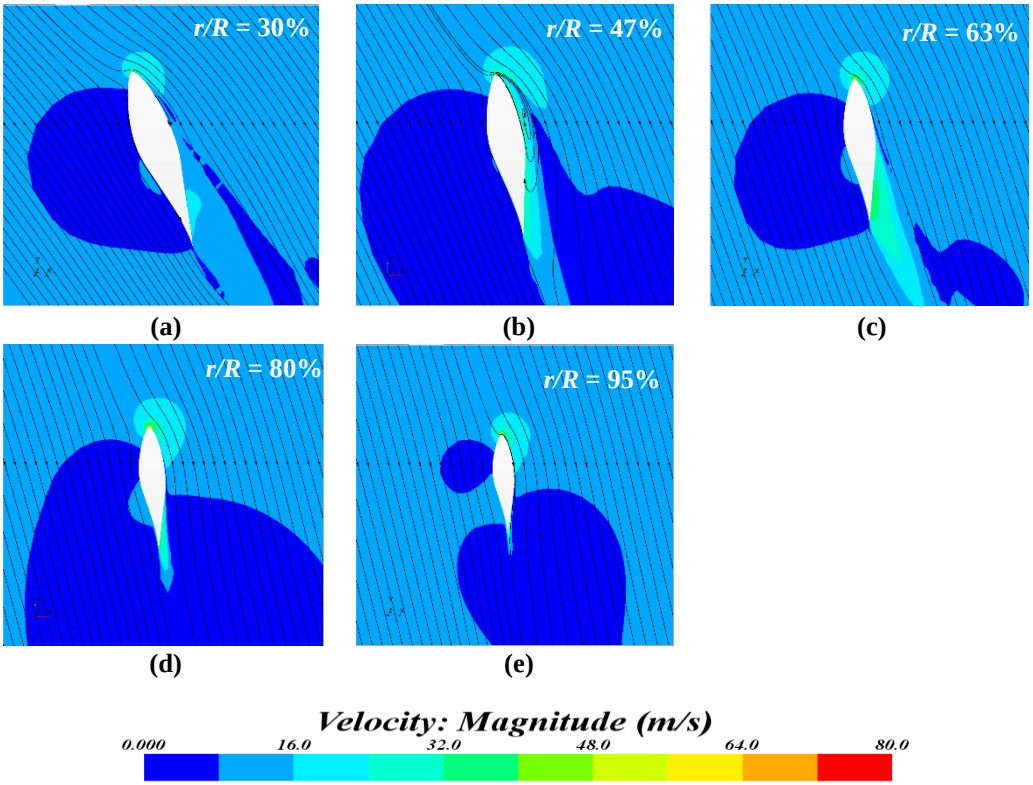

Figure 4-13 : Flow separation at different blade sections at 10 m/s wind velocity

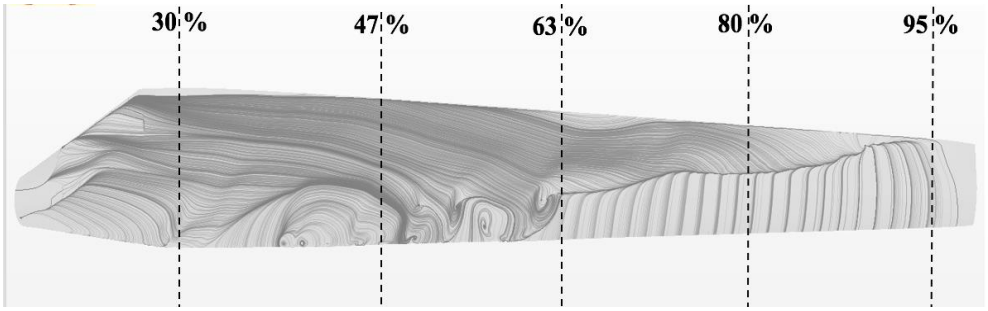

Figure 4-14: Constrained streamlines along the suction side of the blade at 10 m/s wind velocity

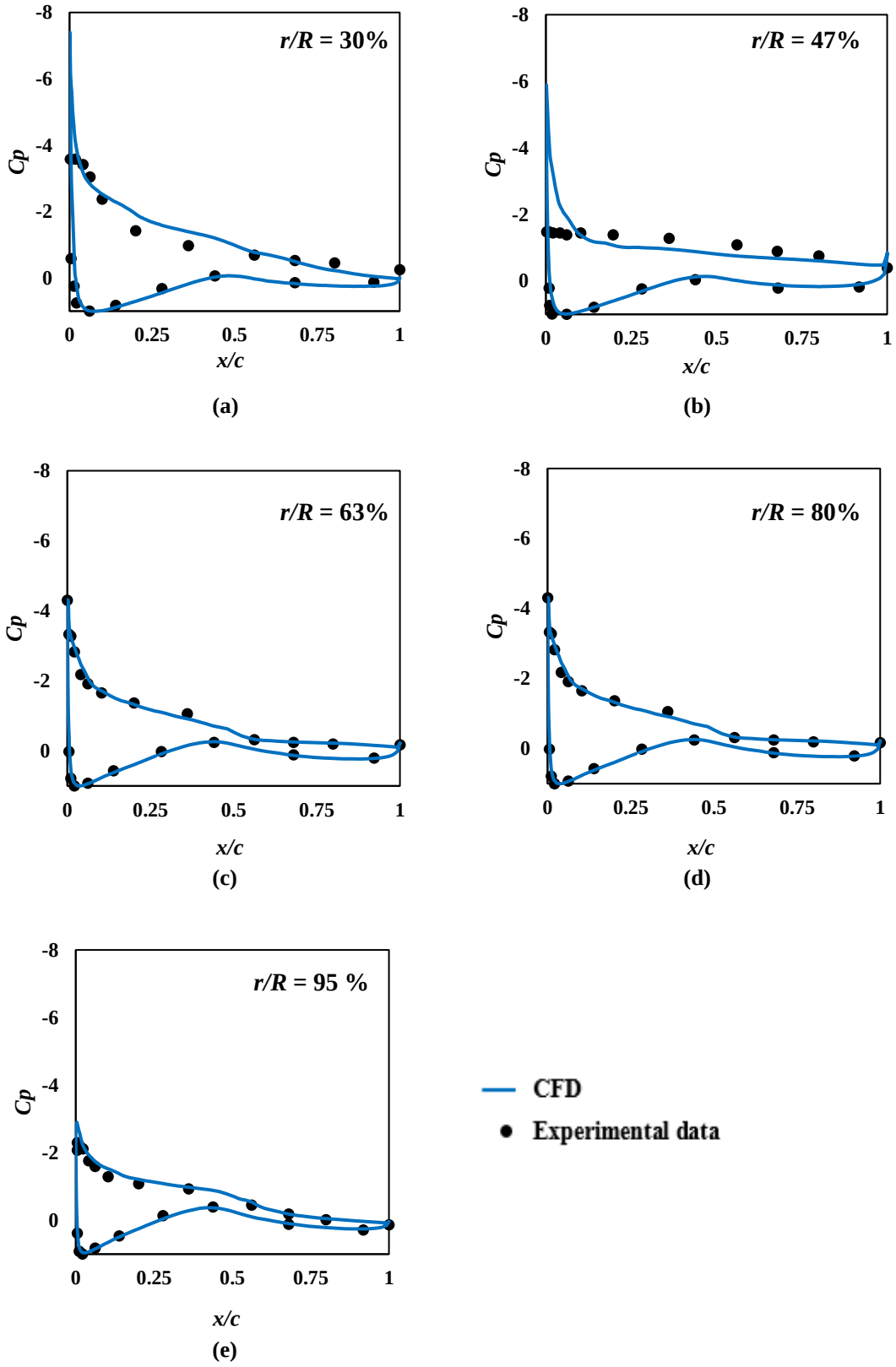

Figure 4-15: Pressure coefficient comparison at different blade sections at 10 m/s wind velocity

4.2.7.3 Post-stall stage

Figure 4.16 highlights the flow pattern at 15 m/s wind velocity with flow separation occurring over the entire blade span. This is indicated in the constrained streamlines along the suction side as well (Figure 4.17). Figure 4.18 shows resulting pressure coefficient distributions. It was observed that the accuracy of the CFD code is largely affected as the wind velocity increased above 10 m/s, due to the flow complexity. The limitations of the turbulence model is highly likely be responsible for the inaccuracy at high wind speeds; the RANS approach which has been adopted cannot accurately predict boundary layer separation, including vortex shedding [91, 93].

Using unsteady solutions could potentially be more accurate [18] but is not necessary since this research focusses on the pre-stall performance of circulation control. As will be shown later, the trailing edge CC becomes ineffective for lift / torque augmentation in the post-stall region because flow separation occurs in an area on the aerofoil suction side far from the T.E., and therefore, the CC jet will not be able to reattach the flow because it is too far away from the separation region to be able to influence it (i.e. reattach). Therefore, steady RANS solutions are chosen for all further CFD studies since they have demonstrated acceptable accuracy (with an average error of 1.5%) within the pre-stall region which is of primary interest.

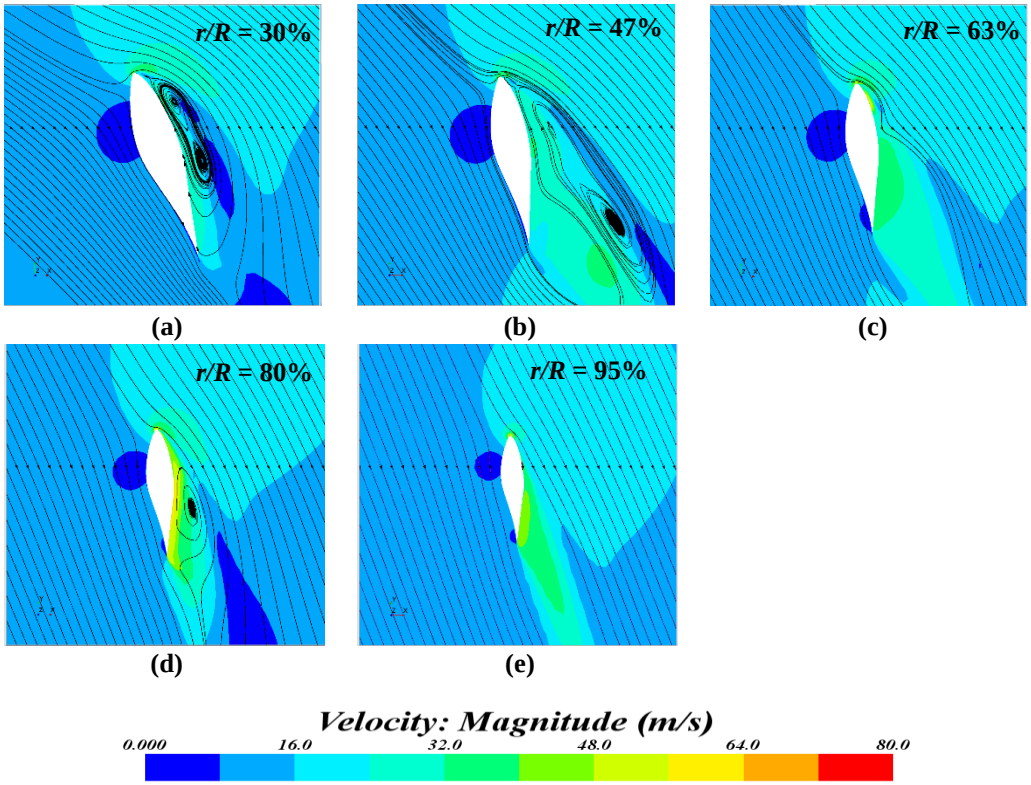

Figure 4-16: Flow separation at different blade sections at 15 m/s wind velocity

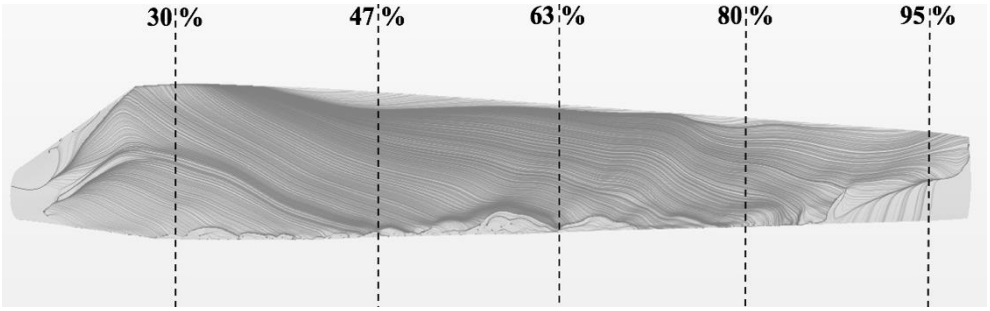

Figure 4-17: Constrained streamlines along the suction side of the blade at 15 m/s wind velocity

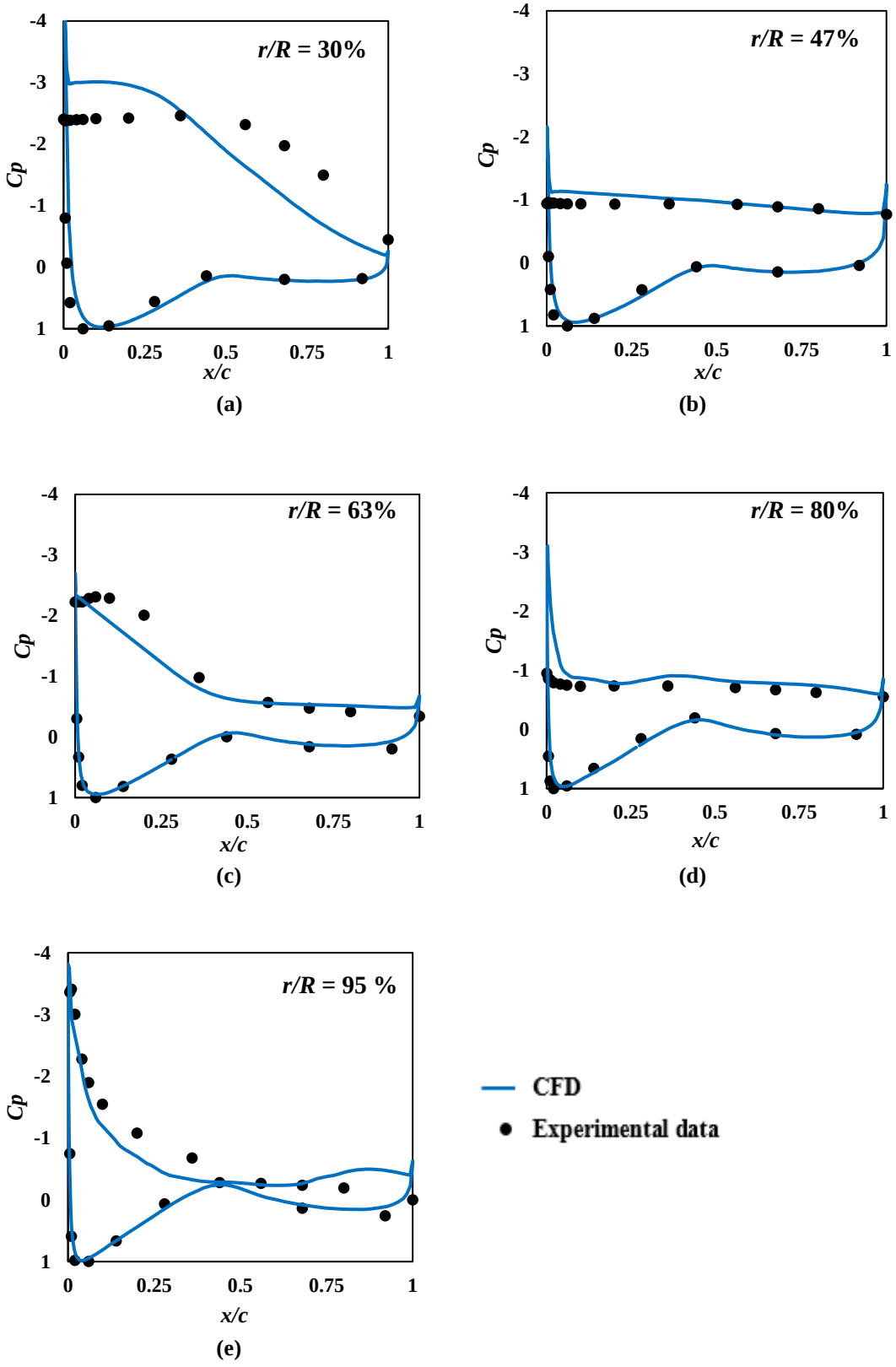

Figure 4-18: Pressure coefficient comparison at different blade sections at 15 m/s wind velocity

4.3 NREL 5 MW Baseline HAWT

The NREL 5MW baseline HAWT turbine was developed from the Dutch Offshore Wind Energy Converter (DOWEC) project using BEM analysis, and is closely based on the REpower 5M turbine. It is a relatively large off-shore HAWT, which consists of three blades of 63m span. The cut in, rated and cut-out wind velocities are 3m/s, 11.4m/s and 25m/s, respectively with a rated generated power output of 5MW. The angular velocity of the rotor rises from 6.9 RPM at the cut-in velocity to 12.1 RPM at rated wind velocity and remains fixed from the rated wind velocity up to the cut-out value. Unlike the NREL phase VI rotor, a pitch control technique is applied above the rated wind velocity to maintain the rated power at 5 MW. Hence the pitch angle of the blade is varied at higher wind velocities up to 23.47^{o} at 25m/s. However, the blade pitch angle is zero below the rated wind velocity.

4.3.1 Blade geometry

This turbine blade consists of six different types of aerofoil at each plane (Table 4-5). From *r/R* = 15 % to 63.5%, the blade consists of the Delft University (DU) series aerofoils and the NACA 64-618 aerofoil for the outer section. Full details of the geometry and performance data are published in [15]. Figure 4.19 shows the generated CAD model using SolidWorks (V2014 x64).

Table 4.5: NREL 5MW blade planes [15]

Plane	RNodes (m)	Chord (c) m	c*AeroOrig	AeroTwst (deg.)	Airfoil type
1	1.5	3.542	1.771	0	Cylinder 1
2	2	3.542	1.771	0	Cylinder 1
3	2.8667	3.542	1.771	0	Cylinder 1
4	5.6	3.854	1.69576	0	Cylinder1
5	8.3333	4.167	1.58346	0	Cylinder2
6	11.75	4.557	1.3671	13.308	DU40-A17
7	15.85	4.652	1.163	11.48	DU35-A17
8	19.95	4.458	1.1145	10.162	DU35-A17
9	24.05	4.249	1.06225	9.011	DU30-A17
10	28.15	4.007	1.00175	7.795	DU25-A17
11	32.25	3.748	0.937	6.544	DU25-A17
12	36.35	3.502	0.8755	5.361	DU21-A17
13	40.45	3.256	0.814	4.188	DU21-A17
14	44.55	3.01	0.7525	3.125	NACA64-618
15	48.65	2.764	0.691	2.31	NACA64-618
16	52.75	2.518	0.6295	1.526	NACA64-618
17	56.1667	2.313	0.57825	0.863	NACA64-618
18	58.9	2.086	0.5215	0.37	NACA64-618
19	61.6333	1.419	0.35475	0.106	NACA64-618
20	62.9	0.7	0.175	0	NACA64-618

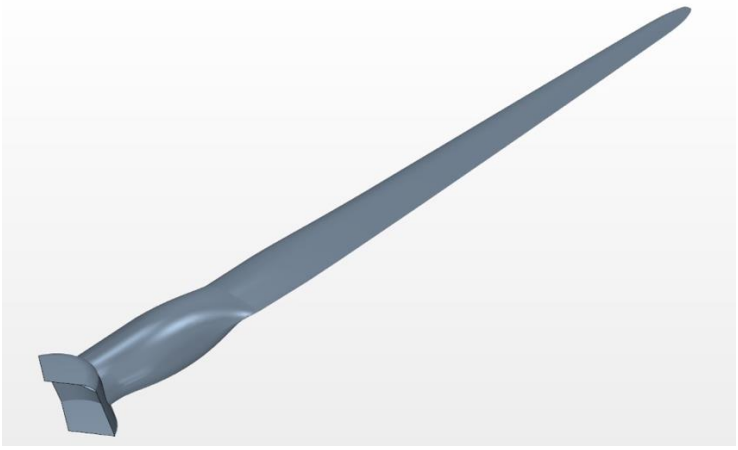

Figure 4-19: NREL 5 MW generated CAD model by SolidWorks (V2014 x64)

4.3.2 Computational domain and boundary conditions

Figure 4.20 illustrates the computational domain and boundary conditions used (see also Table 4.5). The minimum Reynolds number at wind velocity 5 m/s is calculated at the root according to Table 4.5 (section 6) which was around 3.131M. While at the tip (section 20), it was around 2.314M. Therefore, the dominated flow around the whole blade is turbulent. Only one blade is modelled in an axisymmetric domain shape to reduce the computational effort. The blade is mounted inside a cylindrical segment of 120^{o}. Generally, the dimensions and boundary condition settings are the same as those from the earlier NREL phase VI model, except that the domain outer shell is set to be a pressure outlet instead of a slip-wall in the previous case. The reason behind this change is for the actual flow characteristics to be represented; the pressure outlet provides a more realistic boundary condition for unrestricted flow. Previously, the NREL phase VI case set the domain outer shell as a slip-wall, to simulate the wind tunnel condition.

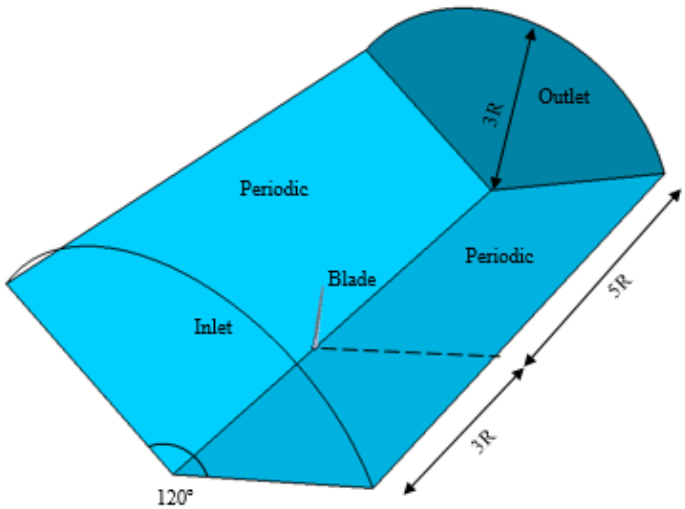

Figure 4-20: Computational domain containing the NREL 5 MW turbine blade

Table 4.6: Computational conditions

No.	Parameter	Value
1	Simulation type	3D, steady, incompressible
2	Fluid	Air
3	Solver type	Segregated flow
4	CFD algorithm	SIMPLE
5	Turbulence model	SST $k-\omega$
6	Blade rotation	7.506 - 12.1 RPM
7	Blade	No-slip wall ($u=v=w$ =0 m/s)
8	Inlet	Velocity Inlet (5-25 m/s)
9	Domain outer shell	Pressure outlet = 0 Pa (gauge)
10	Outlet	Pressure outlet = 0 Pa (gauge)
11	Base	Symmetry, periodic interface, slip wall

4.3.3 Mesh refinement and wall *y+*

The same approach to meshing described in section 4.2.3 is adopted for this wind turbine. Cells are concentrated around the leading and trailing edges and the blade is wrapped in 20 layers of cells to resolve the boundary layers. Figure 4.21 displays the mesh structure in the stream-wise view (figure 4.21 (a)) and close up span-wise views at r/R=50% and 85% sections. Table 4.7 illustrates results from the mesh independence study. Although there is a slight difference between mesh 2 and mesh 3, mesh number 3 is used in the simulation to provide more gradual cell size transition for further study on the blade. Moreover, Figure 4.22, shows that the wall y^+ value is below 5 for most of the blade surface and the average value is about 2.2. As has already been described, there is no experimental data to validate the CFD results for the NREL 5 MW wind turbine, so results are compared with those from the FAST BEM code instead. It should be noted that the suitability of the computational method has already been demonstrated in section 4.2.

Table 4.7: 3D Mesh refinement investigation at 8m/s free-stream velocity

Grid No.	Blade cell size (m)	Number of prism layers	Total prism layers thickness (m)	Total cells number (M)	Mechanical Power (MW)
1	0.020	15	0.012	11.1	1.92
2	0.015	20	0.015	14.2	1.86
3	0.012	20	0.015	17.7	1.85
4	0.010	20	0.012	19.8	1.85
FAST	-	-	-	-	1.77

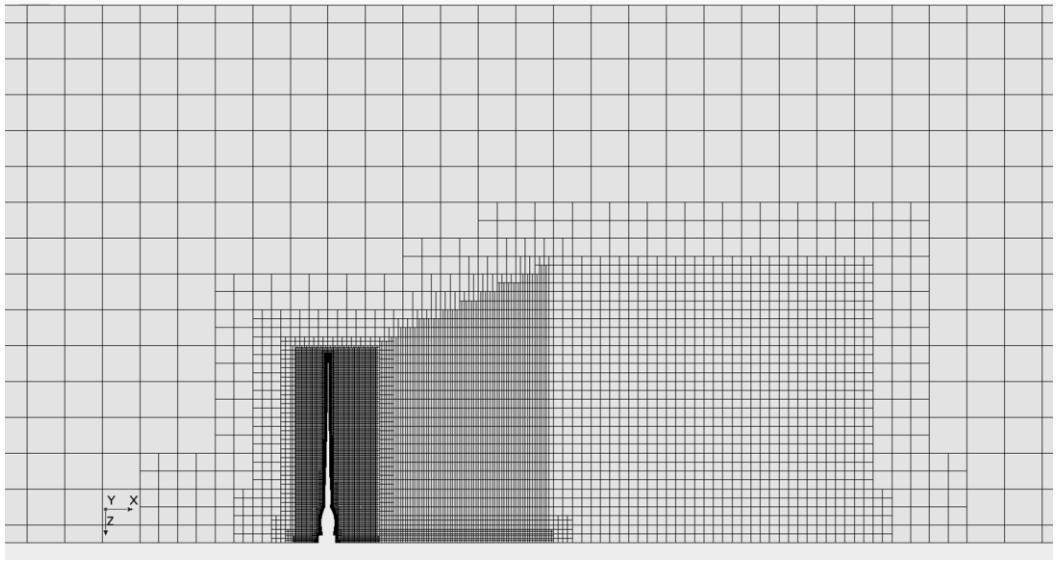

(a)

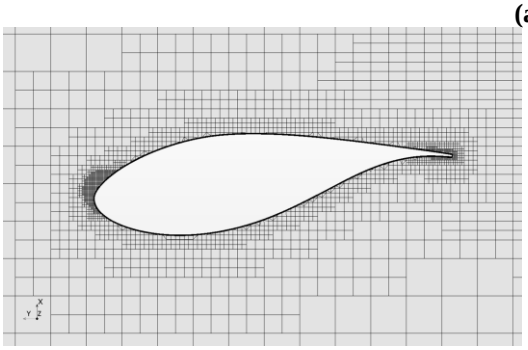

(b)

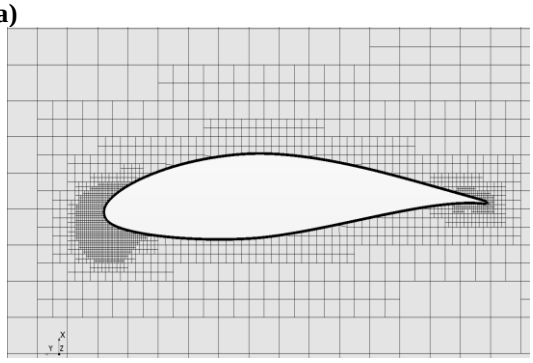

(c)

Figure 4-21: Mesh resolution at (a) mesh at 60º plane, (b) *r/R* =50% section and (c) *r/R* =85% section

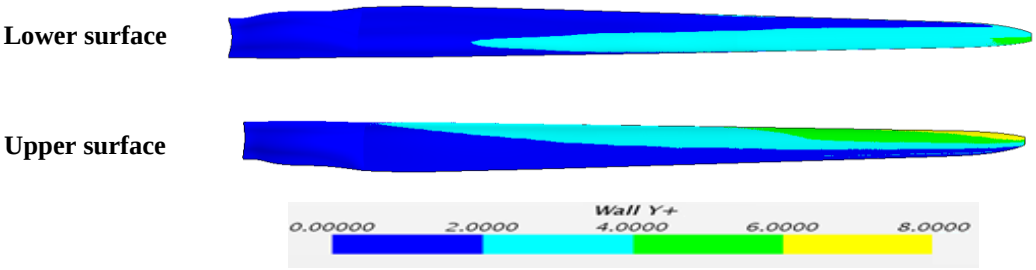

Figure 4-22: Wall *y+* on the blade surfaces, grid number 3 (Table 4-7)

4.3.4 Solver setup

As for the NREL phase VI study, only one blade is modelled in an axisymmetric computational domain to reduce computational resources, using a 120^{o} cylindrical segment shown in Figure 4.20. Periodic inflow and out-flow boundary conditions are used to allow for the blade rotation and wake effects. The SST *k-ω* turbulence model is employed with an incompressible steady-state solver (STAR CCM+, V11.04.012).

4.3.5 Results and discussion

Flow simulations were performed for wind speeds in the range 5 - 25 m/s and corresponding rotational speeds of 7.5 - 12.1 RPM as defined in [15]. Blade variable pitch is only used for wind speeds above the rated condition to control post-stall performance [15]. Furthermore, a rigid blade was assumed. Very good agreement is achieved using the CFD approach and FAST, with CFD over-predicting the mechanical shaft power by approximately 5%, as shown in figure 4.23. From figures 4.24 to 4.28, it can be seen that flow streamlines remain attached to the blade surface even for higher velocities since the NREL 5 MW is a pitch-controlled rotor. This indicates the capability of the CFD simulation to accurately predict the flow around the NREL 5 MW using the above-described setup.

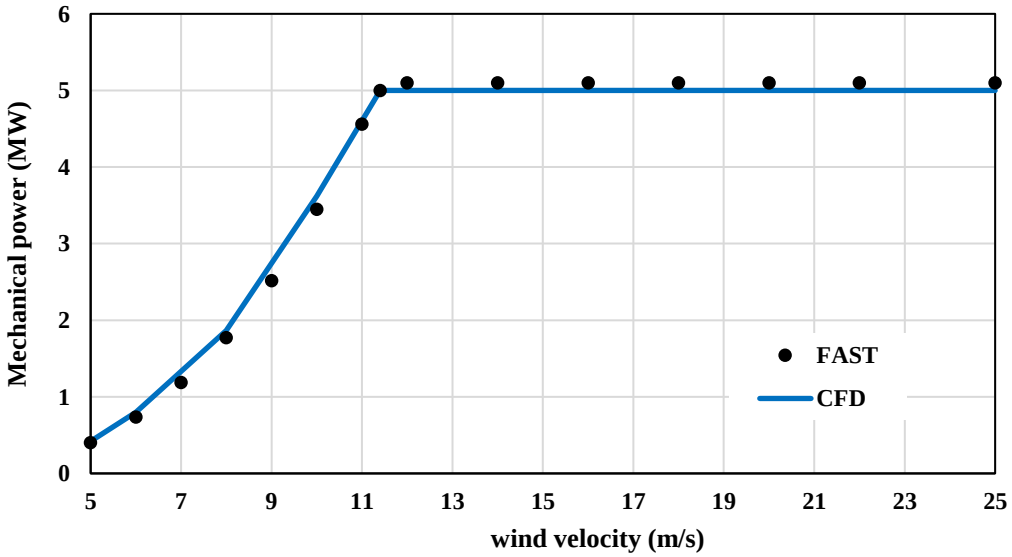

Figure 4-23: Mechanical power comparison

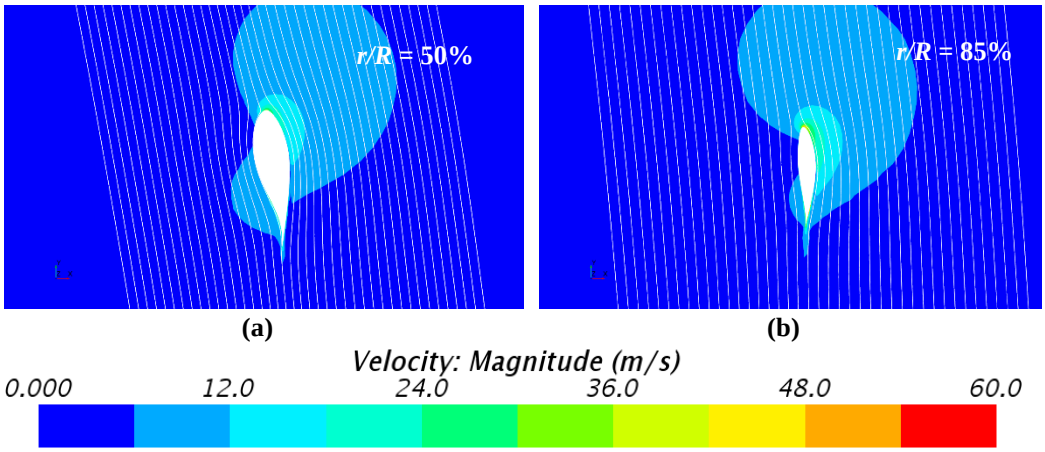

Figure 4-24: Flow streamlines at different blade sections at 6 m/s wind velocity

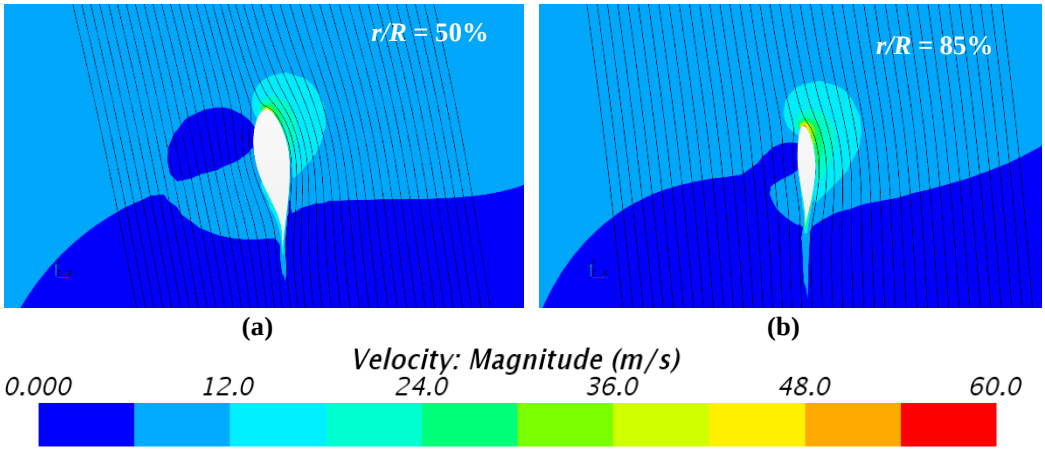

Figure 4-25: Flow streamlines at different blade sections at 8 m/s wind velocity

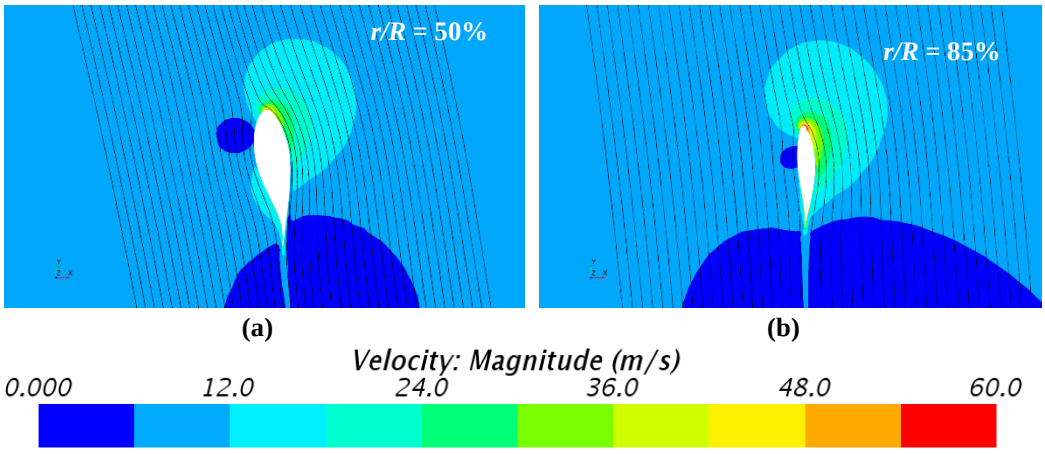

Figure 4-26: Flow streamlines at different blade sections at 10 m/s wind velocity

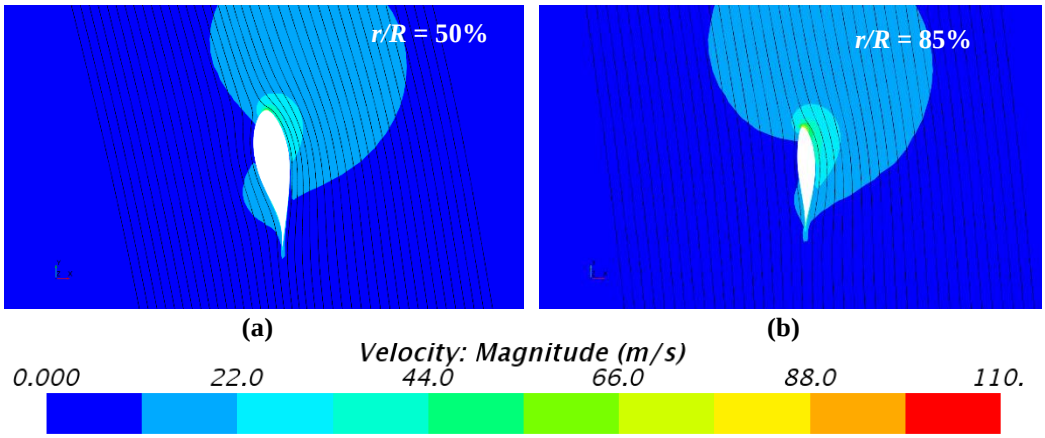

Figure 4-27: Flow streamlines at different blade sections at 11 m/s wind velocity

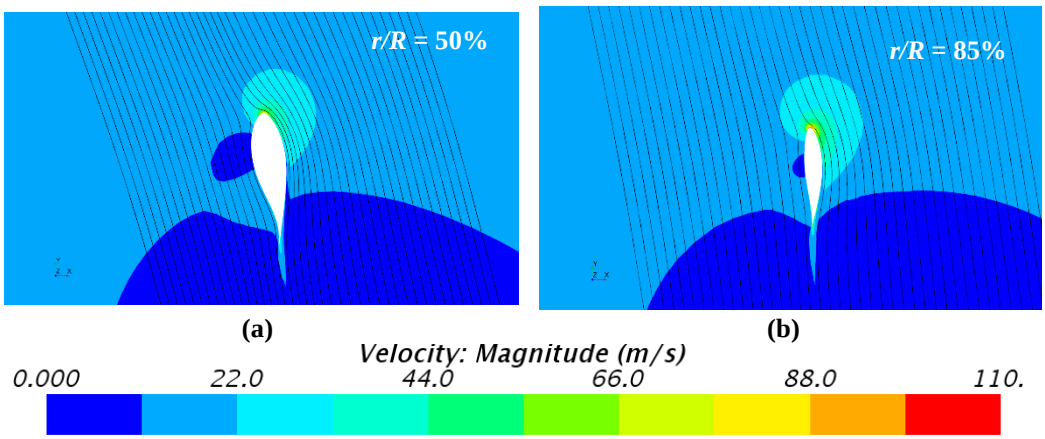

Figure 4-28: Flow streamlines at different blade sections at 15 m/s wind velocity

4.4 Chapter summary

A 3D validation study for 2 types of HAWT was carried out in this chapter. The steady-state CFD results provided good agreement with the available experimental data for both cases within the pre-stall region, while the accuracy of the post-stall region was questionable. The work done in this chapter reveals that the SST *k*-ω turbulence model demonstrates superior performance compared to the other models studied. Therefore, the basis of blade modifications for the next chapters will follow the same computational strategy, including use of the SST *k*-ω model.

Chapter 5 TWO-DIMENSIONAL AEROFOIL MODIFICATION AND PARAMETRIC STUDY

5.1 Introduction

Following on from the validation study, the next stage is to investigate the feasibility of integrating flow control for a suitable blade section. As explained in the literature review, the Coanda effect is a powerful flow control technique which is achieved by blowing a high-velocity flow through a nozzle over a rounded trailing edge of an object, such as an aerofoil. In order to successfully deploy circulation control on an aerofoil, the geometry must be modified in terms of T.E curvature, nozzle location and height [23, 62]. Ideally, the modification should avoid a higher drag penalty which might be expected due to the rounded trailing edge when the jet is not active. To do so, the upper surface (suction side) of the aerofoil under consideration was modified, while leaving the lower surface (pressure side) unmodified [14, 23]. In this chapter, a benchmark aerofoil with circulation control was used to validate a CFD modelling approach, before exploring three different geometric parameters aimed at improving the performance of a CC aerofoil.

5.2 Two-dimensional validation study

A widely used benchmark CC aerofoil developed by Englar *et al* [54] is the CC-E0020EJ, shown in Figure 5.1. This was tested in the Basic Aerodynamic Research Tunnel at NASA Langley as well as the Model Test Facility at the Georgia Tech Research Facility [54]. Although such a symmetric profile is not ideal for aerodynamic applications, the relatively large trailing edge radius (about 9.5% c) enables thorough investigations for the separation behaviour around it. This model has been used as a test case for flow control to develop and validate the CFD modelling approach, as has been achieved in many CC studies [59, 61, 112-114].

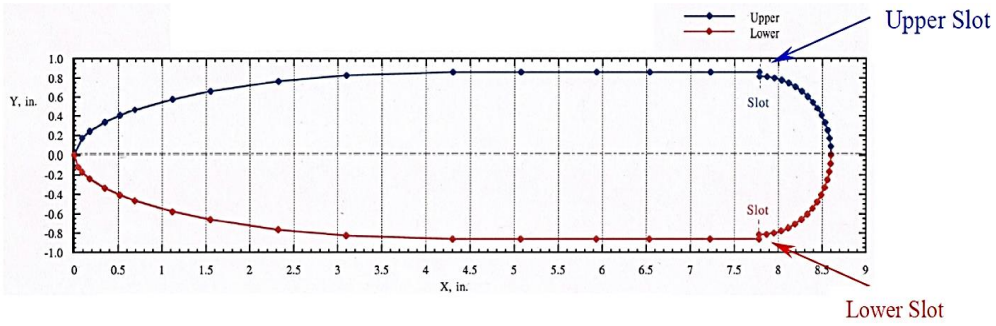

Figure 5-1: 2-D benchmark Geometry of CC-E0020EJ aerofoil [54]

In terms of jet flow modelling, only the upper blowing nozzle was used. Following the recommendations given in [112], an internal plenum chamber was included to ensure the nozzle exit velocity profile was representative (figure 5.2(b)). Although a uniform velocity inlet boundary condition (figure 5.2(a)) can reasonably capture the Coanda effect [61], the interaction between the jet, the upper surface boundary-layer and the free shear layer is better captured using the plenum. Both approaches will be implemented in this validation study to measure the effect of modelling the jet flow using plenum versus a direct uniform blowing source.

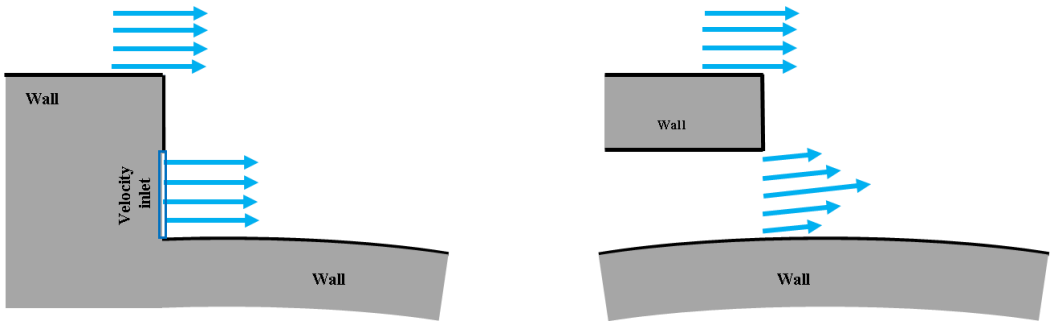

(a) **(b)**

Figure 5-2: Velocity profile for blowing via (a) direct velocity inlet boundary condition and (b) plenum approach

5.2.1 Domain and boundary conditions

The computational domain size and boundary conditions are illustrated in figure 5.3, where the aerofoil chord, *c*, is 0.218 m (8.6 in). All simulated and experimental data presented are for an aerofoil angle of attack of 0°. The jet blowing intensity per unit span is defined by a non-dimensional momentum coefficient, $C\mu$, [54, 59], given by:

$$C_{\mu} = \frac{\rho_j \, h_j \, U_j^2}{q \, c} \tag{5-1}$$

where ρ_j is the air density (1.18415 kg/m^3), h_j is the jet nozzle height (0.000508 m or 0.02 inch case), U_j is the jet velocity and q is the freestream dynamic pressure (718.2 Pa or 15 psf measured in the experiment [54]), with a free stream-stream velocity, U_∞ = 34.8 m/s, corresponding to Re = 0.5M. These parameters matched the free-stream Mach number M_∞= 0.1 case from the wind tunnel tests. Furthermore, for comparison, this study considered two blowing conditions, $C\mu$= 0.047 and 0.115 due to the availability of previous CFD results for these particular blowing coefficient values [54, 112-114].

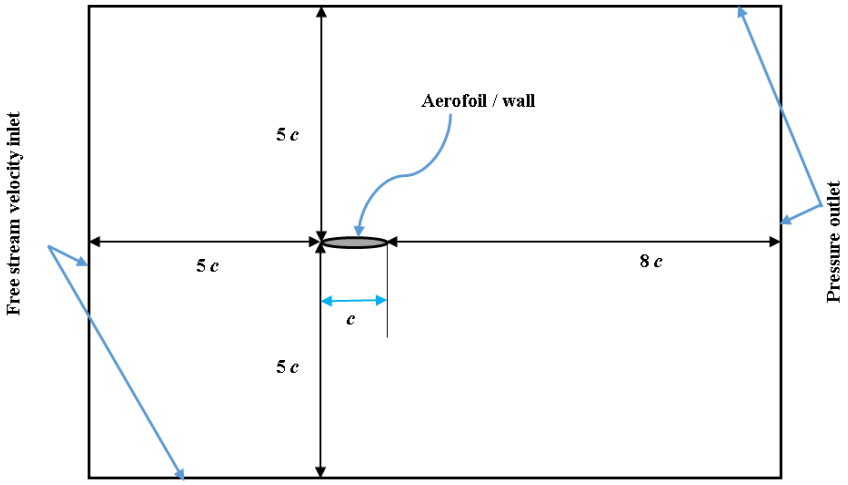

Figure 5-3: 2-D domain size and boundary conditions (not to scale)

In order to define the jet flow using the direct blowing approach, the jet exit boundary line (along the jet height) is defined with a constant velocity inlet condition with flow direction normal to the boundary. Using Equation (5-1), the U_j values were defined as 110.7 m/s and 173.2 m/s corresponding to $C\mu$= 0.047 and 0.115, respectively.

Alternatively, using the plenum approach requires the amount of the stagnation (total) pressure inside the plenum to be defined for the associated momentum coefficient and mean jet exit velocity. This approach is more practical than the first since it matches the plenum stagnation pressure used in the experiment and is potentially more realistic.

The plenum stagnation pressure can be related to the mean jet exit velocity by assuming an adiabatic and isentropic flow in the convergent nozzle with no losses in stagnation flow properties as shown in Figure 5-4. The required NPR value is achieved by means of a compressor located outside of the control volume (*i.e.* the wind tunnel in the experiment). This enables a rise in the stationary ambient pressure up to the required stagnation pressure inside the plenum as illustrated in figure 5-4. The following

isentropic equations are used to relate static and stagnation flow properties, the latter denoted by subscript (o) [35]:

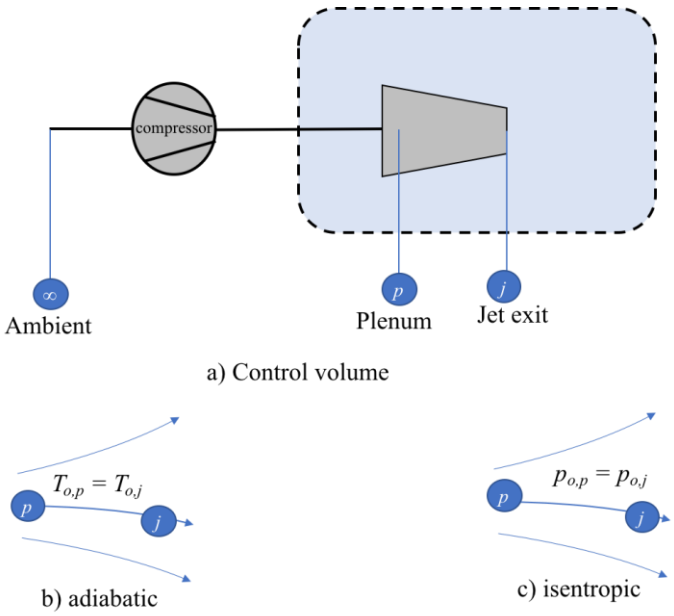

Figure 5-4: Schematic of the adiabatic and isentropic process inside the plenum

$$T_o = T + \frac{U^2}{2\,c_p} \tag{5-2}$$

$$\frac{T_o}{T} = 1 + \frac{M^2\,(\gamma - 1)}{2} \tag{5-3}$$

$$\frac{T_o}{T} = \left(\frac{p_o}{p}\right)^{\frac{\gamma-1}{\gamma}} \tag{5-4}$$

$$\frac{p_o}{p} = \left[1 + \frac{M^2(\gamma - 1)}{2}\right]^{\frac{\gamma}{\gamma-1}} \tag{5-5}$$

The left side term of Equation (5-5) is the ratio of the jet stagnation (total) pressure, $p_{o,j}$, (same as the plenum stagnation pressure $p_{o,p}$) to the jet static pressure, p_j. If the convergent nozzle exit flow is assumed to be subsonic and therefore not choked, flow conditions in the nozzle can adapt to changing conditions outside of the nozzle. The nozzle is therefore fully expanded and the exit static pressure will be equal to the ambient

static pressure, $p_j = p_\infty$ [113]. The ratio is commonly defined as the Nozzle Pressure Ratio *i.e.* NPR = $p_{o,j}/p_\infty$ [54, 114-118]. Therefore,

$$\text{NPR} = \left[1 + \frac{M_j^2(\gamma - 1)}{2}\right]^{\frac{\gamma}{\gamma-1}} \tag{5-6}$$

and solving for M_j,

$$M_j^2 = \frac{2}{\gamma - 1}\left[(NPR)^{\frac{\gamma-1}{\gamma}} - 1\right] \tag{5-7}$$

Assuming a perfect gas, $M_j = U_j/U_s$, where U_s is the speed of sound and is equal to $\sqrt{\gamma R_g T_j}$, therefore:

$$U_j{}^2 = \frac{2\,\gamma\,R_g\,T_j}{\gamma - 1}\left[(NPR)^{\frac{\gamma-1}{\gamma}} - 1\right] \tag{5-8}$$

$$U_j{}^2 = \frac{2\,\gamma\,R_g\,T_j}{\gamma - 1}\,(NPR)^{\frac{\gamma-1}{\gamma}}\left[1 - \frac{1}{(NPR)^{\frac{\gamma-1}{\gamma}}}\right] \tag{5-9}$$

Recalling that

$$\frac{T_{o,j}}{T_j} = \left(\frac{p_{o,j}}{p_j}\right)^{\frac{\gamma-1}{\gamma}} = (NPR)^{\frac{\gamma-1}{\gamma}}$$

$$T_{o,j} = T_j\,(NPR)^{\frac{\gamma-1}{\gamma}}$$

Equation (5-9) can be written as:

$$U_j = \sqrt{\frac{2\,\gamma\,R_g\,T_{o,j}}{\gamma - 1}\left[1 - \frac{1}{(NPR)^{\frac{\gamma-1}{\gamma}}}\right]} \tag{5-10}$$

It is assumed that the stagnation (total) temperature at the jet, $T_{o,j}$ is equal to the plenum stagnation temperature, according to the adiabatic relation as shown in Figure 5-4 (b). Hence, according to Equation (5-10), the mean jet velocity can be determined from the given NPR. This enables the rear wall of the plenum to be set as a stagnation inlet boundary-condition in CFD in order to develop the required jet velocity at the nozzle exit. It should be noted that the actual static pressure at the jet exit is lower than the freestream static pressure since it expands to equal the local static pressure at the aerofoil surface at the jet location (see Figure 5-11) which was also highlighted by [113].

Assuming ideal (adiabatic and isentropic) conditions i.e. no heat or friction losses inside the plenum, leads to a slight difference (less than 4%) in the jet velocity magnitude compared with that measured in the experiment. Therefore, to match the flow conditions of $C\mu$ = 0.047 and 0.115, the experimental NPR values of 1.081 and 1.208 respectively [54] were used in this study.

5.2.2 Mesh refinement

The commercial CFD package STAR CCM+ (V11.04.012) was used to generate all meshes and flow solutions presented in this study. The mesh design philosophy relies on an Oct-tree method to populate the majority of the fluid domain with quadrilateral cells to minimise the effects of numerical diffusion. Several refinement regions are added around the aerofoil to control and refine the cell size relative to the far-field, in order to capture important flow details. In particular, significant refinement is added around the modified trailing-edge and nozzle location to capture the large velocity gradients and the interaction between the jet, the upper surface boundary-layer and the free shear layer, as well as the flow curvature due to the Coanda effect as shown in Figure 5-5. Furthermore, 20 prism layers are attached to the surfaces of the aerofoil and plenum to adequately resolve the attached boundary layers.

A mesh independence study, illustrated in table 5.1, reveals the total number of cells required to achieve an acceptable level of numerical accuracy as well as agreement with the experimental data. Four different grids were generated and defined as coarse, medium, fine, and very fine. For each grid, the same steady state conditions were evaluated with NPR = 1.081 and the same turbulence model (SST k-ω). Figure 5-5 shows different views of the mesh structure for the fine mesh design. Note that this figure shows the mesh comparison between direct blowing and plenum designs, however, the mesh independence results are for the plenum design only. The comparison between direct blowing and plenum is shown in section 5.2.4. As well as the SST k-ω turbulence model, others were also evaluated (see next section) but the resulting lift coefficient variations shown in table 5.1 are representative of all models tested. Lift coefficient, C_l, was obtained by integrating the surface pressure coefficients around the aerofoil (but excluding plenum surfaces) as given in table 5.1.

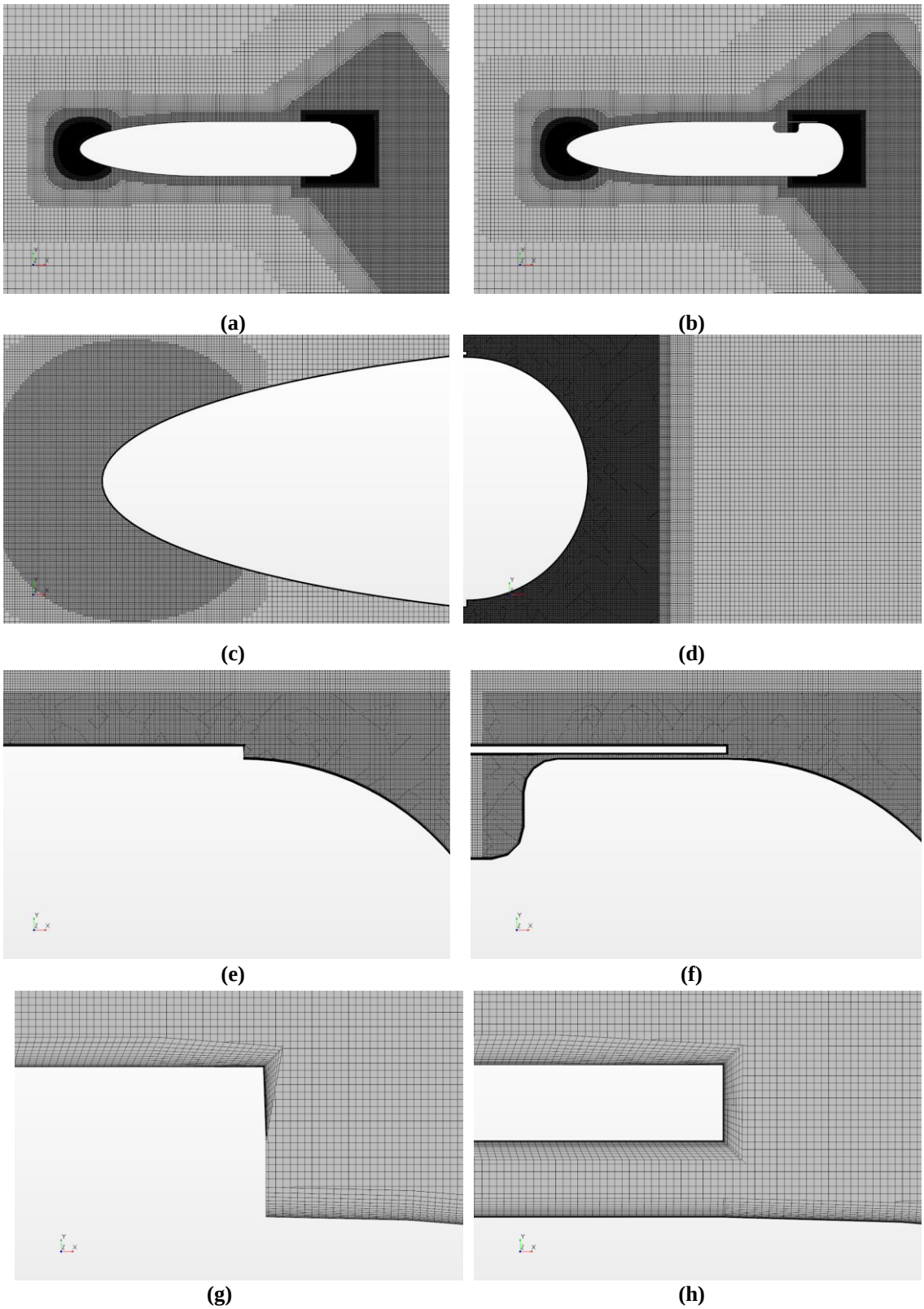

Figure 5-5: Mesh refinement (Fine grid) around (a) Direct blowing model, (b) Blowing via plenum model, (c) L.E, (d) T.E, (e) jet exit in the direct blowing model, (f), jet exit and plenum (g) close-up view of the jet and (h) close-up view of the jet and duct.

Table 5.1: Mesh refinement investigation on the plenum design model at NPR 1.081

Grid	Total Cells	C_l
Coarse	139017	1.507
Medium	203833	1.487
Fine	289793	1.385
Very fine	364882	1.383
Experimental [54]	-	**1.363**

Clearly a mesh independent result is obtained on both fine and very fine grids with a very close agreement with experimental data. Accordingly, the fine grid is used in all subsequent 2D computations. For the plenum model, about 10,000 extra cells were generated, compared to the direct blowing model, to mesh the plenum and the duct as shown in Figure (5-5 f and h).

It should be noted that the wall y^+ value is approximately 1 for all computations on the chosen mesh to ensure the boundary layer (BL) is resolved with sufficient accuracy. The wall y^+ values downstream of the jet location expectedly increase since the BL is separated or close to separation (Figure 5-6).

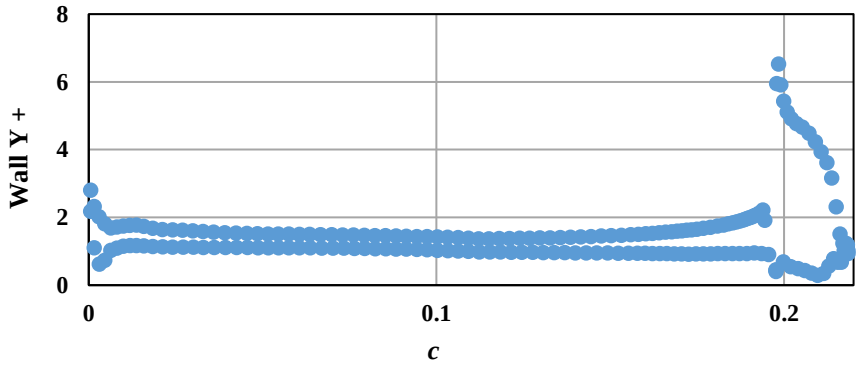

Figure 5-6: Wall y+ distribution around the aerofoil using SST *k-ω* model

5.2.3 Turbulence model

As in Chapter 4, the sensitivity of flow solutions to the turbulence model was considered with three alternatives, namely the Spalart-Allmaras (SA) model, Realisable *k-ε* model, and shear-stress transport (SST) *k-ω* model [54, 59]. As shown in Table 5.2, the turbulence models exhibit some variability in predicting the lift coefficient. Notably, the SST *k-ω* model provides the closest agreement with experimental data. The performance of the SST *k-ω* model in simulating the wake generated behind the T.E is

more accurate than the other investigated turbulence models and therefore, is used for all further flow solutions presented in this study.

Table 5.2: Turbulence model study (plenum design) NPR 1.081 using fine grid mesh

Turbulence model	C_l
SA	1.462
Realizable *k-ε*	1.439
SST *k-ω*	1.385
Experimental [54]	**1.363**

5.2.4 Jet opening

Another aspect of the modelling strategy warranting investigation is the way the jet opening is modelled. Two blowing approaches were implemented, as already shown in Figure 5-5. The direct blowing approach means that the jet opening boundary is defined as a velocity inlet (Figure 5-7a) and a constant velocity magnitude is prescribed on the boundary, as shown in Figure 5-7c. In the alternative approach, blowing via a plenum chamber is achieved by setting the stagnation pressure to an appropriate value on the upstream face of the chamber itself. This allows the flow to develop in a more realistic manner, at the jet exit, as shown in Figure 5-7(b) and (d). Furthermore, it can be seen from Figure 5-7e, that the flow exhibits a parabolic shape which is due to the shear forces (no-slip condition) on the duct wall.

A detailed comparison of the velocity profiles at the jet exit for the two differing CFD approaches are shown in Figure 5-7e for $C\mu = 0.115$, corresponding to an NPR value of 1.208. The same trend was seen at lower NPR ratios. Clearly, the direct blowing method provides a constant jet velocity which in this case is 173.2 m/s to achieve the required NPR. In contrast, the plenum approach produces a peak velocity of about 205 m/s and lower velocities near the duct walls due to the no-slip condition.

Also shown in Figure 5-7e is some overlaid experimental data taken from [54] for a very similar NPR of 1.21. This experimentally determined velocity profile was only provided in still-air conditions (M =0) by [54], however, Figure 5-7f shows that the overall velocity profile is essentially the same shape as that obtained with the plenum approach used here. Based on the CFD analysis in [54] it is clear that the peak velocity through the nozzle with circulation control active is around 10-15% greater for an external flow, compared to the still-air case. Overlaying the still-air experimental data

into the plenum approach used in the present study (Figure 5-7e) shows the same trend i.e. the peak velocity with the blowing plenum is 10-15% greater than the still-air experimental data which is consistent with [54].

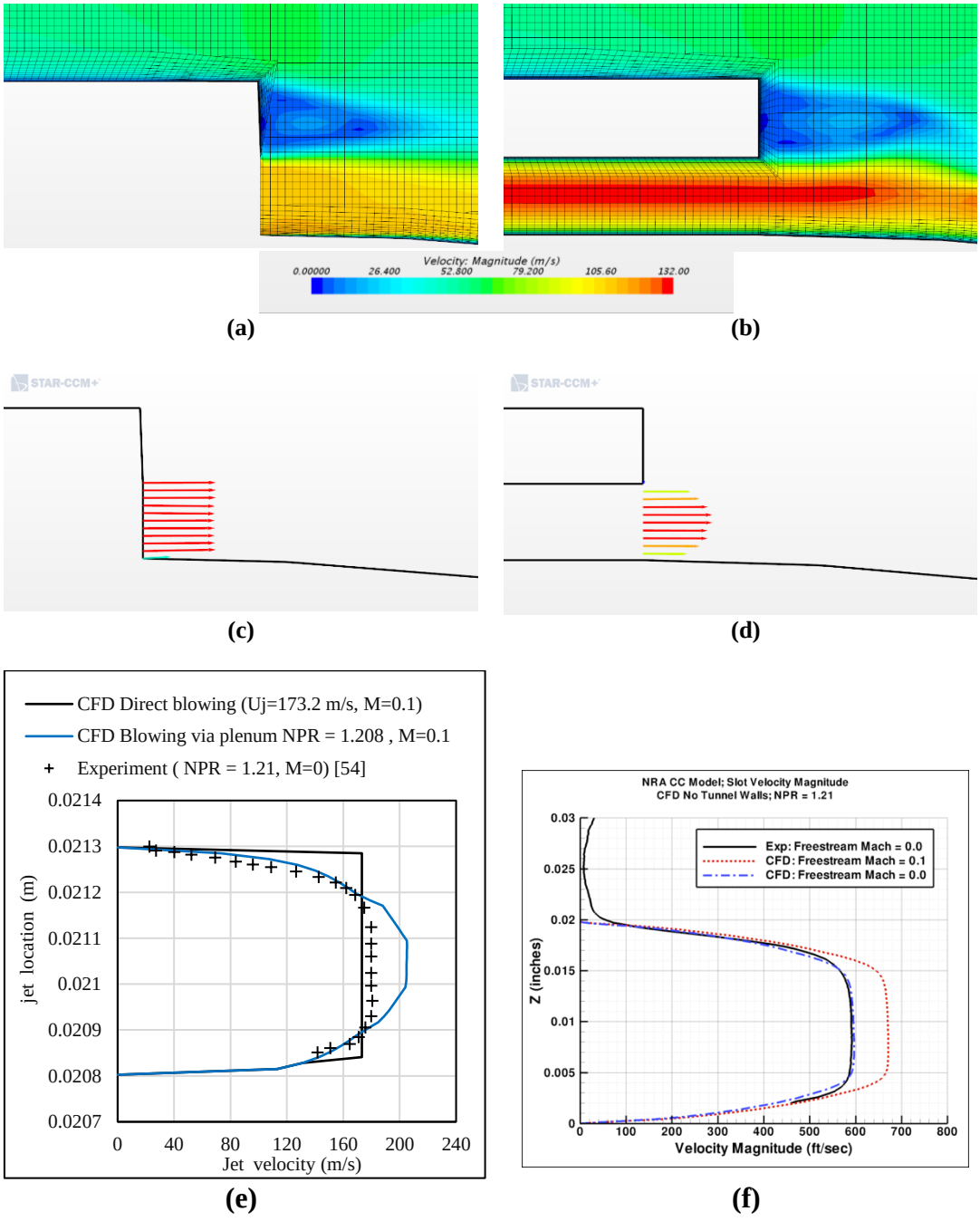

Figure 5-7: Jet exit velocity profile from (a) direct blowing, (b) blowing via a plenum, (c) velocity vectors for direct blowing, (d) and blowing via a plenum, (e) velocity profile comparison using both approaches and still-air experimental data and (f) velocity profile comparisons performed by [54].

Furthermore, it is evident that the plenum approach is much more suitable than the constant velocity profile from the direct blowing method which further justifies its implementation. One final point to note is that although the mesh resolution at the nozzle opening is coarser than that adopted by [54], the results are sensible and a finer mesh here would be prohibitive in later chapters of this thesis as the technology will be extended to 3D flow fields.

In order to compare the capability of each approach in terms of jet exit velocity representation, the momentum coefficient, $C\mu$, was measured at the jet exit by integrating the local blowing coefficient along the jet height. Both approaches predict overall blowing coefficients with acceptable accuracy compared to the experimental results as listed in Table 5-3.

Table 5.3 Momentum coefficient comparison results

Case	Blowing approach	CFD $C\mu$ (*Integrated*)	*Experimental* $C\mu$ [54]
U_j = 110.7 m/s	Direct	0.046	0.047
NPR= 1.081	Via plenum	0.047	
U_j = 173.2 m/s	Direct	0.113	0.115
NPR= 1.208	Via plenum	0.117	

With acceptable momentum coefficients produced by both modelling approaches, the flow field is examined in greater detail in Figures 5-8 and 5-9. They show that the streamlines around the aerofoil are practically the same for both approaches, irrespective of the value of the momentum coefficient. For both approaches, it can be seen that as NPR increases, the higher jet momentum delays the BL separation point until further around the Coanda trailing-edge surface, as shown in Figure 5.8. In both cases, the presence of a jet enhances overall circulation around the aerofoil which generates increased circulation and thus lift.

Although there are few observable differences between direct blowing and the plenum approach as a whole, the development of boundary layers is quite different in the vicinity of the jet opening, recall Figure 5-7(a) and (b). In later sections, many different configurations for the jet opening and the gradient of slope on the aerofoil will be considered. Therefore, it is sensible to pursue the plenum approach which captures the details of the interaction between the jet flow and the outer wall boundary-layer more accurately. Therefore, this method will be used in subsequent sections.

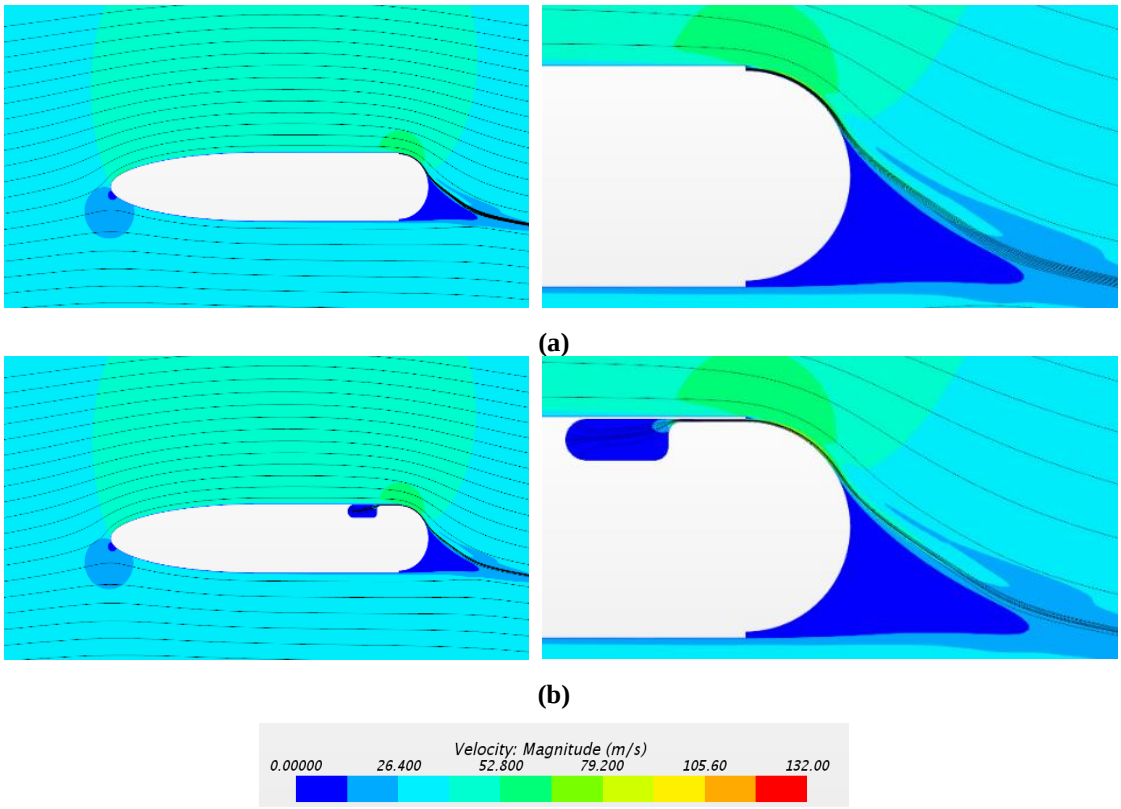

Figure 5-8: Colour shaded contours of velocity magnitude at $C\mu$ =0.047 using (a) direct blowing and (b) blowing via plenum

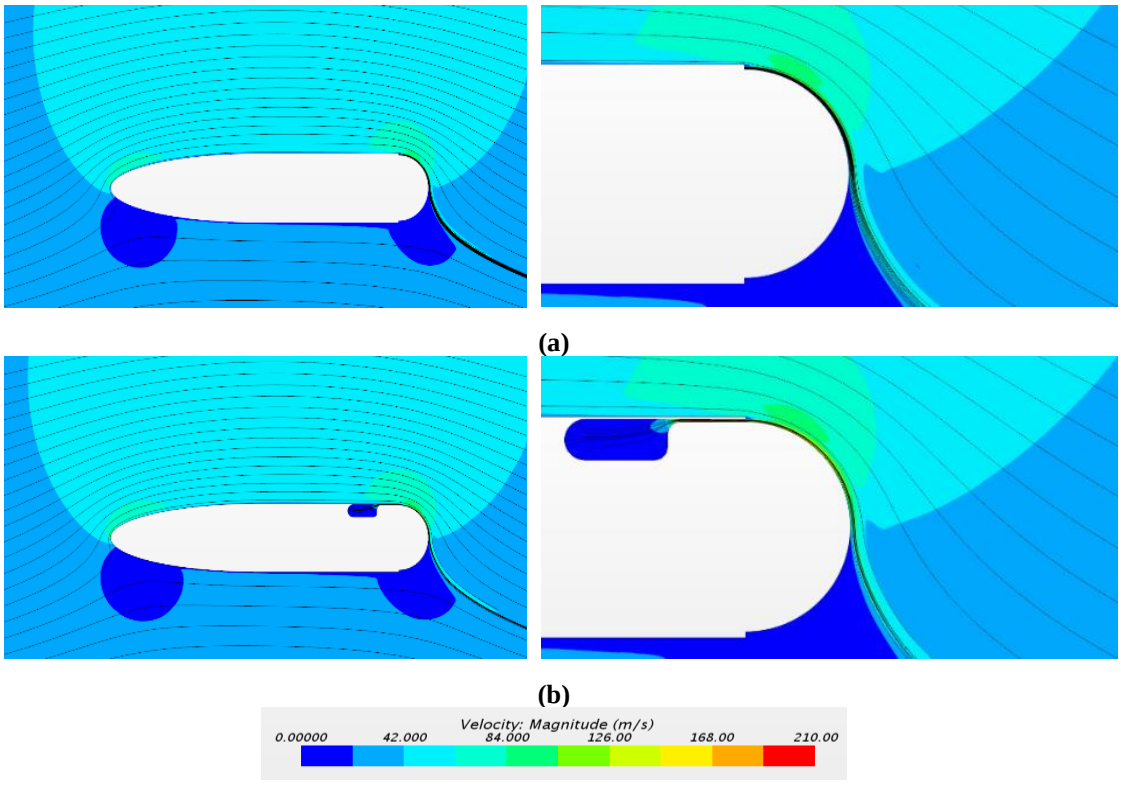

Figure 5-9: Colour shaded contours of velocity magnitude at $C\mu$ =0.115 using (a) direct blowing and (b) blowing via plenum

5.2.5 Validation results

With the mesh design and choice of turbulence model finalised, comparison between CFD results (for the plenum design), experimental values and previous CFD data from [54] are made. The comparison in figure 5-10 shows good agreement between CFD results in the present study and experimental data for the lift coefficient as NPR is increased. Since the aerofoil is symmetrical, $C_l = 0$ is expected for NPR = 1 (i.e. with no blowing). However, when jet blowing is implemented, it generates a very significant increase in lift, even for relatively modest blowing coefficients. Here, CFD predictions tend to over-estimate the lift since it predicts a delayed BL separation point around the Coanda surface, compared with experiment, thereby increasing downwash and hence lift.

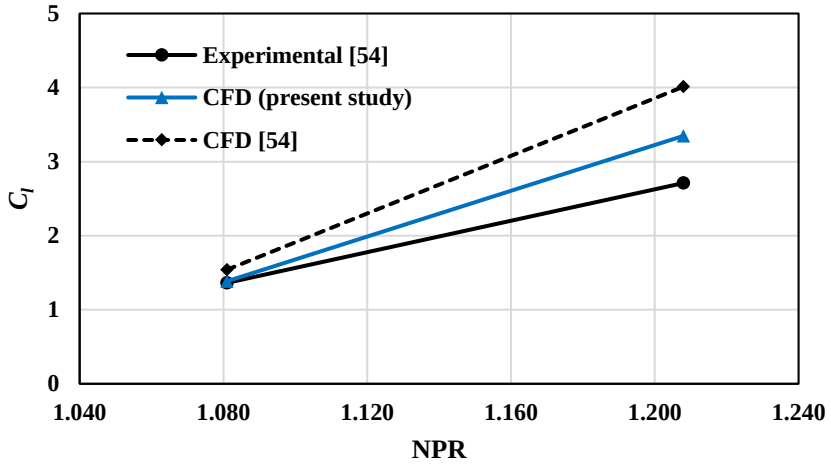

Figure 5-10: Lift coefficient comparison at different NPR values

An inspection of the simulated pressure coefficient distribution for NPR = 1.208 (Figure 5-11) shows increased suction levels over the upper surface (suction side) that result in the observed over-production of lift coefficient. The CFD analysis from the present study is in broad agreement with corresponding CFD analysis also performed by Englar *et al* (2009), and so the over-prediction highlights a limitation of CFD [54]. However, the CFD results from the present study are noticeably closer to the experimental values than [54] on certain regions, especially near the leading edge. Overall, the agreement between experiments and CFD in the present study shown in Figure 5.10 is reasonably good, and it demonstrates that the approach used is suitable for predicting the effect of jet blowing on lift coefficients. No experimental drag data were available for comparison.

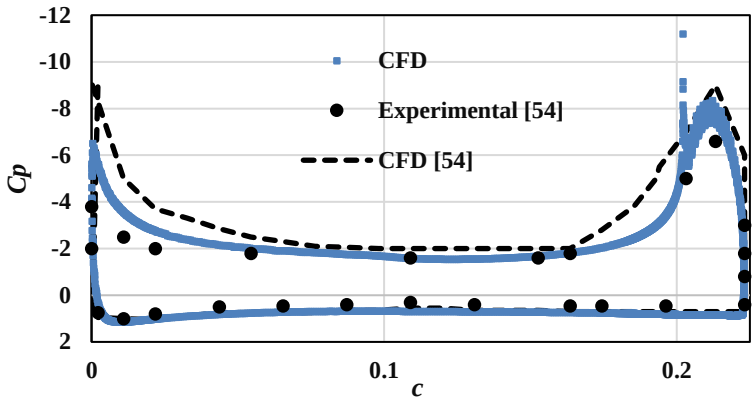

Figure 5-11: Pressure coefficient distribution at NPR 1.208

5.3 CC-aerofoil parametric study

The NREL 5 MW baseline rotor blade geometry must be modified for CC by introducing a curved Coanda surface downstream of a nozzle fed by an internal plenum chamber. Since the low pressure over the rear-facing Coanda surface results in an increase in drag as well as lift, it is necessary to optimise the geometry in terms of Coanda surface curvature, nozzle location and height. Furthermore, the modifications result in an increased aerofoil base thickness that will also increase drag when CC is not in operation [14, 23]. Since only positive lift augmentation is required for the CC-blade however, the lower surface of the blade is unmodified.

The torque generated by the NREL 5MW blade is unequally distributed along the span due to the different aerofoil profiles, chords, twist angles and distance from the hub (r/R). For the parametric study a blade aerofoil located at around 90% span was modified for CC. This region of the blade uses the NACA 64-618 aerofoil with a chord length, c = 2.313 m and a geometric twist angle of 0.863º [15].

An initial computational study for the non-dimensional NACA 64-618 aerofoil (i.e. c =1) was performed and results compared with the aerodynamic coefficients measured by [15] and listed in appendix A1 for a Re = 0.75M and for angles of attack in the range -20º ≤ AoA ≤ +20º. It can be seen from Figure 5.12 (a) that the CFD results for lift coefficient C_l agree quite well with the experimental results and X-foil. X-foil is an interactive code used for the design and analysis of subsonic 2D aerofoils. It is a fast and robust solver based on a high-order panel method with fully coupled viscous and inviscid interaction. It can calculate the pressure distribution on the aerofoil and the corresponding lift and drag coefficient for a given 2D aerofoil with defined Reynolds and Mach numbers [119]. However, the CFD has over-predicted the drag coefficient

compared to experimental values (see Figure 5.12 (b)). The drag can be a difficult quantity to compute as well as to measure experimentally. Nevertheless, the CFD results are in acceptable agreement. The velocity contours highlight flow separation around the aerofoil at different AoA, as shown in figure 5.13.

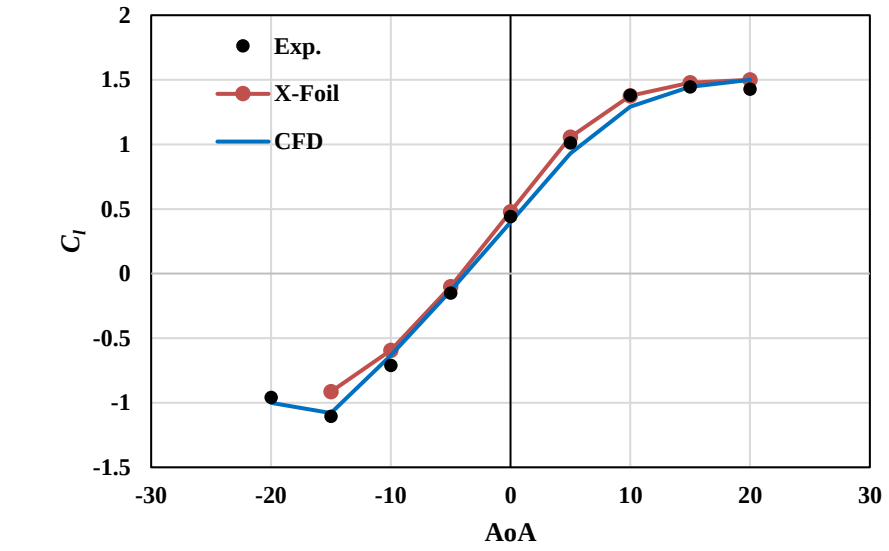

(a)

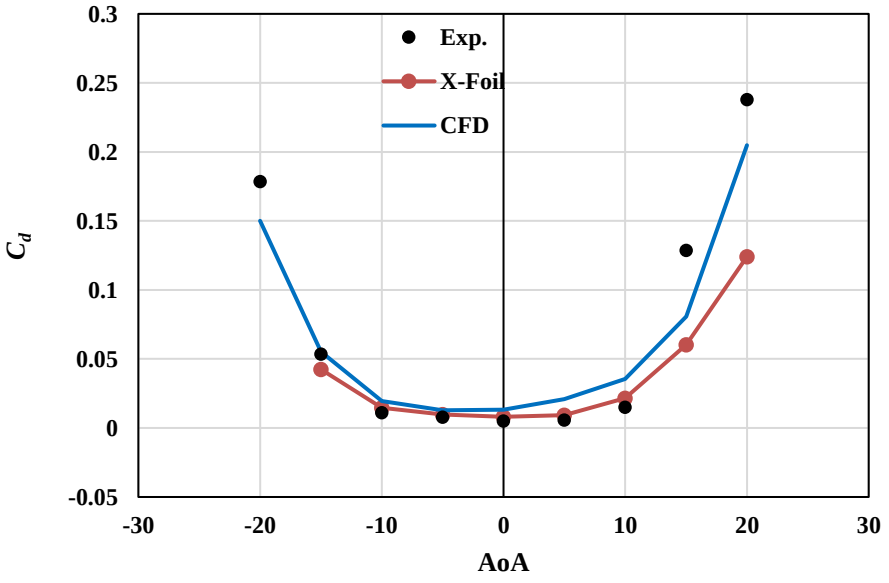

(b)

Figure 5-12 Aerodynamics coefficients and X-foil results compared with experimental results (a) Lift coefficient and (b) Drag coefficient

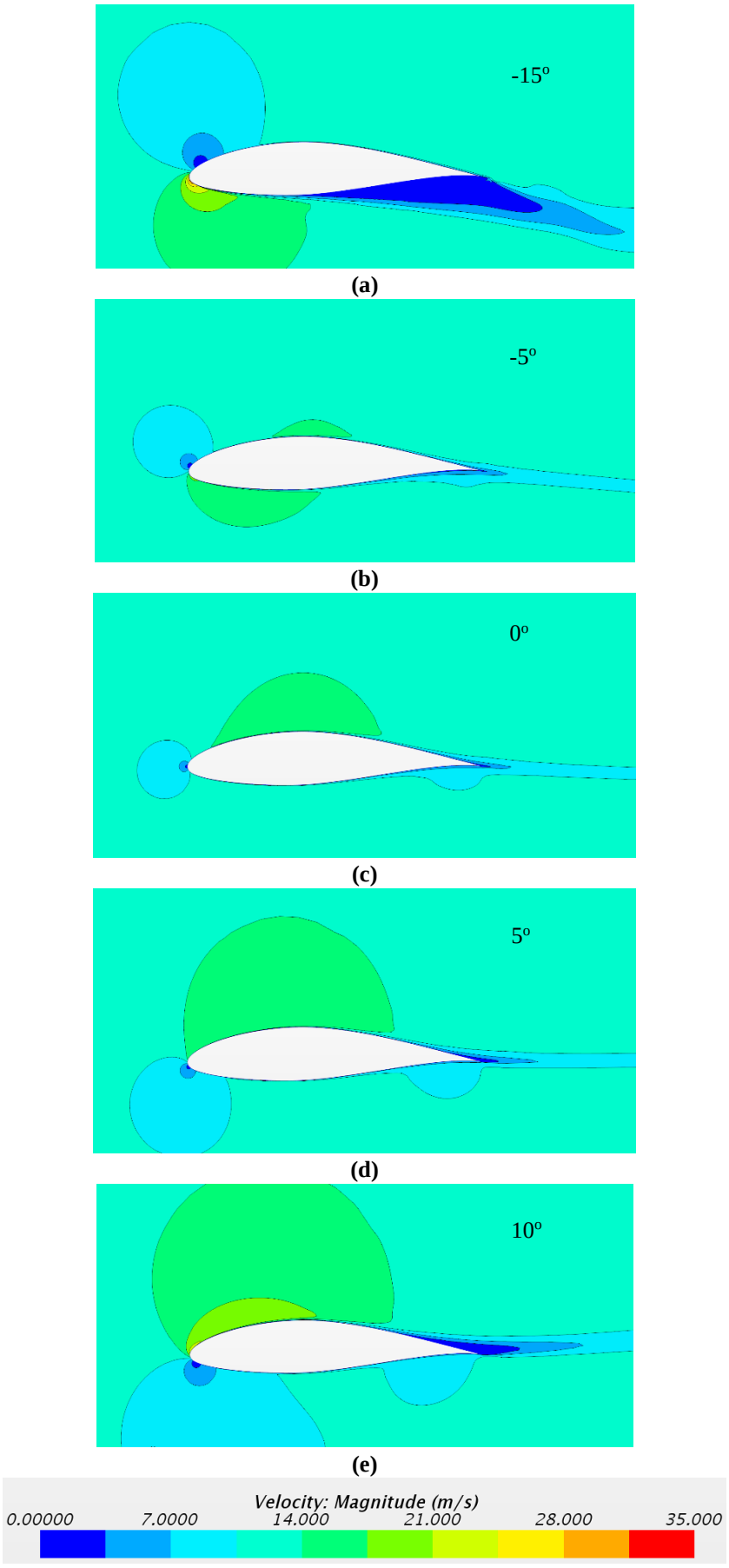

Figure 5-13 Velocity contour around a non-dimensional NACA 64-618 aerofoil at different AoA

5.3.1 Aerofoil modifications

To maximise torque it is necessary to maximise the blade tangential force, F_t, in the plane of rotation, and not necessarily to maximise its lift-to-drag (L/D) ratio. From Blade Element Momentum theory this tangential force is given by Equation 5-11, where the inflow angle (Φ) is determined from the local velocity field.

$$F_t = L \sin(\Phi) - D \cos(\Phi) \quad (5\text{-}11)$$

Twenty-eight different CC-aerofoil shapes were generated as a parametric study to investigate their effect on tangential force and flow behaviour. Firstly, the jet nozzle was positioned at four different chordwise locations between x/c = 0.86 and 0.98. The downstream upper surface was then modified as an ellipsoid to provide a curved Coanda surface. The origin of the ellipse was located on the lower surface of the aerofoil and inline (vertically) with the jet nozzle (see figure 5.14). Once the nozzle height, h, is specified the semi-minor axis, b, of the ellipse was defined as the distance from the lower nozzle surface to the aerofoil lower surface. Three nozzle heights were considered (*i.e.* h/c = 0.1 %, 0.2 % and 0.3 %). Three semi-major axes of the ellipse were also considered (i.e. $a_1 = b$, a_3 at the original aerofoil trailing-edge, and a_2 at mid-point between a_1 and a_3), allowing three different Coanda shapes to be constructed for each nozzle position and height, as indicated by the red lines in figure 5.14. Stretching the semi-major axis in this way produces three different levels of curvature for the trailing edge, which should lead to a range of results from which to find beneficial design characteristics [23].The smaller semi-major axis leads to a more aggressive shape which is similar to the work of Englar *et al* (2009) on the aerofoil with a rounded trailing edge [54] with larger ones producing a more gradual, less-aggressive shapes.

Using these parameters, 28 different configuration shapes were generated as listed in table 5.4. Note that some combinations of parameters produced invalid shapes, particularly with the 86% c nozzle location since the ellipse curve protruded above the baseline aerofoil upper surface. Two such invalid shapes existed and they are labelled as not applicable (*N/A*) in table 5.4.

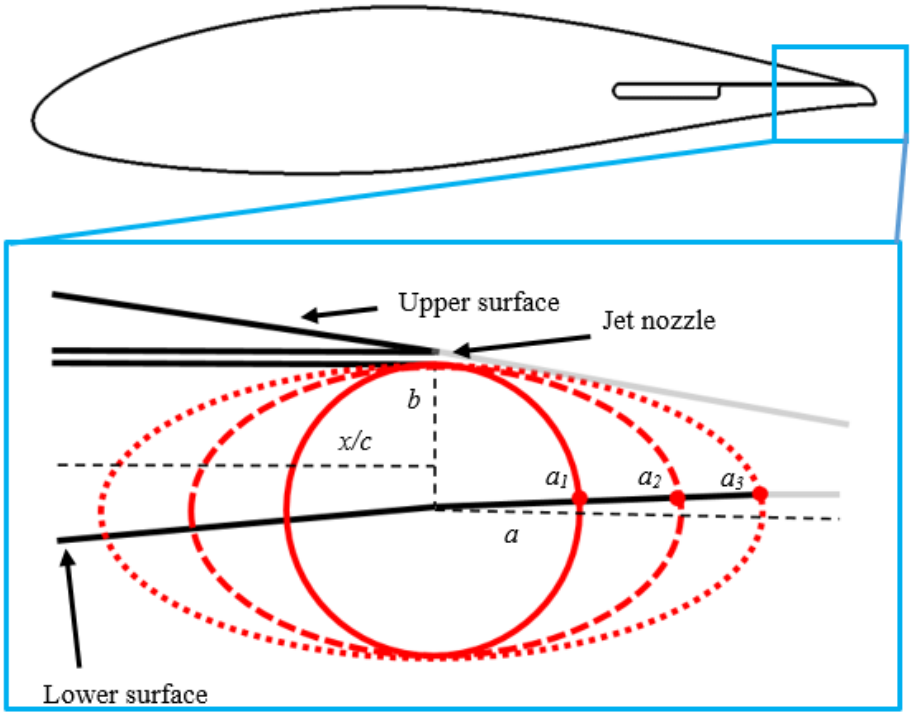

Figure 5-14 Modification Pattern

Table 5.4 Modified aerofoil configuration identifiers

***h/c* = 0.1 %**			
x/c	***a_1***	***a_2***	***a_3***
86 %	A1	N/A	N/A
90 %	B1	B2	B3
94 %	C1	C2	C3
98 %	J1	J2	J3
***h/c* = 0.2 %**			
x/c	***a_1***	***a_2***	***a_3***
86 %	D1	D2	D3
90 %	E1	E2	E3
94 %	F1	F2	F3
***h/c* = 0.3 %**			
x/c	***a_1***	***a_2***	***a_3***
86 %	G1	G2	G3
90 %	H1	H2	H3
94 %	I1	I2	I3

5.3.2 Computational method

Adopting the same domain size and mesh refinement technique used in the validation study, each 2D configuration was meshed using approximately 400k cells as illustrated in Figure 5.15, achieving a mean wall $y^+ \approx 1$. The velocity inlet boundary condition on far-field boundaries was defined with two components, U_x and U_y (neglecting both axial and rotational induced velocity components), where $U_x = 0.89\ \omega r$ (*i.e.* ω is the rotational speed (rad/s) and r is the radial location (m)). The second component, U_y, is the free-stream wind speed (m/s). All cases were initially performed for the same reference wind speed of 8 m/s and rotational speed of 12.1RPM, which is below the rated wind speed and within the pre-stall region of the baseline rotor. A modest NPR = 1.05 was initially used since initial studies indicated that this could be achieved using centrifugal pumping alone, thereby avoiding the need for mechanical pumping. Again, the incompressible, steady-state Reynolds-Averaged Navier-Stokes (RANS) segregated flow equations are solved using the SST k-ω turbulence model.

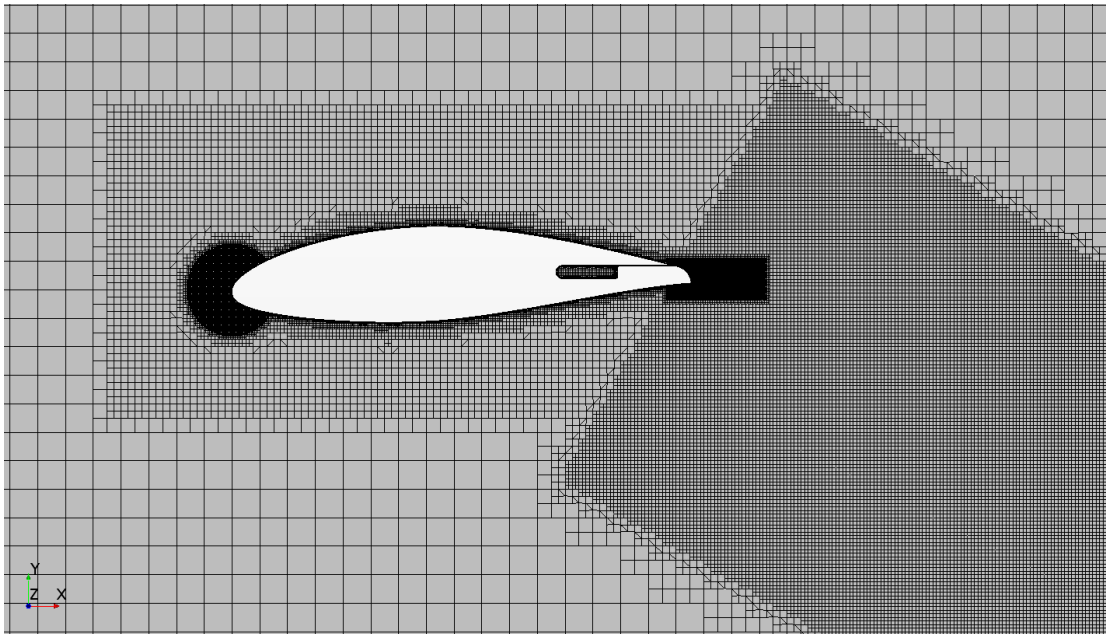

(a)

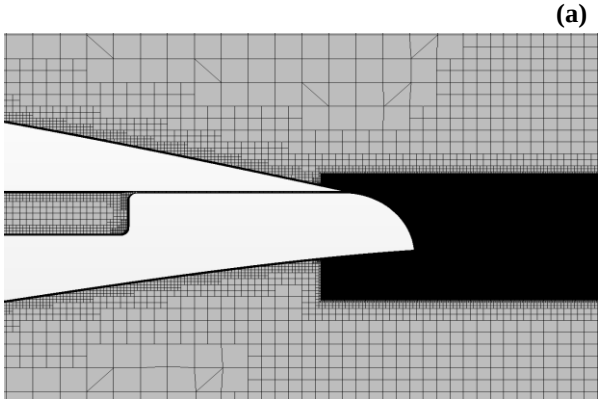

(b)

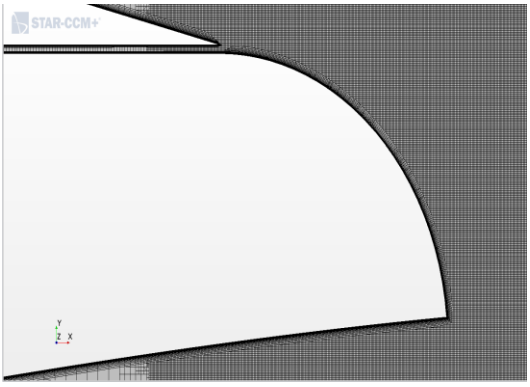

(c)

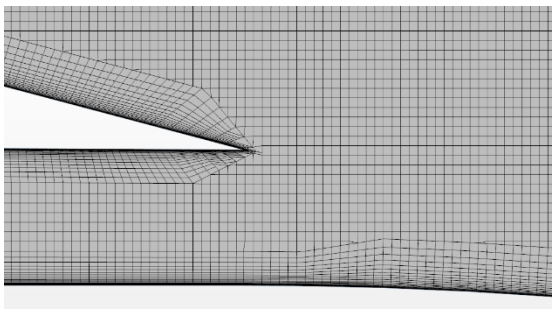

(d)

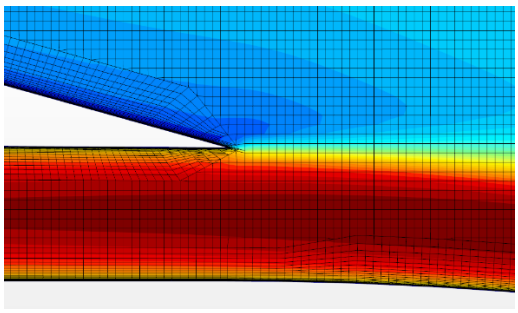

(e)

Figure 5-15 Generated mesh around A1 configuration (a) around the aerofoil, (b) around the plenum and (c) at the trailing edge (d) at the jet exit and (e) at the jet exit with flow development (*x/c*= 86%, *h/c*= 0.1% and *a*= a_1).

5.3.3 Parametric study

The 28 CC-aerofoil configurations shown in table 5.3, representing different nozzle location (x/c), height (h/c) and trailing-edge curvature parameter (a), were evaluated to analyse the aerodynamic forces (figures 5.16 and 5.17) and the flow behaviour which are presented in figures 5.18 to 5.20. Unfortunately all modified configurations gave a tangential force F_t that is lower than the baseline aerofoil (Configuration O) due to the very low NPR, though the parametric study highlighted useful trends for an improved design with the three configurations highlighted in green giving the best performance.

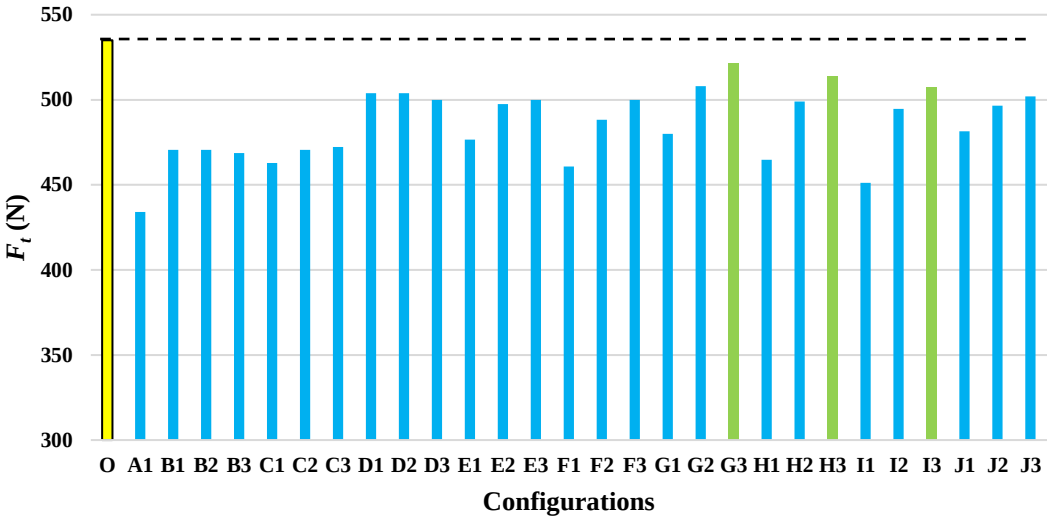

Figure 5-16 Tangential force comparison for the modified configurations against the baseline design (O)

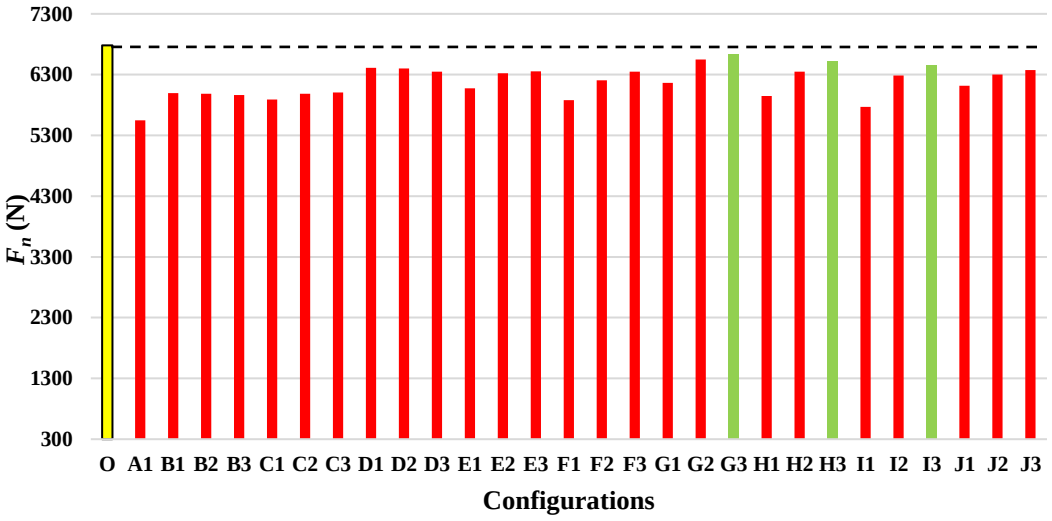

Figure 5-17 Normal force (N) comparison for the modified configurations against the baseline design (O)

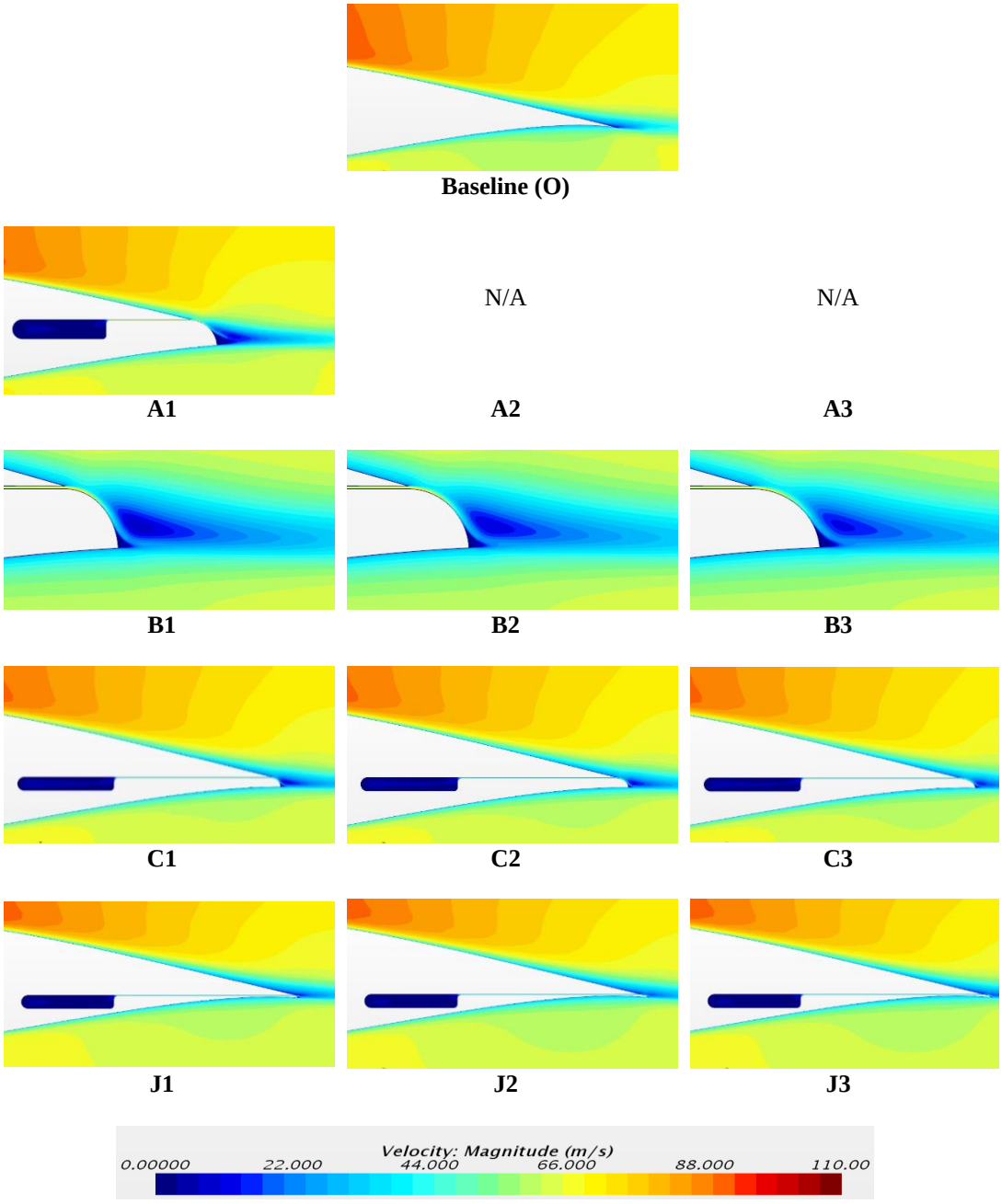

Figure 5-18 Flow behaviour of the modified configuration generated with *h/c* = 0.1%

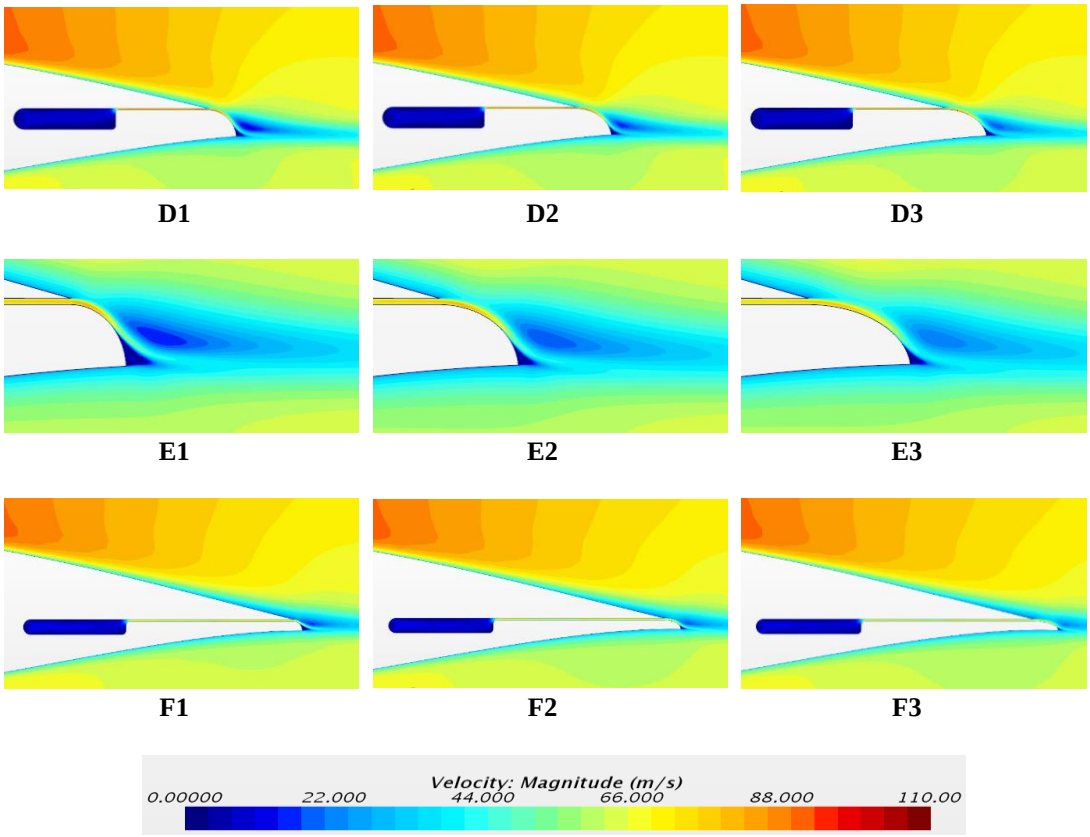

Figure 5-19 Flow behaviour of the modified configuration generated with *h/c* = 0.2%

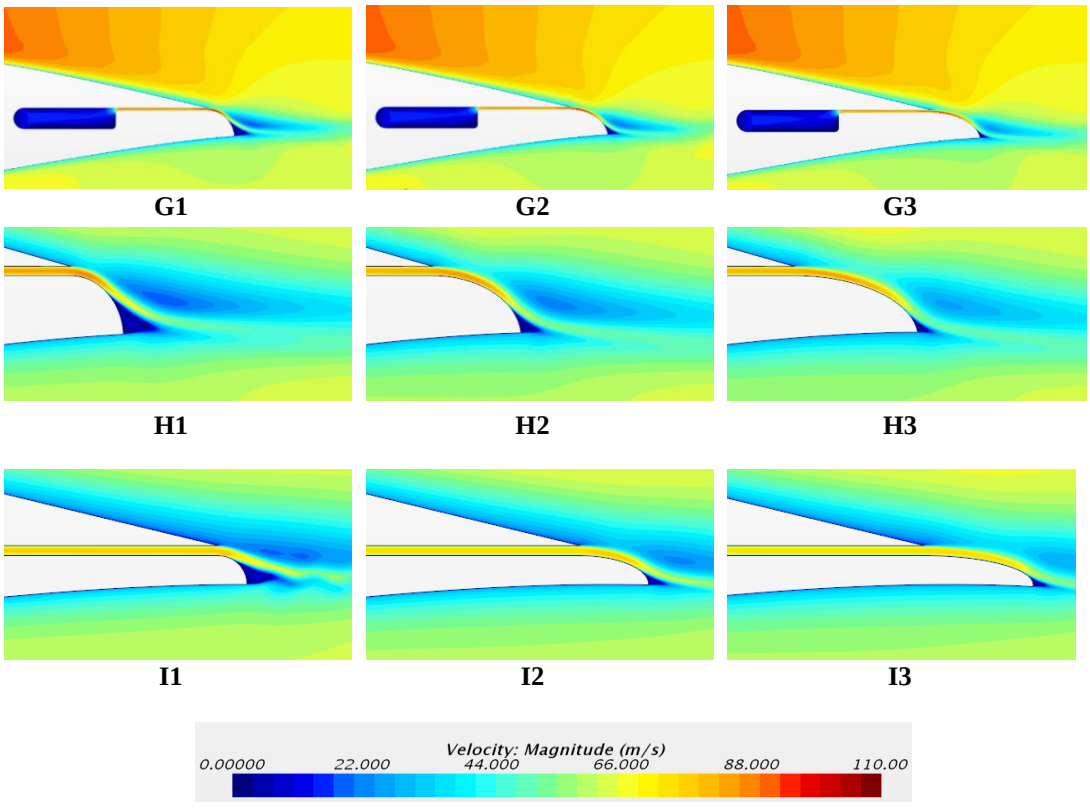

Figure 5-20 flow behaviour of the modified configuration generated with *h/c* = 0.3%

5.3.4 Design sensitivities

Configurations A1, B1, C1 and J1 have the same nozzle height (h/c = 0.1%) and trailing-edge curvature (a_1) but with different nozzle locations (*i.e.* x/c = 86%, 90%, 94% and 98% respectively). For all 4 modifications the flow detaches from the Coanda surface before the trailing-edge. The forward nozzle location (A1) gives the greatest extent of separated flow and therefore the highest drag and lowest tangential force. Tangential force generally increases as the nozzle location is moved aft, which was also observed for nozzle heights, h/c = 0.2% and 0.3%. However, at the most aft location (e.g. configuration J1) the Coanda surface is ineffective in terms of lift augmentation.

The effect of increasing nozzle height on flow behaviour is another important aspect. Consider, for example, configurations C3, F3 and I3, with fixed location (x/c = 94%) and trailing-edge curvature (a_3). An increase in height allows a greater mass flow rate over the Coanda surface that leads to an increase in tangential force, though it does not have a significant impact on boundary layer separation.

Increasing the semi-major axis of the ellipse (a) reduces the Coanda surface curvature which is compared for $a = a_1$, a_2 and a_3 (i.e. configurations G1, G2 and G3 respectively), with a fixed nozzle height and location. As the semi-major axis increases, Coanda surface curvature reduces which serves to delay the BL separation point, reducing drag and increasing the tangential force, compared to other modified designs, as shown in figure 5.16.

5.4 Aerofoil design enhancements

It is apparent from figure 5.16 that the best-performing configurations in terms of tangential force are G3, H3 and I3 (highlighted in green). However, applying circulation control with a low NPR generates tangential forces lower than the original aerofoil. For comparison, the non-blowing case (NPR=1) is also shown in figure 5.21 for configuration G3. Without blowing there is no entrainment of the external flow and the BL separates earlier than with NPR = 1.05. However, the drag coefficient is lower without blowing due the suction levels that are generated with blowing that act on the rearward-facing Coanda surface. To compare the generated drag due to modified T.E., extra care is required for the baseline drag calculation. Another run was conducted for the baseline at a lower AoA, seeking a C_l value close to that generated by the G3 configuration, without blowing. In this case the drag coefficient for the baseline aerofoil

is C_D < 0.07. Although drag increases, lift augmentation ensures that the tangential force increases. Thus, it is clear that a higher NPR is needed, but also that further shape modifications are necessary to minimise drag and ensure that BL separation occurs at the trailing-edge for NPR > 1.

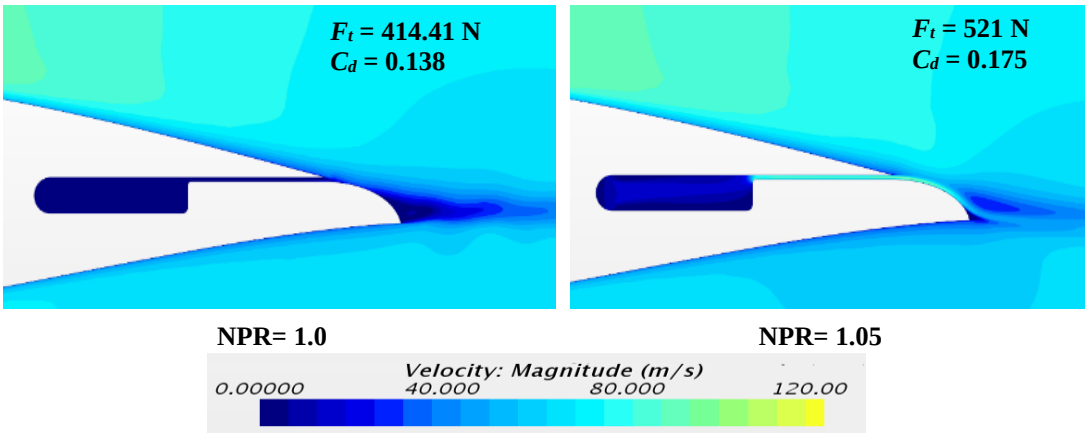

Figure 5-21 Flow behaviour around G3 with different NPR

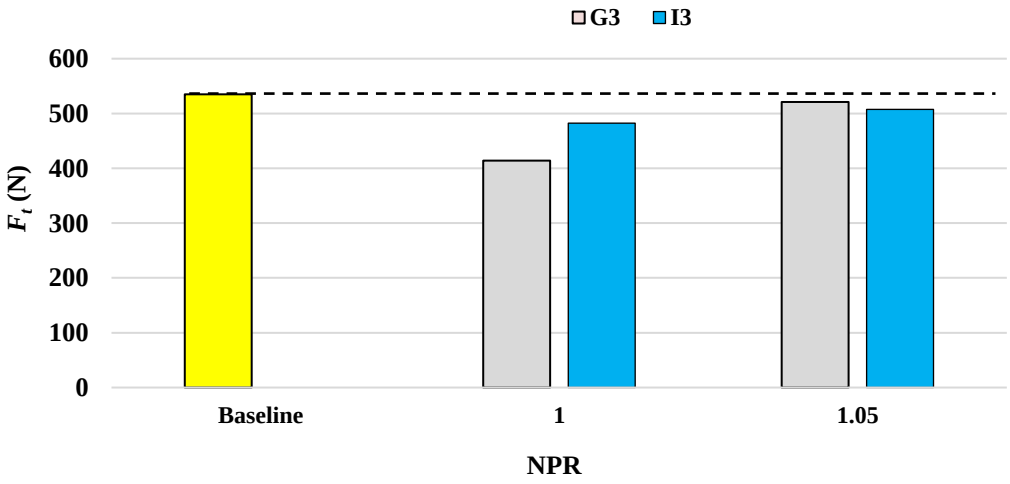

Figure 5-22 Effect of NPR on tangential force

Since configuration I3 (nozzle location x/c = 94%, h/c = 0.3% and $a = a_3$) shows a better aerodynamic performance with no blowing (see figure 5.22), it was selected for further development. As shown in figure 5.23, BL separation occurs upstream of the trailing-edge for configuration I3 at all NPRs and the Coanda effect is not being fully exploited. Consequently, a twofold increase in the semi-minor axis of the construction ellipse was implemented as illustrated in figure 5.24. This reduces the Coanda surface curvature and gives a sharper trailing-edge, with a chord of 98% of the baseline aerofoil. Figure 5.25 compares colour shaded velocity magnitude contours for Configurations I3

and the modified-I3 design and shows that the modified-I3 design maintains attached flow for NPR > 1, which should lead to a greater tangential force.

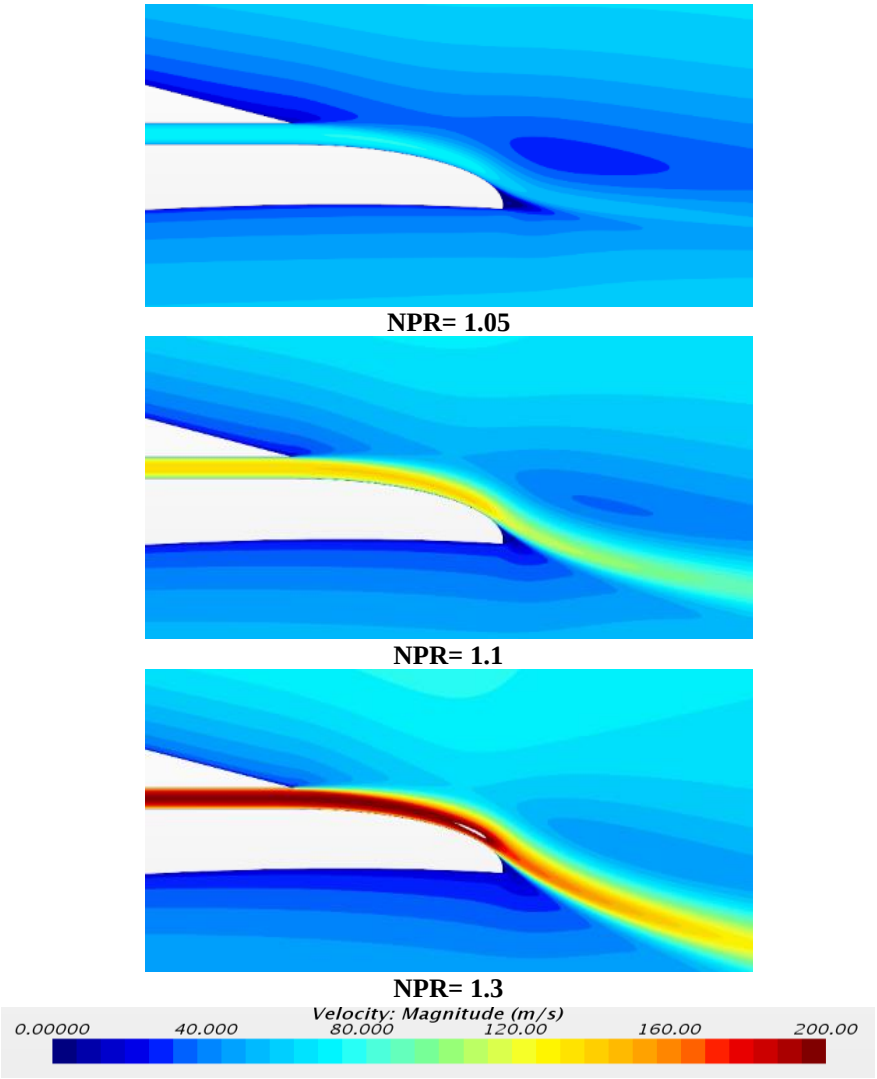

Figure 5-23 Flow behaviour around I3 configuration for different NPR values

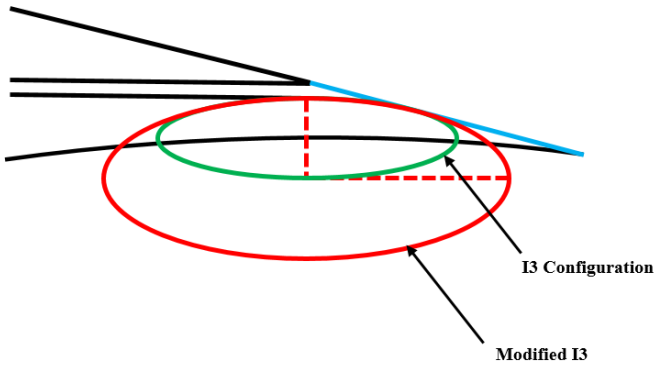

Figure 5-24 Further modification on I3 configuration

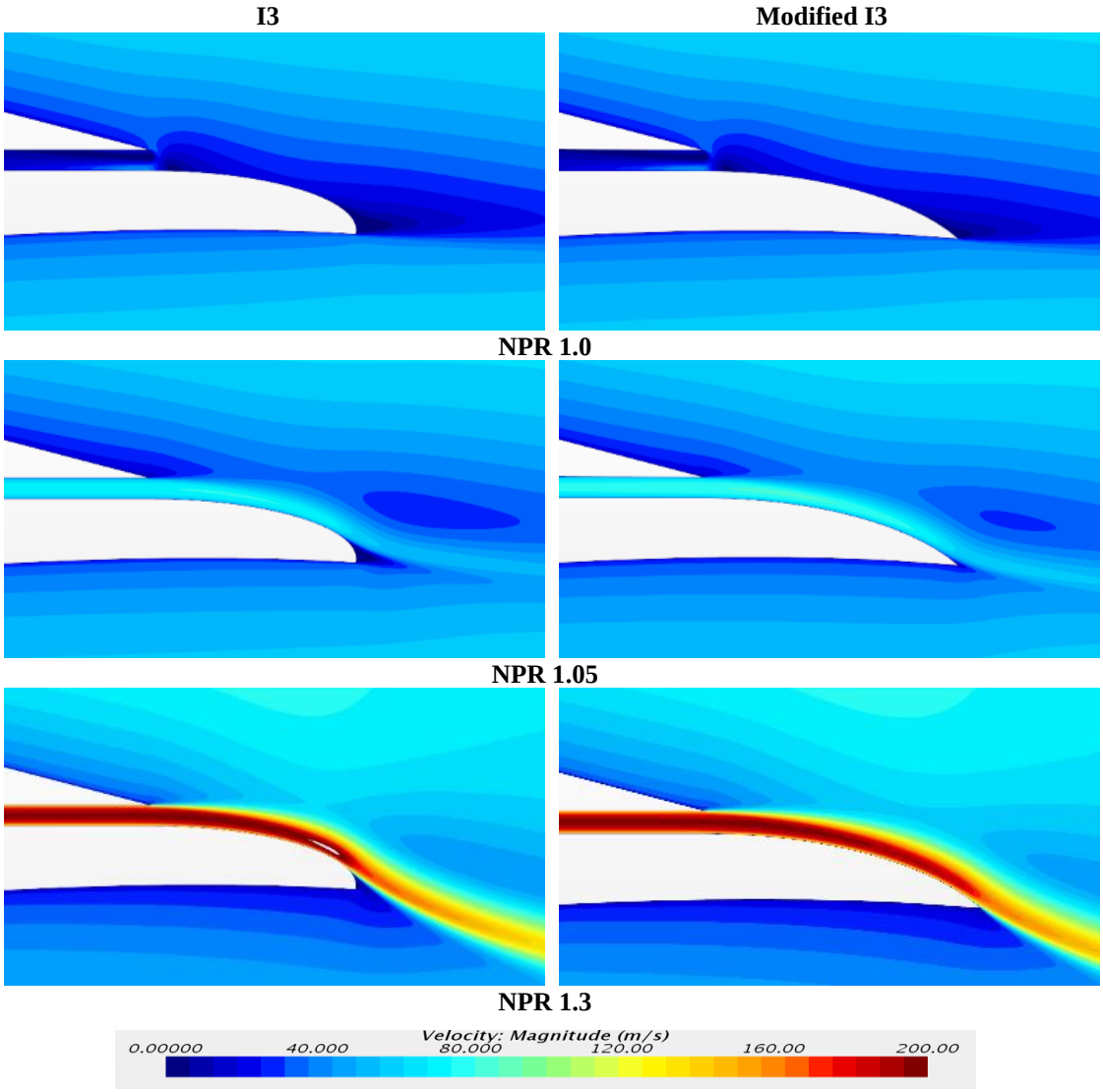

Figure 5-25 NPR effect on Configurations I3 and Modified I3

The increased circulation effects of increasing NPR on the pressure coefficient, C_p, distribution is shown in figure 5.26 relative to the original aerofoil. With no blowing (NPR = 1) a reduction in circulation and lift is obtained, but is augmented at all higher NPRs. Consequently, the tangential force increases with NPR as shown in Figure 5.27, with the modified-I3 configuration producing a positive increment for NPR > 1.05 relative to the baseline aerofoil, and for all NPR values, relative to the I3 configuration.

If we assume an isentropic expansion through the nozzle (with a ratio of specific heats, $\gamma = 1.4$) the critical NPR to just choke the convergent nozzle, i.e. giving a sonic exit Mach number (M_j), is calculated by equation (5-7), giving $NPR_{crit} = 1.89$. The nozzle flow can therefore be assumed to be unchoked for the maximum NPR = 1.8, in this study.

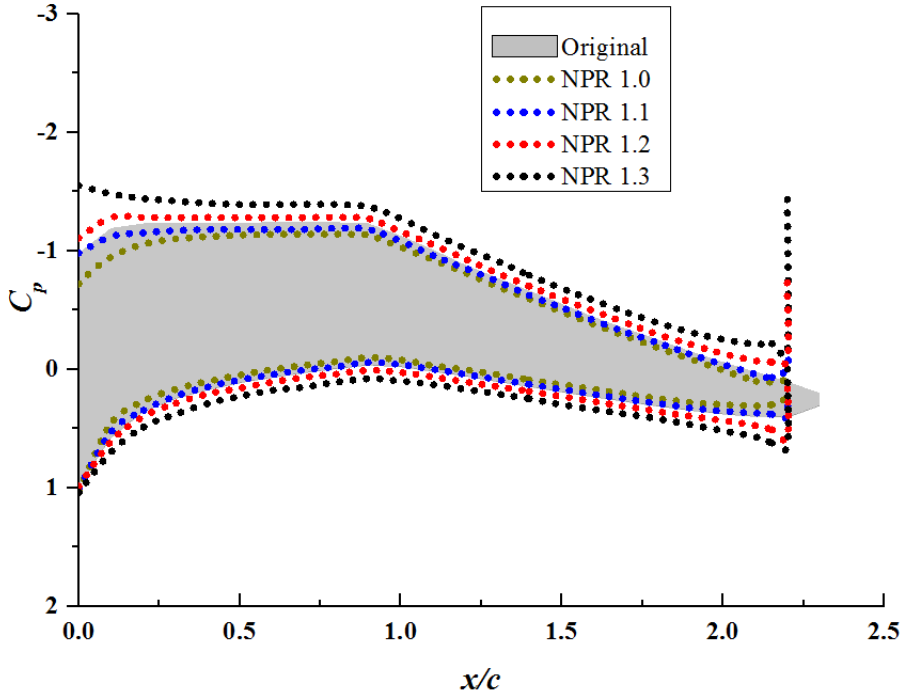

Figure 5-26: NPR effect on pressure coefficient (C_p) of modified I3

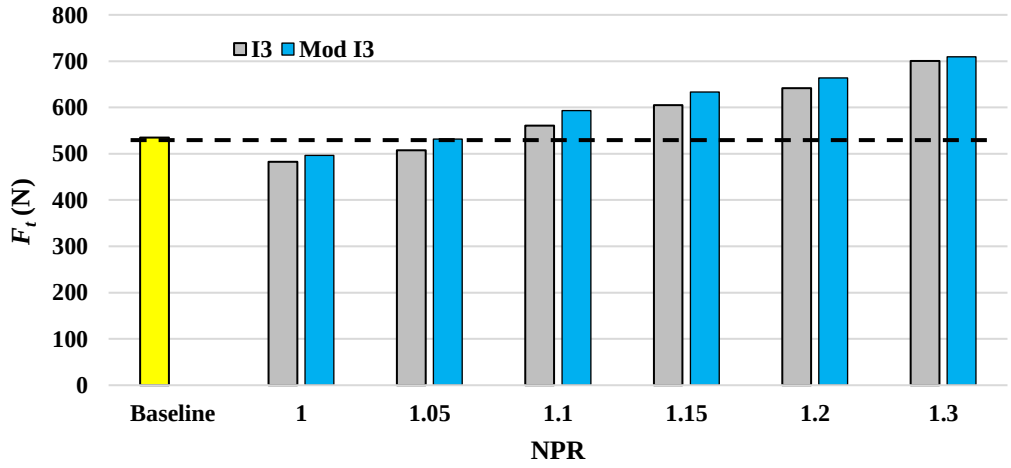

Figure 5-27 Effect of NPR on tangential force

5.5 Potential benefits of the modified-I3 design

The benefit of applying the circulation control to the 2D aerofoil is obtained by calculating the torque Q (N.m) per blade as follows:

$$Q = F_t\ (r/R)R \tag{5-12}$$

Here, r/R is 0.89. The results shown in figure 5.28 indicate that there is a potential torque augmentation of up to 32.5 % which could be achieved by applying NPR = 1.3, however, a decrease of about 7% occurs (compared with the original aerofoil) when the jet is switched off (NPR = 1). The results also show that applying a low NPR overcomes this reduction and more torque is obtained as the NPR increases.

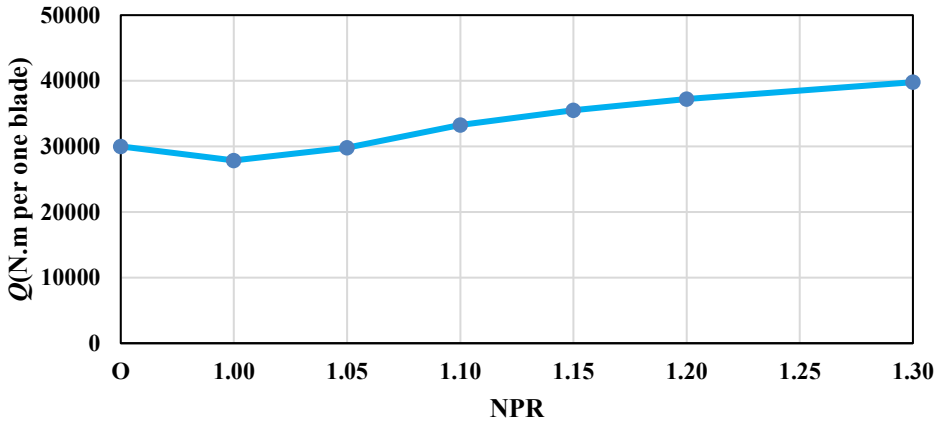

Figure 5-28 Torque (N.m) per one blade

5.6 Chapter summary

The study described in this chapter was to determine what effect the geometric and flow parameters have on the application of circulation control for a 2D aerofoil (NACA 64-618) segment of the NREL 5 MW baseline HAWT. The following conclusions can be drawn:

- The SST k-ω model provides the closest agreement with experimental data. This is due to the increased accuracy of the SST k-ω model in simulating the wake generated behind the T.E. compared to the other investigated turbulence models and therefore, is used for all further flow solutions presented in this study.

- A jet location x/c = 94% gives a better Coanda effect (i.e. increased F_t) due to the more aft flow separation location on the upper surface (suction side) of the aerofoil.
- Jet height h/c = 0.3% enables a greater mass flow rate to exit from the nozzle, and more effective Coanda effect. However, this comes at a higher cost due to increased pumping requirements.
- Increasing the semi-minor axis of the elliptical Coanda surface reduces T.E. curvature which in turn keeps the flow attached for longer, leading to greater tangential forces.
- An increase in torque of up to 32.5% could potentially be achieved by applying this modification, for NPR values of up to 1.3.

Chapter 6 IMPLEMENTATION OF DESIGN ENHANCEMENT AND EVALUATION OF PUMPING COST IN A THREE-DIMENSIONAL WIND TURBINE

6.1 Introduction

Extending the circulation control concept to the NREL offshore 5 MW baseline wind turbine blade requires careful design integration. The primary objective is to increase the mechanical shaft power generated by the CC rotor by an amount greater than that necessary to pump air at the required NPR and mass flow rate. Consequently, lift and torque augmentation must be balanced against the required pumping power, taking into account energy costs. It was therefore considered impractical to apply CC along the entire span of the blade. An effective region for the application of CC to increase torque generation is near the blade tip, where thrust augmentation will create the largest moment. Therefore, the baseline rotor blade was modified between 84 - 89 % of the span (i.e. between radial stations r = 52.75 and 56.17 m). Here, the NACA 64-618 aerofoil used in the 2D parametric study was replaced with the modified-I3 CC-aerofoil, according to the parametric study carried out in the previous chapter.

6.2 Three-dimensional CC-blade study

The same computational domain and boundary conditions were applied to the modified CC blade shown in figure 6.1 as described for the baseline blade in section (4.3.2). The plenum pressure is defined by setting the rear surface of the plenum as a stagnation pressure inlet, as described in chapter 5, section 5.3.2. Geometrically, the blade is only modified in the slot location whereby the NACA 64-618 aerofoil used in the 2D parametric study was replaced with the modified-I3 design (from the previous chapter). A similar mesh refinement technique to that used in the 2D studies was adopted, with leading and trailing-edge refinement and up to 20 inflation layers. This gave a total cell count of 17.7M for the baseline blade and 24.9M for the modified blade due to additional refinement near the nozzle and Coanda surface (with a cell size 0.0048 m). Figure 6.2 shows the mesh structure on the blade surface near the modified region (figure 6.2(a)), at 0.5R (figure 6.2(b)) and 0.85R (figure 6.2(c)-(e)) span-wise locations for both the baseline and modified blades.

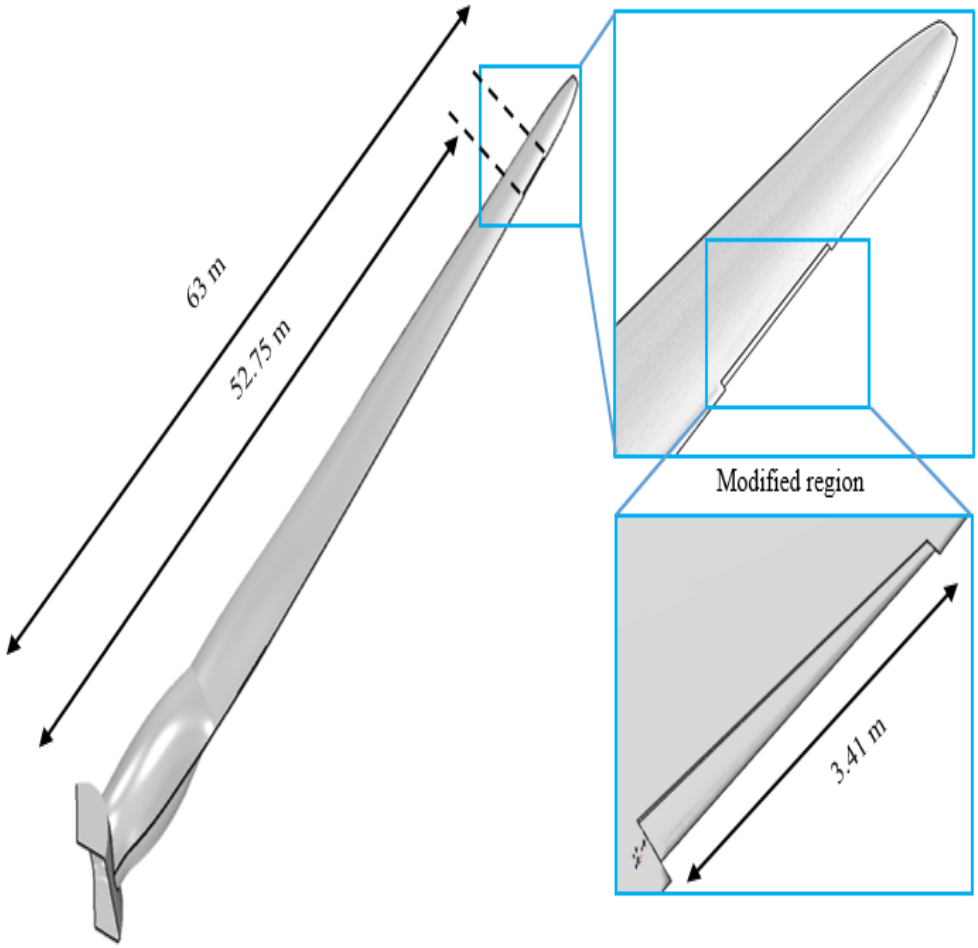

Figure 6-1 Region of modifications to the baseline rotor blade

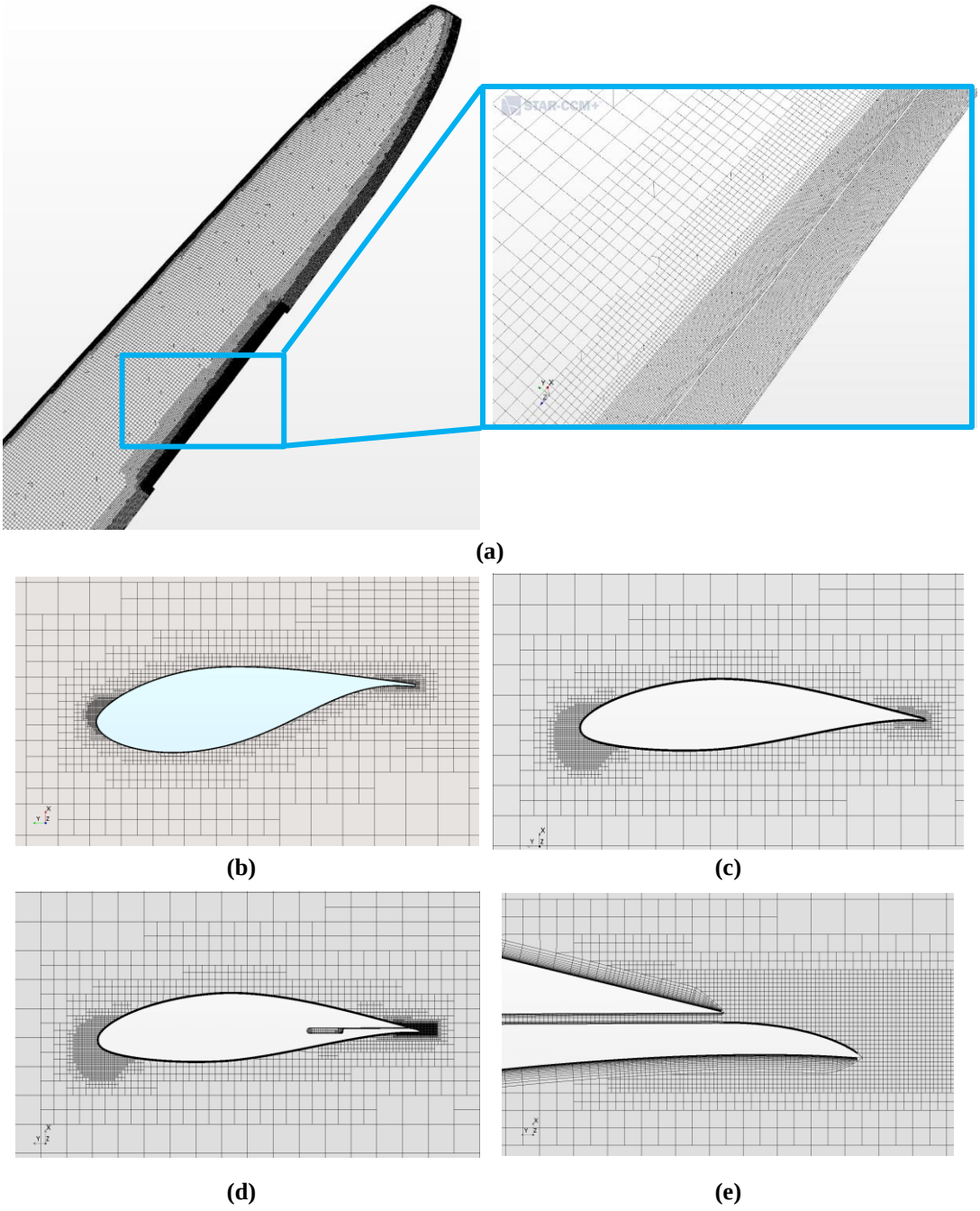

Figure 6-2 Mesh resolution (a) on the modified blade surface (b) *r/R*= 50% baseline section, (c) *r/R*= 85% baseline section, (d) *r/R*= 85% modified section and (e) close-up *r/R*= 85% modified section

6.3 Torque augmentation due to CC

Flow simulations were performed for wind speeds in the range 5 - 11.4 m/s (i.e. up to the rated wind speed) and corresponding rotational speeds of 7.5 - 12.1 RPM as defined in [15]. Variable blade pitch is only used for wind speeds above the rated condition to control post-stall performance [15], and so is not considered in this analysis. The incompressible, steady state Reynolds-Averaged Navier-Stokes (RANS) segregated flow

equations are solved in conjunction with the SST *k-ω* turbulence model. This model demonstrated good prediction performance for both 2D CC and 3D HAWT and so it is used in this study as well.

Figure 6.3 shows the power augmentation comparisons between the baseline and modified CC-blade. For the modified CC-blade without blowing (NPR = 1.0), an average power reduction of approximately 4% was predicted (not shown in figure 6.3) for all wind speeds due to the increased drag and reduced chord over the modified region. However, power augmentation was achieved for higher NPRs with approximately 11% increase for NPR = 1.5 (see figure 6.3) and 18.4% increase for NPR = 1.8. The cost of this augmentation, and calculations of net power are discussed later in section 6.6.

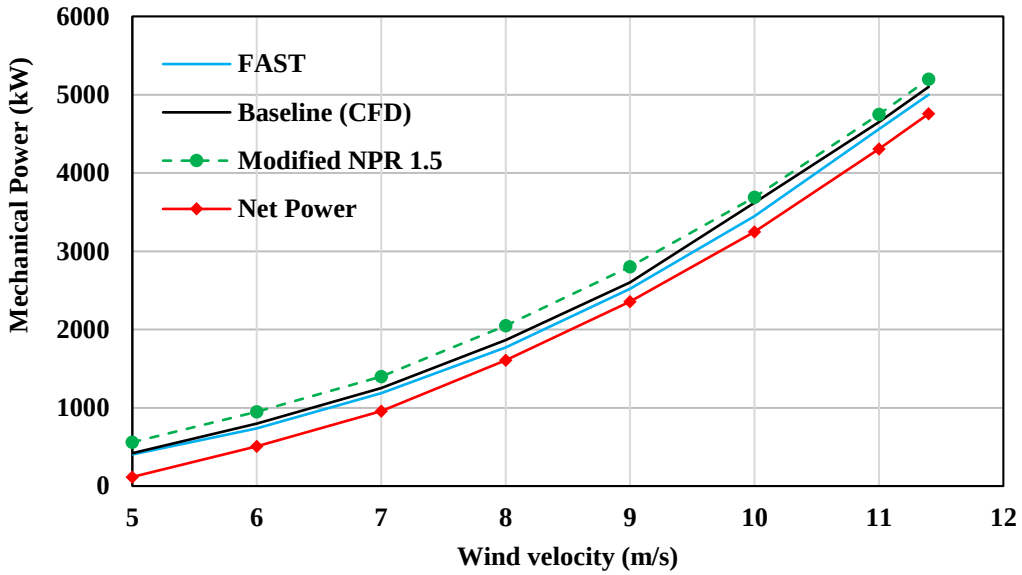

Figure 6-3 Power comparison

6.4 Flow features

The flow behaviour around and downstream of the modified CC-blade section is compared to the baseline blade at *r/R* = 85%, coinciding with the slot. This particular section is compared to the baseline in figures 6-4 which show velocity streamlines at 8 m/s wind velocity, which represents the pattern at all studied wind speeds. The impact of CC on the flow separation near the T.E when the jet is on, is clearly seen. The flow streamlines downstream of the modified aerofoil exhibit downwash as a result of the Coanda effect. This leads to a tangential force enhancement and therefore the generated torque.

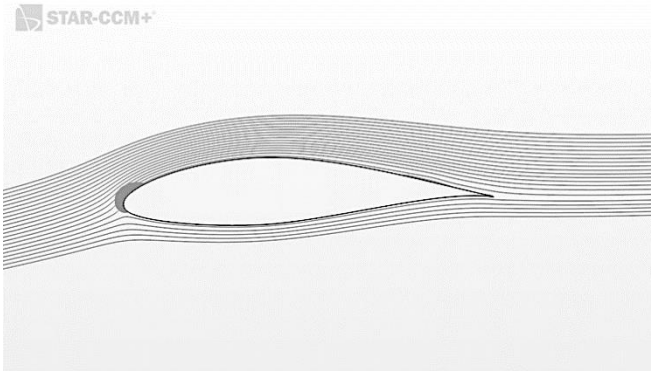

Baseline

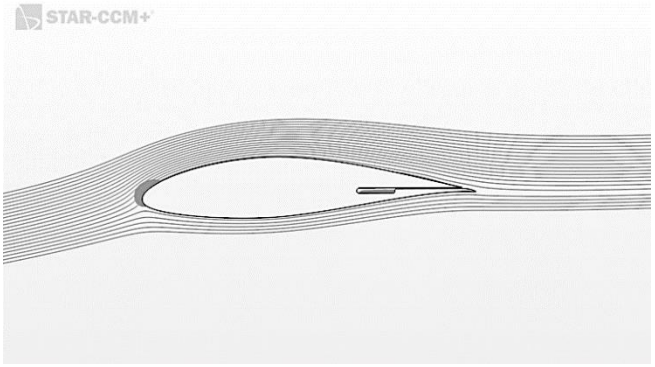

NPR 1.0

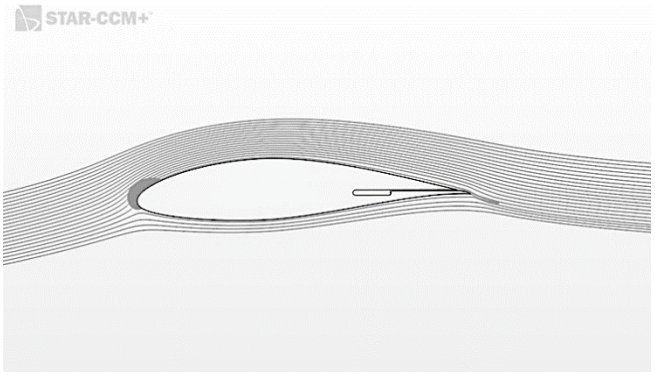

NPR 1.5

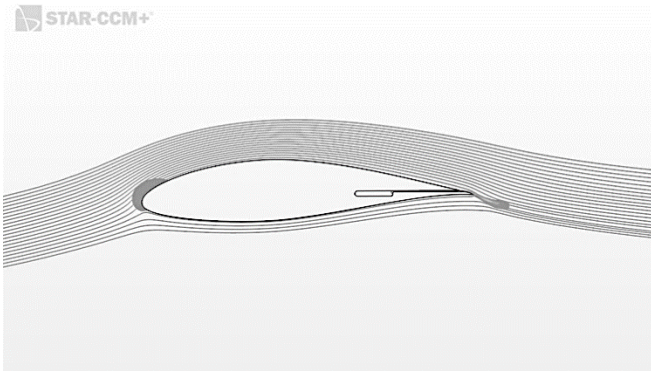

NPR 1.8

Figure 6-4 : Velocity streamlines at *r/R* = 85% at 8 m/s wind velocity with different NPR values

6.5 Pressure distribution

Pressure coefficient distributions are compared for the baseline and modified sections at a mid-span (*r/R*= 50%) position and at the modified location of the blade (*r/R*= 85%) at a wind speed of 8 m/s, see figure 6.5. Similarly, Figure 6.6 compares colour shaded contours of static pressure on both upper and lower surfaces for all cases. It is apparent that the CC-blade modification does not influence the flow development on the inner blade region at this wind speed and the increases in upper surface suction levels using CC are similar to those observed for the 2D analyses (recall figure 5.23), it is clear that there is a suction increment on the upper surface at the modified region when the jet is active. This will lead to greater tangential force generation and therefore the torque increases, resulting in a useful power augmentation.

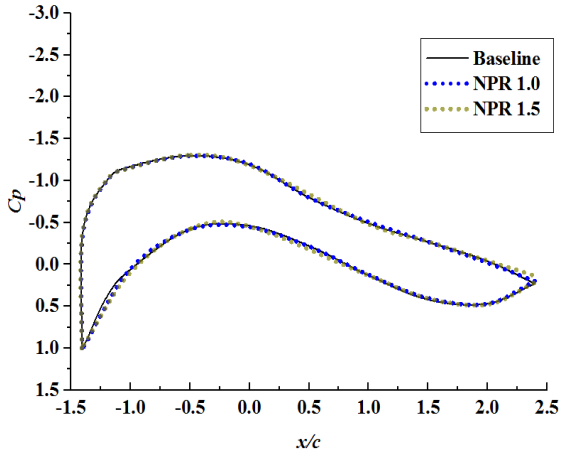

(a)

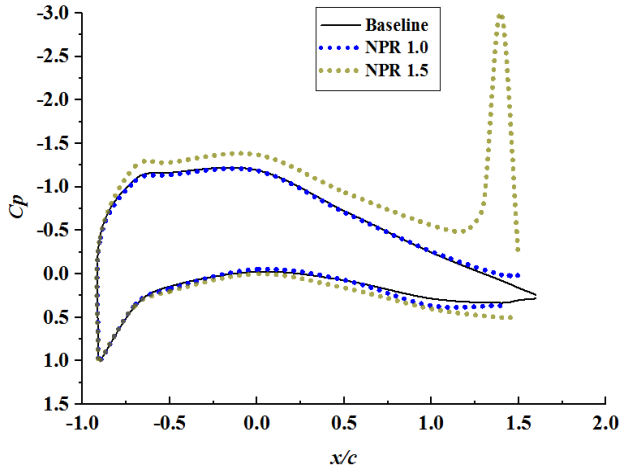

(b)

Figure 6-5 Section pressure coefficient distributions (a) *r/R*= 50% and (b) *r/R*= 85% at 8 m/s wind speed

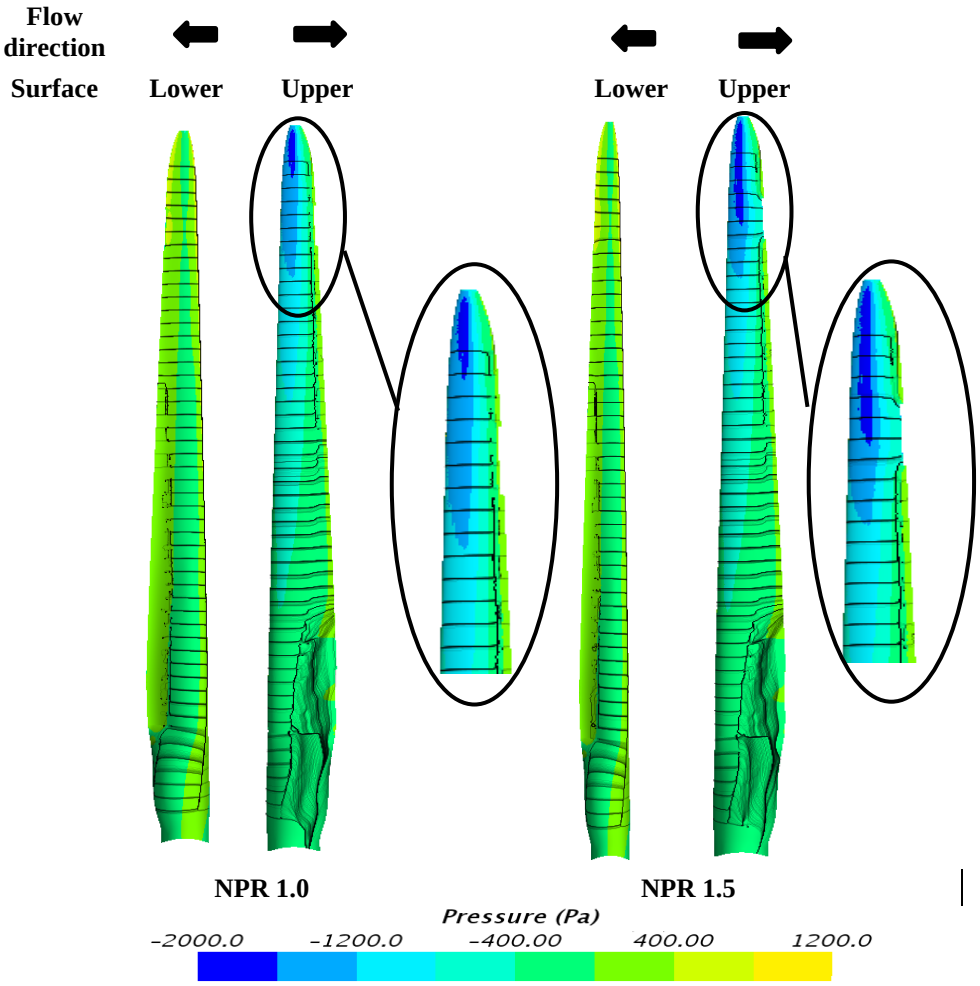

Figure 6-6 Blade pressure contours at 8 m/s wind speed

The pressure force produced by jet streams at higher NPRs overcomes the centrifugal force of the jet by means of the modified T.E.; the flow separation point moves toward the lower side of the aerofoil.

6.6 Accounting for the cost of circulation control

6.6.1 Centrifugal pumping

The results in chapter 5 demonstrated that supplying a plenum with pressure of a sufficient value can provide aerodynamic benefits. Considering a real turbine blade with a large diameter, it may be possible to integrate a channel along its entire span from an inlet at the hub to the jet location. Theoretically, rotation of such a blade would induce a centrifugal pumping action, taking free-stream air at the hub and forcing it radially down the channel to the jet. This has potential to increase plenum total pressure at no cost, effectively providing passive flow control.

Determining whether centrifugal pumping has the potential to develop the required NPR values must therefore be investigated. A method of analysis based on the experimental and numerical study conducted by [120] is adopted to measure the pressure increment inside a 0.00525 m diameter rotating pipe with an open inlet (i.e. at atmospheric pressure). Since the research was aimed at rotorcraft applications, the rotational speed is significantly higher than a typical HAWT. The results reveal that an increment of about 11.38 kPa is achieved for the 1.32 m length pipe rotating at 1000 RPM. This pressure increase can be defined mathematically by considering the acceleration of a fluid element with a width (dr) within a rotating pipe due to centrifugal action ($\omega^2 r$), see figure 6.7.

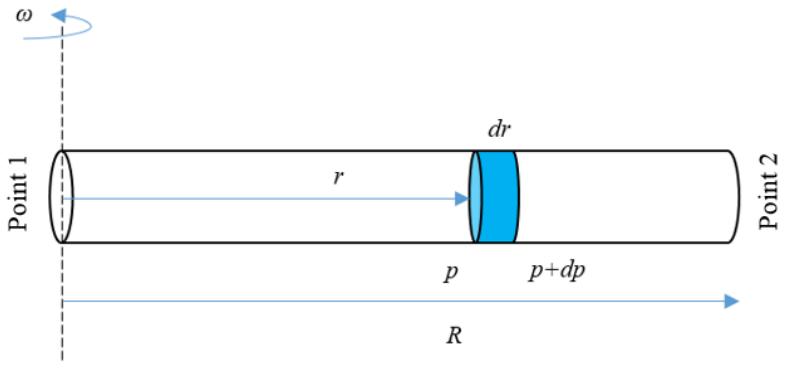

Figure 6-7 Schematic of flow inside a rotating pipe

Applying Newton's second law;

$$dp = dr\ \rho\ \omega^2 r \tag{6-1}$$

$$p_2 - p_1 = \int_0^R \rho\ \omega^2 r\ dr \tag{6-2}$$

$$p_2 = p_1 + \frac{1}{2}\rho\omega^2 R^2 \tag{6-3}$$

Applying equation 6-3 to the data presented by [120] results in a predicted total pressure increment of 11.7 kPa at the end of the 1.32 m pipe which is only 2.8% greater than was measured experimentally; see the close match in figure 6.8.

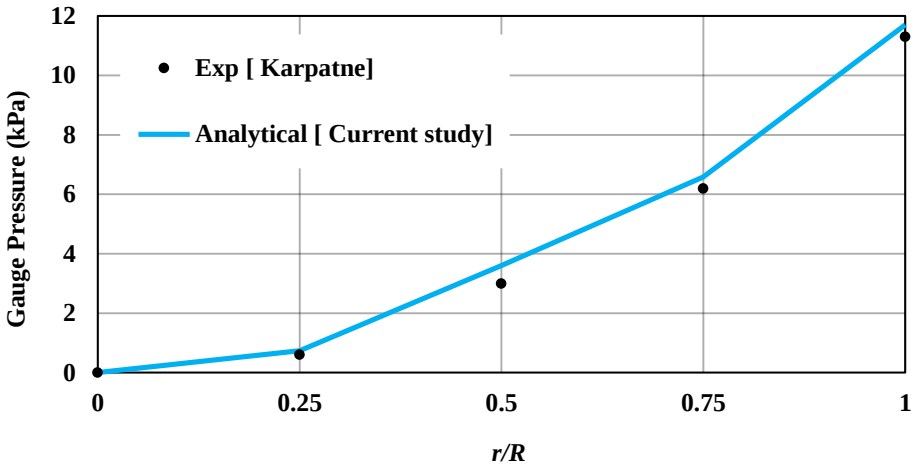

Figure 6-8 Static gauge pressure augmentation along 1.32 m pipe due to centrifugal effect at 1000 RPM compared to experiments from [120]

The close agreement between theory and experiment gave confidence in extending the concept to a 54 m long pipe housed within the wind turbine blade considered in this study, rotating at 12.1 RPM, see figure 6.9. The pipe inlet is assumed to be located near the hub and supplies air directly to the plenum chamber. Unfortunately, due to the relatively low rotational speed a pressure increment, Δp_c, of only 2.8 kPa is achieved which is equivalent to NPR = 1.02; this is insufficient for CC to be efficient using centrifugal pumping alone. Therefore, the only alternative is to make use of an air compressor to supplement the centrifugal pumping effect to obtain the required NPRs identified in chapter 5. Reciprocating single stage air compressors provide a suitable discharge pressure for this application [121], and their requirements will be considered in the next section.

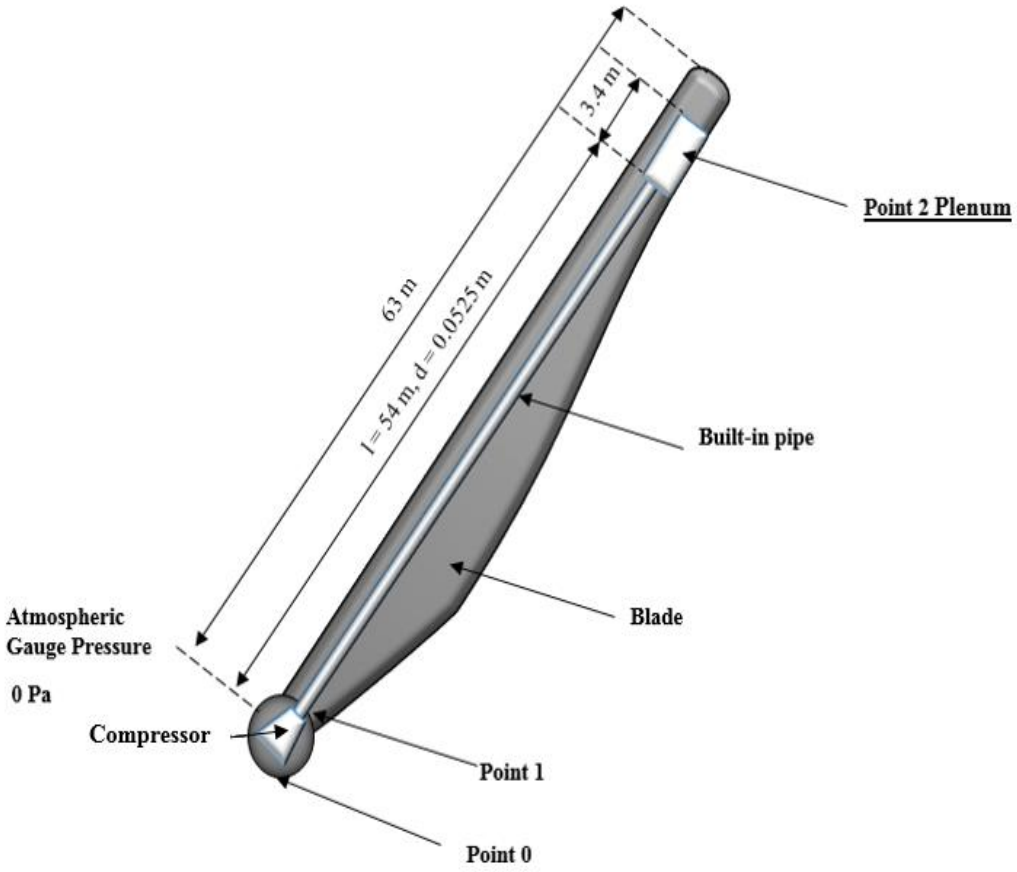

Figure 6-9 Schematic of pumped air supply process

6.6.2 Compressor pumping

To calculate the power required for the compressor for a given NPR, the energy equation for steady, adiabatic flow with no change in kinetic or potential energy between points (0) at the inlet and point (1) at the compressor exit (figure 6.9) is given by:

$$P_{pump} = \eta_{mech}\, P_{shaft} = \eta_{mech} \dot{m}\, c_p (T_{t1} - T_{t0}) \tag{6-4}$$

where P_{pump} is the pump power, η_{mech} is the mechanical efficiency, P_{shaft} is the shaft power required by the compressor, $\dot{m}$ is the pump mass flow rate, c_p is the specific heat capacity and T_{t1}- T_{t0} is the total temperature increase.

The isentropic total temperature at the compressor exit T'_{t1} is defined by the isentropic efficiency (η_{isen}) using:

$$\eta_{isen} = \frac{(T'_{t1} - T_{t0})}{(T_{t1} - T_{t0})} \tag{6-5}$$

For the isentropic flow:

$$\frac{T'_{t1}}{T_{t0}} = \left(\frac{p_{t1}}{p_{t0}}\right)^{\frac{\gamma-1}{\gamma}} \tag{6-6}$$

Combining equations 6-4, 6-5 and 6-6 gives:

$$P_{Shaft} = \frac{\dot{m}\, c_p\, T_{t0}}{\eta_{isen}\, \eta_{mech}} \left(\left(\frac{p_{t1}}{p_{t0}} \right)^{\frac{\gamma-1}{\gamma}} - 1 \right) \quad (6\text{-}7)$$

Since centrifugal pumping can still provide a modest 2.8 kPa pressure contribution, this is accounted for in the calculation of the required pump power.

The jet stream exiting the nozzle will also provide a thrust force that is not accounted for in the determination of the tangential force coefficient from the blade lift and drag coefficients calculated in the CFD analysis. Therefore, assuming a fully-expanded nozzle, the jet thrust is given by equation 6-8:

$$Jet\ thrust = \dot{m}\, U_m \quad (6\text{-}8)$$

where U_m is the mean jet velocity, the jet thrust provides an extra (gain) value as it is in line with the tangential force direction.

6.6.3 Head losses

To determine the pressure drop due to the friction losses Δp_f at point 2 in the pipe, it is necessary to calculate the friction factor, f, used in the Darcy-Weisbach equation.

$$\frac{\Delta p_f}{L} = \frac{\rho\, f\, V^2}{2D} \quad (6\text{-}9)$$

The friction factor is dependent on the internal pipe diameter D, the internal pipe roughness (ϵ = 1.5 x10^{-6} m as used by [120]) and the Reynolds number Re which is in turn calculated from the fluid viscosity μ, density ρ, velocity V and the internal pipe diameter 0.0525 m) from:

$$Re = \rho V D / \mu \quad (6\text{-}10)$$

Head losses due to friction are calculated to be small but significant, ranging from 1.7% for a NPR = 1.1, to 1.4% for a NPR = 1.8. Table (6.1) illustrates the computed head loss values at each NPR considered.

Table 6.1 Head losses values at each NPR

NPR	*p_1 (Pa)*	*$\dot{m}$ (kg/s)*	*V (m/s)*	*Re*	*ΔPf (Pa)*	*Loss %*
1.1	13565	*1.05*	39.61	14076	231.4	1.71
1.2	24005	*1.38*	52.06	18499	399.7	1.67
1.3	34447	*1.62*	61.12	21717	550.8	1.60
1.4	44890	*1.83*	69.04	24532	702.9	1.57
1.5	55332	*2.00*	75.45	26811	839.6	1.52
1.6	65774	*2.16*	81.49	28956	979.3	1.49
1.7	76216	*2.29*	86.39	30699	1100.8	1.44
1.8	86658	*2.42*	91.30	32442	1229.3	1.42

6.7 Net power

In order to determine the net power augmentation for the 3D model, the CFD results are combined with the analytical calculations for a contribution due to jet thrust, the pump power requirement and frictional losses, giving the net power, P_{net} calculated as follows:

$$P_{net} = P_Q - P_{shaft} + P_{thrust} \tag{6-11}$$

where P_Q is power generated due to the aerodynamic forces, including torque augmentation by applying circulation control, P_{shaft} is the power required by the compressor to deliver the required NPR to the plenum, considering centrifugal effects (added values) and friction losses (subtracted value) and P_{thrust} is the power generated due to the thrust force of the jet itself.

Although the implementation of CC provides a power augmentation of up to 11% by applying NPR=1.5, there is no net gain in power from operating the model when considering the cost of pumping which is about 880 kW; this overcomes any power augmentation benefits from CC. This is mainly due to the substantial cost in delivering the required air mass flow rate that is delivered to the plenum chamber. To circumvent this, further consideration was given to reduce the mass flow rate by reducing the nozzle height, despite the clear benefit that larger nozzle heights have on the Coanda effect, as discussed in the 2D parametric study.

6.8 Reduced mass flow investigations

For nozzle heights in the range 0.3%c to 0.05 %c and NPR =1.5 and 1.8, the tangential force F_t and the corresponding torque Q and sectional power generated due to the torque augmentation P_Q (per unit span) were simulated using 2D CFD in the same manner as was described in chapter 5. Consequently, an analytical calculation for the mass flow rate, jet thrust and the compressor shaft power (indicated as a negative value i.e. a loss) per unit span, were calculated using equations 6.7 – 6.11. These data, and the net performance are presented in table 6.2. The baseline aerofoil produced 36.61 kW per unit span, which compares with the best CC configuration providing 30.85 kW per unit span (hj/c = 0.075%c and NPR = 1.5).

Table 6.2 Effect of jet height reduction on the net power for 2D CC-aerofoil span per one blade

CFD (CC-Aerofoil)					Power requirement(Analytical)			
h_j/c %	NPR	F_t (N)	Q (kN.m)	P_Q (kW)	$\dot{m}$ (kg/s)	P_{thrust} (kW)	P_{shaft} (kW)	P_{net} (kW)
0.05	1.5	565	30.5	38.66	0.39	5.52	-14.33	29.86
	1.8	612	33.0	41.88	0.48	8.53	-25.99	24.42
0.075	1.5	643.8	34.8	44.05	0.59	8.290	-21.49	30.85
	1.8	692	37.4	47.35	0.71	12.79	-38.99	21.15
0.1	1.5	696	37.6	47.62	0.78	11.05	-28.66	30.02
	1.8	753.9	40.7	51.59	0.94	17.06	-51.99	16.66
0.125	1.5	708	38.2	48.44	0.98	13.87	-35.83	26.43
	1.8	752	40.6	51.45	1.18	21.32	-64.98	7.80
0.2	1.5	763.6	41.2	52.25	1.57	22.10	-57.33	17.03
	1.8	828.2	44.7	56.67	1.89	34.12	-103.98	-13.19
0.3	1.5	784.8	42.4	53.7	2.34	33.16	-85.99	-0.87
	1.8	*Not converged*			2.83	51.18	-155.97	-
Baseline		534.9	28.9	36.61				36.61

Since a nozzle height h_j/c = 0.075% provides the best compromise between power augmentation due to CC and pump power required, a further investigation was performed with this nozzle height for reduced NPRs as presented in table 6.3. These trends in the different power contributions are also shown graphically in figure 6.10. A small benefit is realised with an NPR = 1.2 and 1.3 (see red lines in figure 6.10) giving the highest net power per unit span, but it is still less than that of the baseline aerofoil without CC. Further attempts to improve active CC by reducing the nozzle height and NPR to lower the mass flow requirements did not improve the net power estimated using 2D CFD.

Table 6.3 Net power per unit span per one blade for *hj /c* = 0.075% (2D aerofoil)

CFD (CC-Aerofoil)						Power requirement(Analytical)			
h_j/c %	NPR	F_t (N)	ΔF_t %	Q (kN.m)	P_Q (kW)	$\dot{m}$ (kg/s)	P_{thrust} (kW)	P_{shaft} (kW)	P_{net} (kW)
0.075	1.1	516.8	-11.31	27.9	35.36	0.30	1.560	-2.30	34.62
	1.2	558.4	-3.40	30.2	38.21	0.40	3.298	-6.20	35.31
	1.3	595.7	4.38	32.2	40.76	0.47	5.010	-10.87	34.90
	1.4	622.4	11.35	33.6	42.59	0.53	6.679	-16.02	33.24
	1.5	643.8	16.34	34.8	44.05	0.59	8.290	-21.49	30.85
	1.6	661.9	20.34	35.7	45.29	0.63	9.845	-27.19	27.94
	1.7	677.7	23.72	36.6	46.37	0.67	11.34	-33.04	24.68
	1.8	692	26.68	37.4	47.35	0.71	12.79	-38.99	21.15
Baseline		534.9		28.9	36.61				36.61

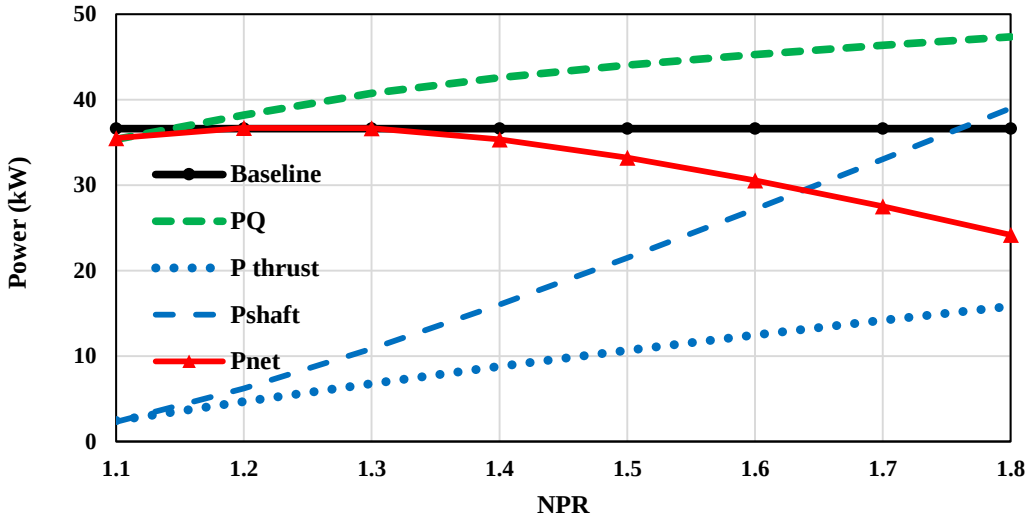

Figure 6-10 Power values at different NPR at h_j/c = 0.075% (2D aerofoil)

6.9 3D correlation

It was desired to evaluate the 2D configurations described in section 6.8 for the 3D rotor. However analysing the airflow around the wind turbine in 3D using the proposed smaller nozzle height of 0.075%c (1.735 mm) was found to be prohibitive using the CFD approach used previously, due to the large number of mesh elements needed to resolve flow features through such a small nozzle. High mesh skewness and convergence issues prevented a CFD analysis on this design. Therefore, as an alternative, a blade element approach was taken by modifying the results obtained using FAST for the baseline rotor. Recall that FAST gives very good agreement with 3D CFD for this baseline rotor (see figure 4.23).

Blade element theory assumes that the blade span can be divided into small elements, each acting independently of the adjacent one. In the FAST analysis the blade span is divided into 20 elements as shown in figure 6.11 based on the data described in table 4.5 in chapter 4 for the blade configuration. The elemental aerodynamic lift and drag forces are transformed into normal and tangential forces, and then integrated over the span of the blade to obtain total forces and moments. The tangential force, F_t, distribution predicted by FAST at a wind speed of 8 m/s is shown in figure 6.12 for the baseline rotor.

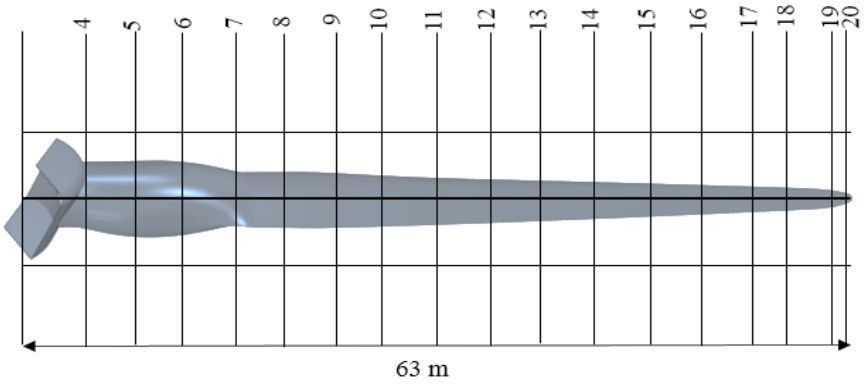

Figure 6-11 Blade elements along the span based on table 4.5 data

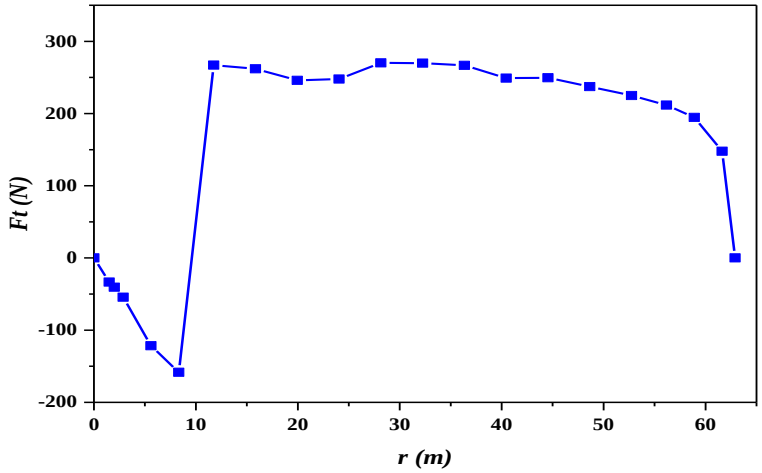

Figure 6-12 Tangential forces, F_t, acting on each element at 8 m/s provided by FAST (baseline rotor)

By modifying this F_t distribution over the region where CC is applied (i.e. element 17) with values obtained from 2D CFD given in table 6.3, the effect of CC on rotor performance can be evaluated. The total torque per blade for example is obtained by integrating the distribution of $F_t.r$ over all elements using the trapezium approximation method. The accuracy of this method was initially assessed for the unmodified FAST result for the baseline rotor. The trapezium integration method underestimates the generated torque by about 5% compared with the torque predicted by FAST. However FAST uses a 4th order Adams-Bashforth-Adams-Moulton predictor-corrector fixed-step integration technique, also performing a time-integration for a full rotation of the rotor. Since we are only concerned with steady wind conditions the time-integration should not result in any discrepancy, and it was deemed that the accuracy of the trapezium approximation technique was sufficient for this study.

The tangential force (F_t) at element 17 provided by FAST is 211.79 N at a wind speed of 8 m/s. Using 2D CFD the tangential force predicted for this NACA 64-618 aerofoil

was 534.98 N assuming the same wind and rotational speeds. However, the BEM method also accounts for both axial and tangential induction factors in its analysis, which tends to reduce wind speed and increase rotational speed. For element 17, the axial (a) and tangential (á) induction factors were predicted by FAST to be 0.541 and 0.0033, respectively. Consequently, these induction factors will result in a significant reduction of the effective inflow angle (see equation 3-8) and a small reduction of the resultant velocity magnitude. Therefore, another 2D CFD simulation was performed using corrected wind and rotational speeds based on these induction factors, giving a tangential force of 68.82 N which is lower than the 211.79 N determined by FAST. This uncertainty may be due to the additional corrections used by FAST to account for tip-losses or dynamic effects, for example. As a consequence, the percentage change in tangential force simulated for the CC aerofoil, relative to that for the baseline NACA 64-618 aerofoil (found in table 6.3) was used to modify the tangential force distribution shown in figure 6.12.

The corresponding elemental contributions to torque are shown in figure 6.13 for the baseline rotor. Each step represents the elemental torque. The value of each step varies due to the different aerofoil profiles, chord length, twist angles and distance from the hub (*r*). For a CC-rotor, it assumed that element 17 utilises a CC-aerofoil with a nozzle height of 0.075%c and NPR =1.5, the result indicates a small increase (represented as red line). Accordingly, the integrated torque for the entire blade exhibits a small difference.

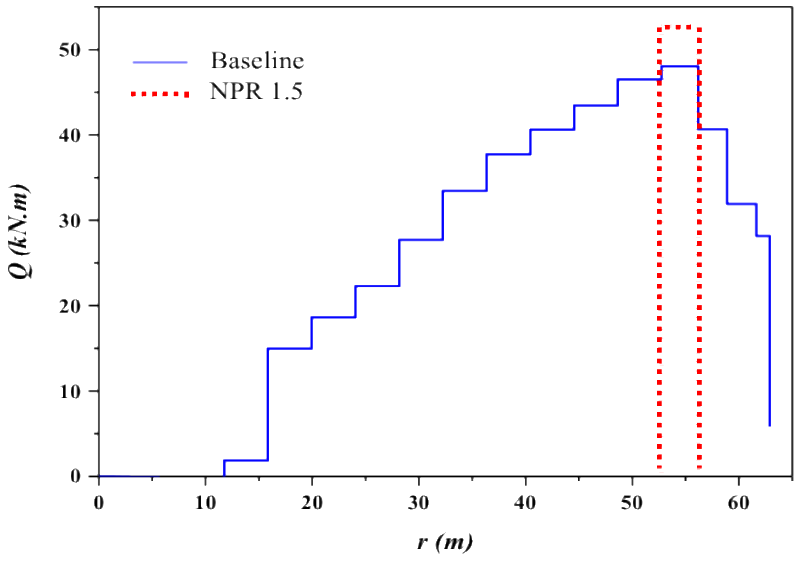

Figure 6-13 Torque, *Q*, acting on each element at 8 m/s

Using the trapezium integration method, the total rotor power generated (P_Q) was obtained for a range of NPRs for this CC-rotor and compared with that for the baseline rotor in figure 6.14. For NPR ≥ 1.2 the CC-rotor generates a higher power. However, the figure also shows the net power once the jet thrust, pump power requirements and frictional losses are accounted for. The net power reduces significantly with NPR and is lower than the baseline rotor power for all the NPRs considered.

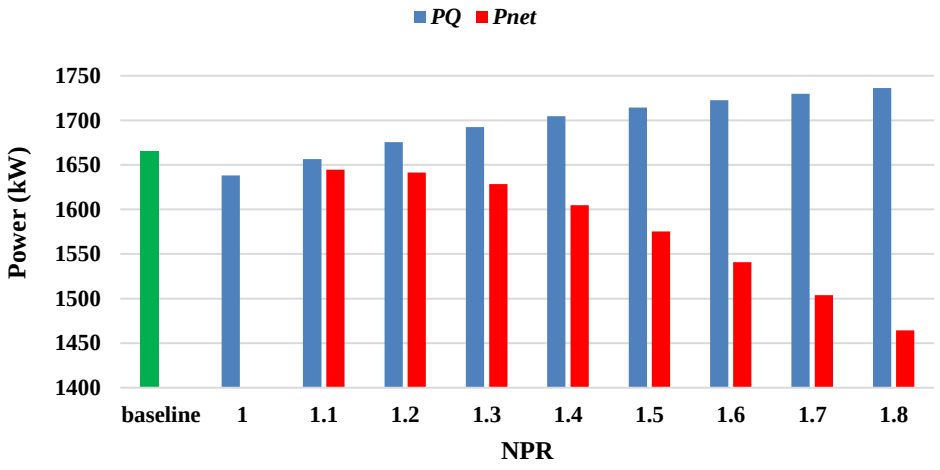

Figure 6-14 Mechanical power comparison at different NPR using the trapezium approximation method, (3 blades, h_j/c = 0.075%)

6.10 Chapter summary

In this chapter, the baseline rotor blade was modified between 84 - 89 % of the span (*i.e.* between radial stations r = 52.75 and 56.17 m), where the NACA 64-618 aerofoil used in the 2D parametric study, was replaced with the modified-I3 CC-aerofoil according to the parametric study carried out in the previous chapter. A significant power augmentation was achieved with an 11% increase for NPR = 1.5 and an 18.4% increase for NPR = 1.8, this was based on considering the aerodynamic benefits alone. In terms of practical application of the modifications, the average net power was calculated to be approximately 22.5% less than that of the baseline rotor due to the power required to pump air to the jet location as well as internal frictional losses. Passive control using centrifugal pumping alone did not generate a sufficiently high NPR. Further attempts to improve active CC by reducing the nozzle height and NPR to lower the mass flow requirements did improve the net power estimated using a hybrid of 2D CFD and BEM, but was still less than the baseline rotor without CC.

Chapter 7 DISCUSSION

7.1 Scope of work

The scope of this study was to investigate the feasibility of applying active flow control (AFC) techniques to a HAWT. A general review in section 2.3.3 described the aerodynamic flow physics of AFC which are applicable to the HAWT. In general, both active flow control (AFC) and passive flow control (PFC) could potentially be implemented in order to enhance wind turbine performance via changing the boundary layer development around the blade surface. Passive flow control, such as blade twist, can potentially raise the turbine's performance without applying external energy [14, 25]. In terms of energy consideration alone, passive methods can offer useful benefits without the need for additional power for their operation. On the other hand, for wind turbine applications, there is no need for continuous use of flow control devices after reaching the rated power where the maximum designed power for a wind turbine is achieved. Hence, AFC for the pre-rated region was the main focus of this research to determine whether a typical wind turbine could commence working at rated power earlier. Using the NREL 5 MW design, this was achieved by integrating CC using a proposed design modification to enable the wind turbine to achieve the rated power at a lower wind velocity of 10.8 m/s instead of 11.4 m/s. This result only considers the results from a torque augmentation point of view, however, when the external power needed to generate the required power is considered, the benefits are lost. This will be discussed in more detail later in this chapter.

7.2 Project outcomes

The main objective of this study was to investigate the aerodynamic effect of circulation control on wind turbine aerodynamic performance, using CFD. The following sub-sections discuss important aspects of the methods used and key insights from the results.

7.2.1 Verification and validation

As described in chapter 3 (section 3.8.4), errors and uncertainty are controlled using robust verification and validation methods. Numerical errors were controlled in the CFD approach used in the present study in various ways. Round-off error was minimised by using a double-precision flow solver with the commercial package STAR-CCM+

V11.04.012. It is worth mentioning that some recent versions offer mixed-precision, which is mainly based on a single-precision solver (requiring reduced memory with smaller run times) with a few variables that are calculated in double precision accuracy. Therefore, it is potentially less accurate [84], however, double precision was used in the present study thereby minimising round-off error.

Discretisation errors are an inevitable consequence of meshing and the only way to minimise them is to complete a mesh sensitivity study. As outlined in section 4.2.5, a mesh independence study was completed for the NREL phase VI 3D wind turbine. It was shown that the second finest mesh of 11.1M cells gave results which were almost identical to an even finer 14.2M cell mesh. Also, the mesh independent solution gave a torque-per-blade output of only 0.3% below the experimental data, for the same rotor. This showed that the mesh refinement process was effective at minimising discretisation errors in the simulations. The same method was applied in other simulations of the NREL 5MW turbine, giving confidence in the results. Furthermore, convergence error was reduced by running simulations until they had properly converged with the residual levels set at 10^{-6} (and always lower than 10^{-5}).

In terms of validation, a robust approach was employed for the NREL phase VI HAWT which has good quality experimental data [102]. As explained in section 4.2.7, the CFD results exhibited a good match to experimental data for both predicted power output and in terms of sectional pressure profiles at various radial stations on the blade. The best match occurred for pre-stall conditions which was the focus of this study, with inconsistent predictions in the deep-stall region where the time-dependent flow physics are not adequately captured [1, 77]. Unfortunately, no experimental data are available for the much larger NREL 5 MW design. However the CFD results obtained for this wind turbine were compared with a BEM code, FAST, which has been shown to give accurate results [70]. It was observed that the accuracy of the CFD code is affected the most as the wind velocity increased above 10 m/s, due to the flow complexity (vortex shedding etc.). Using unsteady solutions could overcome this issue but the simulation time would have been prohibitive in this work, hence the need to use FAST to help determine the accuracy of the CFD solutions. However, as mentioned above, the steady-state solutions achieved were accurate within the pre-stall stage, the area of interest, which justified the use of a steady, RANS-based code.

7.2.2 Modelling approach

A large computational domain, much larger than the wind turbine was used to simulate the flow around the 2 types of HAWT, and results showed sensible power predictions for both cases. However only one blade was modelled to reduce the computational effort.

A very fine mesh was required to successfully capture the flow behaviour around the modified T.E., especially when CC was applied. This was a very challenging process since it required a balance between sizes of the cells around and downstream of the jet to avoid any computational errors. This yielded a very large cell count (up to 24.9M) which required significant high-performance computer (HPC) resources to perform the runs. Dealing with such a fine mesh on large rotors in excess of 60 m in span was one of the major challenges of this work.

As mentioned in the previous section, a CFD simulation using a RANS-based approach was used in this study. Whilst this approach has limitations for complex flow phenomena (e.g. post and deep-stall) [86, 93, 94], the good agreement between experimental data and the SST k-ω turbulence model for predicting torque-per-blade, was sufficient to conduct the remaining simulations with this model. Results generated with both the Spalart-Allmaras and Realizable $k-\varepsilon$ turbulence models over-predicted torque-per-bade compared to experimental and SST k-ω results.

Despite the prohibitive pumping requirements of the jet, it was found that minimising the jet height does help provide more balance between the required mass flow rate and external power. Unfortunately, this proved to be too challenging to simulate with CFD on account of the very fine mesh required to capture the jet in such a small region. To circumvent this, an alternative approach of using a hybrid BEM code combined with 2D CFD was used to evaluate the effect of the jet height reduction.

7.2.3 Design sensitivities

The parametric study conducted in chapter 5 revealed the sensitivity of aft aerofoil design trends both in terms of changes to the flow patterns and, crucially, the resulting tangential force enhancements. Results from this aspect of the work contained in this thesis agrees with previous research [54-56] in that the elliptical shape of the modified T.E. provides greater aerodynamic benefit than a circular configuration. For example, a comparison among the configurations I1 (which is generated with a semi-major axis equal to the semi-minor axis (i.e. circle)), I2 and I3 show how the jet stream stays attached to the modified T.E. further downstream as the curvature decreases which leads

to increased tangential forces for the wind turbine. Further benefits are achieved by doubling the size of the semi-minor axis of the ellipse to generate the Modified-I3 configuration. However, despite the aerodynamic benefits of the Modified-I3 design, a decrease of about 7% in sectional torque generation is observed when the jet is switched off. This was avoided by previous researchers [51, 122-124] by deploying a circular base flap which provides both a circular T.E and jet exit when it operates whilst keeping the original shape of the aerofoil when switched off. This suggestion was not considered in the current study as a less complex CC system was sought.

7.2.4 Required NPR pumping consideration

As CC is an active flow control technique, it comes with a cost which is the necessary additional power to provide the required nozzle pressure ratio (NPR) via a pump or similar device. A major outcome from this work is the realisation that the lift and torque augmentation (the gain) must be balanced against the required pumping power (the cost).

In an effort to circumvent the losses, a concept was explored to use the centrifugal effect to take free-stream air from a central inlet at the hub and accelerate it down a radial channel to feed a CC plenum. Whilst this can be very effective in applications with high rotational velocities [120], for the wind turbine application considered in this study, it only provided a small benefit of 2.8 kPa which is equivalent to NPR = 1.02. The benefit is insufficient to overcome the losses associated with pumping air from the hub to the inlet. Friction losses inside the proposed piping system are small but significant, ranging from 1.7% for a NPR = 1.1, to 1.4% for a NPR = 1.8.

Reducing the mass flow rate by minimising the nozzle height down to 0.075%c, the total rotor power generated (P_Q) increases significantly with increasing NPR and is lower than the baseline rotor power for all the NPRs considered, once the jet thrust, pump power requirements and frictional losses are accounted for.

Taking the above-mentioned expense of CC into account, it was therefore considered impractical to apply it along the entire span of a three-dimensional blade, with a small region near the tip highlighted as a suitable location.

7.3 Limitations

As already discussed, one limitation of the CFD approach used in this study is that only steady state simulations were performed. Although a good agreement with experimental results were achieved in the pre-stall region (which was in fact the focus of

this work), the influence of unsteady flow phenomena can only be investigated with transient simulations [77].

As explained in chapter 6, a major limitation of the CFD approach related to the prohibitive mesh requirements for very small nozzle sizes. This occurred because of the range of sizes in the geometry. With current computational resources, it was found impossible to mesh a turbine blade in excess of 60 m in length when also integrating a nozzle with a height of only 1.735mm; managing to fit an inflation layer of cells to both jet walls meant that the cell count was simply prohibitive. As a result, a hybrid of 2D CFD and FAST (based on BEM) was required to provide meaningful data for very small nozzle heights (recall section 6.9).

Another limitation of this work is that there are no experimental data available for the large NREL 5MW wind turbine which was used in later chapters. Whilst this would have been desirable, the CFD method was rigorously tested using a smaller validation case, for which there was sufficient experimental data. BEM, in the form of the FAST code, was also useful to ensure that the CFD results were sensible throughout the study.

7.4 Contributions to knowledge

The main contributions to knowledge from this study help to introduce a better understanding of applying CC active flow technique to a commercial scale HAWT. The contributions of the current work are summarised as follows:

1. A systematic exploration of design parameters at the trailing edge of a 2D cambered aerofoil found that the integration of an ellipse can achieve aerodynamics benefits, in conjunction with circulation control through a carefully placed nozzle.
2. Despite the aerodynamic benefits of active CC, a major limitation is the cost to supply the required nozzle pressure ratio which exceeds the aerodynamic gains, for the case of a constant mass flow rate through the CC nozzle.
3. Centrifugal pumping, whilst able to provide a small increase in nozzle pressure ratio for no pumping cost, is not significant enough to provide a useful benefit. This is because the span of a large turbine is so large (giving greater frictional losses through ducting) and the rotational velocities are relatively slow.

Chapter 8 CONCLUSION AND FUTURE WORK

8.1 Conclusion

In this research, the influence of using passive and active circulation control to improve the mechanical power output for the NREL 5 MW baseline wind turbine was studied. A RANS-based CFD verification and validation study for the benchmark CC-E0020EJ aerofoil demonstrated very good agreement with experimental trends for lift augmentation. A parametric study of 28 CC aerofoil shapes with different nozzle positions, heights and aft camber, indicated a configuration with the furthest aft nozzle position (94% *c*) and the greatest nozzle height (0.3% *c*) was likely to give the highest tangential force coefficient for a wind turbine application. The aft location helps to minimise drag by reducing the extent of the rearward-facing Coanda surface which experiences low static pressure. A modified version of this CC aerofoil was thus evaluated between 84 - 89 % of the span of the NREL 5 MW baseline wind turbine rotor blade using 3D CFD simulations. Although significant power augmentation was achieved, with an 11% increase for NPR = 1.5 and an 18.4% increase for NPR = 1.8, this was based on considering the aerodynamic benefits alone. In terms of practical application of the modifications, the average net power was calculated to be approximately 22.5% less than that of the baseline rotor due to the power required to pump air to the jet location as well as internal frictional losses. Passive control using centrifugal pumping alone did not generate a sufficiently high NPR. However smaller wind turbines (or helicopter rotors) which typically have a significantly higher rotational speed may be able to utilise centrifugal pumping for effective CC. Further attempts to improve active CC by reducing the nozzle height and NPR to lower the mass flow requirements did improve the net power estimated using a hybrid of 2D CFD and BEM, but was still less than the baseline rotor without CC.

8.2 Recommendations for future work

The following points highlight some aspects which are suggested as possible future research directions:

1. It is recommended to utilize an optimisation tool in order to obtain the optimum 2D CC aerofoil parameters. This could explore a larger design space than the one

considered in the present study and so there is merit in extending the work in this way.

2. Applying a pulsed source of pressure through CC jet openings will reduce the mass flow rate, and thus it could have potential to reduce the power consumption, whilst still extracting the clear benefits of CC. However, this requires more computational effort since an unsteady simulation strategy must be used.
3. Although the CC technique shows aerodynamic benefits, its pumping power is costly for large rotors, however, it is recommended that the technique be investigated and applied to smaller wind turbines or other kinds of rotary machines where the net torque augmentation is favourable. Making use of the centrifugal pumping generated by the rotation of the rotary blade itself may also have a tangible benefit.

REFERENCES

[1] T. Burton, N. Jenkins, D. Sharpe, and E. Bossanyi, "Wind Energy Handbook. 2nd," ed: United Kingdom: A John Wiley and Sons, Ltd., Publication, 2011.

[2] M. H. Ali, *Wind energy systems: solutions for power quality and stabilization*. CRC Press, 2012.

[3] A. R. Jha, *Wind turbine technology*. CRC press, 2010.

[4] Annual Market. "Global wind report." *Global Wind Energy Council* ,2019.

[5] A. K. Gupta, "Efficient Wind Energy Conversion: Evolution to Modern Design," *Journal of Energy Resources Technology*, vol. 137, no. 5, p. 051201, 2015.

[6] D. G. Shepherd, *Historical development of the windmill*. National Aeronautics and Space Administration, Office of Management, Scientific and Technical Information Division, 1990.

[7] N. Stannard and J. Bumby, "Energy yield and cost analysis of small scale wind turbines," in *Universities Power Engineering Conference, 2006. UPEC'06. Proceedings of the 41st International*, 2006, vol. 1: IEEE, pp. 108-112.

[8] A. Reeves and F. A. Beck, *Wind energy for electric power*. Renewable Energy Policy Project, 2003.

[9] M. I. Blanco, "The economics of wind energy," *Renewable and Sustainable Energy Reviews*, vol. 13, no. 6, pp. 1372-1382, 2009.

[10] I. R. E. A. IRENA, "RENEWABLE ENERGY TECHNOLOGIES: COST ANALYSIS SERIES," 2012.

[11] T. Wolff, B. Ernst, and J. Seume, "Aerodynamic behavior of an airfoil with morphing trailing edge for wind turbine applications," in *Journal of Physics: Conference Series*, 2014, vol. 524, no. 1: IOP Publishing, p. 012018.

[12] K. Mikkelsen, "Effect of free stream turbulence on wind turbine performance," 2013.

[13] Vestas. https://www.windpowermonthly.com/article/1435504/mhi-vestas-launches-95mw-v164-turbine-london (accessed 10.10.2018).

[14] S. J. Johnson and D. E. Berg, "Active load control techniques for wind turbines," 2008.

[15] J. Jonkman, S. Butterfield, W. Musial, and G. Scott, "Definition of a 5-MW reference wind turbine for offshore system development," *National Renewable Energy Laboratory, Golden, CO, Technical Report No. NREL/TP-500-38060,* 2009.

[16] U. Fernandez-Gamiz, E. Zulueta, A. Boyano, I. Ansoategui, and I. Uriarte, "Five megawatt wind turbine power output improvements by passive flow control devices," *Energies,* vol. 10, no. 6, p. 742, 2017.

[17] A. Ebrahimi and M. Movahhedi, "Power improvement of NREL 5-MW wind turbine using multi-DBD plasma actuators," *Energy Conversion and Management,* vol. 146, pp. 96-106, 2017.

[18] H. Chen, "Numerical Study of Trailing Edge Flow Control for Horizontal Axis Wind Turbines," University of Sheffield, 2016.

[19] A. Gross and H. F. Fasel, "Flow Control for Wind Turbine Airfoil," in *ASME 2011 5th International Conference on Energy Sustainability*, 2011: American Society of Mechanical Engineers, pp. 2051-2060.

[20] G. Hoholis, R. Steijl, and K. Badcock, "Circulation control as a roll effector for unmanned combat aerial vehicles," *Journal of Aircraft,* vol. 53, no. 6, pp. 1875-1889, 2016.

[21] R. Englar, "Circulation control pneumatic aerodynamics: blown force and moment augmentation and modification-Past, present and future," in *Fluids 2000 Conference and Exhibit*, 2000, p. 2541.

[22] T. Nishino, S. Hahn, and K. Shariff, "Large-eddy simulations of a turbulent Coanda jet on a circulation control airfoil," *Physics of fluids,* vol. 22, no. 12, p. 125105, 2010.

[23] M. A. Naqvi, "Prediction of circulation control performance characteristics for Super STOL and STOL applications," 2006.

[24] A. Hansen and C. Butterfield, "Aerodynamics of horizontal-axis wind turbines," *Annual Review of Fluid Mechanics,* vol. 25, no. 1, pp. 115-149, 1993.

[25] G. Pechlivanoglou, "Passive and active flow control solutions for wind turbine blades," Universitätsbibliothek der Technischen Universität Berlin, 2012.

[26] M. O. Hansen and H. A. Madsen, "Review paper on wind turbine aerodynamics," *Journal of fluids engineering,* vol. 133, no. 11, p. 114001, 2011.

[27] J. F. Manwell, J. G. McGowan, and A. L. Rogers, *Wind energy explained: theory, design and application*. John Wiley & Sons, 2010.

[28] S. Malhotra, *Selection, design and construction of offshore wind turbine foundations*. INTECH Open Access Publisher, 2011.

[29] B. Bavanish and K. Thyagarajan, "Optimization of power coefficient on a horizontal axis wind turbine using bem theory," *Renewable and Sustainable Energy Reviews,* vol. 26, pp. 169-182, 2013.

[30] A. Betz, "Das Maximum der theoretisch möglichen Ausnutzung des Windes durch Windmotoren," *Zeitschrift fur das gesamte Turbinenwesten,* vol. 20, 1920.

[31] I. K. Wiratama, "Aerodynamic Design of Wind Turbine Blades Utilising Nonconventional Control Systems," Northumbria University, 2012.

[32] P. Jain, *Wind energy engineering*. New York: McGraw-Hill, 2011.

[33] L. Huang, P. Huang, R. LeBeau, and T. Hauser, "Numerical study of blowing and suction control mechanism on NACA0012 airfoil," *Journal of aircraft,* vol. 41, no. 5, pp. 1005-1013, 2004.

[34] J. D. Anderson, "Ludwig Prandtl's boundary layer," *Physics Today,* vol. 58, no. 12, pp. 42-48, 2005.

[35] J. D. Anderson, "Fundamentals of aerodynamics," *McGraw,* 2009.

[36] E. L. Houghton and P. W. Carpenter, *Aerodynamics for engineering students*. Elsevier, 2003.

[37] T. A. Talay, *Introduction to the Aerodynamics of Flight*. Scientific and Technical Information Office, National Aeronautics and Space …, 1975.

[38] A. Taheri, "Development and Design of a Form-Adaptive Trailing-Edge for Wind Turbine Blades," Faculty of Engineering, Cairo University-Giza, Egypt, 2015.

[39] D. E. Berg, J. R. Zayas, D. W. Lobitz, C. van Dam, R. Chow, and J. P. Baker, "Active aerodynamic load control of wind turbine blades," in *ASME/JSME 2007*

5th Joint Fluids Engineering Conference, 2007: American Society of Mechanical Engineers, pp. 1119-1127.

[40] T. K. Barlas and G. Van Kuik, "Review of state of the art in smart rotor control research for wind turbines," *Progress in Aerospace Sciences*, vol. 46, no. 1, pp. 1-27, 2010.

[41] C. Kress, N. Chokani, and R. Abhari, "Downwind wind turbine yaw stability and performance," *Renewable Energy*, vol. 83, pp. 1157-1165, 2015.

[42] C. Tongchitpakdee, S. Benjanirat, and L. N. Sankar, "Numerical simulation of the aerodynamics of horizontal axis wind turbines under yawed flow conditions," *Journal of solar energy engineering*, vol. 127, no. 4, pp. 464-474, 2005.

[43] S. Daynes and P. M. Weaver, "A morphing wind turbine blade control surface," in *ASME 2011 Conference on Smart Materials, Adaptive Structures and Intelligent Systems*, 2011: American Society of Mechanical Engineers, pp. 531-540.

[44] T. Lee and Y. Su, "Lift enhancement and flow structure of airfoil with joint trailing-edge flap and Gurney flap," *Experiments in fluids*, vol. 50, no. 6, pp. 1671-1684, 2011.

[45] S. A. Prince and V. Khodagolian, "Low-Speed Static Stall Suppression Using Steady and Pulsed Air-Jet Vortex Generators," *AIAA Journal*, vol. 49, no. 3, pp. 642-654, 2011, doi: 10.2514/1.j050754.

[46] T. Sundaravadivel, S. N. Pillai, and C. S. Kumar, "Influence of Boundary Layer control on wind turbine blade aerodynamic characteristics–Part I–Computational Study," 2013.

[47] A. Choudhry, M. Arjomandi, and R. Kelso, "Methods to control dynamic stall for wind turbine applications," *Renewable Energy*, vol. 86, pp. 26-37, 2016.

[48] H. Mueller-Vahl, G. Pechlivanoglou, C. Nayeri, and C. Paschereit, "Vortex generators for wind turbine blades: A combined wind tunnel and wind turbine parametric study," in *ASME Turbo Expo 2012: Turbine Technical Conference and Exposition*, 2012: American Society of Mechanical Engineers, pp. 899-914.

[49] V. Maldonado, J. Farnsworth, W. Gressick, and M. Amitay, "Active control of flow separation and structural vibrations of wind turbine blades," *Wind Energy,* vol. 13, no. 2-3, pp. 221-237, 2010.

[50] H. Djojodihardjo *et al.*, "Computational study on the aerodynamic performance of wind turbine airfoil fitted with coandă jet," *Journal of Renewable Energy,* vol. 2013, 2013.

[51] H. Djojodihardjo and N. Thangarajah, "Research, development and recent patents on aerodynamic surface circulation control-A critical review," *Recent Patents on Mechanical Engineering,* vol. 7, no. 1, pp. 1-37, 2014.

[52] J. P. Wilhelm, E. D. Pertl, F. A. Pertl, and J. E. Smith, "Performance Predictions of a Circulation Controlled-Vertical Axis Wind Turbine with Solidity Control," in *ASME 2009 3rd International Conference on Energy Sustainability collocated with the Heat Transfer and InterPACK09 Conferences*, 2009: American Society of Mechanical Engineers, pp. 1001-1007.

[53] R. J. Englar, "Two-dimensional subsonic wind tunnel tests of two 15-percent thick circulation control airfoils," DAVID W TAYLOR NAVAL SHIP RESEARCH AND DEVELOPMENT CENTER BETHESDA MD AVIATION AND SURFACE EFFECTS DEPT, 1971.

[54] R. Englar, G. Jones, B. Allan, and J. Lin, "2-D circulation control airfoil benchmark experiments intended for CFD code validation," in *47th AIAA Aerospace sciences meeting including the new horizons forum and aerospace exposition*, 2009, p. 902.

[55] M. G. Alexander, S. G. Anders, S. K. Johnson, J. P. Florance, and D. F. Keller, "Trailing edge blowing on a two-dimensional six-percent thick elliptical circulation control airfoil up to transonic conditions," 2005.

[56] R. Schlecht and S. Anders, "Parametric evaluation of thin, transonic circulation-control airfoils," in *45th AIAA Aerospace Sciences Meeting and Exhibit*, 2007, p. 272.

[57] G. S. Jones and R. D. Joslin, "Proceedings of the 2004 NASA/ONR Circulation Control Workshop, Part 1," 2005.

[58] G. S. Jones and R. D. Joslin, "Proceedings of the 2004 NASA/ONR Circulation Control Workshop, Part 2," 2005.

[59] T. D. Economon, W. E. Milholen II, and C. A. Branch, "Parametric investigation of a 2-D circulation control geometry," *Configuration Aerodynamics Branch Research and Technology Directorate,* 2008.

[60] D. McGrain, G. M. Angle, J. P. Wilhelm, E. D. Pertl, and J. E. Smith, "Circulation control applied to wind turbines," in *ASME 2009 3rd International Conference on Energy Sustainability collocated with the Heat Transfer and InterPACK09 Conferences,* 2009: American Society of Mechanical Engineers, pp. 905-910.

[61] A. Shires and V. Kourkoulis, "Application of circulation controlled blades for vertical axis wind turbines," *Energies,* vol. 6, no. 8, pp. 3744-3763, 2013.

[62] M. Forster, M. Biava, and R. Steijl, "Optimisation of Coanda Surfaces for Transonic Circulation Control," in *6th European Conference for Aerospace Sciences, Krakow, Poland,* 2015, vol. 29.

[63] C. Trevelyan, "Application of circulation control aerofoils to wind turbines," © Conrad Trevelyan, 2002.

[64] K. Kara, M. Gunduz, J. Kim, and L. Sankar, "Effects of circulation control on power production for large scale wind turbines," in *51st AIAA Aerospace Sciences Meeting including the New Horizons Forum and Aerospace Exposition*, 2013, p. 1105.

[65] H. Glauert, "Airplane propellers," in *Aerodynamic theory*: Springer, 1935, pp. 169-360.

[66] G. Ingram, "Wind turbine blade analysis using the blade element momentum method. Version 1.1," *School of Engineering, Durham University, UK,* 2005.

[67] C. Lindenburg, "Investigation into rotor blade aerodynamics," *Energy research Centre of the Netherlands (ECN) Wind Energy publication, ECN-C--03-025,* 2003.

[68] L. Vermeer, J. N. Sørensen, and A. Crespo, "Wind turbine wake aerodynamics," *Progress in aerospace sciences,* vol. 39, no. 6-7, pp. 467-510, 2003.

[69] P. J. Moriarty and A. C. Hansen, "AeroDyn theory manual," National Renewable Energy Lab., Golden, CO (US), 2005.

[70] J. M. Jonkman and M. L. Buhl Jr, "FAST user's guide," *National Renewable Energy Laboratory, Golden, CO, Technical Report No. NREL/EL-500-38230,* 2005.

[71] F. D. Bianchi, H. De Battista, and R. J. Mantz, *Wind turbine control systems: principles, modelling and gain scheduling design*. Springer Science & Business Media, 2006.

[72] Y.-T. Wu and F. Porté-Agel, "Atmospheric turbulence effects on wind-turbine wakes: An LES study," *energies,* vol. 5, no. 12, pp. 5340-5362, 2012.

[73] J. Lundquist and A. Clifton, "How turbulence can impact power performance," *North American Windpower,* vol. 9, no. 8, p. 1, 2012.

[74] B. Sanderse, v. d. S. Pijl, and B. Koren, "Review of computational fluid dynamics for wind turbine wake aerodynamics," *Wind Energy,* vol. 14, no. 7, pp. 799-819, 2011.

[75] A. Kolmogorov, "The local structure of turbulence in incompressible viscous fuid for very large Reynold numbers," *Proceeding of Royal Society of London Series A-Mathematical and Physical,* vol. 434, pp. 9-13, 1991.

[76] Cushman-Roisin B, Gualtieri C, Mihailovic DT. Environmental Fluid Mechanics: Current issues and future outlook. Fluid Mechanics of Environmental Interfaces, Taylor & Francis, Leiden,pp.1-6, 2008

[77] H. K. Versteeg and W. Malalasekera, *An introduction to computational fluid dynamics: the finite volume method*. Pearson education, 2007.

[78] T. B. Gatski, M. Y. Hussaini, and J. L. Lumley, *Simulation and modeling of turbulent flows*. Oxford University Press, 1996.

[79] S. B. Pope, "Turbulent flows," ed: IOP Publishing, 2001.

[80] H. S. Chivaee, "Large eddy simulation of turbulent flows in wind energy," *Uddannelse,* vol. 2011, p. 14, 2014.

[81] N. Stergiannis, C. Lacor, J. Beeck, and R. Donnelly, "CFD modelling approaches against single wind turbine wake measurements using RANS," in *Journal of Physics: Conference Series*, 2016, vol. 753, no. 3: IOP Publishing, p. 032062.

[82] D. J. Mavriplis, "Aerodynamic drag prediction using unstructured mesh solvers," *Lecture notes from the VKI Lecture Series on CFD-Based Drag Prediction and Reduction*, 2003.

[83] P. R. Spalart, "Strategies for turbulence modelling and simulations," *International Journal of Heat and Fluid Flow*, vol. 21, no. 3, pp. 252-263, 2000.

[84] CD-Adapco, "STAR-CCM+ Documentation, Version 11.04," 2016.

[85] A. Al-Abadi, "Novel strategies for aerodynamic performance improvement of wind turbines turbulent flow," Doctoral dissertation, Germany 2014.

[86] D. A. Digraskar, "Simulations of flow over wind turbines," 2010.

[87] C. E. Carcangiu, J. N. Sørensen, F. Cambuli, and N. Mandas, "CFD–RANS analysis of the rotational effects on the boundary layer of wind turbine blades," in *Journal of physics: conference series*, 2007, vol. 75, no. 1: IOP Publishing, p. 012031.

[88] S. Patankar, *Numerical heat transfer and fluid flow*. Taylor & Francis, 1980.

[89] A. Bakker, "Lecture 10-Turbulence Models Applied Computational Fluid Dynamics," *Power-Point presentation*, 2002.

[90] H. Cao, "Aerodynamics Analysis of Small Horizontal Axis Wind Turbine Blades by Using 2D and 3D CFD Modelling," Citeseer, 2011.

[91] M. M. Yelmule and E. A. Vsj, "CFD predictions of NREL phase VI rotor experiments in NASA/AMES wind tunnel," *International Journal of Renewable Energy Research (IJRER)*, vol. 3, no. 2, pp. 261-269, 2013.

[92] A. Gonzalez and X. Munduate, "Three-dimensional and rotational aerodynamics on the NREL phase VI wind turbine blade," *Journal of Solar Energy Engineering*, vol. 130, no. 3, p. 031008, 2008.

[93] M. A. Elfarra, N. Sezer-Uzol, and I. S. Akmandor, "NREL VI rotor blade: numerical investigation and winglet design and optimization using CFD," *Wind Energy*, vol. 17, no. 4, pp. 605-626, 2014.

[94] A. M. Farhan, "Numerical Study of the Effect of Winglets on a Horizontal Axis Wind Turbine Performance," University of Leeds, 2018.

[95] J. O'brien, T. Young, J. Early, and P. Griffin, "An assessment of commercial CFD turbulence models for near wake HAWT modelling," *Journal of Wind Engineering and Industrial Aerodynamics,* vol. 176, pp. 32-53, 2018.

[96] M. Tahani, H. Hosseinzadegan, and M. Moradi, "Comparative Numerical Study of Turbulence Models for Analysis a Commercial HAWT Performance," *American Journal of Renewable and Sustainable Energy,* vol. 1, no. 1, pp. 9-15, 2015.

[97] P. Spalart and S. Allmaras, "A one-equation turbulence model for aerodynamic flows," in *30th aerospace sciences meeting and exhibit*, 1992, p. 439.

[98] W. Jones and B. E. Launder, "The prediction of laminarization with a two-equation model of turbulence," *International journal of heat and mass transfer,* vol. 15, no. 2, pp. 301-314, 1972.

[99] T.-H. Shih, W. W. Liou, A. Shabbir, Z. Yang, and J. Zhu, "A new k-ϵ eddy viscosity model for high reynolds number turbulent flows," *Computers & Fluids,* vol. 24, no. 3, pp. 227-238, 1995.

[100] D. C. Wilcox, *Turbulence modeling for CFD*. DCW industries La Canada, CA, 1998.

[101] F. R. Menter, "Two-equation eddy-viscosity turbulence models for engineering applications," *AIAA journal*, vol. 32, no. 8, pp. 1598-1605, 1994.

[102] M. M. Hand *et al.*, *Unsteady aerodynamics experiment phase VI: wind tunnel test configurations and available data campaigns*. National Renewable Energy Laboratory Golden, Colorado, USA, 2001.

[103] E. P. Duque, M. D. Burklund, and W. Johnson, "Navier-Stokes and comprehensive analysis performance predictions of the NREL phase VI experiment," *Journal of Solar Energy Engineering,* vol. 125, no. 4, pp. 457-467, 2003.

[104] M. A. Hossain, Z. Huque, and R. R. Kammalapati, "Propagation of shock on NREL phase VI wind turbine airfoil under compressible flow," *Journal of Renewable Energy,* vol. 2013, 2013.

[105] X. Chen and S. Kang, "Numerical Simulation on Influence Factors of Aerodynamic Mistuning of Wind Turbine," in *2015 Asia-Pacific Energy Equipment Engineering Research Conference*, 2015: Atlantis Press.

[106] A. Gonzalez and X. Munduate, "Unsteady modelling of the oscillating S809 aerofoil and NREL phase VI parked blade using the Beddoes-Leishman dynamic stall model," in *Journal of Physics: Conference Series*, 2007, vol. 75, no. 1: IOP Publishing, p. 012020.

[107] J. L. Tangler and D. M. Somers, *NREL airfoil families for HAWTs*. Citeseer, 1995.

[108] W. Wolfe and S. Ochs, "CFD Calculations of S809 Aerodynamic Characteristics. 1997," AIAA-1997-0973.

[109] Y. Song and J. B. Perot, "CFD Simulation of the NREL Phase VI Rotor," *Wind Engineering*, vol. 39, no. 3, pp. 299-309, 2015.

[110] N. N. Sørensen, J. Michelsen, and S. Schreck, "Navier–Stokes predictions of the NREL phase VI rotor in the NASA Ames 80 ft× 120 ft wind tunnel," *Wind Energy: An International Journal for Progress and Applications in Wind Power Conversion Technology*, vol. 5, no. 2-3, pp. 151-169, 2002.

[111] M. Hand *et al.*, "Unsteady aerodynamics experiment phase VI: wind tunnel test configurations and available data campaigns," National Renewable Energy Lab., Golden, CO.(US), 2001.

[112] G. Jones, J. Lin, B. Allan, W. Milholen, C. Rumsey, and R. Swanson, "Overview of CFD validation experiments for circulation control applications at NASA," 2008.

[113] B. Allan, G. Jones, and J. Lin, "Reynolds-averaged navier-stokes simulation of a 2-D circulation control wind tunnel experiment," in *49th AIAA Aerospace sciences meeting including the new horizons forum and aerospace exposition*, 2011, p. 25.

[114] G. Hoholis, "Assessment of Fluidic Control Effectors Using Computational Fluid Dynamics," University of Liverpool, 2016.

[115] B. Robertson-Welsh, "On the Influence of Nozzle Geometries on Supersonic Curved Wall Jets," The University of Manchester (United Kingdom), 2017.

[116] W. Milholen, G. Jones, and D. Chan, "High-Reynolds number circulation control testing in the national transonic facility," in *50th AIAA Aerospace Sciences Meeting including the New Horizons Forum and Aerospace Exposition*, 2012, p. 103.

[117] G. S. Jones *et al.*, "Development of the circulation control flow scheme used in the NTF Semi-span FAST-MAC model," in *31st AIAA Applied Aerodynamics Conference*, 2013, p. 3048.

[118] G. S. Jones, "Pneumatic flap performance for a 2d circulation control airfoil, steady and pulsed," 2005.

[119] M. Drela, "XFOIL: An analysis and design system for low Reynolds number airfoils," in *Low Reynolds number aerodynamics*: Springer, 1989, pp. 1-12.

[120] A. Karpatne, "Study of compressible flow through a rotating duct," 2015.

[121] W. E. Forsthoffer and W. E. Forsthoffer, *Forsthoffer's Rotating Equipment Handbooks, Vol. 5: Compressors*. Elsevier, 2005.

[122] A. Dumitrache, F. Frunzulica, H. Dumitrescu, and V. Cardos, "Blowing jets as a circulation flow control to enhancement the lift of wing or generated power of wind turbine," *INCAS Bulletin*, vol. 6, no. 2, p. 33, 2014.

[123] R. Golden and D. Marshall, "Design and performance of circulation control flap systems," in *48th AIAA Aerospace Sciences Meeting Including the New Horizons Forum and Aerospace Exposition*, 2010, p. 1053.

[124] K. C. Pfingsten and R. Radespiel, "Experimental and numerical investigation of a circulation control airfoil," in *47th AIAA Aerospace Sciences Meeting Including The New Horizons Forum and Aerospace Exposition*, 2009, p. 533.

APPENDIX

A1. Aerodynamics coefficients of NACA64-A17 aerofoil

AoA (^{O})	C_l	C_d	C_m
-1.80E+02	0.00E+00	1.98E-02	0.00E+00
-1.75E+02	3.74E-01	3.41E-02	1.88E-01
-1.70E+02	7.49E-01	9.55E-02	3.77E-01
-1.60E+02	6.59E-01	2.81E-01	2.75E-01
-1.55E+02	7.36E-01	3.92E-01	3.13E-01
-1.50E+02	7.83E-01	5.09E-01	3.43E-01
-1.45E+02	8.03E-01	6.27E-01	3.65E-01
-1.40E+02	7.98E-01	7.43E-01	3.82E-01
-1.35E+02	7.71E-01	8.54E-01	3.94E-01
-1.30E+02	7.24E-01	9.57E-01	4.01E-01
-1.25E+02	6.60E-01	1.05E+00	4.04E-01
-1.20E+02	5.81E-01	1.14E+00	4.05E-01
-1.15E+02	4.91E-01	1.21E+00	4.03E-01
-1.10E+02	3.90E-01	1.27E+00	3.98E-01
-1.05E+02	2.82E-01	1.31E+00	3.92E-01
-1.00E+02	1.69E-01	1.34E+00	3.84E-01
-9.50E+01	5.20E-02	1.36E+00	3.74E-01
-9.00E+01	-6.70E-02	1.36E+00	3.64E-01
-8.50E+01	-1.84E-01	1.35E+00	3.52E-01
-8.00E+01	-2.99E-01	1.32E+00	3.39E-01
-7.50E+01	-4.09E-01	1.28E+00	3.25E-01
-7.00E+01	-5.12E-01	1.22E+00	3.10E-01
-6.50E+01	-6.06E-01	1.15E+00	2.94E-01
-6.00E+01	-6.89E-01	1.07E+00	2.77E-01
-5.50E+01	-7.59E-01	9.82E-01	2.60E-01
-5.00E+01	-8.14E-01	8.82E-01	2.41E-01
-4.50E+01	-8.50E-01	7.74E-01	2.21E-01
-4.00E+01	-8.66E-01	6.61E-01	2.01E-01
-3.50E+01	-8.60E-01	5.45E-01	1.79E-01
-3.00E+01	-8.29E-01	4.30E-01	1.56E-01
-2.50E+01	-8.53E-01	3.07E-01	1.16E-01
-2.40E+01	-8.70E-01	2.81E-01	1.04E-01
-2.30E+01	-8.90E-01	2.56E-01	9.16E-02
-2.20E+01	-9.11E-01	2.30E-01	7.85E-02
-2.10E+01	-9.34E-01	2.04E-01	6.49E-02
-2.00E+01	-9.58E-01	1.79E-01	5.08E-02
-1.90E+01	-9.82E-01	1.53E-01	3.64E-02
-1.80E+01	-1.01E+00	1.29E-01	2.18E-02
-1.70E+01	-1.08E+00	1.04E-01	1.29E-02

-1.60E+01	-1.11E+00	7.86E-02	-2.80E-03
-1.50E+01	-1.11E+00	5.35E-02	-2.51E-02
-1.40E+01	-1.08E+00	2.83E-02	-4.19E-02
-1.35E+01	-1.05E+00	1.58E-02	-5.21E-02
-1.30E+01	-1.02E+00	1.51E-02	-6.10E-02
-1.20E+01	-9.04E-01	1.34E-02	-7.07E-02
-1.10E+01	-8.07E-01	1.21E-02	-7.22E-02
-1.00E+01	-7.11E-01	1.11E-02	-7.34E-02
-9.00E+00	-5.95E-01	9.90E-03	-7.72E-02
-8.00E+00	-4.78E-01	9.10E-03	-8.07E-02
-7.00E+00	-3.75E-01	8.60E-03	-8.25E-02
-6.00E+00	-2.64E-01	8.20E-03	-8.32E-02
-5.00E+00	-1.51E-01	7.90E-03	-8.41E-02
-4.00E+00	-1.70E-02	7.20E-03	-8.69E-02
-3.00E+00	8.80E-02	6.40E-03	-9.12E-02
-2.00E+00	2.13E-01	5.40E-03	-9.46E-02
-1.00E+00	3.28E-01	5.20E-03	-9.71E-02
0.00E+00	4.42E-01	5.20E-03	-1.01E-01
1.00E+00	5.56E-01	5.20E-03	-1.08E-01
2.00E+00	6.70E-01	5.30E-03	-1.13E-01
3.00E+00	7.84E-01	5.30E-03	-1.16E-01
4.00E+00	8.98E-01	5.40E-03	-1.20E-01
5.00E+00	1.01E+00	5.80E-03	-1.24E-01
6.00E+00	1.10E+00	9.10E-03	-1.23E-01
7.00E+00	1.18E+00	1.13E-02	-1.18E-01
8.00E+00	1.26E+00	1.24E-02	-1.16E-01
8.50E+00	1.29E+00	1.30E-02	-1.16E-01
9.00E+00	1.33E+00	1.36E-02	-1.16E-01
9.50E+00	1.36E+00	1.43E-02	-1.15E-01
1.00E+01	1.38E+00	1.50E-02	-1.15E-01
1.05E+01	1.40E+00	2.67E-02	-1.15E-01
1.10E+01	1.42E+00	3.83E-02	-1.14E-01
1.15E+01	1.43E+00	4.98E-02	-1.15E-01
1.20E+01	1.43E+00	6.13E-02	-1.16E-01
1.25E+01	1.44E+00	7.27E-02	-1.17E-01
1.30E+01	1.45E+00	8.41E-02	-1.15E-01
1.35E+01	1.45E+00	9.54E-02	-1.13E-01
1.40E+01	1.45E+00	1.07E-01	-1.11E-01
1.45E+01	1.44E+00	1.18E-01	-1.10E-01
1.50E+01	1.45E+00	1.29E-01	-1.10E-01
1.55E+01	1.45E+00	1.40E-01	-1.11E-01
1.60E+01	1.45E+00	1.51E-01	-1.11E-01
1.65E+01	1.44E+00	1.62E-01	-1.11E-01
1.70E+01	1.44E+00	1.73E-01	-1.10E-01
1.75E+01	1.44E+00	1.84E-01	-1.08E-01

1.80E+01	1.45E+00	1.95E-01	-1.08E-01
1.85E+01	1.45E+00	2.06E-01	-1.09E-01
1.90E+01	1.45E+00	2.17E-01	-1.09E-01
1.95E+01	1.44E+00	2.27E-01	-1.08E-01
2.00E+01	1.43E+00	2.38E-01	-1.10E-01
2.10E+01	1.40E+00	2.59E-01	-1.17E-01
2.20E+01	1.36E+00	2.80E-01	-1.19E-01
2.30E+01	1.30E+00	3.00E-01	-1.24E-01
2.40E+01	1.22E+00	3.20E-01	-1.39E-01
2.50E+01	1.17E+00	3.38E-01	-1.44E-01
2.60E+01	1.12E+00	3.55E-01	-1.49E-01
2.80E+01	1.02E+00	3.92E-01	-1.58E-01
3.00E+01	9.26E-01	4.29E-01	-1.67E-01
3.20E+01	8.55E-01	4.69E-01	-1.76E-01
3.50E+01	8.00E-01	5.32E-01	-1.90E-01
4.00E+01	8.04E-01	6.45E-01	-2.13E-01
4.50E+01	7.93E-01	7.57E-01	-2.34E-01
5.00E+01	7.63E-01	8.66E-01	-2.55E-01
5.50E+01	7.17E-01	9.71E-01	-2.75E-01
6.00E+01	6.56E-01	1.07E+00	-2.94E-01
6.50E+01	5.82E-01	1.16E+00	-3.12E-01
7.00E+01	4.95E-01	1.24E+00	-3.29E-01
7.50E+01	3.98E-01	1.32E+00	-3.44E-01
8.00E+01	2.91E-01	1.38E+00	-3.59E-01
8.50E+01	1.76E-01	1.43E+00	-3.73E-01
9.00E+01	5.30E-02	1.46E+00	-3.86E-01
9.50E+01	-7.40E-02	1.45E+00	-3.97E-01
1.00E+02	-1.99E-01	1.43E+00	-4.08E-01
1.05E+02	-3.21E-01	1.40E+00	-4.16E-01
1.10E+02	-4.36E-01	1.35E+00	-4.23E-01
1.15E+02	-5.43E-01	1.29E+00	-4.28E-01
1.20E+02	-6.40E-01	1.21E+00	-4.31E-01
1.25E+02	-7.23E-01	1.12E+00	-4.30E-01
1.30E+02	-7.90E-01	1.02E+00	-4.27E-01
1.35E+02	-8.40E-01	9.06E-01	-4.20E-01
1.40E+02	-8.68E-01	7.87E-01	-4.08E-01
1.45E+02	-8.72E-01	6.63E-01	-3.90E-01
1.50E+02	-8.50E-01	5.36E-01	-3.67E-01
1.55E+02	-7.98E-01	4.12E-01	-3.35E-01
1.60E+02	-7.14E-01	2.93E-01	-2.94E-01
1.70E+02	-7.49E-01	9.71E-02	-3.77E-01
1.75E+02	-3.74E-01	3.34E-02	-1.88E-01
1.80E+02	0.00E+00	1.98E-02	0.00E+00